

University Library

Author/Filing Title RODRIGUES, S.

.....
Class Mark T

Please note that fines are charged on ALL
overdue items.

FOR REFERENCE ONLY

0403481678



Mean Field Modelling of Human EEG: Application to Epilepsy

by

Serafim Rodrigues

Advisor

Dr. John Terry

Jury

Prof. Karl Friston (Univeristy College London, Functional Image Laboratory)

Prof. Roger Smith (Loughborough University, Dept. Mathematical Sciences)

A Doctoral Thesis

Submitted in partial fulfillment of the requirements
for the award of

Ph.D. in Mathematics of Loughborough University

December 2006

©by Serafim Rodrigues 2006



Loughborough
University
Pilkington Library

Date 6/2008

Class T

Acc
No. 0403481678

This thesis is dedicated to my Parents

Dedicado aos meus queridos pais, que deram toda as suas vidas para mim e os
meus irmãos...

Contents

1	Introduction	1
1.1	The need to study the central nervous system	1
1.1.1	Why study epilepsy?	2
1.2	The brain as a complex multi-scale system	3
1.2.1	Structure and functionality of the brain	3
1.2.2	Neocortex	3
1.2.3	Theoretical hypothesis and mathematical modelling	6
1.3	Aim and Scope of this work	9
2	Mathematical Framework and Methodologies	12
2.1	Dynamical Systems	12
2.1.1	Ordinary differential equations - ODE	13
2.1.2	Delay differential equations - DDE	14
2.1.3	Dynamics in the hyperbolic space	15
2.1.4	Dynamics in the Centre Space	17

2.1.5	Centre Manifold Reduction	18
2.1.6	Normal Form Theory	19
2.1.7	Separation of time scales	20
2.1.8	Local Bifurcations	21
2.2	Constructive Global Analysis of Hybrid systems	24
2.2.1	Local Stability	26
2.2.2	Poincaré Mappings	26
2.2.3	Global asymptotic stability	28
2.2.4	Impact Maps	29
2.2.5	Quadratic surface Lyapunov functions	30
2.3	Numerical simulation of Delay Equations	33
2.3.1	Implementation of the numerical code	35
2.4	Numerical Continuation	37
2.4.1	XPP-Auto	37
2.4.2	Parameter continuation	37
2.4.3	Continuation of stationary solutions	38
2.4.4	Continuation of periodic solutions	39
2.4.5	Locating Codimension-1 bifurcations	41
2.4.6	DDE-Biftool	42
2.4.7	Continuation of steady state solutions	42

2.4.8	Continuation of periodic solutions	43
3	Field Theories and Brain dynamics	45
3.1	EEG and quantitative states of the brain	45
3.1.1	Sources contributing to EEG	46
3.2	Thalamocortical networks and absence seizures	50
3.2.1	Cellular mechanism of thalamic neurons	51
3.2.2	Spindle waves	52
3.2.3	Slow waves	53
3.2.4	Spike-waves	54
3.3	Macroscopic brain models and EEG	56
3.3.1	Neural Field models	56
3.3.2	Spatial propagation of neuronal activity	62
3.3.3	Population density models	64
3.3.4	Mass Action models	68
4	Analysis of the neural mass corticothalamic model	72
4.1	Corticothalamic Brain Model	73
4.2	Method for the analysis of the EEG data	77
4.2.1	Methodology for Nonlinear data analysis	77
4.2.2	Methodology for Numerical Data	78

4.3	Understanding of absence seizures	79
4.3.1	Results from the corticothalamic model	79
4.3.2	Results from the data	83
4.4	Two-bump solution in a piecewise linear reduction	87
4.5	Analysis of the periodically forced model	89
4.5.1	Forcing function $\phi_{\text{cortical}} = \sin(\omega t)$	90
4.5.2	Description of the spike-wave solution	93
4.6	Summary	95
5	Numerical continuation and Local stability of reduced model (RKII set)	97
5.1	Stability analysis	97
5.1.1	Autonomous case	100
5.1.2	Analysis of RKII set driven by a constant signal	105
5.2	Summary	112
6	Normal forms and Global stability analysis of reduced model (RKII set)	113
6.1	Normal form calculation for an RKII set	114
6.1.1	Notation	115
6.1.2	Setup and Statement	115
6.1.3	Computation of the normal form	119
6.2	Global analysis of limit cycles in the piecewise linear model	123

6.2.1	Limit Cycle γ with period t^*	129
6.2.2	Local stability of Limit cycle γ	131
6.2.3	Global stability of limit cycle γ	132
6.3	Summary	135
7	General discussion and conclusions	136
7.1	Discussion	136
7.2	Future directions	139
7.2.1	Mapping between Neural mass and conductance models	139
7.2.2	Bifurcation and synchronization of piecewise RKII sets	142
7.2.3	Seizure prediction	143
A		145
A.1	Elements of a neuronal system	145
A.2	EEG frequency bands	147
A.3	EEG electrode placement	149
B		150
B.1	First order delay differential equations for the global invariant model	150
B.1.1	Parameters values employed in the model	152
B.2	Frequency domain linear stability analysis and reduced parameter space	152
B.3	DDE-Biftool results for corticothalamic model	154

B.3.1	XPPAuto results for corticothalamic model without delay	158
B.4	Two-bump solution of a reduced piecewise linear RKII set	159
B.4.1	Interval I: $0 \leq t \leq \frac{\hat{b}-\delta}{\omega}$	161
B.4.2	Interval II: $\frac{\hat{b}-\delta}{\omega} < t \leq \frac{\pi-\hat{b}-\delta}{\omega}$	162
B.4.3	Interval III: $\frac{\pi-\hat{b}-\delta}{\omega} < t \leq \frac{2\pi}{\omega}$	163
C		165
C.1	Eigenvalues of the RKII model	165
C.2	Rate of change of Equilibria with respect to parameters	166
C.3	Calculation of the stability curve	167
C.3.1	Stability curve in parameter space	167
C.3.2	The Lienard-Chipart stability criterion	168
C.4	Numerical Bifurcations in RKII set	170
D		171
D.1	Derivation of the Homological Equation	171
D.2	Derivation of the $\mathcal{O}(1)$ normal form coefficients	172
D.3	Derivation of the $\mathcal{O}(2)$ normal form coefficients	173
D.3.1	Derivation of the $\mathcal{O}(3)$ normal form coefficients	176
D.4	Poincaré surface coordinates of the piecewise linear RKII set	179

Acknowledgements

I would like to express my special gratitude to the following people for their support and assistance during my work on this thesis:

John Terry who provided me with excellent and enthusiastic supervision together with continuing motivation and encouragement. I could not have imagined having a better advisor and mentor for my Ph.D. John as well as being my supervisor has been a good friend. Dr. John Ward from Loughborough University for useful discussions. Dr. Michael Breakspear, and Prof. Peter Robinson from the Brain Dynamics Centre (Sydney Australia) for their collaboration. Prof. John Hogan and Dr. Kirk Green from Bristol University for providing guidance in the use DDE-Biftool for delay differential equations equations. Dr. Anton Chizhov from IOFFE Physical-Technical Institute for enlightening many topics in mathematical neuroscience. Dr. Mark Groves from Loughborough University for the indispensable discussions on normal forms theory. Dr. Jorge Gonçalves from Cambridge University for his significant guidance in piecewise linear hybrid systems. This research would not be possible by the financial support given by the Mathematical Sciences Department and also the Sleep Research Centre through Prof. Jim Horn. The mathematical biology group of Loughborough University, for their help and advice. Thanks as well to the academic and support staff of the Mathematical Sciences Department at Loughborough University for their kind assistance in many different ways. My close friends for their understanding and encouragement. Last but not least, my family for their love and support, ever present in my life.

Abstract

Aggregated electrical activity from brain regions recorded via an electroencephalogram (EEG), reveal that the brain is never at rest, producing a spectrum of ongoing oscillations that change as a result of different behavioural states and neurological conditions. In particular, this thesis focusses on pathological oscillations associated with absence seizures that typically affect 2-16 year old children. Investigation of the cellular and network mechanisms for absence seizures studies have implicated an abnormality in the cortical and thalamic activity in the generation of absence seizures, which have provided much insight to the potential cause of this disease. A number of competing hypotheses have been suggested, however the precise cause has yet to be determined. This work attempts to provide an explanation of these abnormal rhythms by considering a physiologically based, macroscopic continuum mean-field model of the brain's electrical activity. The methodology taken in this thesis is to assume that many of the physiological details of the involved brain structures can be aggregated into continuum state variables and parameters. The methodology has the advantage to indirectly encapsulate into state variables and parameters, many known physiological mechanisms underlying the genesis of epilepsy, which permits a reduction of the complexity of the problem. That is, a macroscopic description of the involved brain structures involved in epilepsy is taken and then by scanning the parameters of the model, identification of state changes in the system are made possible. Thus, this work demonstrates how changes in brain state as determined in EEG can be understood via dynamical state changes in the model providing an explanation of absence seizures. Furthermore, key observations from both the model and EEG data motivates a number of model reductions. These reductions provide approximate solutions of seizure oscillations and a better understanding of periodic oscillations arising from the involved brain regions. Local analysis of oscillations are performed by employing dynamical systems theory which provide necessary and sufficient conditions for their appearance. Finally local and global stability is then proved for the reduced model, for a reduced region in the parameter space. The results obtained in this thesis can be extended and suggestions are provided for future progress in this area.

Keywords: Mathematical EEG modelling, Ki sets, generalised epilepsy, Nonlinear dynamics, Normal forms, Bifurcations, Piecewise Linear Systems, Limit Cycles, Global Stability.

Chapter 1

Introduction

In this chapter, an overview of the problem is provided. We first highlight the importance and the complexity in studying the central nervous system and then bring to the attention the theoretical hypothesis under which we pursue our study. A summary of basic neurophysiological terminology can be found in Appendix A.

1.1 The need to study the central nervous system

The central nervous system - the brain - is an intriguing, complex and unique biophysical system. Significantly, it determines the behaviour of an individual organism and allows for it to interact with the surrounding world. The remarkable capabilities of the brain naturally gives rise to challenging questions regarding the underlying mechanisms responsible for all activity arising, in normal and pathological states. Through increasing knowledge of the nervous system, diagnosis and therapy of many neurological disorders such as epilepsy, depression, Parkinson's and schizophrenia has improved. Furthermore, understanding the neurophysiological basis of brain activity may inspire great ideas in other scientific and engineering fields and lead to the development of new technologies. The complexity of the brain is such that neuroscience is now an aggregate of different scientific fields and to unveil the secrets of the brain may only be possible by unifying the efforts of these different methodologies and expertise.

1.1.1 Why study epilepsy?

In particular, this thesis focusses on epilepsy, one the most common neurological disorders, with studies indicating a life-time prevalence of between 0.5% and 1% of the total population [6]. For instance, approximately 2 million people in the United States have epilepsy, and 3% of the general population will experience a seizure at some point in their lives [7]. As a chronic disorder, epilepsy carries significant mortality (> 2000 deaths per annum in the UK) [34] and morbidity [25] as well as reduced quality of life. It is a disease with high medical costs, for example, estimated £1.93 billion per year in the UK alone. The term ‘epilepsy’ encompasses over 40 recognized types of seizure syndromes [117] and because of this variety, diagnosis can be complicated. This diversity arises from the numerous underlying molecular, cellular and network mechanisms, as well as from the spatial and temporal characteristics of the seizure oscillations. These may be observed via electrical recordings using scalp electrodes (EEG). Most seizure types are grouped in two basic categories: partial and generalised. Partial seizures occur within localised regions of the brain, whereas generalised seizures appear throughout the forebrain. If the partial seizure does not cause a disruption of consciousness, it is said to be simple; if it does, then it is referred to as complex. Medical sciences have made significant progress in diagnosis and treatments of both types of seizures leading to the development of a number of anti-epileptic drugs (AEDs) and surgery [140]. The majority of patients have partial epilepsy, of which only 25% have a good response to AEDs and 30% show no response to AEDs at all [53]. In fact, in some cases, chronic use of AEDs can cause toxic syndromes. These patients, with poor or absent response to AEDs, account for the majority of costs and mortality. Alternatively, surgery may provide a cure or alleviate the syndrome if AEDs fail. The goal of surgical treatment is to remove the focal area producing the seizure. However, only a minority of patients are suitable candidates for surgery as some types of seizure lack a well defined focal region, which may happen in the case of generalised seizures and some forms of complex partial syndromes. Furthermore, surgery should be carefully considered after establishing if the correct drugs were used in the diagnosis, seizure frequency, severity of the attacks and risk of the surgery, where in some cases neurological complications can develop [16, 115]. The shortcomings of these existing methods encourage the search for new forms of treatments. One interesting option of study is to try to identify the cellular or network mechanisms by which epilepsy develops (epileptogenesis), as this could provide

a means to control the cellular or neuronal network abnormalities. Importantly, an insight into the control mechanisms could provide a technique to suppress the seizure, which, in turn would provide a novel approach to treatment. While compelling, this direction of study confronts the inherent structural and functional complexity of the central nervous system. Thus, to make progress in linking seizure activity with the underlying physiology, we must begin by understanding the architectural organisation of the brain.

1.2 The brain as a complex multi-scale system

1.2.1 Structure and functionality of the brain

The brain may be viewed as a collection of interconnected neurons (typically 10^{12} in the human brain), and each neuron has approximately 10^4 chemical and electrical synaptic connections in addition to being surrounded by glial cells. At an abstract level we could say that behaviour results due to the direct sum of the neuronal activity. However, this view point does not address the critical issue of neurons processing information at different spatio-temporal scales and their organisation into functional circuits mediating behaviour. Furthermore, macroscopic brain activity could result as more than simply the sum of the involved microscopic dynamics (e.g. single neuron or neural circuitry). Some neuroscientists believe that the brain developed by successive addition of more complex parts and behaviours imposing regulation on more primitive parts [112]. Thus the brainstem, limbic system and neocortex form three distinct levels of increasing complexity both in spatial organisation and evolutionary development.

1.2.2 Neocortex

The top hierarchical level of spatial cortical organisation is described via cytological studies [137], revealing an average cortical thickness of 3mm and having a layered appearance because of differences in the relative densities of different types of neurons at different cortical depths. The total cortical area is divided into 2 *hemispheres* each approximately 400mm in diameter with about 10^{10} neurons. Within each hemisphere exists 10 *lobes* each roughly

170mm in diameter with around 10^9 neurons. Each lobe is defined in terms of prominent features called sulci and gyri formed by the folding of the cortex. Pioneering work of Broca supported the evidence of a regional functional organisation linking an impaired function to well defined regional activation [24]. These regions are more or less 50mm in diameter with nearly 10^8 neurons. They are connected via corticocortical axons which may span 1cm, connecting adjacent gyri (lobes/regions) or linking two separate cortical regions, such as frontal and occipital lobes having axons nearly 20cm long! The largest functional elements have been called cortical fields or *macrocolumns* approximately 0.5 – 3mm in diameter and 10^5 - 10^6 neurons reflecting ensemble activation in response to a stimulus.

This range of spatial operation is reported by several authors using techniques such as EEG [113], functional Magnetic Resonance Imaging (fMRI) [112] or experiments using a Golgi-staining method [19] showing that within a macrocolumn the majority of cells project their axons to distances, of no more than 3mm. Furthermore, high-resolution techniques indicate subdivisions (possibly overlapped) of cortical fields (*columns*) [24, 86] or *laminar-vertical* organisation of neurons with a diameter in the range of 0.3mm and with about 10^3 - 10^4 neurons forming a unit with a precise function, for instance a response to a specific stimuli (e.g. the visual cortex). This type of modular unit is defined by the spatial extent of its extracortical-columnar input. That is, cortical axons that are not specific to sensory input (limbic and brainstem systems) but originate from another column. Quantitative anatomic estimates, suggest there exists 2×10^6 columns where each project excitatory axons to between 10 and 100 other columns and receive input from a similar number [158]. This high degree of interconnectivity makes it difficult to define any specific ‘neural circuit’.

Smaller scale activations are measured using extracellular electrodes which determines neural ensemble activity spanning $10\mu m$ or more. These methods include Single Unit Activity (SUA) and Multi Unit Activity (MUA) [3, 99] and Local Field Potentials (LFP), of the order mm to cm scale [76, 118]. At small spatial scales the complexity of neural interactions increases dramatically and the lack of specificity of intracortical connections contradicts the traditional view of the neural circuit (micro circuits). Neurophysiological data demonstrates a high degree of interconnectivity among neurons which suggests the idea of a ‘neural thong’, which is not a circuit in the traditional sense but rather a mass of tissue [26]. These views are supported by quantitative anatomical findings which shows that almost every cortical neurons

lies within two or three synapses of any other cortical neuron and are densely interconnected with approximately 4-km of axon length per cubic millimetre [19]!

However, other experimentalists continue to seek a basic functional unit. The *minicolumn*, approximately $20 - 50\mu\text{m}$ in diameter and containing roughly 10^2 neurons, has been proposed as the basic unit [112]. These units can be defined by the characteristic short lateral spread of axons of inhibitory interneurons. The axons of these cells run along the minicolumn axes, so that interneurons are more densely connected along the cortical depth. These findings are supported by physiological experiments using extracellular electrodes which show high correlation of electric potentials at different locations along the axes, whereas lateral shifts of the electrodes beyond the diameter of minicolumns have lower correlations. Estimates suggest that approximately 85% of cortical neurons are pyramidal cells and the remaining inhibitory interneurons [19], implying a column might be subdivided into approximately 100 minicolumns. Furthermore, physiologists conjecture that minicolumns sharpen the boundaries of modules by inhibiting pyramidal cells of adjacent columns, thereby limiting dynamic interactions to more local regions [112]. A schematic of the multiscale structure of the brain is illustrated in Fig 1.1.

Having considered the spatial extent, we now focus on temporal issues. The time scales of processes occurring at the macro-column scale vary dramatically and most of these activities occur simultaneously. For instance, multiple methods of information transfer occur concurrently at different time scales over short distances [26]. These include reciprocal synapses directly between adjacent dendrites [129], fast chemical transport, and the passive spread of extra-cellular fields that can excite adjacent neurons [159, 160].

A neuron itself is an elaborate dynamical element with a number of diverse dynamical processes occurring on different time scales ranging from sub-milliseconds (opening and closing of single ionic channels) to seconds (flow of ‘slow’ ionic currents), minutes (changes in synaptic conductances), days (growth and development of new synaptic connections) and decades (death of neurons). Each neuron generates a brief electric impulse which lasts $1 - 2\text{ms}$ and is sent along its axon, which synapses into the next neuron. The electric impulse stimulates the next neuron generating a post-synaptic potential at the level of the dendrites, which lasts about 1 to 10ms . The extracellular field produced by an action potential is less than the

diameter of a minicolumn [1] which suggests nonsynaptic interactions between neurons within the same minicolumn. Thus the concept of ‘neural circuitry’ at small scales may also be inaccurate. A burst of action potential discharge from corticocortical columns produces excitatory input to other corticocortical columns. Since the distance between columns vary, their activation depends on the rise times of post-synaptic potentials and on delays due to finite velocity of action potential propagation (6-9m/second in myelinated axons). For instance, in columns linked by small axons about 1cm in length, i.e. connected to an adjacent lobe, the activation delay neglecting the post-synaptic potential is 1ms. Whereas, delays along long axons 20cm in length are around 20 to 30ms. However, corticocortical axons consistently tend to project more densely to close regions than to remote ones, which suggests the possibility of travelling waves at relatively large scales spanning 1cm or more. All these processes occurring at different spatio-temporal scales give rise to complex behaviour such as oscillations, synchronisation and regularisation and as well as changes in the structure of local connectivity which is believed to be related to learning or even to more complex behaviour.

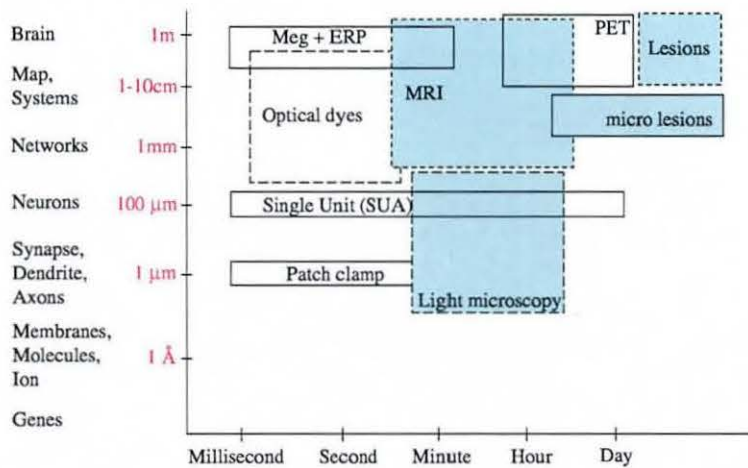


Figure 1.1: *Levels of neural organisation and spatial temporal scales at which experimental studies of brain systems are performed. Figure adapted from Churchland and Sejnowski [33].*

1.2.3 Theoretical hypothesis and mathematical modelling

Systematic experimental results on the multi-scale characteristics of the brain have induced a number of theoretical and modelling approaches. The concept of *modularity* proposed by

Fodor suggested that the brain is composed of modules that perform ‘computations’ [56]. Modularism is an empirical formulation based on lesion studies and pathological damage in humans and reflects the underlying structure of rational thought and not the anatomy and physiological structure of the brain. Alternatively, Shepherd considers the brain as being composed of *functional units* and these elementary units are formed at different levels of organisation [143]. The general approach here is to model brain function using networks. However, the limitations of network theory stems from its failure to deal with the hierarchical organisation of the brain: microscopic, mesoscopic and macroscopic. The previously highlighted experiments demonstrate that at small scales the concept of ‘neuronal networks’ is not well established, at least when attempting to model a complex system such as the neocortex. However, network theory suffices to model neural chains in limbic and brainstem systems (e.g. sensorimotor systems).

Additionally, scientific theory must make connections to experiments determining laws that characterise the observations. The *dynamical hypothesis* by Gelder [61] proposes that the same laws that govern physical systems also govern the laws of cognitive systems, and that therefore, cognitive science should use dynamical systems theory rather than syntax rules. This view assumes that the brain operates on many spatio-temporal levels of organisation. However, one of the reasons for the great progress seen in the study of non living matter is the presence of the so-called *separation of scales* between fundamental forces of nature. *Separation of scales* is a mathematical technique that allows to subdivide a complex problem into smaller and manageable building blocks, each having a set of rules of interaction on various scales. However, the presence of *separation of scales* in complex living matter, such as the central nervous system, is not apparent and is still a source of great debate among neuroscientists. One explanation for the uncertainty of this approach in neuroscience is the fact that many processes in the brain operate on several spatial and/or temporal scales, thus providing strong interactions between them. For instance, neurons produce spikes whose timing is in some cases up to a millisecond precise [17, 103, 166]. On the other hand, there are examples showing that a lot of information is transmitted between neurons via variations in the average firing rate, which occur on the time scale of hundreds of milliseconds [18, 71]. Thus, it is still unclear when and how to ‘coarse-grain’ in order to move from one scale to another, as well as if this procedure is applicable at all. This difficulty leaves open the question of what is most important in the ‘neural code’, precise spike timing or average firing rate?

The emerging answer seems to indicate that both of them are essential and that their relative importance may depend on the situation and context [48, 101, 111, 165]. It may therefore be impossible to separate temporal scales in this case and the dynamical processes with time scales from 1 ms to 100 ms or even minutes should be analyzed simultaneously. Despite this latter argument, *dynamics* - the modelling of change, is applicable at every level, from subcellular to populations of neurons and using this theory mathematical models have proven successful in characterising neuronal events at various scales. For example, *Axonal activity* by Hodgkin and Huxley [73] which allowed one to explain the generation of action potentials, and the extension of the dynamical equations using the cable equation explained the propagation of electric activity along the axon. Assemblies of interconnected neuron models have been shown to display synchrony and local oscillations [62]. Large scale simulations whereby the trajectory of individual neurons are followed have been valuable in providing hypothesis of how brain activity might be organised. An example of latter is a simulation of an orientation hypercolumn of the visual cortex providing new insight into the origin of orientation in the visual cortex [147].

The extreme complexity of neural interactions at small scales, in which dynamic function is determined largely by physiological parameters of unknown magnitudes, provides substantial motivation for the development of macroscopic theories of neocortical dynamics - *Neural field theory*. The neural field theory views brain operation at hierarchical levels above the single neuron, i.e the principal functional unit is a neural-ensemble (e.g. cortical column in the cortex or glomerulus in the olfactory bulb) and not a single neuron. Properties of neuronal-ensembles differ as much from those of a neuron as neuron properties differ from those of a patch membrane. Different field theories have been developed, however, these are in general all tied to the *brain redundancy hypothesis*. This assumes that strongly interconnected neurons within a column have approximately the same pattern of synaptic connections and respond similarly to very nearly identical stimuli. This redundancy might have various purposes, for example, to increase reliability. Because of redundancy, we can study networks of local populations of neurons by using continuum averages to obtain variables representing for example the average number of action potentials generated by the neurons from a cortical column per unit time, or any other averaged neuron characteristic. An example of this form of modelling approach is that of Wilson and Cowan [169] where they use continuum variables to describe the average time activity of the interaction of inhibitory and excitatory neural populations of specific

regions in the brain. An interesting application of this modelling approach was used to make quantitative comparisons with the measured response of a rat whisker barrel neurons and the resulting model provided insight in the understanding of spatial and temporal integration of ensemble activity [124]. Alternatively, studies by Freeman [57] through physiological experiments determined the dynamical model equations characterising the response dynamics of a neural mass (generally columns) when stimulated by electrical currents. These studies demonstrate that the neural-mass can be thought of as the principal functional unit to appropriately characterise EEG and this is the approach chosen herein.

1.3 Aim and Scope of this work

One form of generalised epilepsy that has received particular attention during the last two decades, and that this work further explores is the absence (or *petit-mal*) seizure [125]. These seizures typically affect 2-16 year old children, and are associated with loss of cognitive abilities and behavioural arrest, which may last a few seconds. When returning to normal activity the patients have no memory of the event. Since these seizures can occur tens or hundreds of times a day, an incorrect diagnosis of attention-deficit disorder or daydreaming is frequently made. There is a classic pattern of three per second, generalised spike-wave discharges observed in EEG during petit-mal seizures. This is illustrated in Fig 1.2 showing an intracranial EEG trace.

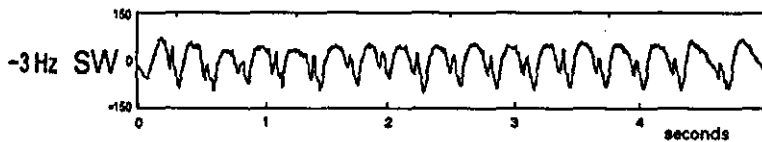


Figure 1.2: A 3Hz spike wave intracranial EEG trace of a patient undergoing an absence attack. (Figure adapted from [157]).

For many years, the anatomical origin of absence seizures and the accompanying EEG pattern were debated. The results of some experiments supported the hypothesis that absence seizures originated in the thalamus. For example, electrical stimulation of the thalamus in cats produced synchronous EEG discharges that resembled the absence pattern [81]. Also, record-

ings from electrodes implanted in the thalamus of a child with absence epilepsy demonstrated three-per-second EEG discharges during typical seizures [167]. Other work, suggested that the cerebral cortex itself was the primary origin of these seizures. For example, similar EEG discharges can be produced by applying proconvulsant agents to the cortical surface [105]. The mechanism that generates absence seizures is now believed to involve an alteration in the circuitry between the thalamus and the cerebral cortex [58, 93, 145]. The accepted *thalamocortical loop hypothesis* for the epileptogenesis of absence seizure is supported by electrophysiological *in-vivo* recordings (i.e. measuring directly from live neurons in an animal) and from *in-vitro* neural-tissue slice preparations. In addition, neuronal network models [43, 151] have complemented mostly *in-vitro* recordings which have allowed a hypothesis of a possible ‘control mechanism’ within the circuitry loop causing the seizure. However, these models have only been able to replicate the *in-vitro* findings which have led to some controversies about the ‘control mechanism’ in the *thalamocortical loop* [39, 123]. Thus this work is driven by the controversies and difficulties in implementing neuronal models at the microscopic scale by alternatively proposing Freeman type macroscopic scale models [57] inspired by the *thalamocortical loop* findings. This type of approach is appropriate since during seizure, the brain enters a hypersynchronous state entraining nearby neural-mass to the same dynamical oscillations. The second motivation for this approach is because scalp EEG is a non-invasive technique and is readily available to easily assist diagnosis.

The rest of this thesis is arranged as follows: **Chapter 2** provides a general introduction to dynamical systems theory, bifurcation analysis, normal forms and computational tools that allows analysis of dynamical models. A section is also provided on the implementation of the numerical integration and bifurcation code we developed to analyse our systems of equations. We further introduce the concept of hybrid systems and piecewise linear systems and show how this method can be used to understand oscillations in high dimensional systems. In particular, this theory enables a proof of global stability of periodic solutions appearing in dynamical models. These solutions are ubiquitous in brain oscillations, particularly in epilepsy, and understanding their local and global properties is crucial. **Chapter 3** gives an introduction to the theory and mathematical description of EEG explaining the origin of electric potential appearing in extracellular space. The complexity of the brain makes these mathematical first principles inadequate to interpret spatio-temporal dynamics generally observed in EEG. This difficulty leads to alternative mathematical approaches termed *neural*

fields, population density and mass action. In particular this thesis follows the *mass action* framework as it based on electrophysiological experiments measuring local field responses of neural masses to stimuli or induced by electrical pulses. We also review the main brain structures believed to be implicated in absence seizures. Previous experiments and detailed computational models have clarified many competing hypotheses in the literature and the overriding hypothesis explaining these types of seizures is presented. However, controversies on the underlying mechanisms for epileptogenesis still persist mostly because of the difficulty in replicating *in-vivo* activity observed when measuring the implicated neurons. Despite this difficulty, ‘order parameter field models’ (i.e. models that lump important variables of a physical system into a parameter) can still be applied and by applying bifurcation theory it is possible to search for the important activity transitions in the parameter space. Thus the main methodology used in this thesis is *neural mass - order parameter field models* (a combination of mass action models and some features of neural field models). **Chapter 4**, presents the mathematical formulation of the *neural mass - order parameter field model* which incorporates key brain structures implicated in absence seizures. We then demonstrate how changes in brain state as determined using EEG can be understood via dynamical state changes in the model, which then provides an explanation for the observed pathological oscillations. Various key observations in the global model leads us to a reduction of the model which allows for some analytical interpretation of spike-wave activity. The solutions are termed ‘two-bump’ solutions as they resemble spike-wave forms, however they are not spike-wave as these are only approximations and a possible interpretation. **Chapter 5** is motivated by these reduction findings and we further investigate these oscillations by applying numerical continuation tools to understand the bifurcations appearing in this system and also by presenting analytical conditions for their appearance. **Chapter 6** further extends the results from chapter 5 by applying normal form theory to the reduced system and then finally we apply hybrid systems and piecewise linear systems to prove global stability of the periodic oscillations appearing in the model, however in a restricted parameter set of the model. **Chapter 7** concludes this thesis by outlining the contributions achieved and suggests possible future work. All relevant material and calculations performed in the thesis are provided in the appendix and numerical codes developed are to be found in the attached CD.

Elements of chapter 4 appear in [21] and [136]. Results from Chapter 6-7 have been submitted and are available as a preprints [134, 135].

Chapter 2

Mathematical Framework and Methodologies

This chapter reviews some of the mathematical and computational methodologies used in this thesis. The first section introduces relevant theory from dynamical systems, bifurcation analysis and normal forms. Here we assume that an ensemble of neurons can be represented as a dynamical system. The next section introduces a new approach for the analysis of hybrid systems and piecewise linear dynamical systems. The proposed approach allows for investigation of some of the global properties of a system. The following section provides the ideas used to implement the numerical simulation code to find approximate solutions of dynamical systems with delays and associated bifurcation diagrams. The final section then considers a brief discussion of continuation packages to numerically analyse the solution behaviour of a dynamical system.

2.1 Dynamical Systems

The notion of a dynamical system is the mathematical formalisation of the general scientific concept of a *deterministic process*. The future and past states can be computed to a certain extent by the present state and the laws governing their evolution, provided these laws do not change in time.

Definition 2.1.1 A dynamical system is a triple $\{T, U, \Phi^t\}$, where T is a time set, U is a state space, and $\Phi^t : U \rightarrow U$ is a family of evolution operators parameterised by $t \in T$.

For the precise definition and proofs refer, for example, to [20]. The state space U can be any differential manifold, such as a circle, sphere or torus. However, this thesis will only consider the Euclidean domain. T is a unidimensional set representing time. For example when $T \in \mathbb{Z}$ the system is called a map, however when $T \in \mathbb{R}$ the dynamical system is called a *flow*. Generally the flow is a solution to an initial value problem and we only consider the following types: *Ordinary Differential Equations* (ODEs), *Delay Differential Equations* (DDEs) and *Delay Partial Differential Equations* (DPDEs). In particular for DPDEs a search for global uniform solutions in an infinite domain allows the reduction of this description to an DDE. Furthermore, in some cases it is possible to reduce a DDE into an ODE.

2.1.1 Ordinary differential equations - ODE

In this framework, the evolution of the system is described in terms of a relationship that contains functions of only one independent variable (usually time), and one or more of its derivatives with respect to the state variables. This may be written in the following form:

$$\begin{cases} \dot{x} = F(x, \nu) \\ x(0) = x_0, \end{cases} \quad (2.1)$$

where x_0 is the initial state and $F \in C^k(\mathbb{R}^n \times \mathbb{R}^m, \mathbb{R}^n)$ is the tangent field of the flow (a vector field) given by

$$F(x, \nu) = \frac{d\Phi^t(x)}{dt},$$

where ν should be thought of as the control parameters. The term *dynamics* generally denotes the description of solution behaviour obtained through quantitative, qualitative or numerical techniques. Moreover, the solution $x(t) = \Phi^t(x_0) : I \times U \rightarrow U$ is guaranteed to exist and be unique in some interval $I = (-\tau_1, \tau_2), \tau_i > 0$ by the smoothness of F . Furthermore, the following conditions hold for any initial condition x_0 and any $t, s \in T$:

1. If $T \in \mathbb{R}$ the flow is continuous. If $T \in \mathbb{Z}$ the flow is discrete

2. The flow preserves the identity, i.e $\Phi^0(x_0) = x_0$ (no time, no evolution)
3. The flow maps a point in phase space back into the phase space; that is, $\Phi^{t+s}(x_0) = \Phi^t(\Phi^s(x_0))$ (determinism).

An *orbit* is a set of the form $Or(x_0) = \{x : x = \Phi^t(x_0), t \in I\} \subset U$ and the *phase portrait* is the classification of the different types of orbits in the phase space. In particular two special solutions that can occur on a vector field are:

1. *Stationary solutions* (or equilibria) $x^* \in U$ are those that solve $F(x^*, \nu) = 0$. Equivalently, we have $\Phi^t(x^*, \nu) = x^*$ for all $t \in \mathbb{R}^n$ and hence $\{x^*\}$ is invariant.
2. *Periodic orbits* (or limit cycles) are points $x^* \in U$ such that there exists $\tau \in \mathbb{R}$ ($\tau > 0$) and $\Phi^\tau(x^*, \nu) = x^*$. The periodic orbit is defined as the closed curve $\{x : x = \Phi^t(x^*), 0 \leq t < \tau^*\}$, where τ^* is the smallest number τ such that $\Phi^\tau(x^*, \nu) = x^*$, and it is called the period of the periodic orbit.

2.1.2 Delay differential equations - DDE

A delay equation depends on both the present and previous state of the system. This work focusses on delay equations with a single fixed delay which is represented as follows:

$$\begin{cases} \dot{x} = F(x(t), x(t-\tau), \nu), & t > 0 \\ x(t) = \varphi(t), & t \leq 0 \end{cases} \quad (2.2)$$

where $F \in C^k(\mathbb{R}^{2n} \times \mathbb{R}^m, \mathbb{R}^n)$ and $\tau \in \mathbb{R}$ is the fixed delay, while $\nu \in \mathbb{R}^m$ represents a number of control parameters and the functional component $\{x(t-\tau), -\tau < t-\tau < 0\}$ represents past states. The existence of a unique solution requires a continuous function (*history*) as initial data on the interval $[-\tau, 0]$, i.e $\varphi : [-\tau, 0] \rightarrow \mathbb{R}^n$. The latter implies that the phase space is an infinite dimensional space of continuous functions with values in the physical space \mathbb{R}^n . Denoting the infinite dimensional space as \mathcal{C} then $\varphi \in \mathcal{C}$ (contrast this with an ODE setting where both physical space and state space are \mathbb{R}^n). The evolution operator is now defined as $\Phi^t(\varphi) : \mathcal{C} \rightarrow \mathcal{C}$ which describes how the initial conditions $\varphi \in \mathcal{C}$ evolve in time, t . The solution is then given by a vector valued function $x(t) : [0, \infty) \rightarrow \mathbb{R}^n$.

2.1.3 Dynamics in the hyperbolic space

Once a dynamical system is defined it is necessary to study the solution behaviour in different regions of its phase space. To predict the directions taken by phase trajectories of a system at some location x of the phase space, one can compute the gradient of the flow in each direction of x (i.e. evaluate the partial derivatives of the flow). The formalisation of this process is given below, which under certain conditions will determine trajectories of the system. Consider the vector field (2.1) with an isolated equilibrium $x^* \in U$ and let J be the partial derivative of F with respect to x at (x^*, ν^*) , i.e.

$$J = DF(x^*, \nu^*) = \left(\frac{\partial F_i}{\partial x_j} \right)_{i,j=1,\dots,n}.$$

Consider that the parameter(s) ν are fixed. Let $\sigma \in \mathbb{C}$ be the spectrum of J , i.e. the set of all complex eigenvalues of J , where an eigenvalue of the matrix J is a scalar $\lambda \in \sigma$ such that the system of equation $(J - \lambda)e = 0$ has nontrivial solutions. The eigenvalues are then solutions to the *characteristic polynomial* $\det(J - \lambda I) = 0$. Furthermore, suppose that $E = \{e_1, \dots, e_m\} \subset \mathbb{R}^n$ is the set of generalised eigenvectors of J (i.e. the set of eigenvectors of J that solve in e the above system of equations which form a vector space with a basis in \mathbb{R}^n and such that the action of the matrix J on E as an operator becomes one of scalar multiplication). These sets can be split into three disjoint sets in the following way:

1. Let $E_s = \text{span}\{e_1, \dots, e_{m_1}\}$ be the stable linear-invariant subspace corresponding to the eigenvalues of J having negative real part, i.e $\sigma_s = \{\lambda \in \sigma | \text{Re}\lambda < 0\}$.
2. Let $E_u = \text{span}\{e_{m_1+1}, \dots, e_{m_2}\}$ be the corresponding unstable subspace associated to the eigenvalues having positive real part $\sigma_u = \{\lambda \in \sigma | \text{Re}\lambda > 0\}$.
3. Let $E_0 = \text{span}\{e_{m_2+1}, \dots, e_m\}$ be the centre space corresponding to the eigenvalues of J having zero real part, i.e $\sigma_0 = \{\lambda \in \sigma | \text{Re}\lambda = 0\}$.

The phase space is then the direct sum of the subspaces, that is, $\mathbb{R}^n = E_s \oplus E_0 \oplus E_u$. Let also $E^h = E_s \oplus E_u$ denote the hyperbolic space. Furthermore we have the following definitions for stationary solutions:

Definition 2.1.2 *The equilibrium point x^* is called*

1. *hyperbolic if J has no eigenvalues with zero real parts. More precisely that $\det J \neq 0$.i.e, is nonsingular.*
2. *non-hyperbolic if J has at least one eigenvalue with zero real part. It may still be non-singular.*
3. *elliptic, if all eigenvalues have zero real part (but requires that the imaginary parts are not zero).*

The dynamics in the hyperbolic space is given locally by the flow $x(t) = e^{Jt}$ and its qualitative behaviour is completely given by the spectral properties of the linear map J . This is given in the following Theorem:

Theorem 2.1.1 (Hartman-Großman) *If the dynamical system (2.1) has an isolated hyperbolic equilibrium $x^* \in U$, then (2.1) is locally topologically conjugate to its linearisation*

$$\dot{x} = Jx. \quad (2.3)$$

That is, there is a local homeomorphism (continuous mapping with continuous inverse) $f : \mathbb{R}^n \rightarrow \mathbb{R}^n$ taking each orbit $\Phi^t(x)$ of (2.1) to an orbit in $\Psi^t(x)$ of (2.3). The homeomorphism is not required to preserve parameterisation in time; that is, for any x and t , there is a t_1 , which could differ from t , such that

$$f(\Phi^t(x)) = \Psi^{t_1}(f(x)).$$

If it preserves time parameterisation ($t = t_1$), the equivalence is called conjugacy.

If the system has initial condition, x_0 , in E_s or E_u , then $x_0 e^{tJ}$, remains in E_s or E_u for all t . Thus for any dynamical system with hyperbolic equilibrium x^* , the flow will remain on the following invariant sets:

$$\begin{aligned} M_s^{loc}(x^*) &= \{x \in U : \Phi^t x \rightarrow x^*, t \rightarrow \infty, \Phi^t x \in U \text{ for } t \geq 0\} \\ M_u^{loc}(x^*) &= \{x \in U : \Phi^t x \rightarrow x^*, t \rightarrow -\infty, \Phi^t x \in U \text{ for } t \leq 0\} \end{aligned}$$

M_s^{loc} and M_u^{loc} are the local submanifolds of U with the same dimensions as E_s and E_u and tangent to these eigenspaces at x^* . The corresponding global manifolds allowing time to flow forward/backward for the unstable/stable respectively are defined as

$$\begin{aligned} M_s(x^*) &= \bigcup_{t \leq 0} \Phi^t(M_s^{loc}(x^*)) \\ M_u(x^*) &= \bigcup_{t \geq 0} \Phi^t(M_u^{loc}(x^*)) \end{aligned}$$

Local stable (unstable) manifolds corresponding to distinct equilibria points cannot intersect. However, intersections of stable and unstable manifolds of distinct equilibrium points or of the same fixed points can occur. Such intersections are the source of complex dynamics.

2.1.4 Dynamics in the Centre Space

The flow of a dynamical system is considerably different if some of its eigenvalues have zero real part. In the directions of the phase space where the eigenvalues have zero real parts the systems behaviour cannot be predicted by Theorem 2.1.1. Thus the flow of the linear version of a system cannot be directly related with its nonlinear counterpart. Fortunately, in this case, one can address whether the nonlinear system possesses a manifold having similar properties to the linear space spanned by the centre eigenspace and this can be answered by the following centre manifold theory.

Theorem 2.1.2 (Centre Manifold) *Suppose the following dynamical system*

$$\dot{x} = Jx + N(x, \nu), \quad x \in \mathbb{R}^n, \nu \in \mathbb{R}^m. \quad (2.4)$$

If the spectrum σ_0 of J is nonempty, then there exists a nonlinear mapping

$$h \in C^k(E_0 \times \mathbb{R}^m, E_h), \quad h(0, 0) = 0, \quad Dh(0, 0) = 0$$

and a neighbourhood U of $x = 0$ in \mathbb{R}^n such that the centre manifold

$$M_0^\nu = \{(z, h(z, \nu)) | z \in E_0\}, \quad |\nu| \ll 1$$

has the following properties:

1. (Invariance) The centre manifold M_0^ν is locally invariant with respect to (2.4). More precisely, if an initial state $x(0) \in M_0^\nu \cap U$, then $x(t) \in M_0^\nu$ as long as $x(t) \in U$. That is, $x(t)$ can leave M_0^ν only when it leaves the neighbourhood U .
2. (Attractivity) If the unstable subspace $E_u = \{0\}$, that is, if no eigenvalues of J has positive real part, then the centre manifold is locally attractive. That is, all solutions staying in U tend exponentially to some solution of (2.4) on M_0^ν .

The centre manifold M_0^ν is parameterised by $z \in E_0$ and therefore it has the same dimension as the centre space E_0 . Moreover, it passes through the origin $x = 0$ and is tangent to E_0 at the origin. The centre manifold is not unique, though any two such manifolds have the same initial terms in their Taylor series.

2.1.5 Centre Manifold Reduction

To find the centre manifold and the restriction of (2.4) to it, the Iooss and Adelmeyer methodology [78] is employed in this thesis. Let Π_h and Π_0 be projectors from \mathbb{R}^n to the subspaces E_h and E_0 respectively. It is required that

$$\ker \Pi_h = E_0, \quad \text{and} \quad \ker \Pi_0 = E_h,$$

that is, $\Pi_h E_0 = 0$ and $\Pi_0 E_h = 0$. The projectors can easily be found by determining the dual basis to E_0 and E_h . Recall, that the set of row-vectors f_1, \dots, f_m is dual to the set of columns vectors e_1, \dots, e_m if it satisfies the *Kronecker delta* function:

$$\langle e_i, f_j \rangle = \sum_k^m e_{ik} f_{jk} = \delta_{ij} = \begin{cases} 0 & i \neq j \\ 1 & i = j \end{cases}$$

where $\langle \cdot, \cdot \rangle$ is the inner product of two vectors. The projectors are then given by

$$\Pi_h = \sum_{i=1}^{m_2} e_i f_i \quad \text{and} \quad \Pi_0 = \sum_{i=m_2+1}^m e_i f_i.$$

Notice that $\Pi_h + \Pi_0 = I$, where I is the identity matrix. The projectors also commute with the Jacobian J , that is,

$$\Pi_h J = J \Pi_h \quad \text{and} \quad \Pi_0 J = J \Pi_0.$$

Let $x(t)$ be the solution of (2.4) such that $x(t) \in M'_0 \cap U$. Since by invariance the solutions stays on M'_0 for some time t , then it be can represented as the following near identity transformation:

$$x(t) = z(t) + h(z(t), \nu) \quad (2.5)$$

where $z(t) = \Pi_0 x(t)$ is the projection onto the centre subspace E_0 . Differentiating this with respect to t and using equation (2.4) gives

$$\dot{z} + Dh(z, \nu)\dot{z} = Jz + Jh(z, \nu) + N(z + h(z, \nu), \nu) \quad (2.6)$$

It is now possible to project both sides of the above equation (2.6) to E_0 and to E_h . Since $\Pi_0 Jh(z, \nu) = 0$ and $\Pi_h Jz = 0$ two equations are obtained, the first one gives the flow on the centre manifold:

$$\begin{cases} \dot{z} = J_0 z + \Pi_0 N(z + h(z, \nu), \nu), \\ \dot{\nu} = 0 \end{cases}$$

and the second equation is a quasi-linear partial differential equation that can be used to determine the unknown function h as follows:

$$Dh(z, \nu)\dot{z} = J_h h(z, \nu) + \Pi_h N(z + h(z, \nu), \nu)$$

2.1.6 Normal Form Theory

Normal form theory allows one to reduce an analytical vector field to a simpler set of system equations describing the flow locally near a fixed point. The simpler set of equations contains the essential terms of the Taylor series of the vector field.

Theorem 2.1.3 (Normal Form) *There are polynomials $P \in C^k(\mathbb{R}^n \times \mathbb{R}^m, \mathbb{R}^n)$ and $G \in C^k(\mathbb{R}^n \times \mathbb{R}^m, \mathbb{R}^n)$ of degree $\leq k$ with $P(0, 0) = 0$, $D_z P(0, 0) = 0$ and $G(0, 0) = 0$ and $D_z G(0, 0) = 0$ such that by the near identity transformation*

$$x = \tilde{x} + P(\tilde{x}, \nu) \quad (2.7)$$

equation (2.4) transforms to the following

$$\dot{x} = J\tilde{x} + G(\tilde{x}, \nu) \quad (2.8)$$

where $G(\tilde{x}, \nu)$ is the normal form in a new coordinate system \tilde{x} containing only the essential terms of the Taylor series of $N(x, \nu)$ around $x = 0$.

The Ioss and Adelemyer method makes it possible to combine the centre manifold and normal form reduction in one unique step. This technique was initially proposed by Elphick [49], where it was shown that it is always possible to find a near identity coordinate transformation that maps the centre space to the hyperbolic space and one can then incorporate this transformation directly into the normal form. It is found in [49] that the near identity transformation (2.7) can be substituted by (2.5). In this case, equation (2.8) is instead transformed to a new coordinate system, having the following form:

$$\dot{z} = Jz + G(z, \nu). \quad (2.9)$$

With this polynomial substitution it is possible to find the so called homological operator which allows one to evaluate the coefficients of the reduced vector field $G(z, \nu)$ and the reduction function $h(z, \nu)$ in one unique computation. However, the procedure differs from other methodologies (for example Birkhoff normal form) in that it does not perform the Taylor expansion directly, rather it assumes that the structure of the vector field on the centre manifold is known. The Ansätze of the reduced vector field and the near identity transformation are inserted into the homological operator to obtain the coefficients. Under this observation we obtain the homological operator by substituting equation (2.9) into (2.6) and rearranging terms which results as

$$Jh(z, \nu) - D_z[h(z, \nu)](Jz) = G(z, \nu) - N(z + h(z, \nu), \nu) + D_z[h(z, \nu)](G(z, \nu)). \quad (2.10)$$

2.1.7 Separation of time scales

A direct application of the centre manifold is the so called separation of time scales, a method often used in neural field models. Consider a generic two-dimensional system given by the following

$$\begin{aligned} \frac{dx}{dt} &= \frac{1}{\tau_x} F(x, y), \\ \frac{dy}{dt} &= \frac{1}{\tau_w} G(x, y), \end{aligned}$$

where τ_x and τ_w are time constants. If $\tau_w \gg \tau_x$ then the time scale that governs the evolution of x is much faster than that of y . In this case y can be treated as a constant in the fast equation and the fast system will evolve in time until it reaches a (possibly time dependent)

steady state $x_{ss}(y, t)$ which depends on the “parameters” y . Note that this procedure is only valid if the fast variable has a unique solution when holding the slow variable fixed. That is, suppose the slow variable is varied in a nearby region, then there must be only a single behaviour for the fast system. Substituting the steady state solution $x_{ss}(y, t)$ into the slow system the following reduced system is obtained:

$$\frac{dy}{dt} = \frac{1}{\tau_w} G(x_{ss}(y, t), y).$$

If the fast system tends to a time-dependent solution, such as a periodic solution, then it is possible to apply the “Averaging Theorem” which states that the behaviour of

$$\frac{dy}{dt} = \frac{1}{\tau_w} G(y, t), \quad \text{with} \quad G(y, t + T) = G(y, t),$$

is close to the behaviour of the averaged system

$$\frac{d\bar{y}}{dt} = \frac{1}{\tau_w T} \int_0^T G(\bar{y}, T) dT,$$

where T is the period of the system, \bar{y} is the average of the system and the resulting averaged equations depends only on the slow variables.

2.1.8 Local Bifurcations

Bifurcation theory is concerned with the persistence of steady state solutions and the change of the flow of a dynamical system as the system parameters are varied. Smoothly changing the system parameters corresponds to a change in the eigenvalues of the system and in-turn the dynamics may switch from hyperbolic space to the centre space or vice versa. Thus a continuous change in system parameters may result in a discontinuous change in system dynamics. The continuity of the eigenvalues and persistence of hyperbolic equilibria with respect to the parameters is determined by the following theorem.

Theorem 2.1.4 (Implicit Function Theorem) *Consider the dynamical system (2.1) with a hyperbolic equilibria at (x^*, ν^*) , also consider the definition of the spectrum of a dynamical system. If $0 \notin \sigma$ then $\det J \neq 0$ and J is invertible at (x^*, ν^*) , then there is neighbourhood of ν^* in which the stability/instability is preserved under small changes of ν . More precisely, it is possible to find a unique C^∞ function $g : \mathbb{R}^m \rightarrow \mathbb{R}^n$ such that $x^* = g(\nu)$ and $F(g(\nu), \nu) = 0$.*

This work only presents the Andronov-Hopf and Saddle-Node Theorems as they are the bifurcation types found so far in the model studied in this Thesis. However the reader is asked to refer to [63] for detailed accounts of other local and global bifurcations sets.

Saddle-Node

The saddle-node bifurcation is the basic mechanism by which fixed points are *created* and *destroyed*. As a parameter is varied, two fixed points move toward each other, collide, and mutually annihilate.

Theorem 2.1.5 (Saddle-node bifurcation) *Consider the vector field (2.1) on \mathbb{R}^n and assume that for all (x, ν) near some point $(x^*, \nu^*) = (0, 0)$ F has some continuous (mixed) derivatives up to and including third order, i.e., $\frac{\partial F}{\partial x}, \frac{\partial F}{\partial \nu}, \frac{\partial^2 F}{\partial x^2}, \dots, \frac{\partial^3 F}{\partial x \partial \nu \partial \nu}, \frac{\partial^3 F}{\partial \nu \partial \nu \partial \nu}$. If the following conditions are satisfied:*

1. $F(0, 0) = 0$,
2. The equilibrium is non-hyperbolic; that is, $\frac{\partial F}{\partial x}(0, 0) = 0$,
3. The vector field has a nonzero quadratic term at the bifurcation point; that is, $\frac{\partial^2 F}{\partial x^2} \neq 0$,
4. The vector field is non-degenerate with respect to the bifurcation parameter $\nu = (\nu_1, \dots, \nu_m)$; that is, the m -dimensional vector $\mathbf{a} = \frac{\partial F}{\partial \nu}(0, 0) = (\frac{\partial F}{\partial \nu_1}, \dots, \frac{\partial F}{\partial \nu_m})^T \neq 0$. (This is referred to the transversality condition),

then the vector field (2.1) has a saddle-node bifurcation with quadratic tangency at the equilibrium. From the above conditions it follows that any system with saddle node bifurcation has Taylor series of the form: $\dot{x} = a + bx^2 + \text{higher order terms}$, where a is given by the dot product $a = \mathbf{a} \cdot \nu$ and $b = \frac{1}{2} \frac{\partial^2 F}{\partial x^2} \neq 0$. Although ν is a multidimensional parameter, only its projection on the vector \mathbf{a} is relevant (to the leading order).

Andronov-Hopf

Andronov-Hopf bifurcations first considered in [74] are amongst the most important bifurcations observed in neuronal dynamics, since they describe the onset (or disappearance) of periodic activity, which is ubiquitous in the brain. A more intuitive version of the Hopf theorem by Mee [109, 110] which allows for a graphical interpretation of the theorem is presented.

The theorem states that if an n -dimensional ordinary differential equation depends on a real parameter ν , and if on linearising about an equilibrium point, pairs of complex conjugate eigenvalues of the linearised system cross the imaginary axis as ν varies through certain critical values, then for near critical values of ν there exists a limit cycle close to the equilibrium point. Just how near to criticality ν is, is only determined when the *curvature coefficient* is nonzero. The curvature coefficient determines the stability of the limit cycle. The global Hopf theorems do not transfer easily from 2 to n dimensions. The Hopf bifurcation theorem, however, is local and the transition is possible due to the invariant manifold and centre manifold theorem which lets us take the eigenspace of the bifurcating eigenvalues as an approximation to a two dimensional manifold (the centre manifold) that contains the limit cycle (if there is one). The Hopf bifurcation theorem for two dimensions can thus be used to establish existence of limit cycles in the centre space, which then implies existence in the whole phase space.

Theorem 2.1.6 (Hopf bifurcation) *Consider the vector field (2.1) on \mathbb{R}^n ($n \geq 2$) and C^k ($k \geq 4$) jointly in $x \in \mathbb{R}^n$ and $\nu \in \mathbb{R}^m$. Let $(x^*, \nu^*) = (0, 0)$ be the critical point. Suppose*

1. $F(0, 0) = 0$,
2. The Jacobian J at the critical point has a pair of complex conjugate eigenvalues $\pm i\omega$ ($\omega > 0$) and no other eigenvalues with zero real part,
3. The curvature coefficient (2.11) is nonzero,

then there is a range either positive or of negative values $\Delta\nu = \nu - \nu^$ in which every value of ν corresponds to a unique limit cycle at a distance $\mathcal{O}(\sqrt{|\Delta\nu|})$ from ν^* , and of period $\frac{2\pi}{i\omega} + \mathcal{O}(\Delta\nu)$. Furthermore,*

1. *If $a < 0$ and the real parts of all the other eigenvalues are strictly negative then the limit cycle is attracting (supercritical), while if $a > 0$ and the real parts of other eigenvalues are strictly positive the limit cycle is repelling (subcritical).*

The curvature coefficient a is given by:

$$\begin{cases} a = \text{Re}(\psi), \\ \psi = u_p v_j v_k \bar{v}_l (F_{jkl}^p - 2F_{jm}^p J_{mq}^{-1} F_{kl}^q - F_{lm}^p (J - 2i\omega)_{mq}^{-1} F_{jk}^q), \end{cases} \quad (2.11)$$

where $u^T \in E_h$ and $v \in E_0$, normalised so that $u^T v = 1$. Repeated subscripts imply summation from 1 to n and $F_{jk}^p = \frac{\partial F_p(x, \nu)}{\partial x_k \partial x_j}$ (where $F_p(x, \nu)$ is the p^{th} component of the vector field $F(x, \nu)$ evaluated at the critical point (x^*, ν^*)). For two dimensional systems it is shown in [109] that the curvature coefficient is given by

$$a = \frac{1}{16} (F_{111}^1 + F_{122}^1 + F_{112}^2 + F_{222}^2) \quad (2.12)$$

$$- \frac{1}{16\omega} (F_{12}^1 (F_{11}^1 + F_{22}^1) - F_{12}^2 (F_{11}^2 + F_{22}^2) - F_{11}^1 F_{11}^2 + F_{22}^1 F_{22}^2) \quad (2.13)$$

If the curvature is non-vanishing then the limit cycle manifold is parabolic and the limit cycle grows as $\sqrt{|\nu - \nu^*|}$ (i.e. much faster than $|\nu - \nu^*|$ at first). If the curvature vanishes, it is possible, though not certain, that the parabolic manifold is flat out to infinity, in which case the periodic orbits exists only at the critical parameter value. An example of this case is given by the linear system $\ddot{x} + \nu\dot{x} + x = 0$ and an example where the curvature coefficient vanishes but the manifold is nevertheless not flat is given by, $\ddot{x} + \nu\dot{x} + x = g(x, \dot{x})$, where all the partial derivatives of g at the origin vanish up to the 4th order, but there is non-vanishing 5th partial derivative. It is “unlikely” and generically does not happen in the *one-parameter* family of systems that two pairs of complex eigenvalues or a pair and a real eigenvalue cross simultaneously into the positive half of the complex plane. In the case of systems that depend on two or more parameters, such cases may generically occur, giving rise to so-called “co-dimension two or higher bifurcation”; see e.g. [66, 98].

2.2 Constructive Global Analysis of Hybrid systems

This section reviews a recent mathematical formalism for the analysis of Hybrid systems proposed by Gonçalves [28]. The theory presented in [28] can be seen as an extension of theory of *Poincaré Mappings* for the local analysis of limit cycles on maps, but also generalises to global stability analysis. *Hybrid systems* are characterised by interactions between continuous (smooth) dynamics and discrete events. These systems typically contain variables or signals that take values from a continuous set and also variables that take values from a discrete, typically finite set. Discrete events, such as saturation limits, can act to trap the evolving system state within a constrained region of state space. Therefore even when the underlying continuous dynamics are unstable, the discrete events can introduce a stable limit set. In

particular, we are interested in the results obtained for a class of *Hybrid systems* known as *Piecewise Linear Systems (PLS)*.

PLS are characterised by three components; a set of *affine linear systems*; a *switching rule* to switch among them, which depends on present values of x and possibly on past values of the state and *switching surfaces* consisting of hyper-planes of dimension $n - 1$ defined respectively as:

$$\begin{cases} \dot{x} = A_\alpha x + B_\alpha, & x \in \mathbb{R}^n \\ \alpha(x) \in \{1, \dots, M\} \\ S_J = \{x | C_J x + d_J = 0\}, & j = \{1, \dots, N\} \end{cases} \quad (2.14)$$

This work only considers switching rules that only depend on the present values of the state x . In such case the state space is partitioned into M (possibly unbounded) sets called *cells* defined as $U_i = \{x | \alpha(x(t)) = i\}$ with $i = \{1, \dots, M\}$ such that $U_i \cap U_j = \emptyset, i \neq j$. Altogether there are $M \times N$ boundaries. In each cell, U_i , the system dynamics is given by a linear system $\dot{x} = A_i x + B_i$. A solution of (2.14), is a function $(x(t), \alpha(x(t)))$ satisfying (2.14), where $x(t)$ is simply the flow of the affine system within a cell and $\alpha(x(t))$ is piecewise constant. t is the *switching time* of a solution of (2.14).

Assume that the existence of a solution is always guaranteed for any initial condition. If an initial condition is an interior point of a cell, then the existence of a solution is guaranteed at least from the initial condition to the first intersection with a switching surface. This follows since the system is affine linear in the cell. When an initial condition belongs to a switching surface, however, there may be a unique solution, multiple solutions, or no solution. Multiple solutions can occur if the vector fields from either side of the switching surface flow in opposite directions, i.e. an initial condition x_0 belonging to the switching surface cannot be uniquely attributed by a *switching rule* $\alpha(x_0)$ to either vector field. The non existence of solutions may occur if the vector fields from either side of the switching surface point towards the switching surface. In this case as soon as a switching rule $\alpha(x_0)$ is assigned to one of the vector field, it must switch immediately. Since, by definition a switching rule is piecewise constant, arbitrarily fast switches are not possible. Therefore this scenario does not result in a solution. The reader will verify in Chapter 6 that this last case scenario does not occur in the system model analysed in this thesis and thus the above technique is applicable. However this problem has been extensively studied in [55], where the approach is to define a dynamical

system on the switching surface and let the trajectory evolve until it can “escape” to either side of the switching surface. This technique is known as *sliding modes*.

2.2.1 Local Stability

The section reviews the theory of Poincaré mappings to establish a link with the theory of local stability of limit cycles in piecewise linear system.

2.2.2 Poincaré Mappings

The proofs and computational details can be found in [72, 119]. Consider a dynamical system of the form:

$$\dot{x} = F(x), \quad x \in \mathbb{R}^n, \quad (2.15)$$

having a periodic solution (or limit cycle) with period T , i.e. $x(t) = x(t + T) \quad \forall t \geq 0$ and denote it by $\gamma \subset \mathbb{R}^n$. Let $S \subset \mathbb{R}^n$ be an $(n - 1)$ -dimensional hyperplane (*Poincaré surface of section*) transversal to γ as well as all orbits close to γ . Without loss of generality assume that γ intersects S in a unique point x^* . Due to the continuity of the flow $\Phi^t(x)$ with respect to the initial condition, trajectories starting on a neighbourhood $D \subset S$ of x^* will, in approximately finite time T , intersect S in the vicinity of x^* . That is, a *Poincaré map* effectively samples the flow of a periodic system once every period. Hence the first return map can be defined as follows:

$$x_{k+1} = P(x_k) := \Phi^{T(x_k)}(x_k), \quad T(x_k) \approx T, \quad k \in \mathbb{Z}^+. \quad (2.16)$$

The stability of the *Poincaré map* (2.16) is determined by linearising P at the fixed point x^* . i.e.

$$\Delta x_{k+1} = DP(x^*)\Delta x_k. \quad (2.17)$$

From the definition (2.15), it follows that $DP(x^*)$ is closely related to the trajectory sensitivities $\frac{\partial \Phi^{T(x_k)}(x^*)}{\partial x}$ (*Monodromy matrix*). In fact it is shown in [72] that

$$DP(x^*) = \left(I - \frac{F(x^*)C^s}{C^s F(x^*)} \right) \frac{\partial \Phi^{T(x_k)}(x^*)}{\partial x}, \quad (2.18)$$

where C^s is a vector normal to the hyperplane S . It is also shown in [72] that one eigenvalue of the *Monodromy matrix* is always 1 and the corresponding eigenvector lies along $F(x^*)$. The remaining eigenvalues of $\frac{\partial \Phi^{T(x_k)}(x^*)}{\partial x}$ coincide with the eigenvalues of $DP(x^*)$, and are known as the *characteristic multipliers* m_i of the periodic solution. Characteristic multipliers are independent of the choice of the cross-section S and hence the following:

1. If all m_i lie within a unit circle, i.e $|m_i| < 1, \forall i$, then the map is stable and periodic solution is stable.
2. If all m_i lie outside the unit circle then the periodic solution is unstable.
3. If some m_i lie outside the unit circle then the periodic solution is unstable in some directions, but stable in other directions. This can occur for example in saddle cycles.

Interestingly, there exists a particular hyperplane S^* , such that

$$DP(x^*)\lambda = \Phi^{T(x)}(x^*)\lambda,$$

where $\lambda \in S^*$. This hyperplane S^* is the hyperplane spanned by the $n - 1$ eigenvectors of $\Phi^{T(x)}(x^*)$ that are aligned with $F(x^*)$. Therefore the vector C^* that is normal to S^* is the eigenvector of $\Phi^{T(x)}(x^*)$ corresponding to the eigenvalue 1. The hyperplane S^* is invariant under $\Phi^{T(x)}(x^*)$, i.e $\Phi^{T(x)}(x^*)$ maps vectors $\lambda \in S^*$ back into S^* .

An extension to the *Poincaré mappings* for local analysis of limit cycles in piecewise linear systems is given by the following propositions (the proofs are found in [28]).

Proposition 2.2.1 (Existence of Limit Cycles for PLS) *Consider the PLS. Assume there exists a limit cycle γ with k switches per cycle and with period $t^* = t_1^* + t_2^* + \dots + t_k^* > 0$. Then the following conditions hold:*

$$g_k(t_1^*, \dots, t_k^*) = C_k(I - E_k \dots E_1)^{-1} \left[\sum_{i=1}^{k-1} E_k \dots E_{i+1}(E_i - I)z_i + (E_k - I)z_k \right] - d_k = 0,$$

where $E_i = e^{A_i t_i^*}$ and $z_i = A_i^{-1} B_i$. The periodic orbit is governed by system 1 on $[0, t_1^*)$, and the by the system i on $[t_1^* + \dots + t_{i-1}^*, t_1^* + \dots + t_i^*)$, $i = 2, \dots, k$. Furthermore, the periodic solution γ can be obtained with the initial condition $x_0^* \in S_k$

$$x_0^* = (I - E_k \dots E_1)^{-1} \left[\sum_{i=1}^{k-1} E_k \dots E_{i+1}(E_i - I)z_i + (E_k - I)z_k \right].$$

Proposition 2.2.2 (Local Stability for PLS) *Consider the PLS. Assume there exists a limit cycle γ with period t^* and transversal to the switching surfaces S_1, \dots, S_k at x_1^*, \dots, x_k respectively. The Jacobian of the map P is given by the concatenation of the intermediate Jacobians $W = W_k W_{k-1} \dots W_2 W_1$ where*

$$W_i = \left(I - \frac{v_i C_i}{C_i v_i} \right) e^{A_i t_i}, \quad v_i = A_i x_i^* + B_i, \quad i = 1, \dots, k, \quad (2.19)$$

where C_i are vectors normal to the hyperplane S_i . The limit cycle γ is locally stable if W has all its eigenvalues inside the unit disc. Note the similarity of equations (2.18) and (2.19).

2.2.3 Global asymptotic stability

The fundamentally new concept introduced in *Constructive Global Analysis of Hybrid Systems* [28] is to infer global dynamical properties of a system through finding quadratic Lyapunov functions on the switching surfaces. Earlier studies [69, 122] had proposed continuity of the Lyapunov functions along the switching surfaces and this result lead to the idea that the intersection of two Lyapunov functions at a switching surfaces (one from each side) defined a unique quadratic Lyapunov function on the switching surface. It is then demonstrated in [28] that a quadratic Lyapunov function on the switching surface in a PLS denoted *Quadratic Surface Lyapunov Function* (SuLF) exists and that SuLF (as opposed to searching for Lyapunov functions in the state space) is sufficient to efficiently analyse global stability of equilibriums and limit cycles. This follows since a PLS behaves linearly inside a cell and only three scenarios can occur to a trajectory entering a cell at some point x_0 on a switching surface:

1. The cell is unbounded and there exists a trajectory that will grow unbounded without ever switching. This occurs when x_0 belongs to an unstable region. If the piecewise linear system has one equilibrium point or limit cycle, then these are not globally stable.
2. There is a locally stable equilibrium point in the cell and the trajectory will asymptotically converge and will not switch.

3. The trajectory will switch in finite time. This case is interesting as a system can switch between cells and exhibit complex dynamics, in particular, limit cycles can occur.

In order to analyse a PLS using SuLF it is first necessary to define *impact maps* from one switching surface to the next and by combining all the impact maps associated with the PLS it is possible to study the above scenarios, in particular infer global stability of limit cycles.

2.2.4 Impact Maps

The central concept used to analyse the flow of a PLS from one switching surface to the next switching surface is that of *Impact Maps*. An impact map is simply a function that maps vectors from one switching surface to the next switching surface. To make things clear consider system (2.14) where we only analyse locally the flow from switching surface S_1 to S_2 . Let both S_1 and S_2 be defined on the boundaries of subset of cell $U \in \mathbb{R}^n$ and the linear time invariant system $\dot{x} = A_0x + B_0$, $x \in U$ is allowed to have stable, unstable or pure imaginary eigenvalues. Define the *departure set* $S_1^d \subset S_1$ where any trajectory starting at S_1^d satisfies $x(t) \in S_2$, for some finite *switching time* $t \geq 0$, and $x(\tau) \in U^*$ on $[0, t]$, where U^* is the *closure* of U (i.e $U^* = U \cup \{x | x \text{ is a limit point } U\}$). Let the *arrival set* $S_2^a \subset S_2$ be the set of those points $x_2 = x(t)$, that is, the image of S_1^d . Any point belonging to the switching surface $x_1 \in S_1^d$ and $x_2 \in S_2^a$ can be parameterised in their respective hyperplanes. For that, let $x_1 = x_1^* + \Delta_1$ and $x_2 = x_2^* + \Delta_2$, where $x_1^* \in S_1$, $x_2^* \in S_2$ and Δ_1, Δ_2 are any vectors such that $\Delta_1 \in S_1^d - x_1^*$ and $\Delta_2 \in S_2^a - x_2^*$. In this case $C_1\Delta_1 = C_2\Delta_2 = 0$. The impact map then reduces to the study of a map from Δ_1 to Δ_2 . However, since the map is multi-valued (i.e. the same initial condition Δ_1 can have multiple switching times) the following definition can be introduced:

Definition 2.2.1 (Expected switching times) Let $x(0) = x_1^* + \Delta_1$. Define t_{Δ_1} as the set of all times $t_i \geq 0$ such that the trajectory $x(t)$ with initial condition $x(0)$ satisfies $C_2x(t_i) = d_2$ and $x(t) \in U^*$ on $[0, t_i]$. Define also the set of expected switching times of the impact map from $\Delta_1 \in S_1^d - x_1^*$ to $\Delta_2 \in S_2^a - x_2^*$ as

$$\mathcal{T} = \{t | t \in t_{\Delta_1}, \Delta_1 \in S_1^d - x_1^*\}.$$

In general a map between switching surface is nonlinear, however a map induced by a linear time invariant flow, can be represented as a *linear transformation* analytically parameterised by a scalar function of the state (in this case switching times t_{Δ_i}) and this is given by the following theorem:

Theorem 2.2.1 (Impact Map) *Assume $C_2 x_1^*(t) \neq d_2$ for all $t \in \mathcal{T}$. Define the transition function as*

$$\begin{cases} H(t) = e^{At} + (x_1^*(t) - x_2^*)w(t), & H(t) : \mathbb{R} \rightarrow \mathbb{R}^{n-1}, \\ w(t) = \frac{C_2 e^{At}}{d_2 - C_2 x_1^*(t)}. \end{cases}$$

Then, for any $\Delta_1 \in S_1^d - x_1^$ there exists a $t \in \mathcal{T}$ such that the impact map is given by*

$$\Delta_2 = H(t)\Delta_1,$$

such $t \in t_{\Delta_1}$ is the switching time associated with Δ_2 .

From the above theorem it is clear that Δ_1 is a nonlinear function of Δ_2 . However, fixing the switching time t determines the set of points $x_1^* + \Delta_1 \in S_0$ such that every point in that set has a switching time t . In this view the map is linear. Furthermore, the set of points S_1^d that have a switching time t is a convex subset of a linear manifold of dimension $n - 2$ which is denoted as S_t and defined as $S_t = \{t | t \in t_{\Delta_1}, x_1^* + \Delta_1 \in S_1^d\}$. Note that since the impact map is multi-valued, a point S_1^d may belong to more than one set S_t . Also as $t \in \mathcal{T}$ changes, S_t covers every single point of S_1^d , i.e $S_0^d = \{x | x \in S_t, t \in \mathcal{T}\}$. Finally note that the above theorem states that a trajectory cannot intersect the switching surface S_2 for all $t \in \mathcal{T}$.

2.2.5 Quadratic surface Lyapunov functions

Previous studies [69, 122] have tried formulating piecewise quadratic Lyapunov functions for piecewise linear systems and with success these results are able to analyse equilibrium points of piecewise linear systems. These techniques are based on the search of Lyapunov functions and determining their stability in the state space. Recall the following definitions for Lyapunov stability testing:

Definition 2.2.2 (Stability in the sense of Lyapunov) *An equilibrium point x^* of the system $\dot{x} = A(t)x$ is Lyapunov stable, if for any $\epsilon > 0$, there exists a value $\delta(t_0, \epsilon) > 0$ such that if $\|x(t_0) - x^*\| < \delta$, then $\|x(t) - x^*\| < \epsilon$, regardless of $t(t > t_0)$. The equilibrium point is uniformly stable in the sense of Lyapunov if $\delta = \delta(\epsilon)$, i.e., if the constant δ does not depend on initial time t_0 .*

The above definition makes clear that a stable time-invariant system is uniformly stable because the initial time t_0 does not affect the qualitative behaviour of the system. Furthermore, the state vector will remain within distance ϵ of the x^* , only if the initial condition is set to be at a distance from x^* by an amount no larger than δ . Clearly, the condition $\delta < \epsilon$ must be satisfied or else the system will have an initial condition not satisfying the desired bounds of the state vector. Lyapunov stability does not require that the system in question approach x^* , but only that it remains within the bounding radius ϵ . A Lyapunov stable system further requires x^* to be *asymptotically stable*, i.e. if $\|x(t) - x^*\| \rightarrow 0$ as $t \rightarrow \infty$. An equilibrium that is globally stable is one such that the constant δ can be chosen arbitrarily large. This implies any initial condition will take the system to be bounded near x^* or asymptotically approach x^* . For linear systems all stability is global since equilibria x^* are either isolated points or subspaces. However, for nonlinear systems multiple equilibria can exist, which means it is sometimes necessary to define regions of attraction around attractors, i.e. stable equilibria. These are called *basins of attraction*, denoting the region in the state space from which an initial condition will approach the equilibrium point. While the definitions above give the meaning of stability, they do little to determine stability of a given system (except that it is now easy to anticipate the stability conditions for a time-invariant system based on the locations of its eigenvalues and in this case determine the directions of the phase trajectories). One possible form to determine stability is to use the results of section (2.1.3) which uses the spectrum of the matrix to determine the stability. Alternatively, a different method for testing stability of linear, zero-input system is called Lyapunov's direct method. It is based on the concept of energy and dissipative systems and is given by the following theorem:

Theorem 2.2.2 (Lyapunov Global Stability) *Consider the vector field (2.1), with $x \in U$ and the parameters ν fixed. The origin x^* of the vector field (2.1) is Lyapunov stable if there exists a Lyapunov function (energy function) $V(x) : U \rightarrow \mathbb{R}$ such that the following conditions are satisfied:*

1. $V(x) > 0$ for all $x \neq 0$ and for all t , $V(x) = 0$ only when $x = x^*$. i.e $V(x)$ is positive definite.
2. $\frac{dV(x)}{dt} \leq 0$ for all $x \neq 0$ and for all t , i.e. decreases along trajectories, in other words, the $\frac{dV(x)}{dt}$ is negative semidefinite.

Futhermore, x^* is globally Lyapunov stable, if in addition to the above conditions, $V(x)$ is unbounded as $\|x\| \rightarrow \infty$. If the second condition is altered to $\frac{dV(x)}{dt} < 0$ for all $x \neq 0$ and for all t (negative definite) then the theorem is strengthened to asymptotic stability.

Definition (2.2.2) and Theorem (2.2.2) are also applicable to discrete-time systems. However, it is necessary to substitute the derivative $\frac{dV(x)}{dt}$, by first difference, $\Delta V(x_k) = V(x_{k+1}) - V(x_k)$. In the case of linear systems, it is sufficient to consider quadratic forms as Lyapunov functions. This is largely because for linear systems, stability implies global stability, and the parabolic shape of a quadratic function satisfies all the criteria of Theorem (2.2.2).

The above results are suitable when considering global stability of equilibriums of piecewise linear systems, however they do not generalise to the study of piecewise linear systems that exhibit limit cycles. In this case it is possible to construct Lyapunov functions on the switching surface (SuLF) and from this determine stability of equilibriums and also of limit cycles. The following section reviews the main results proved [28].

Consider system (2.14) with the impact maps defined in section (2.2.4). It follows that to demonstrate global stability it is first necessary to define quadratic Lyapunov functions V_1 and V_2 respectively on the switching surfaces S_1^d and S_2^a given by:

$$V_i(x) = x^T P_i x - 2x^T g_i + \alpha_i,$$

where $P_i > 0$, g_i and α_i are parameters to be determined, with $i = \{1, 2\}$. Once the parameters are determined then the next step is to show that the impact map from S_1^d to S_2^a are contracting in some sense. In particular, an impact map is quadratically stable if there exist $P_i > 0$, α_i , g_i such that

$$V_2(\Delta_2) < V_1(\Delta_1), \quad \text{for all } \Delta_1 \in S_1^d - x_1^*. \quad (2.20)$$

Applying Theorem (2.2.1) to the above inequality (2.20) and using both facts that the map Δ_1 to Δ_2 is linear in S_t and that, as t ranges over \mathcal{T} , S_t covers every point in S_1^d the main global stability theorem for impact maps is obtained:

Theorem 2.2.3 (Stability of impact map) *Define*

$$R(t) = P_1 - H(t)^T P_2 H(t) - 2(g_1 - H(t)^T g_2)w_t + w_t^T(\alpha_1 - \alpha_2)w_t \quad (2.21)$$

The impact map from $\Delta_1 \in S_1^d - x_1^$ to $\Delta_2 \in S_2^a - x_2^*$ is quadratically stable if and only if there exist $P_1, P_2 > 0$ and $g_1, g_2, \alpha_1, \alpha_2$ such that*

$$R(t) > 0 \quad S_t - x_1^*, \quad (2.22)$$

for all expected switching times $t \in \mathcal{T}$.

Thus, if the above piecewise linear system exhibits a limit cycle (i.e. having trajectories from S_1 to S_2 and in turn from S_2 to S_1) then it is first necessary to determine SuLF on S_1 and S_2 . Once the quadratic functions are determined it is easy to show that the limit cycle is stable or not by applying Theorem (2.2.3) which proves that the impact maps S_1 to S_2 and from S_2 to S_1 are contracting. In other words, the trajectories contract to a global stable fixed point in the hyper-planes.

2.3 Numerical simulation of Delay Equations

At present theoretical aspects of DDEs theory are elaborated with almost the same completeness as the corresponding parts of ODE theory. However, unlike ODE even for linear DDE there are no general methods of finding solutions in explicit form. Various *specific* numerical methods are constructed for solving *specific* delay differential equations. For development of DDE numerical analysis consult for example [12, 90, 120].

In general the procedure taken to numerically solve DDEs is to transform the DDE into an ODE at each time step, and thus one can use the usual numerical schemes for ODE's to solve the equation at every time step. This method is known as the **method of steps**. For

example, consider (2.2), if $x(t) = \varphi(t)$ for $t \in [-\tau, 0]$, where φ is a given continuous function, then the solution $x(t)$ for $t \in [0, \tau]$ for equation (2.2) satisfies the following ODE:

$$\frac{d}{dt}x(t) = H(x(t), \nu) \quad \text{for} \quad t \in [0, \tau], x(0) = \varphi(0), \quad (2.23)$$

where $H(x(t), \nu) = F(x(t), \varphi(t - \tau), \nu)$. This equation has a unique solution and the solution of equation (2.23) coincides with the solution of equation (2.2) on $[0, \tau]$. Once the solution $x(t)$ is known on $[0, \tau]$, then the same procedure can be repeated to compute $x(t)$ for $[\tau, 2\tau]$ and so on. However it should be noted that additional numerical interpolation scheme is required when solving DDE with variable delays, this requirement is necessary since sometimes points (*in between points*) of the solution which were not computed are needed to evaluate the vector field F at a later time step. The above requirement is reported in [120] and stated in the following theorem, which in turn is proved in [8]:

Theorem 2.3.1 (Order of convergence) *Given an ODE method of order p combined with an interpolant of order q , if discontinuities not exceeding order r , occur only at meshpoints, then the order of the resulting DDE solver is $\min(p, q, r)$.*

The above theorem underlines the fact that ODE methods can be used to solve DDEs with the same *order of convergence* provided the right interpolating scheme is used. Hence this results in the following numerical algorithm:

1. Consider a uniform partition $t_r = t_0 + rh$, $r = \{0, 1, \dots, N\}$, of the interval $[t_0, t_0 + t_f]$ where $h = t_f/N$ and assume the ratio $\tau/h = N_\tau$ is a positive integer. Where t_0 and t_f is the initial and final time of the simulations respectively.
2. Compute the approximate solution $x_{r+1} \in \mathbb{R}^n$ of the true solution $x(t_r)$ by first interpolating the pre-history $\{x_i : i \geq 0, r - N_\tau \leq i \leq r\}$ denoted by $\{x_i^r\}$ (corresponds to the discretised version of $\varphi : [-\tau, 0] \rightarrow \mathbb{R}^n$) of the discrete model on the interval $[t_r - \tau, t_r]$. The result of this interpolating is *continuous* set of values in this interval and will be denoted by $I(\{x_i^k\})$ where I is the interpolating function. Secondly calculate $x_{r+1} = x_r + hF^*(x_r, I(\{x_i^r\}), \nu)$ where F^* is some ODE numerical integration method.
3. Repeat the process until the final simulation time t_r is reached. So $x_{[t_0, t_r]}$ will be the approximate solution to the DDE.

2.3.1 Implementation of the numerical code

For our purpose of this thesis the method as described in the previous section 2.3 is used. In particular, the *fourth order Runge-Kutta* and *cubic spline interpolation* schemes are employed. The relevant functions stem from [126] and the code developed can be found in a CD provided in the appendix. The following next explains the specific implementation developed in this thesis. Recall that the standard *Runge-Kutta 4th order* for the non-autonomous (i.e. explicit dependence on time) ODE $\dot{x} = H(t, x(t), \nu)$, where $H \in C^k(\mathbb{R} \times \mathbb{R}^n \times \mathbb{R}^m, \mathbb{R}^n)$ and the parameter ν is considered fixed is given by:

$$\begin{aligned}
p_1 &= hH(t_r, x_r, \nu), \\
p_2 &= hH(t_r + \frac{h}{2}, x_r + \frac{p_1}{2}, \nu), \\
p_3 &= hH(t_r + \frac{h}{2}, x_r + \frac{p_2}{2}, \nu), \\
p_4 &= hH(t_r + h, x_r + p_3, \nu), \\
x_{r+1} &= x_r + \frac{1}{6}(p_1 + 2p_2 + 2p_3 + p_4) + O(h^5).
\end{aligned} \tag{2.24}$$

Since the objective is to solve an autonomous DDE the following transformation is applied, $H = F(x(t), \varphi(t - \tau), \nu)$ which gives rise to the following extended scheme:

$$\begin{aligned}
p_r^1 &= hF(x_r, x_{r-N_\tau}, \nu), \\
p_r^2 &= hF(x_r + \frac{p_r^1}{2}, x_{r-N_\tau} + \frac{p_{r-N_\tau}^1}{2}, \nu), \\
p_r^3 &= hF(x_r + \frac{p_r^2}{2}, x_{r-N_\tau} + \frac{p_{r-N_\tau}^2}{2}, \nu), \\
p_r^4 &= hF(x_r + p_r^3, x_{r-N_\tau} + p_{r-N_\tau}^3, \nu), \\
x_{r+1} &= x_r + \frac{1}{6}(p_r^1 + 2p_r^2 + 2p_r^3 + p_r^4) + O(h^\alpha),
\end{aligned} \tag{2.25}$$

where the error term $O(h^\alpha)$ should be determined by the *order convergence theorem*. The extended scheme can be seen as acting as a second order interpolant to find the midpoint for the delayed values via steps k_r^2 and k_r^3 . In other words, the scheme uses three time points t_{r-N_τ} , $t_{N_\tau+h/2}$ and $t_{r-N_\tau+1}$ in order to evaluate at t_r the next approximation value x_{r+1} . Since for the delayed variables the initial and end points are known it is possible to use cubic splines. Thus by the *order convergence theorem* the method is third order accurate.

The pre-history function $\varphi : [-\tau, 0] \rightarrow \mathbb{R}^n$ was defined to be zero vectors for $-\tau \leq t < 0$ and a non-zero vector for $t = 0$. The discretised function $\{x_i^\tau\}$ was implemented by a FIFO (*First In*

First Out table) where for every new x_{r+1} value evaluated the FIFO shifts values one position, updating x_{r+1} in the first index (*head*) of the table. Since at t_r every new approximation value x_{r+1} depends on three time points t_{r-N_τ} , $t_{N_\tau+h/2}$ and $t_{r-N_\tau+1}$ $(2 * \tau/h) + 1$ entries are required in the FIFO.

The main code execution considers two nested loops, in total, $N_j * [Transient + Print]$ iterations where the inner-loop (*Transient*) ignores transient effects and only asymptotic dynamics (*Print*) are observed, where $N_j = j * N$, $j \in \mathbb{N}$ (i.e. the code is divided into sequences of loops of intervals $[t_0, t_0 + t_f]$ where $t_r = t_0 + rh$, $r = \{0, 1, \dots, N\}$). At every j the parameter of interest ν is increased or decreased uniformly. The next iteration $j + 1$ allows the initial conditions to be either initialised to some random values or to be updated with the data from the previous iteration (i.e. if the system starts in some basin of attraction it will remain closely to it). In the latter case, to evolve nearby the basin of attraction the subsequent *Transient* loops are omitted. In addition the *Print* stage allows one to print out both the data for the time series solution $x(t)$ at every change of parameter and the stable bifurcations. The bifurcations are evaluated by determining the relative maximum and minimum of the observable(s). Thus the amplitudes of the stable manifolds reveal the different dynamics.

Future adjustments to the code could address the following aspects:

1. Searching for discontinuities in the derivatives could be important if smooth solutions to the time series are required. However from simulation we observe that the numerical scheme is stable enough and provides an excellent approximation. Guide lines on numerical treatment on this issue can be found in [50, 121]
2. If the system model depends only on a fixed delay τ which in some sense is an easier system to handle, then if we consider $\tau = N * h$ (h = time step) then interpolation is no longer required, this implies that only *true* pre-history values are used. With this approach one can expect faster convergence to the solution and better results. The EEG model used in this thesis could benefit with this change if future large scale simulations is required.

2.4 Numerical Continuation

The intention of this section is not to provide an exhaustive explanation of continuation methods as the purpose here is only to provide a brief explanation of the figures produced by the continuation packages *XPPAuto* and *DDE-Biftool* that are used in thesis. For an excellent introduction to the subject refer to the fundamental paper of Keller [89], along with other comprehensive books [96, 142]. Numerical continuation is concerned with analysing the solution behaviour and determining the bifurcations that occur on a dynamical system as the systems parameters are varied. Solutions in general vary as the parameters are changed and in this view the solutions can be seen as being parameterised forming a smooth continuum, which are called *solution continuation branches* or termed *solution paths*. In particular, a brief review on continuation of only one-parameter family of stationary and periodic solutions is presented.

2.4.1 XPP-Auto

XPPAuto is an integrated software package to compute numerically solutions of ODE and to follow numerically solutions paths in parameter space. For early contributions in the development of the package consult Doedel [44, 45, 46]. In particular this work uses the current version by Ermentrout [52].

2.4.2 Parameter continuation

Parameter continuation is a numerical technique used to compute invariant sets or attractors (e.g. equilibria or periodic orbits) by directly solving a set of algebraic equations which are the defining conditions for the invariant sets to exist. This is achieved by following solution paths in the parameter space of smooth parameterised system (algebraic conditions) of n equations in n unknowns

$$\mathcal{F}(x, \nu) = 0, \quad F : \mathbb{R}^n \times \mathbb{R}^1 \rightarrow \mathbb{R}^n. \quad (2.26)$$

That is, the goal is to use a numerical strategy to compute a sequence of points along the solution curve $g(\nu) \approx \{(x_i, \nu_i), i = 0 \dots N\}$ such that $\mathcal{F}(x_i, \nu_i) = 0$. The key idea to solve parameterised nonlinear systems of equation is to use the implicit function Theorem 2.1.4, where a smooth path of solutions $g(\nu)$ can be continued locally if the Jacobian of \mathcal{F} is nonsingular. As these solutions are followed, extra algebraic conditions can be monitored to detect bifurcations and compute stability of the attractors. The resulting bifurcation diagram is the *signature* of the problem.

2.4.3 Continuation of stationary solutions

Consider the initial value problem (2.1) where the aim is to follow a branch of stationary solutions $F(x, \nu) = 0$ as one of the parameters in the vector ν is varied. In this case the algebraic equations to be solved are just the vector field of the initial value problem $\mathcal{F}(x, \nu) \equiv F(x, \nu) = 0$. One strategy to solve the nonlinear equation as the parameter ν is varied is to use a fixed point iteration method such as the Newton's method. That is, suppose a solution x_i of equation (2.26) at ν_i exists, as well as its derivative \dot{x}_i^ν with respect to the parameter ν . The next iteration is to compute the solution x_{i+1} at $\nu_{i+1} = \nu_i + \Delta\nu$ such that $\mathcal{F}(x_{i+1}, \nu_{i+1}) = 0$. By Newton's method the following applies:

$$\begin{cases} J(x_{i+1}^{(j)}, \nu_{i+1}) \Delta x_{i+1}^{(j)} = -\mathcal{F}(x_{i+1}^{(j)}, \nu_{i+1}), \\ x_{i+1}^{(j+1)} = x_{i+1}^{(j)} + \Delta x_{i+1}^{(j)}, \quad j \in \mathbb{N}_0, \end{cases}$$

with $x_{i+1}^0 = x_i + \Delta\alpha \dot{x}_i^\nu$. If the Jacobian J is nonsingular, $\Delta\nu$ is sufficiently small and the initial guess x_i is sufficiently close to the true solution then Newton's method will converge. After convergence, the new derivative vector \dot{x}_{i+1}^ν with respect to the parameter can be obtained by solving the following:

$$J(x_{i+1}, \nu_{i+1}) \dot{x}_{i+1}^\nu = -J_\nu(x_{i+1}, \nu_{i+1}),$$

where J_ν is the matrix with partial derivatives with respect to the parameters. This equation follows from differentiating $\mathcal{F}(g(\nu), \nu) = 0$ with respect to ν at $\nu = \nu_{i+1}$.

The above method works well if the solutions are regular, however will fail if a Fold bifurcation occurs, since the implicit function theorem is not satisfied. That is, the Jacobian of the

vector field becomes nonsingular. To solve this problem Keller [89] proposed the *pseudo-arclength* method which allows the continuation of any regular solution, including folds. The pseudo-arclength differs from other methods by not parameterising the solution curve (to be found g) by the physical parameter ν . Instead, it uses a geometrical parameter s . Thus a parameterisation by s means that solutions of $\mathcal{F}(x, \nu) = 0$ depend at least locally on s , i.e. the solution curve is now $g(s) = (x(s), \nu(s))$. In this case for a particular value of s , the system $\mathcal{F}(x, \nu) = 0$ consists of n equations for the $(n + 1)$ unknowns (x, ν) and thus one additional scalar equation is needed to form an extended system. One possibility is to parameterise the curve by some approximation to the arc length s along a curve, thus the following formulation holds true, $arc(x, \nu, s) = (x_{i+1} - x_i)^2 + (\nu_{i+1} - \nu_i)^2 = \Delta s^2$. However, since this equation is nonlinear, Keller proposes to linearise and replace the above with pseudo-arc length version, thus the resulting method is the following extended system:

$$\mathcal{F}(x, \nu) \equiv \begin{pmatrix} F(x_{i+1}, \nu_{i+1}) \\ \langle \dot{x}_i, (x_{i+1} - x_i) \rangle + \langle \dot{\nu}_i, (\nu_{i+1} - \nu_i) \rangle - \Delta s \end{pmatrix} = 0,$$

where $(\dot{x}_i, \dot{\nu}_i)$ is the tangent vector to the curve $(x(s), \nu(s))$ at (x_i, ν_i) .

2.4.4 Continuation of periodic solutions

Finding limit cycles $x(t)$, $t \in (0, T)$ of the vector field (2.1), and following them as the parameter ν changes is more complicated and there are no regular ways to solve this problem. Note that the period T of the solution is not known a priori, and moreover T might vary with the parameter ν . One possible form of solving this is to fix the interval of periodicity by the transformation $\tau \rightarrow t/T$ and formulate the problem as a periodic *boundary-value* problem (BVP) on a fixed interval. Thus equation (2.1) transforms to the following:

$$\begin{cases} \frac{dx}{d\tau} = TF(x(\tau), \nu), \\ x(0) = x(1), \end{cases} \quad (2.27)$$

where solutions of period 1 are to be found (i.e. T-periodic solution of equation (2.1)). Assume that points $(x_{k-1}(\cdot), T_{k-1}, \nu_{k-1})$ have been computed and it is required to iterate forward to find $(x_k(\cdot), T_k, \nu_k)$. However, note that equation (2.27) does not uniquely specify x and T , since $x(\tau)$ can be translated freely in time, that is, if $x(\tau)$ is a periodic solution then so is $x(\tau + \delta)$ for any δ . Thus, an extra *phase condition* ϕ is needed in order to “select” a solution

among all those corresponding to the cycle $\phi(\{x(\tau), \tau \in [0, 1]\}) = 0$. There are several ways to set up a phase condition. One possibility is using a Poincaré section by defining a hyperplane S_0 that selects a solution passing at $\tau = 0$ through a point on the following surface:

$$S_0 = \{x \in \mathbb{R}^n : h(x) = 0\},$$

where $h(x)$ is some smooth scalar function. In this case the following phase condition is obtained:

$$\phi(x) = h(x(0)) = \langle x(0) - x_{k-1}(0), \dot{x}_{k-1}(0) \rangle = 0. \quad (2.28)$$

The above equation (2.28) specifies a solution $x_{k-1}(\tau)$ passing at $\tau = 0$ through the hyperplane orthogonal to the closed curve $\{x : x = x_{k-1}(\tau), \tau \in [0, 1]\}$. However, the most reliable numerical condition is known as the *integral phase condition* which corresponds to the following:

$$\phi(x) = \int_0^1 \langle x(\tau), \dot{x}_{k-1}(\tau) \rangle d\tau = 0. \quad (2.29)$$

The above condition (2.29) is obtained by minimising the distance of the true solution $x(\tau)$ (possibly shifted $x(\tau + \delta)$ to $x_{k-1}(\tau)$). That is, a minimisation of the following equation has to be carried out:

$$D(\delta) = \int_0^1 \|x(\tau + \delta) - x_{k-1}(\tau)\|^2 d\tau.$$

The optimal solution $x(\tau + \delta)$ satisfies $\frac{dD}{d\delta} = 0$, which results in:

$$\int_0^1 \langle x(\tau) - x_{k-1}(\tau), \dot{x}(\tau) \rangle d\tau = 0.$$

Integrating by parts the above equation and using periodicity results in the integral phase condition (2.29). So equation (2.27) and the phase condition (2.29) represent a well-posed continuation problem for computing the unknowns $x(0)$ and T . In practice, the XPPAuto package uses the Keller's method [89] to trace out a branch of periodic solutions. In particular, this allows calculation of folds along such a branch. The Keller's continuation equation has the following form:

$$\int_0^1 \langle x(\tau) - x_{k-1}(\tau), \dot{x}(\tau) \rangle d\tau + \langle T - T_{k-1}, \dot{T}_{k-1} \rangle + \langle \nu - \nu_{k-1}, \dot{\nu}_{k-1} \rangle - \Delta s = 0. \quad (2.30)$$

The complete formulation then consists of equations (2.27)-(2.30), which are to be solved for $x(\cdot)_k$, T_k , and ν_k . These equations can then be solved by any boundary value problem

(BVP) numerical technique. The most frequently used discretisation method for boundary value problems are *collocation*, *finite differences* or *multiple shooting* methods which are not presented here. However, for a complete reference on these techniques consult for example [44, 97, 106]. This then leads to a large system of algebraic equations $\mathcal{F}(x, \nu) = 0$, where here $x = (x_k, T_k)$ with $k = \{1, \dots, N\}$.

2.4.5 Locating Codimension-1 bifurcations

When following a stationary or periodic solution branch, one can encounter bifurcation points, where the solution loses hyperbolicity (i.e. eigenvalues with zero real part, or a periodic solution with at least one nontrivial Floquet multipliers of unit modulus). To detect codimension-1 bifurcations of stationary and periodic solutions of (2.1) continuation algorithms use test functions. Such a test function $\psi(x, \nu)$ is evaluated along a branch during continuation. The basic feature of a test function for detecting a bifurcation (x^*, ν^*) is $\psi(x, \nu) = 0$. That is, the bifurcation is a zero of the test function. Moreover, it is required that ψ be continuous in a neighbourhood of (x^*, ν^*) , and to change sign. With such a test function a bifurcation point is detected between two successive points (x_{i+1}, ν_{i+1}) and (x_i, ν_i) on the curve and the test function has opposite signs at these points $\psi(x_{i+1}, \nu_{i+1})\psi(x_i, \nu_i) < 0$. In such a case, one can attempt to locate the bifurcation ν^* by applying some root finding algorithm (e.g. Newton's method) to the extended system:

$$\begin{pmatrix} \mathcal{F}(x, \nu) \\ \psi(x, \nu) \end{pmatrix} = 0,$$

with initial point (x_i, ν_i) for example. The simplest test function is for Fold bifurcations. At a fold point, the Jacobian has an algebraically simple zero eigenvalue and no other eigenvalue on the imaginary axis. Thus the test function is the following

$$\psi_{fold}(x, \nu) = \det J(x, \nu) = \lambda_1(x, \nu) \cdots \lambda_n(x, \nu),$$

where $\lambda_j(x, \nu)$ are the eigenvalues of the Jacobian J .

The test function for Hopf bifurcation is the following

$$\psi_{Hopf}(x, \nu) = \prod_{i>j} (\lambda_i(x, \nu) - \lambda_j(x, \nu)),$$

where, as before, the λ_j are the eigenvalues of the Jacobian J . This function vanishes at a Hopf bifurcation point, where there is a pair of eigenvalues $\lambda_{1,2} = \pm i\omega$. Clearly, ψ_{Hopf} is also zero if there is a pair of real eigenvalues $\lambda_1 = k$ and $\lambda_2 = -k$, in this case such points have to be excluded when searching for Hopf bifurcations.

To test stability of an *attractor* the eigenvalues $\lambda_1, \dots, \lambda_n$ of the Jacobian are computed, with $\lambda_i = \alpha + i\omega$ and the test is performed by the following test function:

$$\psi_s = \max\{\alpha_1, \dots, \alpha_n\}.$$

There are many more test functions for detecting other bifurcation sets, for review consult for example the following books [96, 142].

2.4.6 DDE-Biftool

DDE-Biftool is a Matlab package for numerical continuations for delay differential equations with several fixed, discrete delays. The package was initially developed by Engelborghs [51] and is freely available for scientific use. The package consists of a collection of Matlab routines for analysis of which only fixed point and periodic solutions schemes are presented as these were used in this thesis.

2.4.7 Continuation of steady state solutions

Consider the delay equation (2.2) with initial condition $\varphi(t)$. The linearisation of equation (2.2) around a solution $x^*(t)$ is the *variational equation* given by the following:

$$\frac{dy(t)}{dt} = A_0(t)y(t) + A_1(t)y(t - \tau), \quad (2.31)$$

where, using $F \equiv F(x^0, x^1, \nu)$,

$$A_i(t) = \frac{\partial F}{\partial x_i} \Big|_{(x^*(t), x^*(t-\tau), \nu)}, \quad i = \{0, 1\}$$

If $x^*(t)$ corresponds to a steady state solution,

$$x^*(t) \equiv x^* \in \mathbb{R}^n, \quad \text{with} \quad F(x^*, x^*, \nu) = 0, \quad (2.32)$$

then the matrices $A_i(t)$ are constant, $A_i(t) \equiv A_i$. Substituting the sample eigensolution $y(t) = ve^{-\lambda t}$ into the variational equation (2.31) leads to a characteristic equation which results from evaluating the following:

$$\det J = 0, \quad (2.33)$$

where J is an $n \times n$ dimensional matrix defined as:

$$J = \lambda I - A_0 - A_1 e^{-\lambda \tau}.$$

Equation (2.33) has an infinite number of roots $\lambda \in \mathbb{C}$ called the *characteristic roots*, which determine the local stability of the steady state solution x^* .

2.4.8 Continuation of periodic solutions

In studying the existence of periodic solutions of period T for a DDE, a Poincaré operator is considered, which associates with each initial function φ defined on the interval $[-\tau, 0]$ the function $P\varphi = \Phi^T(\varphi)$, i.e. the segment of the solution defined on $[T - \tau, T]$. Thus to compute a periodic solution of a DDE it is necessary to find the solution of the fixed point problem $P\varphi^* = \varphi^*$, where the fixed point φ^* is a point in an infinite dimensional space (i.e. a periodic function in \mathcal{C}).

For a periodic solution equation (2.2) the linearised Poincaré operator $DP(.) = \frac{\partial \Phi^T(\varphi)}{\partial \varphi}$ is defined by the following equality:

$$DP(.)\Delta\varphi = Y^T(\Delta\varphi),$$

where $Y^T(\Delta\varphi)$ is the solution on $[T - \tau, T]$ of the variational equation (2.31) with initial function $\Delta\varphi$. In this case the variational equation (2.31) is obtained by linearising equation (2.2) along the solution $x^*(t)$ (with initial function φ , i.e. denoting $x^*(t, \varphi)$).

The eigenvalues of the operator $DP(.)$ are the Floquet multipliers of the periodic solution $x^*(t, \varphi)$. Thus, a periodic solution equation (2.2) is determined by the initial function $\varphi(\theta)$, $-\tau \leq \theta \leq 0$, and the period T . These unknowns are found by the following:

$$\Phi^T(\varphi) - \varphi = 0, \quad (2.34)$$

$$\phi(\varphi, T) = 0, \quad (2.35)$$

where equation (2.35) defines the phase condition needed to remove the indeterminacy due to the fact that phase shift of any periodic solution is also a periodic solution. For details on the actual continuation and bifurcation algorithms refer to [51].

Chapter 3

Field Theories and Brain dynamics

3.1 EEG and quantitative states of the brain

Spontaneous rhythmic activity was first observed in electrical recordings from the scalp of animals by Caton (1875), and later by Berger (1924) in humans. They observed that electrical activity of the brain is dominated by oscillations that have frequency and amplitude patterns varying widely across different behavioural states such as level of attentiveness, sensation, cognitive effort or vigilance. These oscillations not only occur in spontaneous brain activity but also arise in response to a stimulus (e.g. electrical, auditory, visual, etc.) known as *evoked response potentials* (ERP). Such signals are usually below the noise level (spontaneous activity) and thus are not readily distinguished. To do so requires the use of a train of stimuli and signal averaging to improve the signal-to-noise ratio. In general, high frequency, low amplitude rhythms are associated with alertness and wake or the during rapid-eye-movement (REM) sleep. Low frequency, high amplitude oscillations on the other hand are associated with non REM (NREM) sleep stages and with pathological states such as strokes or coma. EEG frequencies in humans typically vary from 0.5 - 80 Hz, and the amplitudes typically lie between -100 and 100 μ V, however more commonly between 10- 50 μ V. In the power spectrum of the EEG these oscillations are represented by certain peaks superimposed to a $1/f$ continuum where f is the frequency. The five dominant frequency bands typically observed in the human EEG are *delta* (0.5 - 4 Hz), *theta* (4 - 7 Hz), *alpha* (8-13 Hz), *beta* (13 - 30 Hz), *gamma* (30-80Hz) and ripples

(100-600Hz). A brief description of each frequency band is given in section (A.2). Today EEG is widely used to diagnose a number of neurological pathological conditions, particularly in determining seizures [144] or comas [114]. It is also used for understanding behavioural events where EEG is sensitive to changes occurring over milliseconds which is comparable to the time scales of cognitive and behavioural brain activity [104]. Some progress has been made in understanding the relation between EEG underlying brain dynamics, however associating the spatiotemporal patterns observed in EEG with brain events is still poorly understood. In the absence of any real theoretical description of cortical function, the most reasonable framework to interpret spatiotemporal patterns of EEG is by using signal processing. The temporal patterns can be understood by employing for instance spectral measures and/or alternatively using new dimensionality measures proposed for nonlinear and chaotic systems [22, 23]. The spatial information is usually studied via measures of coherency (as with spontaneous EEG) or correlation measures (as with evoked potentials). However, mapping spatiotemporal patterns to brain activity may be much more effective if based, at least partially, on theoretical models of brain dynamics, so that the model parameters are fitted from EEG data. In this case, several quantitative issues must be addressed before any attempt to connect brain functioning with EEG. These include the spatiotemporal scales to be assumed and what are the primary sources that contribute to EEG.

3.1.1 Sources contributing to EEG

EEG measures spatial averages of neuronal source activity. However these sources occur at different scales. These sources are believed to be the electrical potentials that are generated by large formations of mostly pyramidal cells. These cells roughly possess an axial symmetry and they are aligned in parallel, perpendicular to the surface of the cortex [38], as illustrated in Fig. (3.1). This alignment of pyramidal cells occurs mostly within a gyri (typical length is approximately 3-5cm and width is nearly 1cm), however within a sulci the pyramidal cells generally have their axis tangent to the surface of the scalp. Pyramidal cells receive excitatory input at superficial apical dendrites from sub-cortical neurons (e.g. thalamus) as well as from nearby excitatory neurons from either within the same column or from other cortical regions and collect inhibitory inputs at the basal dendrites and their soma from local inhibitory interneurons [38]. Excitatory and inhibitory synapses stimulate opening and closing of different

ionic channels in the cell membranes leading to either depolarisation or hyperpolarisation, respectively. In most excitatory synapses sodium ions flow into the cell, making the extracellular space negatively charged; whereas in most inhibitory synapses potassium ions leave the interior of the neuron, leading to a positively charged extracellular space. When both types of synapses are simultaneously active, a single pyramidal cell behaves as a microscopic electric dipole surrounded by its characteristic electrical field (Local Field Potential) [38, 113]. When a mass of pyramidal cells within a cortical column (approximately 10^4 neurons) synchronise they form a dipole layer whose field potentials sum up to an electric field polarizing the outer tissues and scalp which act as a low pass filter [38]. Note that the cortical column must lie within a gyri as the dipoles formed here sum up according to linear superposition. However, within a sulci the dipoles have opposing directions and thus cancel out. It is possible to define a macroscopic state variable $\bar{\Phi}(r, t)$ which is related to observed potentials measured at location r and time t as the space average over a micro-electrode surface tip in the following way:

$$\bar{\Phi}(r, t) = \frac{1}{S} \int_{S(r)} \Gamma(r, r', t) \Phi(r', t) d^3r', \quad (3.1)$$

where S is the surface area of the electrode. The transcortical potential $\bar{\Phi}(r, t)$ is defined over even smaller volume which can be denoted the ‘descriptive scale’ (chosen to match experiments performed at that scale). Thus $\Phi(r, t)$ measures the electrical potential in the ‘descriptive scale’. Since brain dynamics may involve interaction at several scales, $\Gamma(r, r', t)$ is defined to represent a probability density function that weights ranges of the integral thus expressing the dependence of the measured variables across different spatial and temporal scales. Because the cortical macrocolumn of 3mm diameter lies just below the apparent limit of spatial resolution of scalp EEG recordings it is convenient to choose this ‘descriptive scale’ to define scalp EEG state variables [113]. At the level of the macrocolumn activity arises from approximately $10^5 - 10^6$ neurons and nearly 10^{10} synapses. The neurons and synapses cause micro-source membrane currents $i_m(r, t)$ that sum up to form the transmembrane current density $I_m(r, t)$ which can be defined as follows:

$$I_m = \frac{A}{L} \left(\int_C i_m^{ext} \rho^{ext} dc + \int_C i_m^{inh} \rho^{inh} dc \right), \quad (3.2)$$

where L represents the depth of the cortical macrocolumn and A the surface area of the macrocolumn. dc is the cross-section surface of a cable (in this case the dendritic branch) and the surface area defined as $\Delta C = 2\pi rL$, with r being the radius of a dendrite. The

number of dendritic branches per unit surface area associated with excitatory and inhibitory cells is defined by ρ^{ext} and ρ^{inh} respectively. Thus I_m sums the sources from both excitatory pyramidal cells and inhibitory interneurons resulting in a current distribution per unit volume of the ‘descriptive scale’. Since $\rho^{inh} \ll \rho^{ext}$ (since pyramidal cells outnumber inhibitory interneurons by four to one) it is generally assumed that contributions are dominated by pyramidal cells. Furthermore the currents generated at these dendritic branches are governed by the following cable equation [87]:

$$\begin{cases} i_m^n = C_m \frac{\partial V}{\partial t} + I_{Na} + I_K + I_L + I_{syn}^n, \\ i_m^n = \frac{1}{2\pi r} \frac{\partial}{\partial r} \left(\frac{1}{r_i + r_e} \frac{\partial V}{\partial r} \right), \end{cases} \quad (3.3)$$

where $n = \{ext, inh\}$, r_i and r_e are the resistance per unit length of the intracellular and extracellular media respectively. Since $r_e \ll r_i$ then only r_i is taken into account and generally r_i is assumed to be passive (i.e. constant). Finally, the current source density I_m is related to extracellular potentials $\Phi(r, t)$ by the current conservation Poisson equation

$$\nabla \cdot \sigma(r) \nabla \Phi(r, t) = -I_m(r, t), \quad (3.4)$$

where σ is the local tissue conductivity [113]. The above equations ((3.1)-(3.4)) only explain how electrical potentials emerge in extracellular space, they do not allow deduction of how different cells or key neuronal ensembles organise themselves to form the complex activity observed in EEG. Suppose N electrodes are placed on the scalp where a large fraction of the approximately 10^{12} neurons are recorded, or perhaps more manageable to mathematical consideration, a large fraction of nearly 10^4 macrocolumns are monitored. How is it possible to apply the above equations to make sense of this incredible volume of data? Since these equations contain many unknowns, for example: the distribution of synapses and conductivity, distribution of maximal conductance for all different types of ionic currents along a dendritic branch makes the problem of characterising EEG unwieldy. Is it therefore difficult to understand the following: 1) Localisation of the fine distribution of electrical activation; 2) Understanding if local synaptic interactions are responsible for the neuronal synchrony underlying cortical field potentials that form EEG; 3) Do rhythms in EEG originate from neuronal pacemakers; 4) Do the dynamics of population of neurons lead to emergence of novel properties not apparent at the neuronal level, but observed in EEG. In the subsequent section it is shown that some EEG rhythms can be explained by neuronal pacemakers or ensembles of neurons that share the same properties projecting their activity into the cortex. In particular,

focus is placed on thalamic neurons which are able to display intrinsic oscillatory behaviour, even after synaptic transmission is blocked. This characteristic of thalamic neurons plays a fundamental role in absence seizures making it a crucial physiological brain structure to take into account and thus emphasis is placed on this topic. In an effort to circumvent the above problems of interpreting EEG, models can be employed as an alternative method to understand the spatiotemporal characteristics of EEG. The dynamics observed in these models can then be mapped to EEG state equations ((3.1)-(3.4)). The last section of this chapter introduces some of the most influential neural field models that have been developed to understand and account for some of the spatio-temporal dynamics observed in EEG.

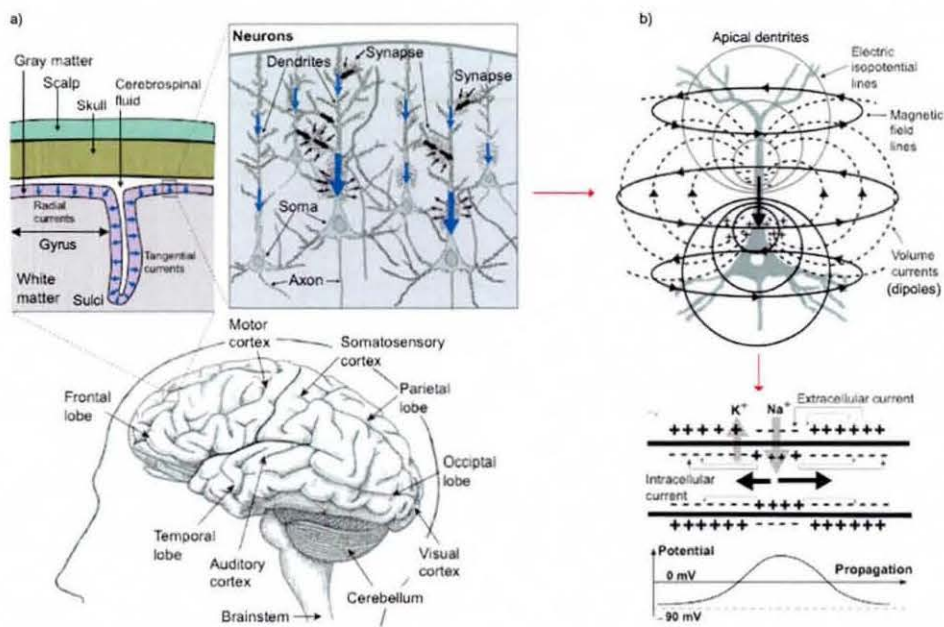


Figure 3.1: a) Section of the cerebral surface: the orientation of the pyramidal cells are normal to the cortex surface except within a sulci. b) Cellular basis of EEG: Extra-cellular ion currents from inhibitory synapses at the basal parts and excitatory synapses at the apical dendrites of cortical pyramidal neurons give rise to source dipole currents. These are mainly due to inflow of Na^+ and outflow of K^+ currents due to postsynaptic potentials, which leads to the depolarisation of the membrane potentials. The leading edge of the depolarisation activates other nearby Na^+ channels and a wave of depolarisation spreads from the point of initiation. The EEG is the spatial sum of these potentials generated by a mass of about 10,000 neurons. Figure adapted from [70].

3.2 Thalamocortical networks and absence seizures

Investigation of the cellular and network mechanisms for absence seizures studies have implicated an abnormality in cortical and thalamic activity in the generation of absence seizures [9, 102, 155]. The cortex and the thalamus are particularly prone to the generation of the synchronized bursts of activity underlying absence seizures, owing to the presence of inhibitory and excitatory neurons that intrinsically generate burst activity. A loss of balance between excitatory and inhibitory influences can take the form of either tonic depolarisations or repetitive rhythmic burst discharges that may give rise to 2.5-3.5Hz spike-wave oscillations. A schematic showing the connection loop between the cortex and thalamus is illustrated in Fig. (4.1). The thalamus is the main relay station for sensory inputs (audition, vision) and somatosensory signals (arriving from the brain stem) and relays to the cerebral cortex (auditory, visual) and motor cortex respectively. Additionally, sensory and motor signals can be blocked in the thalamus during sleep or absence seizures. The two functional modes (relay and non-relay) of the thalamus are associated with two distinct modes of action potential generation by the thalamic neurons. The tonic firing mode is associated with the relay function of the thalamic cells which can occur during wakefulness and during REM sleep. In this state, incoming sensory information may be transmitted accurately to the cortex. On the contrary, burst firing occurs during NREM sleep and is associated with synchronized oscillations in the thalamus during which the transmission of incoming sensory signals is depressed. During NREM sleep, thalamic relay (TC) neurons burst activity arrives at the cortex in a synchronous manner, creating visible patterns in EEG, such as sleep spindles [88, 150]. This “sleep state” of the thalamocortical circuits is in contrast to the normal “wake state”, in which the thalamic relay neurons fire tonically and the thalamocortical projections are transferring sensory input to the cortex in a nonrhythmic manner. During absence seizures, abnormal circuitry causes rhythmic activation of the cortex (typical of normal non-REM sleep) during wakefulness, which results in the characteristics EEG spike-wave discharges. The precise abnormality of the circuits has yet to be determined, but there are multiple possibilities. The overriding concept however, is that absence seizures are generated through alteration of the normal cellular and thalamocortical network mechanisms underlying the generation of slow-wave sleep EEG rhythms: the *spindle wave* [64, 65]. The reader is asked to refer to Fig. (7.3) on page 231 of [43] for illustrations of these oscillations occurring in the thalamus and cortex. This concept is reviewed as it has

been investigated through detailed computation models [43] which have clarified many of the competing hypothesis and also because it directly relates to the macroscopic thalamocortical model analyzed in subsequent chapters.

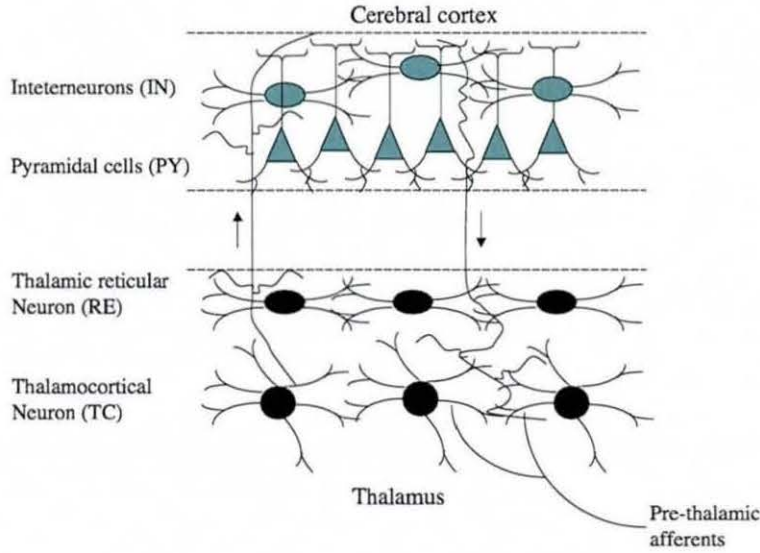


Figure 3.2: A schematic of the thalamocortical loop proposed for absence seizures: Thalamic system consists of thalamic reticular (RE) which project GABAergic inhibitory connections to thalamic relay neurons (TC). TC cells receive prethalamic afferent connections consisting of sensory or motor inputs and relay thalamocortical excitatory fibre inputs to RE and cortical cells where these connections are mediated by mainly AMPA receptors. The cortex is organised mainly by pyramidal cells (PY) which project NMDA and AMPA mediated excitatory connections to inhibitory inter-neurons (IN) and also send corticothalamic feedback back to the thalamus. The IN neurons synapse onto PY cells which is mediated GABAergic receptors. (Figure adapted from [43]).

3.2.1 Cellular mechanism of thalamic neurons

The firing pattern of a cell is controlled by the level of its membrane potential. When a cell is relatively depolarized it generates a train of single spikes (action potentials). A hyperpolarized state promotes burst firing. However, the electrophysiological properties of a cell can broaden or diminish the repertoire of possible firing modes. In TC and RE neurons, single spikes (*tonic* firing) are mediated by the voltage-dependent sodium (Na^+) and potassium (K^+) and

this is a similar response in most types of neurons. In particular, TC cells (at depolarized resting, membrane potential -50mv) fire action potentials at a frequency proportional to the amplitude of the injected currents. In contrast, RE (rest membrane potential -68 mv) cells fire 20-60Hz. Through *in-vitro* slice preparations Jahnsen and Llinas [79, 80] demonstrated that following a IPSP (inhibitory post synaptic potential), which provides hyperpolarisation of the membrane potential (-80mv) TC cells enter burst mode (300Hz) due to slow calcium currents, also known as low-threshold Ca^{2+} or as T-current (I_T). Due to the burst only occurring upon release from sustained inhibition, this phenomena was termed *post-inhibitory rebound burst*. The same phenomena occurs in RE cells (at hyperpolarised membrane potentials of -90mv) where Ca^{2+} spike bursts of 400Hz are initiated by the rising phase of EPSPs (excitatory post synaptic potential). However, the kinetics of I_T currents seem to be slower in RE cells, hence termed I_{T_s} [10]. The existence of mixed Na^+ and K^+ currents termed I_H was determined by McCormick and Pape [108] which is a current that can also be activated at the hyperpolarised level. It is found that the interplay of I_H and I_T currents can generate delta frequencies (0.5Hz-4Hz) in TC cells, while the interplay of other currents, namely $I_{K[Ca]}$ (calcium-activated potassium current) and the non-specific currents I_{CAN} and I_{T_s} are identified in the genesis of 7 – 12Hz (alpha oscillations) in RE cells [14]. The TC cells display an extra oscillatory mode of 0.5-3.2Hz which is composed of *waxing-and-waning* (waxing corresponding to growth phase and waning to burst firing) envelopes of duration 1-2s and silent phases of 5-25s (the reader is asked to refer to Fig (4.1) of [43] on page 90). This firing mode is activated by increasing the amplitude of the I_H current which transforms delta oscillations into *waxing-and-waning*. The electro-physiological properties of TC and RE neurons make it possible for TC-RE network to account for *spindles waves* and slow oscillations ($< 1Hz - 4Hz$).

3.2.2 Spindle waves

Spindles waves are 6-15Hz oscillations in the EEG that *wax and wane* (dictated mainly by the cycle to complete a loop of activity between RE and TC neurons, taking approximately 70 – 150ms) over a period of 1-2s and recur approximately once every 5-10s during early stages of sleep. The reader can refer to Fig (7.7) of [43] on page 237 for an illustration of spindle waves in thalamic systems. The TC cells excite RE cells with glutamatergic AMPA synaptic transmission whereas the activity from RE to TC neurons is an inhibitory action

which hyperpolarizes the TC cells by means of GABAergic neuromodulators [95, 156]. This hyperpolarisation is mediated mainly by fast $GABA_A$ receptors in TC cells, since $GABA_B$ receptors have a higher threshold for activation. The hyperpolarisation is high when RE cells are burst firing which cause temporal summation of IPSPs. The summed IPSP may result in (via inactivation of enough low-threshold Ca^{2+} currents in the recipient TC cell) a rebound low-threshold spike (LTS) [79, 80]. This in turn activates a burst of 1 to 4 action potentials (due to Na^+). Because TC and RE cells are reciprocally connected, the burst of action potentials in thalamocortical cells once again excites the RE cells (through I_T), thereby initiating the next cycle in the spindle. The generation of spindle waves requires both TC and RE cells be relatively hyperpolarized so that low-threshold Ca^+ current may be activated. This requirement explains the suppression of spindle waves by arousal. The increased activity that underlies arousal (i.e. hypothalamus) releases neuro-modulators causing the net depolarisation of RE, TC (enhancement of I_H current) and some cortical neurons through the reduction of K^+ conductances [107, 153].

3.2.3 Slow waves

Importantly, RE cells are linked via mutual inhibitory connections mediated by $GABA_A$, and also through longer lasting $GABA_B$ receptor [139, 163]. The role of these connections is to control the discharge (amplitude and duration of excitation) of these cells by thalamic and cortical activity, which may have important consequences for the generation of slow oscillations ($< 1Hz - 4Hz$) and consequently spike-wave activity [91, 146]. This can be observed by application of intrathalamic injection (*in-vivo* or *in-vitro* slices) of $GABA_A$ antagonists that block $GABA_A$ receptors through which RE-RE inhibition is mediated [88, 100, 150, 154]. This results in a pronounced increase in action potentials, presumably from disinhibition of other RE cells [13, 15]. Following disinhibition, RE neurons respond to bombardment of EPSPs (either from the cortex or TC cells), which generate a prolonged burst of action potentials and subsequently activate slow, $GABA_B$ -mediated IPSPs in their post-synaptic TC cells. Functionally, the activation of $GABA_B$ receptors result in a slowing of the oscillatory activity between RE and TC neurons, owing to slow kinetics and prolonged duration (150-300ms) of these IPSPs. This is efficient in the removal of inactivation of the I_T current in TC neurons thus causing longer bursts in these cells. Following the near complete block of $GABA_A$ receptors,

the time to complete a loop of activity between RE and TC neurons lengthens to between 300 and 400ms, therefore the network generates rhythmic oscillations between 2 and 3Hz. Because this frequency is similar to that at which TC cells prefer to endogenously oscillate, owing to I_T and the pacemaker I_H , the TC neurons discharge several action potentials every cycle of the network oscillation. Blocking $GABA_A$ receptors in the thalamus may therefore result in the transformation of spindle waves to 2-3Hz.

3.2.4 Spike-waves

Investigations of spike-wave seizures in cats have emphasized the important role of the cortex in conjunction with corticothalamic interaction in generating pathological discharges [36]. While intrathalamic injections of high doses of $GABA_A$ antagonists results in highly synchronized 2-3Hz (*slow-wave*) oscillations without any spike-wave discharge, on the contrary, the same drug application to the cortex results in spike-wave seizures as long as the thalamocortical network is intact [64]. This is based on experimental evidence, where lesions of the RE nucleus causes cessation of spike-wave activity demonstrating the involvement of the thalamus [11, 27]. The participation of the thalamus in these pathological discharges is shown to be mediated by $GABA_B$ receptors via intrathalamic injection of $GABA_B$ agonists which promote spike-wave oscillations, whereas administration of $GABA_B$ antagonists suppress them [75]. Furthermore, the removal of the cortex causes the underlying thalamus to generate only spindle waves without seizures, but the removal of one cortical hemisphere shows seizures occurring in the intact hemisphere [154]. These studies indicate that disinhibition of neuronal activities in either the cerebral cortex or thalamus may result in abnormal 2-4Hz oscillation in the EEG, in particular, with disinhibition of the neocortex resulting in activity that is most similar to spike-wave oscillations in human epilepsy [64, 152]. One possibility, is that the abnormal discharge of corticothalamic neurons, owing to an imbalance of excitation and inhibition in the cerebral cortex, results in the strong phasic excitation of RE, TC and local GABAergic neurons. Thus the strong activation of the corticothalamic pathway may result in both the direct excitation of TC cells and the hyperpolarisation of these cells through disynaptic inhibition via RE cells and local GABAergic neurons [42]. Initially, all cells, including the cortical neurons discharge only weakly and intermittently in response to each phase of the spindle wave, while the development of spike-wave discharges is associated with synchronised strong bursting in

these cells during the spike and periods of hyperpolarization and silence during the wave. The reader is asked to refer to Fig (8.28 A) of [43] on page 328 demonstrating how these oscillations are generated.

Despite the progress made in developing computational models by Destexhe and Sejnowski [43], questions and controversies regarding the underlying epileptogenesis of absence seizures still persist. These models have been valuable in clarifying competing hypotheses in the literature and showing that the switch to spike-wave occurs as a result of the blocking of $GABA_A$ IPSPs and increase in $GABA_B$ IPSPs, and the resulting increase in burst firing in the TC neurons. However, the biological evidence for this sequence of events is only from *in-vitro* work (i.e. slices). *In-vivo* experiments do not find any increased burst firing during slow wave activity, indeed the opposite is true. That is, the vast majority of TC neurons are hyperpolarized as a result of the strong firing from the reticular neurons [39, 123]. To date there has been no models explaining this behaviour and this is mainly because of the difficulty in replicating *in-vivo* dynamics due to high variability of the intrinsic activity of *in-vivo* neurons and the dynamics occurring as a result of the interacting populations of neurons. One plausible way to circumvent these shortcoming is to first apply physiologically realistic neuronal macroscopic models based on ‘order parameter fields’. This is a concept used in statistical mechanics where the important variables of the system say $GABA_B$, I_T and I_H are lumped into a single parameter say, $\nu = M(GABA_B, I_T, I_H)$, where M is a function mapping the physical space to the parameter space. The key aspect here is to search in the parameter space changes in dynamics that correspond to the dynamics we search in the real system. Secondly, once suitable parameters are found then mappings from the macroscopic models to realistic computational models (which include the relevant physical variables) may be considered to reveal the source of the underlying activity. However, finding suitable ‘order parameter fields’ and suitable models is scientifically challenging and this is the topic of next section which provides the most influential ideas used in macroscopic brain dynamics.

3.3 Macroscopic brain models and EEG

Different modelling approaches have been proposed for macroscopic dynamics and they are essentially categorised into three main groups: *Neural Field*, *Population Density* and *Mass Action* models, however variants and mixes of these approaches exist. These different variants are an attempt to gain insight into the complexity of brain dynamics by avoiding the overwhelming details of individual neurons as predicted by models of action potential generation, e.g. the Hodgkin and Huxley model [73]. As presented in Chapter 1, neuronal activity occurs at different spatiotemporal scales and in general the dynamical range that must be modelled extends over several orders of magnitudes. However, existing modelling techniques are incapable of dealing with such complexity and as such the general approach is to project this huge range to a single scale and concentrate on a particular feature of the activity. These models work under the assumption that precise trajectories for all single neuron activity is not knowable and need not be known, but averages are sufficient to describe ensemble dynamics. However, this is only true if spatially localized neural populations share nearly identical responses to identical stimuli. This would allow to characterization of the population by a single state variable.

3.3.1 Neural Field models

The first model to be considered was proposed Wilson and Cowan [168]. It suggests that a population of neurons can be described by a single state variable representing the proportion of neurons becoming active per unit time, which corresponds to the generation of action potentials. In the following sections the Wilson and Cowan model is derived in a different manner enabling a better understanding of the assumptions of their approach. The subsequent derivations consider only temporal dynamics for a single recurrent population. Each individual neuron is considered to be one compartment, that is, a neuron is a zero-dimensional process. Furthermore the equations are formulated using the idea of *separation of time scales* (refer to section (2.1.7) for details).

How do we model a neuronal ensemble consisting of N neurons with all to all coupling, that is N^2 connections and relate the output to EEG? As a first attempt to model the system a single

compartment Hodgkin-Huxley model [73] could be employed, where every neuron possesses many synaptic gating variables from different ionic currents and a membrane voltage. Numerically simulating such a system will be computationally demanding because every neuron constitutes several dynamic variables (at different time scales) and also because information (in this case spikes) has to flow within the network affecting responses of another neurons. A first simplification that is often performed in the literature, is to reduce the complexity of gating variables by ignoring the detailed dynamics of transmitter concentration in the synaptic cleft. Instead, the transmitter-activated ion channels are described by an explicitly time-dependent conductivity $g_{ij}(t)$ at neuron i that will open whenever a pre-synaptic spike from neuron j arrives. In this simplification neuronal activity is governed by perturbations of the cells voltage V_i , and $g_{ij}(t)$ which can be seen having invariant dynamics. The temporal evolution of the above state variables can be written in the following form:

$$C_m \frac{dV_i}{dt} = -g_{Li}(V_i - V_L) - \bar{g}_{ij} \sum_j^N g_{ij}(V_i - V_{ij}) + I_{app,i}, \quad (3.5)$$

$$g_{ij} = \int_{t_0}^t g_{syn}^{ij}(t-s) \sum_{m \in \mathbb{Z}} \delta(s - t_{ij}^m) ds, \quad (3.6)$$

where $R = 1/g_L$ is the resistance of the membrane of a neuron and C_m is the capacitance. V_L is the resting potential of the neuron, \bar{g}_{ij} is the maximal conductance and an external current I_{app} can be applied to measure the electrical response of the neurons. Equation (3.5) defines the time course of the neuron voltage V_i with a response similar to a resistance-capacitance ($\tau_m = RC$) circuit, where τ_m defines the constant of leakage. That is, for small current amplitudes, the membrane potential increases exponentially to an asymptotic value which depends roughly linearly on the applied current and in turn proportional to R . This linear response is only valid for small applied currents. If the current exceeds some threshold value V^{thr} (which depends on the neuron type), the behavior becomes highly nonlinear. A positive pulse in the voltage is generated (i.e. action potential), with an amplitude of up to 100 mV and a duration of about 1 ms. The activation of the circuit also depends on the synaptic currents, $g_{ij}(V_i - V_{ij})$ where g_{ij} corresponds to the synaptic conductance and V_{ij} a reversal potential. If $V_{ij} > V^{thr}$ then the reversal potential tries to pull V towards V_{ij} which excites the neurons, i.e. an excitatory synapse, otherwise it is an inhibitory synapse. Equation (3.6) defines the synapse g_{ij} as a temporal convolution of sequences of spikes $\sum_{m \in \mathbb{Z}} \delta(t - t_{ij}^m)$ with some integral kernel g_{syn}^{ij} . t_0 is some initial time and t_{ij} is the time during which the action potential travelled from the axon of neuron j to the presynaptic terminal of neuron i . The

above network formulation results in a system consisting of $N^2 + N$ dynamical variables, resulting in demanding processing time and the data produced is hard to compare with the important macroscopic EEG dynamics especially in the limit of large N .

To circumvent this complexity, neural field approaches assume that the firing rate of the action potential is the desired measure of neuronal response to a stimulus, although additional information may be encoded in other characteristics of the firing patterns. To see under which conditions a firing rate description might be valid, first consider the simplest firing rate. We choose a time interval T , count the number of spikes within this time period and then define the rate as the number of spikes divided by the length of the interval. Suppose that a neuron j is firing at a constant rate with period T_j , then the postsynaptic input is defined as the following firing rate variable

$$\begin{aligned}\hat{g}_{ij} &= \frac{1}{T_j} \int_0^{T_j} dt \int_{t_0}^t g_{syn}^{ij}(t-s) \sum_{m \in \mathbb{Z}} \delta(s - t_{ij}^m) ds \\ &\Leftrightarrow \int_{t_0}^t g_{syn}^{ij}(t-s) v_j(s - t_{ij}) ds,\end{aligned}\tag{3.7}$$

where $v_j(s - t_{ij}) = \frac{1}{T_j} \int_0^{T_j} dt \sum_{m \in \mathbb{Z}} \delta(s - t_{ij}^m)$. From equation (3.7) we can investigate under what conditions a spiking model can be turned into a non-spiking model for macroscopic dynamics. Suppose that the response of the post-synaptic conductance g_{syn}^{ij} to a single spike corresponds to a rapid rise and subsequently an exponential decay with some time constant τ_{ij} , where the rise represents the opening of ion channels and decay the closing. Furthermore, assuming that τ_{ij} has a much larger time scale than the interspike interval T_j of the pre-synaptic neuron, then \hat{g}_{ij} approaches periodic behaviour. During each interspike interval, \hat{g}_{ij} decays exponentially by the same amount that it is incremented by the next spike, in this case we have $\hat{g}_{ij} = v_j$. However, in reality neurons do not fire with perfect periodicity indefinitely, and some care must be taken to define appropriately the firing rate of a neuron.

Defining the firing rate of a neuron as a function of the membrane potential, that is, $v_j = \varsigma_j(V_j)$, allows to some extent generalisation of the above discussion for varying firing rate. The preceding discussion was for constant pre-synaptic frequency. If the frequency of the pre-synaptic neuron $v_j = \varsigma_j(V_j)$ varies slowly, then the approximation, $\hat{g}_{ij} \approx v_j$ will still hold, allowing a definition of a macroscopic firing rate model. For this to be possible it must be assumed that the synapses evolve on a much slower time scale than that of the voltage, i.e. $\tau_m \ll \tau^{ij}$, which implies that voltage reaches its steady state faster than that of the

synapses. However, in reality τ_m and τ^{ij} are of the same order of magnitude and thus the separation of scales cannot be performed cleanly. Using separation of scales allows the solutions of fast dynamics for its asymptotic value V_∞ and then use this solution in the slow dynamics to understand the slow process. A further assumption for this is to assume that all conductances are constant in time. In particular, the reversal potentials $V_i - V_{ij}$ in Equation (3.5) should be constant to allow the voltage settle to an asymptotic value. However note, this might be a reasonable assumption for excitatory neurons, but a very strong assumption for inhibitory neurons. For example, consider $g_{AMPA}(t)(V - V_{AMPA})$ which is an excitatory synapse, with the reversal potential $V_{AMPA} = 5mv$. Also consider the resting potential of a pyramidal cell $V_{rest} = -70mv$ and threshold $V^{thr} = -50mv$. In general experimental studies show the following amplitude difference $|V - V_{AMPA}| \approx 70mv$, however the fluctuations (deviation σ_V) are very small $\sigma_V \ll |V - V_{AMPA}|$. In this case it is possible to apply the approximation $g_{ij}(t)(V_i - V_{ij}) \approx g_{ij}(t)(V_{rest} - V_{ij}) = g_{ij}\Delta V_{ij}$, where ΔV_{ij} is now a constant. On the contrary, using the above procedure for the inhibitory synapse $g_{GABA}(t)(V - V_{GABA})$ is not a correct one, since $V_{GABA} = -70mv$ and because the fluctuations are large $\sigma_v \approx 10mv$. However, for the derivation of nonspiking models to be possible the above assumptions are necessary which then allow the determination of the asymptotic voltage by setting $\frac{dV_i}{dt} = 0$. This then yields a steady state value for the voltage $V_i^\infty = V_L + \frac{\bar{g}_{ij}}{g_{Li}} \sum_j \hat{g}_{ij} \Delta V_{ij} + \frac{I_{app,i}}{g_{Li}}$. In this case, a given setting of the post-synaptic conductance cannot produce spiking unless $V_i^\infty > V_i^{thr}$. Without loss of generality further simplification is made by assuming $V_L = 0$, $I_{ext,i} = \frac{I_{app,i}}{g_{Li}}$ and by defining the synaptic weights $\nu_{ij} = \frac{\bar{g}_{ij}}{g_{Li}} \Delta V_{ij}$. The separation of scales essentially reduces the system from $N^2 + N$ to the following N^2 equations.

$$\hat{g}_{ij}(t) = \int_{t_0}^t g_{syn}^{ij}(t-s) \varsigma_j(V_j^\infty(s-t_{ij})) ds. \quad (3.8)$$

Because all internal neuronal structure has been ignored (such as dendritic tree and the finite propagation times along dendrites), the synaptic activity (3.8) in cell i can be linearly summed to obtain the following

$$\hat{g}_i(t) = \sum_j \int_{t_0}^t g_{syn}^{ij}(t-s) \varsigma_j(V_j^\infty(s-t_{ij})) ds. \quad (3.9)$$

Under additional constraints the network may be simplified. Most of the time course of the postsynaptic potential g_{syn}^{ij} depends only on the postsynaptic cell i which is captured by the following equation (from [83]):

$$g_{syn}^{ij}(t) = \kappa_{ij} G_{ij}(t), \quad (3.10)$$

where $G_{ij}(t)$ is related to the time course of the diffusion process of transmitters in the synaptic cleft after release at the pre-synaptic terminal and their binding process to the receptors on the postsynaptic terminal. κ_{ij} is a constant scaling factor representing the magnitude of the this process. Applying equation (3.10) allows us to rewrite equation (3.9) in the following form

$$\hat{g}_i(t) = \int_{t_0}^t G_{ij}(t-s) \sum_j \kappa_{ij} \varsigma_j \left(\sum_j \nu_{ij} \hat{g}_j(s - t_{ij}) + I_{app,i} \right) ds, \quad (3.11)$$

where the inverse $G_{ij}(\cdot)^{-1}$ of the integral operator $G_{ij}(\cdot)$ will be the sum of differentials with constant coefficients c_n .

$$G_{ij}(\cdot)^{-1} \hat{g}_i(t) = \sum_{n=0}^{\infty} c_n \frac{\partial^n}{\partial t^n} \hat{g}_i.$$

$G_{ij}(t-s)$ can have either exponential or polynomial form, however synaptic activity is best represented as either bi-exponential with an exponential finite response rise time representing opening of channels and an exponential decay time identifying the closing of channels. For example, a simple, but often used, integral kernel is $G_{ij}(t-s) = e^{-(t-s)/\tau_{ij}}$ that assumes an infinite rapid response time and a finite exponential decay. This then leads to the following differential equation for sufficiently small time delay, $t_{ij} \approx 0$ with $c_0^i = 1$, $c_1^i = \tau_{ij}$ and $c_n^i = 0$; $n \geq 2$:

$$\tau_{ij} \dot{\hat{g}}_i = -\hat{g}_i + \sum_j \kappa_{ij} \varsigma_j \left(\sum_j \nu_{ij} \hat{g}_j(t) + I_{app,i} \right). \quad (3.12)$$

A further reduction is to assume that all synaptic time constants are the same $\tau_{ij} = \tau$. Then all synapses g_{1j}, \dots, g_{Nj} emanating from a single presynaptic neuron have the same temporal behaviour. With this simplification, the model (3.12) reduces from N^2 to N variables defined as follows:

$$\tau \dot{\hat{g}}_i = -\hat{g}_i + \lambda_{ij} \varsigma_j (w_{ij} \hat{g}_j(t) + I_{app,i}), \quad (3.13)$$

where $w_{ij} = N_j \nu_{ij}$ defines the synaptic weights and the coefficient $\lambda_{ij} = N_j \kappa_{ij}$ can for example regulate the firing rate.

The final simplification is to assume that macroscopically, the behaviour of a cell assembly can be characterized in terms of the time or ensemble averaged behaviour of a homogenous collection of neurons that populate it. For large assemblies, we can consider an individual

cell variable $\hat{g}_i(t)$ a sample path from a random process, $\hat{g}(t)$. The corresponding system level parameter of interest is the sample mean, $\overline{\hat{g}(t)}$, or expectation $\langle \hat{g}(t) \rangle$. A macroscopic average model reduces the system description from a set of N coupled equations to a few equations involving expectations and standard deviations of these random variables. The Law of large numbers shows that the expectation approaches the sample average as $N \rightarrow \infty$. Thus the following averages are defined:

$$\bar{\hat{g}}(t) \triangleq \frac{1}{N} \sum_{j \in N} \hat{g}_j \approx \langle \phi(t) \rangle,$$

and by definition

$$\frac{d\bar{\hat{g}}(t)}{dt} = \frac{d}{dt} \left[\frac{1}{N} \sum_{j \in N} \hat{g}_j(t) \right] = \frac{1}{N} \sum_{j \in N} \frac{d\hat{g}_j(t)}{dt} = \frac{d\overline{\hat{g}_j(t)}}{dt}.$$

Applying the above average equations to the model (3.13) results in a single recurrent mean neural field model equation:

$$\tau \dot{g} = -g + \lambda \varsigma(wg(t) + I_{app}), \quad (3.14)$$

where it is assumed that τ , g , λ, w and I_{app} represent averages. Equation (3.14) equation is equivalent to the Wilson and Cowan model [168]. However, Wilson and Cowan defined empirically the dynamic variables to represent the proportion of active neurons in a population per unit time, whereas in the above derivation the variables show explicit dependence with the temporal dynamics of the synapses. Also in their model they also accounted for the refractory period and later publications accounted for spatially interacting excitatory and inhibitory populations [169].

An alternative formulation of neural field equation was proposed by Nunez [113] and further generalized by Jirsa and Haken [84]. In this approach, the activity of the neuronal ensemble is governed by the time scale of the membrane voltage, that is, the synaptic conductance are assumed to have a faster time scale. Consequently, a model of N interacting populations will have the following structure

$$\tau \dot{v}_i = -v_i + \sum_j w_{ij} \varsigma(v_j(t)), \quad (3.15)$$

where τ defines the intrinsic time scale on which the voltage v_i evolves. The model equations (3.14) and (3.15) are in essence similar and capture essential temporal macroscopic dynamics.

3.3.2 Spatial propagation of neuronal activity

The previous section introduced equations for temporal dynamics where the assumption was that each neuron is a point process (zero dimensional). However, neuronal activity is also spatially distributed and in general this activity is a function of the network topology defined with some boundary conditions and synaptic weights. The network connectivity addresses how the effective geometry affects dynamics while synaptic weights introduce a quantitative measure of these connections. Moreover, there are multiple spatial scales of brain organisation traversing single neuron to the level of scalp EEG. Over these scales the connection topologies change from perhaps probabilistic to structured and hierarchical as found in the neocortex presented in Chapter 1, which shape the spatial dynamics observed at each level.

At the level of EEG Amari was among the first to study spatially and temporally continuous neural fields [4]. The temporal dynamics correspond to equation (3.15), however to account for spatial activity it incorporates a continuum physical space: $w_{ij} \rightarrow w(r, R)dr$, $v_i(t) \rightarrow \phi(r, t)$ and $\sum_j \rightarrow \int_D$ where r and R are identified as being two different spatial locations and D represents a cortical surface area (of some geometrical form) and thus the equations are defined as follows:

$$\tau \frac{\partial \phi(r, t)}{\partial t} = -\phi(r, t) + \int_D w(r, R) \varsigma(\phi(R, t)) dR. \quad (3.16)$$

In this model formulation, time delays caused by propagation times are ignored. This assumption is valid if the delay is small compared to the time scale on which the system is studied. The macroscopic EEG connectivity of the system is defined in $w(r, R)$ which in general is defined as being excitatory for proximate connections and inhibitory for greater distances as observed in macrocolumns. Furthermore, Amari considered the macrocolumns to be spatially symmetric and translationally invariant in which $w(r, R) = w(|x - R|)$. This type of model does not account for oscillations, but locally excited regimes may exist and self-sustain without external inputs.

Later work by Jirsa and Haken [84] incorporated delays in the above equations to consider long range connections between cortical regions that resulted in the well known wave-like equation. These equations allow the study of propagation and oscillatory properties of the cortical surface. In this section the derivations of the wave-like equations are provided as

the primary model studied in this thesis incorporates this. Incorporating delays into Amaris equations (3.16) results in the following:

$$\tau \frac{\partial \phi(r, t)}{\partial t} = -\phi(r, t) + \int_D w(r, R) \varsigma(\phi(R, t - \frac{r-R}{v_a})) dR, \quad (3.17)$$

where $\varsigma(\phi(R, t - \frac{r-R}{v_a}))$ is the firing rate of action potentials at location R resulting in late synaptic activity at location r , dependent on the separation distance $|r - R|$ and the action potential velocity v_a . $\phi(r, t)$ represents the field activity at the end of axon terminal. The number density of fibres connecting locations R and r with propagation velocity v_a is described by a connectivity (distribution) function

$$w(|r - R|) = \frac{e^{-\frac{|r-R|}{r_a}}}{2r_a}.$$

Here the spatial connectivity of the activity is assumed to decay with distance, which is in agreement with experimental observations [149]. r_a is the spatial range (i.e mean axonal range) which also indirectly defines a hierarchy of time scales over which ϕ operates. Furthermore, an isotropic distribution of axons is assumed. Equation (3.17) can be re-written as

$$\phi(r, t) = \int_0^\infty dv \int_D w(r, R) \varsigma(R, t - \frac{r-R}{v_a}) dR. \quad (3.18)$$

Phenomenologically the spike velocity and spike shape does not change along an axon and incorporating this observation reduces (3.18) to:

$$\phi(r, t) = \int_D w(r, R) \varsigma(R, t - \frac{r-R}{v}) dR. \quad (3.19)$$

Expressing the time delay via propagation along corticocortical fibers as a delta function $\delta(t - T - \frac{|r-R|}{v_a})$ the solution of equation (3.19) can be written in-terms of a Green's function G of the following form:

$$\phi(r, t) = \int_D \int_{-\infty}^\infty G(r - R, t - T) \varsigma(R, T) dT dR, \quad (3.20)$$

with

$$G(r - R, t - T) = \delta(t - T - \frac{|r - R|}{v_a}) \frac{e^{-|r-R|/r_a}}{2r_a}.$$

This permits Fourier transformations of the individual terms in (3.20) as follows:

$$\begin{cases} \phi(r, t) = \frac{1}{2\pi} \int_{-\infty}^\infty \int_{-\infty}^\infty e^{ikr - i\omega t} \phi(k, \omega) dk d\omega, \\ \varsigma(r, t) = \frac{1}{2\pi} \int_{-\infty}^\infty \int_{-\infty}^\infty e^{ikr - i\omega t} \varsigma(k, \omega) dk d\omega, \\ G(r - R, t - T) = \frac{1}{2\pi} \int_{-\infty}^\infty \int_{-\infty}^\infty e^{ik(r-R) - i\omega(t-T)} g(k, \omega) dk d\omega, \end{cases}$$

Thus in Fourier space the following relations are obtained:

$$\phi(k, \omega) = g(k, \omega)\varsigma(k, \omega). \quad (3.21)$$

Specifically, applying the inverse Fourier transform of $g(k, \omega)$ results in the following:

$$g(k, \omega) = \int_{-\infty}^{\infty} \int_{-\infty}^{\infty} G(r - R, t - T) e^{ik(r-R) + i\omega(t-T)} = \frac{\gamma_a^2 - i\gamma_a\omega}{(\gamma_a - i\omega)^2 + k^2 v_a^2} \quad (3.22)$$

where the parameter $\gamma_a = \frac{v_a}{r_a}$. Finally, substituting (3.22) into equation (3.21) and rewriting the resulting relation back into the space and time domain yields the following wave-like equation:

$$\left(\frac{\partial^2}{\partial t^2} + 2\gamma_a \frac{\partial}{\partial t} + \gamma_a^2 - v_a^2 \nabla^2 \right) \phi_e = (\gamma_a^2 - \gamma_a \frac{\partial}{\partial t}) \varsigma(r, t), \quad (3.23)$$

where ∇^2 is the Laplacian operator. Thus equation (3.23) describes pulse propagation along an axon in terms of the generated firing rates $\varsigma(r, t)$. For inhibitory neurons connectivity is short range, typically axonal ranges of about 0.1cm. This implies that the connectivity function for inhibitory connections reduces to the following $\Gamma(r, R) = \delta(r - R)$ which results in a simpler formulation. Alternatively $\gamma_a \rightarrow \infty$ which implies that equation (3.23) transforms to $\phi(r, t) = \varsigma$.

Neural field models are nonlinear spatially extended systems and thus support pattern formation. The analysis of such behaviour typically involves linear Turing instability, nonlinear perturbation theory and numerical simulations. The pattern formation include global periodic, standing and spiral waves [37] and as well other complex patterns, for example related to epilepsy [35]. The nature of these patterns solutions to some degree relate to the wave patterns observed in EEG and local field potentials, however the theory is far from being complete in that it cannot interpret the observed and simulated global patterns in terms of lower scales of activity. This difficulty arises because of the separation of scales assumed in neural field models and thus information exchange between levels of activity is lost.

3.3.3 Population density models

As an alternative to neural field approaches, population density models can be applied. The population density method allows grouping of neurons into populations and tracking the

distribution of neurons over the state space of each population. Neural field models also group neurons into populations, but on the contrary, the state of each neuron is lumped into a single state variable. For this reason neural field models can be seen as a particular case of population density models, where the density distribution is uniform or alternatively a delta function (i.e. higher statistical moments are not considered). The population density approach allows modelling of fast temporal dynamics observed in transient activity [62], and also a more accurately representation of refractory activity by incorporating refractory densities. However, it is computationally more demanding than the neural field approach. For excellent reference papers on this topic see for example [47, 116].

The theoretical approach taken is to consider a reduction of the phase space of the dynamics governing the activity of single neuron, where it is then possible to define the fraction of neurons per unit volume of the phase space in the mathematical limit of an infinite number of neurons. This then allows use of the Kolmogorov-Fokker-Planck equation which describes the time evolution of the probability density function. The advantage of this formulation is that it allows one to model the variability of neural activity as probability densities over trajectories through the state space and thus, for example taking, into account stochastic processes. However, it assumes that the such processes are smooth, which then allows interpretation of the randomness as a diffusive process. To make things clear, suppose that the state of neuron x is governed by some dynamical system of the following form

$$\frac{dx}{dt} = F(x) + S(x, g(t)),$$

where F is the vector field, which could be that of the Hodgkin-Huxley model [73] and $S(x, g(t))$ denotes incoming synaptic currents that depends on x and conductances $g(t)$ (which may represent noise input). The state space for each neuron in the Hodgkin-Huxley model is four dimensional $x = (V, m, h, n)$, where V is the membrane potential, m governs the sodium activation, h the sodium inactivation, and n the potassium activation. A direct simulation by following the trajectories of all neurons in a network of Hodgkin-Huxley like models introduces high computational cost and is not amenable to mathematical analysis. Suppose it is possible to find the probability density function $\rho(x, t)$ for a neuron, that is, a function that satisfies $\int_{-\infty}^{\infty} \rho(x, t) dx = 1$, and in this case $\int_{\Omega} \rho(x, t) dx = Pr(\text{the state of a neuron} \in \Omega)$. By ignoring the trajectories of individual neurons and assuming a population of N similar neurons, $\rho(x, t)$

can be interpreted as a *population density*, that can be defined as

$$\lim_{N \rightarrow \infty} \left(\frac{\text{neurons with } x \in \Omega}{N} \right) = \int_{\Omega} \rho(x, t) dx = \text{Fractions of neurons whose state } \in \Omega.$$

The evolution of density in the phase space can then be described by the Kolmogorov-Fokker-Planck equation (KFP):

$$\frac{\partial \rho(x, t)}{\partial t} = -\frac{\partial}{\partial x} \cdot (F(x) \rho(x, t)) - \frac{\partial}{\partial x} \cdot J, \quad (3.24)$$

$$\rho_0 = \rho(x, 0), \quad (3.25)$$

where ρ_0 is the initial distribution and J is the flux in terms of probability of neurons crossing the boundary Ω , dependent on the $S(x, g(t))$ term. The sum of the terms $\frac{\partial \rho(x, t)}{\partial t} + \frac{\partial}{\partial x} \cdot (F(x) \rho(x, t)) = 0$ in equation (3.24) defines the transport or drift equation, while the derivative of the flux represent a diffusion term. The KFP equations with ρ depending on the full phase space x is computationally demanding. To reduce computational effort, two different approaches have been suggested to reduce the phase space of neural system to one dimension. Consider for example a homogenous population of leaky integrate-and fire (LIF) neurons with the input to the population dispersed by noise

$$\begin{cases} C_m \frac{\partial V}{\partial t} = -g_L(V - V_L) + I + \sigma \xi(t), \\ \text{if } (V > V^{thr}) \Rightarrow V = V^{reset}. \end{cases} \quad (3.26)$$

A homogenous network implies that all neurons have the same parameters, C_m membrane conductance, the same leaky currents, identical threshold V^{thr} and reset values V^{reset} . The input current I contains both the external drive and synaptic coupling. The term σ corresponds to a noise dispersion and $\xi(t)$ is a white noise process, i.e. the average of the process $\xi(t)$ is zero for all time: $\langle \xi(t) \rangle = 0$ and the autocorrelation function has infinite power: $\langle \xi(t) \xi(t') \rangle = \tau_m \delta(t - t')$ which implies power spectral density $P(\xi(t)) = \tau_m$, where τ_m is the membrane time constant).

The first approach assumes the evolution operator ρ is fully described by the membrane voltage V . This approach is valid only if the voltage is a monotonically increasing function in time. However, if at two distinct time moments t and $t + \Delta t$ the voltage have the same value, i.e. $V(t) = V(t + \Delta t)$, then the approach fails since it is impossible to distinguish between the two voltages in phase space. Thus this solution is only typically employed to describe a population of LIF neurons [62] and thus $\rho(V, t)$ is the *membrane potential density*

of the population. A derivation of $\rho(V, t)$ into as a KFP is demonstrated in [62] which can be expressed in the following form:

$$\begin{cases} \frac{\partial \rho(V, t)}{\partial t} + [-g_L(V - V_L) + I] \frac{\partial \rho(V, t)}{\partial V} + \frac{\sigma(t)^2}{2} \frac{\partial^2 \rho(V, t)}{\partial V^2} = 0, \\ \rho(V, t)|_{V=V^{thr}} = 0, \\ \rho(v, t)|_{t=0} = \delta(V - V_L), \end{cases} \quad (3.27)$$

where the first two terms of the KFP is the transport equation and the third term due to noise defines a diffusion term. The second equation defines the boundary condition when neurons reach a threshold. The third equation relates to the initial condition. This approach has been applied in modelling for example event-related potentials (ERP) [67]. In this work, the noise term $\xi(t)$ is modeled by measuring and quantifying the averaged firing response of a population of neurons to different experimental trials of the same experimental stimulus paradigm. This allows one to encode to some degree the variability of ensemble responses. However this is valid under the assumption that the averaged firing rate of a neuron constitutes the primary variable relating neuronal responses to sensory experience.

An alternative and more robust method is to use an auxiliary variable usually denoted t^* , which for a single neuron is the time elapsed since its last spike [47]. Here, $\rho(t, t^*)$ is referred to as the refractory density [62]. This approach has the ability to distinguish in phase space two spike time moments having the same membrane voltage. In this case the KFP for the LIF ensemble (3.26) has the following form:

$$\frac{\partial \rho(V, t^*, t)}{\partial t} + \frac{\partial \rho(V, t^*, t)}{\partial t^*} + [-g_L(V - V_L) + I] \frac{\partial \rho(V, t^*, t)}{\partial V} + \frac{\sigma(t)^2}{2} \frac{\partial^2 \rho(V, t^*, t)}{\partial V^2} = 0. \quad (3.28)$$

A population model of the form (3.28) has been extensively studied by Chizhov [32] where the third and fourth terms of equation (3.28) was substituted into the right hand side and a good approximation give the hazard function $\rho(t, t^*)H$. The final form of the equation is then by the following:

$$\begin{cases} \frac{\partial \rho(t, t^*)}{\partial t} + \frac{\partial \rho(t, t^*)}{\partial t^*} = \rho(t, t^*)H(V) \\ C\left(\frac{\partial V}{\partial t} + \frac{\partial V}{\partial t^*}\right) = -g_L(V - V_L) + I \end{cases} \quad (3.29)$$

where the first KFP equation is reduced to a drift equation with source term being the hazard (firing rate) function, $\rho(t, t^*)H$, which is dependent on the noise amplitude σ and the firing threshold V^{thr} . The second equation defines the drift equation of voltage V dynamics V for all t^* . This approach has been further refined in [32] to take into account averages of fast and

slow ionic currents over the cell populations and the variability in intrinsic cell properties and in synaptic input. The model has been shown to simulate to a good precision extra-cellular stimulated postsynaptic responses and gamma-oscillation of a hippocampal CA1 tissue [31].

3.3.4 Mass Action models

Mass action models were first proposed by Freeman [57] as an alternative approach to modelling population dynamics. The crucial difference being they were based on results obtained from electrophysiological experiments, measuring local field responses of neural masses to known stimuli or induced by electrical pulses. These experiments aimed to relate single cell recordings at the microscale and demonstrate that the macroscopic dynamic properties of a neural mass are related to, but distinct from those of an individual neuron (i.e. neural masses cannot be understood at the level of action potentials). In these experiments neural masses are electrically stimulated by extracellular electrodes which activate large numbers of axons (termed nerve tracts) that synapse into an ensemble of neurons and cause their activation. The ensemble output response field potential, after, suitable averaging to remove the background activity is treated as an impulse response of the system. In a series of recordings carried out on the olfactory system of both trained rabbits (i.e. to recognise smells and to respond with particular behaviours to particular smells) and untrained ones, Freeman developed a set of dynamical phenomenological models called the Ki set hierarchy, where $i = \{0, I, II, III\}$. These sets are both a model of population dynamics and a description of the connectivity architectures to describe interactions made by neural masses. The K0 set is the most basic and simplest component in the hierarchy consisting of three parts, biologically resembling a real neuron. Specifically, K0 sets model a neuronal ensemble forming part of a cortical column within which all neurons share the same physiological and functional properties. They receive spatial inputs (dendrites) that are weighted and summed. Further they include a soma where pulse spike densities are produced and the internal dynamics (the transmembrane potential of a neuron) follow a linear time invariant system with second order dynamics. The output is then shaped by a nonlinear saturating function, that essentially provides a measure of the relationship between the transmembrane potential and the pulse density of the neuronal mass.

The response of the model to an impulse $P(t)$ function is described as follows:

$$\begin{cases} \frac{d^2}{dt^2}V(r, t) + (\alpha + \beta)\frac{d}{dt}V(r, t) + \alpha\beta V(r, t) = P(r, t), \\ \phi(r, t) = \varsigma(V(r, t)), \end{cases} \quad (3.30)$$

where r varies continuously over some domain and represents the spatial location of the process. $V(r, t)$ is the transmembrane potential at the ‘neural mass soma’. $\varsigma(r, t)$ is a sigmodal function relating the $V(r, t)$ to the firing rate $\phi(r, t)$ (pulse density) of the ensemble of neurons and α and β correspond to the rise and decay of the response signal. Observing the dynamics of the first equation it could be argued that they correspond to post synaptic dendritic responses of a single neuron, only here representing aggregated synaptic events. However, note that the precise relationship between the electrical potentials of single dendrites and the resulting summed dendritic potential of an ensemble of neurons is not known. Nevertheless, in the literature (e.g. [130]) it is assumed to be related to synaptic dendritic responses where these are written alternatively and interpreted in the following way:

$$V(r, t) = l \int_{-\infty}^{\infty} L(t - t')P(r, t')dt'. \quad (3.31)$$

In this version all observables represent local averaged values of some physiological process and now this equation relates the averaged induced transmembrane voltage $V(r, t)$ at the soma with the incoming averaged post-synaptic potentials $P(r, t')$ after these have been filtered in the dendritic tree and summed. The induced transmembrane voltage perturbation propagates along the dendrites and reaches the cell body with some attenuation and lag. Both depend on the distance of the synapse from the cell body, with the factor l used to represent the average attenuation and convolution of $P(r, t)$ with a unit-area function $L(t)$ representing lag. α and β are now constants representing the inverse rise and decay times parameterising the dendritic response to an impulse. In effect, diffusion during dendritic propagation smears out the temporal response and the dendritic tree acts as a low-pass filter. The kernel of the convolution usually assumes the following form:

$$L(t) = \begin{cases} \frac{\alpha\beta}{\beta-\alpha} (\exp(-\alpha t) - \exp(-\beta t)) & \alpha \neq \beta \\ \alpha^2 t \exp(-\alpha t) & \alpha = \beta \end{cases}$$

The final chapter of this thesis will suggest yet another possible interpretation of these equations, which is shown to be important if mappings between scales are to be considered.

On the next level of the hierarchy, a KI set is formed by two K0 sets and defines the coupling relationship between them. However, this structure allows populations to be only either

exclusively excitatory or inhibitory and no auto-feedback is allowed. Subsequently, a KII set consists of two KI sets (or four K0 sets). KII networks can function as an encoder of signals or as an auto-associative memory, [57, 128]. Mathematically, KII sets may have several fixed points and can also have limit cycle attractors depending on the parameters of the system and the initial conditions. At the final level of the hierarchy is the KIII set. These KIII networks may have different layers of KII sets representing for example different anatomical regions of the mammalian brain. As an example, a computational KIII network designed to model the olfactory system has been studied by Heng-Jen et al. [30]. The KIII network may have strange attractors and positive Lyapunov exponents, consequently exhibiting chaotic oscillations [128, 68]. A complete understanding of the total hierarchy would represent the knowledge to mimic and predict EEG signals and thus comprehend brain functioning at the macroscopic level [94]. In general, a N th order system is defined as follows

$$\begin{aligned} \frac{d^2}{dt^2}V_i(r, t) + (\alpha + \beta)\frac{d}{dt}V_i(r, t) + \alpha\beta V_i(r, t) &= \sum_{j \neq i}^N \left(\nu_{ij}\varsigma(V_j(r, t)) + \nu'_{ij}f_j[\varsigma(V_j(r, t))] \right) \\ &+ \phi_{external} \end{aligned}$$

where f_j can represent the extracellular field potential spread affecting nearby neuron ensembles and $\phi_{external}$ an external stimuli or impulse. Reductions to Ki sets are also possible by considering subsets of connections. In particular, this thesis is concerned with a subset of the KII models denoted reduced KII (RKII). In this simplification each column within the RKII set consists of a coupled inhibitory and excitatory neural population. Thus a set of N coupled columns (or local brain region) may be represented by the following form:

$$\begin{cases} \frac{d^2}{dt^2}V_e(r, t) + (\alpha + \beta)\frac{d}{dt}V_e(r, t) + \alpha\beta V_e(r, t) = \alpha\beta \left(\nu_{ei}\varsigma[V_e(r, t)] + \frac{1}{N} \sum_{p=1}^N \nu_{ep}\varsigma(V_p(r, t)) \right) \\ \frac{d^2}{dt^2}V_i(r, t) + (\alpha + \beta)\frac{d}{dt}V_i(r, t) + \alpha\beta V_i(r, t) = \alpha\beta \nu_{ie}\varsigma[V_e(r, t)], \end{cases} \quad (3.32)$$

where V_e represent the average field potentials of an excitatory population and V_i of an inhibitory population observed at a macroscopic level. The parameter ν_{ie} gives the coupling gain or strength from the excitatory (V_e) to the inhibitory (V_i) population whereas ν_{ei} is the strength of the reciprocal coupling. The coupling strength ν_{np} is the gain from an external excitatory population from columns p (since long range connections are only established by excitatory neurons). These parameters can be interpreted as having the following form $\nu_{ab} = N_{ab}S_b$ where, N_{ab} is anatomical or structural in character representing the mean number of connections from neural ensemble of type b on a population of type a . The term S_b

is physiological or functional in nature representing the size of the impulse response associated with synapses of type b , i.e the time integral of the perturbation to the transmembrane potential, as measured at the synapse. The nonlinear interaction is in general realised by some sigmoidal function $\varsigma[\cdot]$. External inputs or stimuli can be applied to either excitatory or inhibitory population.

The theoretical framework most often applied to neural mass approach is signal processing techniques and this context only some understanding is possible. When compared to neural field and population density approach, neural mass models are the least studied in the context of dynamical systems theory. Thus the understanding of their dynamics is still scarce. Perhaps this could be related to the fact that it is not clear how to interpret the equations, specifically, those second order in voltage dynamics and the parameters modulating the dynamics of the K0 set. It is reasonable to think that relating multi-scale recording and multi-scale modelling of the observed signals is the key to modelling brain dynamics at different spatiotemporal scales. Hence, with this in mind, the mass action approach deserves further research to understand how macroscopic dynamics and Ki sets could be mapped to lower scales of activity, which could then lead to interesting results.

Chapter 4

Analysis of the neural mass corticothalamic model

The aim of this chapter is to explain the critical features of human generalized seizures by investigating the dynamical bifurcations of a global (spatially invariant) corticothalamic brain mean-field model. The model belongs to the class of *mass action* models. However, it also incorporates further refinements to take into account key physiological processes such as propagation delays, corticothalamic feedback, and as well as treating the cortex as a medium for propagation of waves of electrical activity. Previous analyses have demonstrated descriptive validity in a wide range of healthy states, such as the alpha and gamma rhythms. Further it is here shown that mapping the structure of the nonlinear bifurcation set predicts a number of crucial dynamic processes, including the onset of periodic dynamics which explains the transitions observed in generalized seizures. A quantitative study of electrophysiological data supports the validity of these predictions. Hence we argue that absence seizures are predicted by the bifurcation diagram of the model's dynamics. Finally a reduction of the model is considered, which allows for analytical treatment and interpretation of these pathological rhythms.

4.1 Corticothalamic Brain Model

The model described and analysed herein stems from [131]. This system can be viewed as a merge of three theoretical viewpoints: Freeman's mass action to describe the population dynamics within a macrocolumn [57]; The thalamocortical feedback loop as a physiologically motivated feature to allow interpretation of generalized seizures at the macroscopic level (refer to section (3.2)); and the wave-like equation formalism to model the EEG wave propagation phenomena on the cortical surface [84]. Given that the model is formulated within these three theoretical standpoints it inherits the assumptions made by each and because it merges these it is denoted as the neural mass corticothalamic model. However, in this thesis it is simply called the corticothalamic model. The model also incorporates a further refinement to account for signal propagation delays in the thalamocortical and corticothalamic projections.

The thalamocortical loop hypothesizes that four main types of neurons are involved in generalized seizures and these consist of excitatory and inhibitory neurons in both the cortex and the thalamus. The hyper-synchronized state of local neurons observed in generalized seizures makes it reasonable to group and average over the ensemble of neurons. Thus, each brain region can be modelled by an RKII set (introduced in section (3.3.4)) which describes the interaction of a population of excitatory and inhibitory neurons. Hence, coupling two RKII sets forms the corticothalamic feed back loop. The dynamical variables within each population are the local mean potential, V_a , the mean firing rate, ς_a and the propagating axonal fields, ϕ_a . Consequently, each neural mass is governed the following three equations

$$\left[\frac{1}{\alpha\beta} \frac{\partial^2}{\partial t^2} + \left(\frac{1}{\alpha} + \frac{1}{\beta} \right) \frac{\partial}{\partial t} + 1 \right] V_a(r, t) = P_a(r, t), \quad (4.1)$$

$$\varsigma_a(r, t) = \frac{Q_a^{max}}{1 + \exp \left(-\frac{\pi}{\sqrt{3}} \left(\frac{V_a(r, t) - \theta_a}{\sigma_a} \right) \right)}, \quad (4.2)$$

$$\frac{1}{\gamma_a^2} \left[\frac{\partial^2}{\partial t^2} + 2\gamma_a \frac{\partial}{\partial t} + \gamma_a^2 - \nu_a^2 \nabla^2 \right] \phi(r, t) = \varsigma_a(r, t), \quad (4.3)$$

where a refers here and in subsequent equations in this chapter to the neural population (e =excitatory pyramidal cells, i =inhibitory inter-neurons, s =specific relay nuclei, r =reticular nucleus, and n =nonspecific sub-cortical inputs). The first equation (4.1) corresponds to voltage response $V_a(r, t)$ of a $K0$ set to incoming averaged post-synaptic potentials $P_a(r, t)$ after these have been filtered in the dendritic tree and summed. The second state equation (4.2) refers

to the generation of action potentials, $\varsigma_a(r, t)$, (mean firing rate or pulse density) whenever the membrane potential $V_a(r, t)$ reaches a threshold θ_a . In other words $V_a(r, t)$ determines the output firing rate of the neuronal population and the level of activity is modulated by a response probability sigmoidal function $\varsigma[V_a(r, t)]$. The response is a smooth transition from 0 to Q_a^{max} , with a standard deviation, σ_a , that reflects the variation of threshold levels encountered in real populations. Note that the maximum of $\frac{dQ_a}{dV_a}$ is $\frac{CQ_a^{max}}{4\sigma_a}$ at $V_a = \theta_a$ and the constant $C = \frac{1}{\sqrt{3}}$ was chosen so that the $\frac{dQ_a}{dV_a}$ approximates a Gaussian. The last equation (4.3) uses the wave-like equation developed by Jirsa and Haken [84] to model the propagation of the firing rates ς_a as fields ϕ_a (for details refer to section 3.3.2). However, Robinson et al. [131] find that the term $(\gamma_a^2 - \gamma_a \frac{\partial}{\partial t})$ on the right hand side of the wave-like equation can be dropped as this does not influence the numerical simulations. A characteristic axonal propagation velocity, $v_a = 6 - 10 \text{ ms}^{-1}$, is assumed as well as an isotropic distribution of axons.

Coupling of the cortex and thalamus by directly incorporating the above equations gives rise to a high dimensional system of equations, thus reductions should be considered. Reducing a system of equations should be carefully considered and any reduction must lie within the limits of physiological constraints. There are significant differences in the mechanisms underlying the spread of activity in cortical and thalamic slices. Computational models and experimental animal models of spindle waves and epilepsy, indicate that thalamic slices waves propagate at velocities of less than 1 cm/s whereas cortical neurons discharges propagate with a velocity range $6 - 10 \text{ ms}^{-1}$ [43]. The differences in velocities are due to axonal range within each brain area. Within the thalamus the axons of both excitatory and inhibitory neurons project closely to nearby neurons. This observation allows a reduction of the wave-like equation to $\phi_a = \varsigma_a(r, t)$, because $\gamma_a \rightarrow \infty$. Within a column of the cortex the same holds true. However, only pyramidal cells project their axons to other cortical regions (long range connections) where these fields are readily measured in EEG. Thus, the wave equation is considered for the pyramidal cells. An observation worth pointing out is the fact that the wave equation indirectly introduces delays to these connections. For the connectivity between the cortex and the thalamus these are considered to be long range connections as the cortex and the thalamus are far apart. Since corticothalamic and thalamocortical projection activity are not measured at the EEG (i.e. as these are closed fields) the wave equation is dropped. However, the activation of one brain region due to another brain region depends on the rise times of post-synaptic potentials and delays due to finite velocity of action potential propagation,

thus delays are considered. A final assumption is that incoming fields from different neural population are linearly summed at dendrites of a neural mass. This allows to define the coupling between the different neural populations as follows:

$$D_\alpha V_e(r, t) = \nu_{ee}\phi_e(r, t) + \nu_{ei}\phi_i(r, t) + \nu_{es}\phi_s(r, t - \tau), \quad (4.4)$$

$$D_\alpha V_i(r, t) = \nu_{ie}\phi_e(r, t) + \nu_{ii}\phi_i(r, t) + \nu_{is}\phi_s(r, t - \tau), \quad (4.5)$$

$$D_\alpha V_r(r, t) = \nu_{re}\phi_e(r, t - \tau) + \nu_{rs}\phi_s(r, t), \quad (4.6)$$

$$D_\alpha V_s(r, t) = \nu_{se}\phi_e(r, t - \tau) + \nu_{sr}\phi_r(r, t) + \nu_{sn}\phi_n(r, t), \quad (4.7)$$

where $D_\alpha = \left[\frac{1}{\alpha\beta} \frac{\partial^2}{\partial t^2} + \left(\frac{1}{\alpha} + \frac{1}{\beta} \right) \frac{\partial}{\partial t} + 1 \right]$, $\tau = t_0/2$, with t_0 considered to be the total propagation time for signals to project to the cortex and return back to the thalamus. Only the specific relay nuclei (TC neurons) receive sensory inputs ϕ_n which may be either a time invariant signal or noise. The model is further reduced by dropping equation (4.5), because the existence of spatial symmetry between populations of pyramidal cells and inhibitory inter-neurons is assumed as in [131]. The argument presented is that intracortical connectivities are proportional to the numbers of synapses involved, which implies $V_i = V_e$ and $Q_i = Q_e$. However, we assume that the author meant that EEG is mostly contributed by pyramidal cells and thus fields produced by inter-neurons are negligible. Finally, during generalized seizures, brain activity may be dominated by very large scale, or even whole brain processes. In this case the dynamical variables may not depend greatly on the spatial position r . Hence we drop the spatial variable r and consequently the Laplacian term $\nu_a^2 \nabla^2$, along with the boundary conditions dependent on r , are ignored. In this case only global invariant solutions can be considered. However, note this is only an approximation and spatially varying behaviour can be recovered by coupling N discrete nodes ($i = 1, \dots, N$), each governed by a corticothalamic model. The coupling would consist of cortico-cortical excitatory projections defined as follows

$$D\phi_e^i(t) = Q_e^i(t) + C_{ij}(\phi^i, \phi^j)/r_e^2,$$

where r_e is the characteristic axonal range, D is the wave-like equation (without the Laplacian) and the connectivity matrix C_{ij} is a suitable numeric approximation of the Laplacian operator ∇^2 (e.g. first order approximation to ∇^2 [2]).

A complete derivation of the spatially invariant system is shown in section B.1 and a schematic of the model is illustrated in Fig. (4.1 a) and the firing rate shown in Fig. (4.1 b). The parameters of the model were fitted from data using an algorithm developed in [132, 138]. The relevant parameters can be found in section B.1.1 in Table B.1.

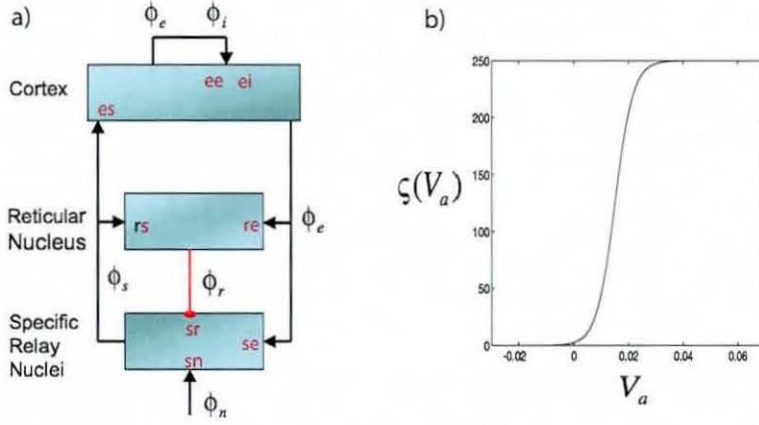


Figure 4.1: a) *Thalamocortical model, schema of principal neural fields and loops within the corticothalamic model. Fields include e=excitatory cortical; i=inhibitory cortical; s=specific thalamic nucleus; r=thalamic reticular nucleus; n=nonspecific subcortical noise. Connectivity and loops include intracortical (ee,ei), corticothalamic (er,se,es),intrathalamic (sr,rs) and ascending noise sn. b) The neurons (inhibitory and excitatory) are coupled by a unipolar sigmoidal function, which transforms the neurons transmembrane potential V_a (generally expressed as wave amplitude) into the firing rate $\zeta(V_a)$ (termed pulse density), i.e voltage-frequency relation. Note the scale of the x-axes and y-axes $(-0.03,0)$ to $(0.07, 250)$. This is related to the averaging performed over a mm^3 of neural tissue, which is a highly nonlinear operation.*

For purpose of discussion and completeness, results from [131] are provided in section B.2. These are linear stability analysis in the frequency domain, describing healthy EEG instability boundaries parameterised by x , y and z variables, which measure the level of activity in the cortex, reticular-specific and specific-reticular connections respectively.

Clinical research suggests that several pathological processes, such as seizures [5] and abnormal rhythms in pathological states [148] have a strong nonlinear component. In [131] it was proposed that the transition from resting-state EEG to seizure activity may be viewed as a bifurcation from linear to nonlinear oscillations, whereas different types of seizures may be

viewed as bifurcations between distinct types of nonlinear dynamics [133]. In particular, this chapter focuses on 3Hz instability associated with the frequency at which absence seizures initiate. The behaviour of the model at and beyond such instabilities is compared with EEG data sets. Beyond the 3Hz instability an extra structure in the bifurcation diagram is found whose origin remains unresolved. In an attempt to understand this phenomena a piecewise approximation of an RKII set is considered to explain the genesis of absence seizures.

4.2 Method for the analysis of the EEG data

The absence seizure data sets were drawn from a database of 13 adolescent epileptic patients from the Department of Neurology, Westmead Hospital, Sydney where the ethics approval was obtained prior to data collection. The scalp EEG electrode placement followed the international 10-20 system (refer to section A.3 for details) with linked earlobe reference and the data were collected at a rate 200Hz and filtered with 70Hz low-pass filter. The Analysis of the data was also performed as a collaboration work with M. Breakspear.

4.2.1 Methodology for Nonlinear data analysis

In order to test whether seizure activity is associated with nonlinearity (implicit in the hypothesis that a seizure occurs after a nonlinear bifurcation) a nonlinear prediction algorithm from [29] was employed. Briefly, the data is divided into discrete time windows. In each window a “nonlinear prediction error” is calculated. This error reflects the ability of a local nonlinear model to predict the data. Low errors indicate a good fit and hence a nonlinear structure. Using a resampling scheme (applied to the original data), an ensemble prediction error is then calculated to represent the null hypothesis that the values of the errors are due to purely linear correlation within the data [162]. The data are said to contain nonlinear structure if the observed (experimentally derived) prediction error lies outside the distribution of these “surrogate” errors [161]. Nineteen surrogates were constructed to allow for nonparametric statistical inference at 95% confidence within each window. For graphical clarity, the inverse of the prediction errors, which we term the “nonlinear prediction indices” is plotted. A

modification to this algorithm allows multichannel EEG data to be tested for evidence of nonlinearities [161]. A multivariate surrogate algorithm in [127] is then employed to exclude the contributions of purely linear correlations. This can be used in conjunction with the general version of the thalamocortical model to estimate the predicted nonlinear interdependencies.

4.2.2 Methodology for Numerical Data

The numerical data is constructed by performing the numerical integration of the systems equations (B.2) according to the scheme described in section 2.3. To analyse the asymptotic systems behaviour, bifurcation diagrams across a varying range of the parameter ν_{se} (the excitatory influence of cortical pyramidal cells in the specific thalamic nuclei) are produced. This parameter is chosen because of its simple physical meaning and the role of excitatory corticothalamic feedback in the pathophysiology of absence seizures [43] (for details refer also to section 3.2). The resulting time series of the bifurcation data is plotted for each parameter value. For the time series comparison of the model and EEG data, the macroscopic excitatory field ϕ_e is plotted as these best represent the cortical correlate of scalp potentials up to a linear transformation of the amplitudes [114]. Specifically, the scalp potential is proportional to the cortical potential, which is proportional to the mean cellular membrane current, which in turn proportional to the firing rate. Hence, apart from a (dimensional) constant of proportionality and the effects of volume conduction, scalp EEG signals correspond closely to ϕ_e [114]. To better simulate a real physiological system, small amplitude (signal noise ratio=0.90) autocorrelated stochastic terms were added to the parameters (system noise) to produce numerical time series plot. Such noise was generated according to

$$s(t_n) = \rho s(t_{n-1}) + \sqrt{1 - \rho^2} r(t_n),$$

where $r(t)$ is drawn from a set of zero mean independent random numbers, $s(t_0) = r(t_0)$, and the desired autocorrelation factor t_c between adjacent time series steps is related to the fixed parameter ρ by

$$t_c = \frac{-\Delta t}{\ln(\rho)}.$$

Such a model of parameter noise represents the simplest method for the simulation of an autocorrelated stochastic process. It should be noted that such noise is only used in the time series plots and has no impact on the calculation of the bifurcation diagram.

4.3 Understanding of absence seizures

4.3.1 Results from the corticothalamic model

The nonlinear instability occurring at approximately 3Hz is studied by first choosing physiologically plausible parameters that place the system in the vicinity of a weak 3Hz instability as given in Table B.1 in section B.1.1. As stated above, ν_{se} is then varied to study the geometry of the bifurcation set.

Some results are presented in Fig. (4.2). The bifurcation diagram Fig (4.2 a) exhibits a Hopf bifurcation to periodic dynamics with an initial (supercritical) instability at $\nu_{se} \approx 1.8 \times 10^{-3}Vs$ and beyond the instability an extra structure appears at $\nu_{se} \approx 3.4 \times 10^{-3}Vs$ and $\nu_{se} \approx 4.2 \times 10^{-3}Vs$ whose origin remains unclear, but for the sake of this discussion the term ‘spike-bifurcation’ is adopted. These are noise-free plots and it can be seen that only periodic oscillations occur. Complementary numerical results are provided in section B.3 with the analysis performed using DDE-Biftool and XPPAuto. However, the origin of the ‘spike-bifurcation’ remains unresolved as DDE-Biftool is unable to flag the corresponding conditions for this bifurcation. These could correspond to a global bifurcation which is a feature that goes undetected in DDE-biftool and so a more detailed numerical treatment should be considered in the near future. An interesting feature of the ‘spike-bifurcation’ is that by varying the time delay (τ) parameter this structure is observed to appear at different parameters of ν_{se} and disappear if the delay τ is removed. This is illustrated in Fig. (B.4) in section B.3 (a discussion of this instability is also presented). An exemplar model simulation, with added system and measurement noise, is given in Fig. (4.2 b). This was created by dynamically ramping ν_{se} from the linearly stable (weakly damped region) upward into the region of linear instability illustrated in Fig. (4.2 d). The dashed lines in Fig. (4.2 a) show the extreme values of the ramp function. Close up images of the onset Fig. (4.2 c) and offset Fig. (4.2 e) of the seizure exhibit a number of key phenomena: 1) Shortly after the onset of ramp-up of ν_{se} at $t = 5s$ periodic oscillations of growing amplitude appears in the field potential. These occur as the system passes through the periodic regime in the bifurcation plot. 2) After 2-3 cycles, spike and slow-wave oscillations appear. These continue throughout the seizure, although their amplitudes are modulated by the combined effects of system and measurement noise. 3)

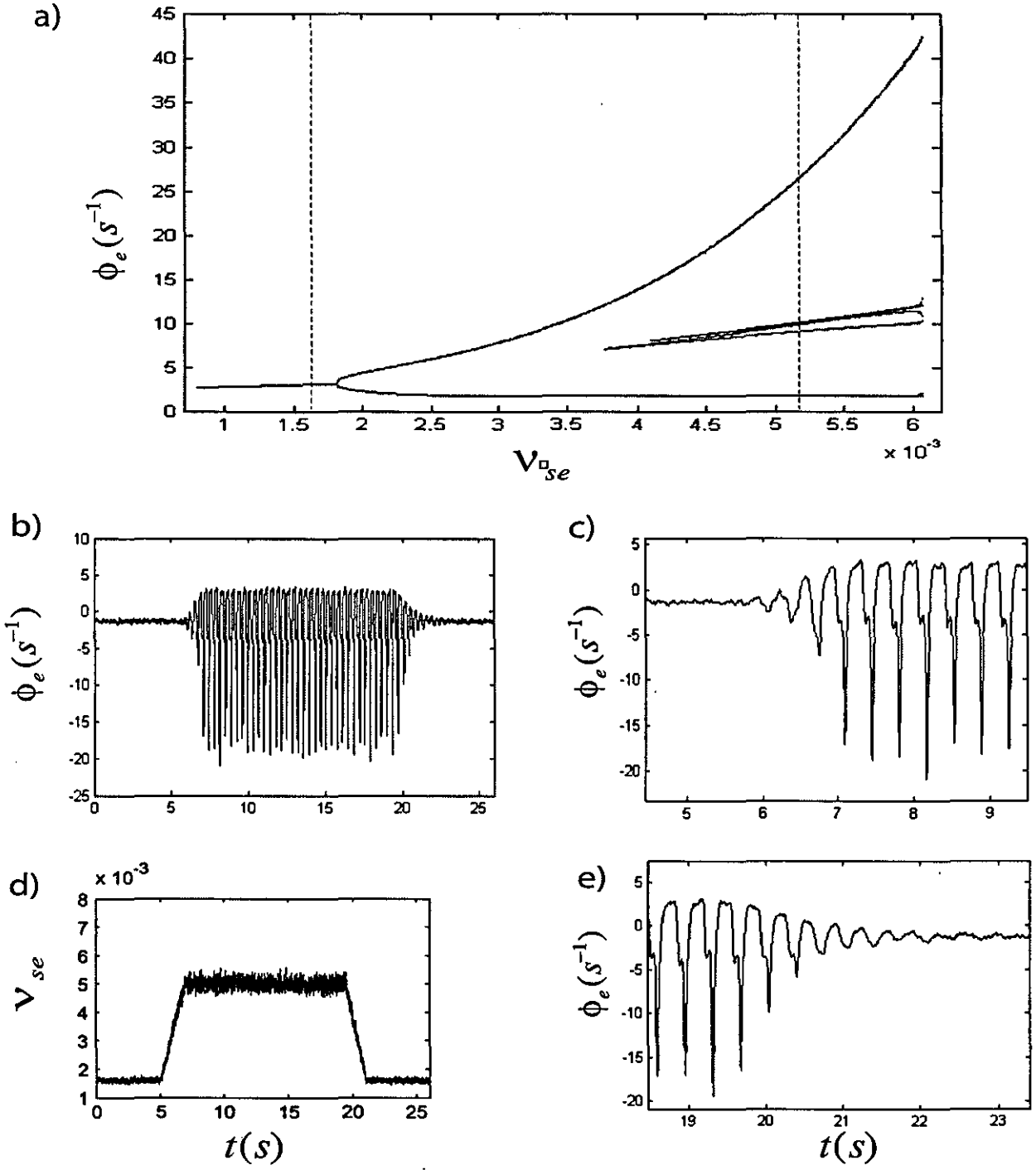


Figure 4.2: Results for 3Hz bifurcation analysis in the corticothalamic model. a) Bifurcation diagram. Time series of: b) the cortical ϕ_e . Period-doubling oscillations evident at the seizure onset c) and offset e). d) These time series are performed by ramping the (noise perturbed) corticothalamic “gain” parameter ν_{se} .

During the ramping down of ν_{se} at $t = 19.5s$ the amplitude of the spike and wave oscillations diminish. The spikes disappear at approximately $t = 20.5s$ as the system passes through the simple period 1 regime. 4) Finally, the remaining oscillations are damped away, and the system returns directly to the same pre-ictal EEG state, governed by stable damped stochastic fluctuations. This is reflected in the spectrum of the seizure given in Fig. (4.3 a), showing similar pre-and post-ictal spectra. The seizure spectrum is dominated by the 3Hz spike and wave oscillation and its harmonics.

A 3-dimensional time-delay-embedded phase portrait of a simulated (noise-free) seizure is shown in Fig. (4.3 b). Gray arrows indicate the flow of orbits away from the unstable fixed point subsequent to the bifurcation and onto the limit-cycle attractor. The growth in amplitude of the spike (at the far side of the attractor) can be seen as the orbits spiral outward. The orbits follow the same unstable manifold (but spiraling downward) at the conclusion of the seizure (not shown). Fig. (4.3 d) depicts the morphology of the seizure in the space spanned corticocortical, corticothalamic, and intrathalamic “stability” variables x , y , and z (as given in section B.2). As expected, the seizure is located outside the tent-shaped stability zone. Because the seizure corresponds to limit-cycle dynamics, it can be embedded in this 3 dimensional space without crossing the orbits (i.e., with uniqueness of the solution curves). This indicates that, during such seizures, a dynamical system of reduced dimensionality should be able to sufficiently describe the macroscopic neural dynamics, or equivalently, a relatively small number of physiological processes may be responsible for the onset and maintenance of the seizure activity.

Fig. (4.3 c) shows the 3 principal fields ϕ_a ($a=\{e,r,s\}$) during the model seizure, normalized by their own means, to illustrate the underlying mechanism from which the waveform is generated. For convenience the peak of ϕ_s is chosen for the starting point, which corresponds to $t \sim 10.0s$. It must be stressed that this is an arbitrary choice because the periodic nature of the dynamics imply that the waveforms have no particular beginning or end but are an emergent feature of the entire corticothalamic system. When ϕ_s (dashed line) is at its highest value, ϕ_e (solid) is at an intermediate value and ϕ_r (dotted) is low. The thalamus is in its positive-feedback, excitatory state. The reticular nucleus responds immediately to the high activity in the specific nuclei and in addition to the incoming signal leaving the cortex at $t_0/2$ earlier. This sudden increase in ϕ_r acts to suppress ϕ_s rapidly, and the thalamus switches to

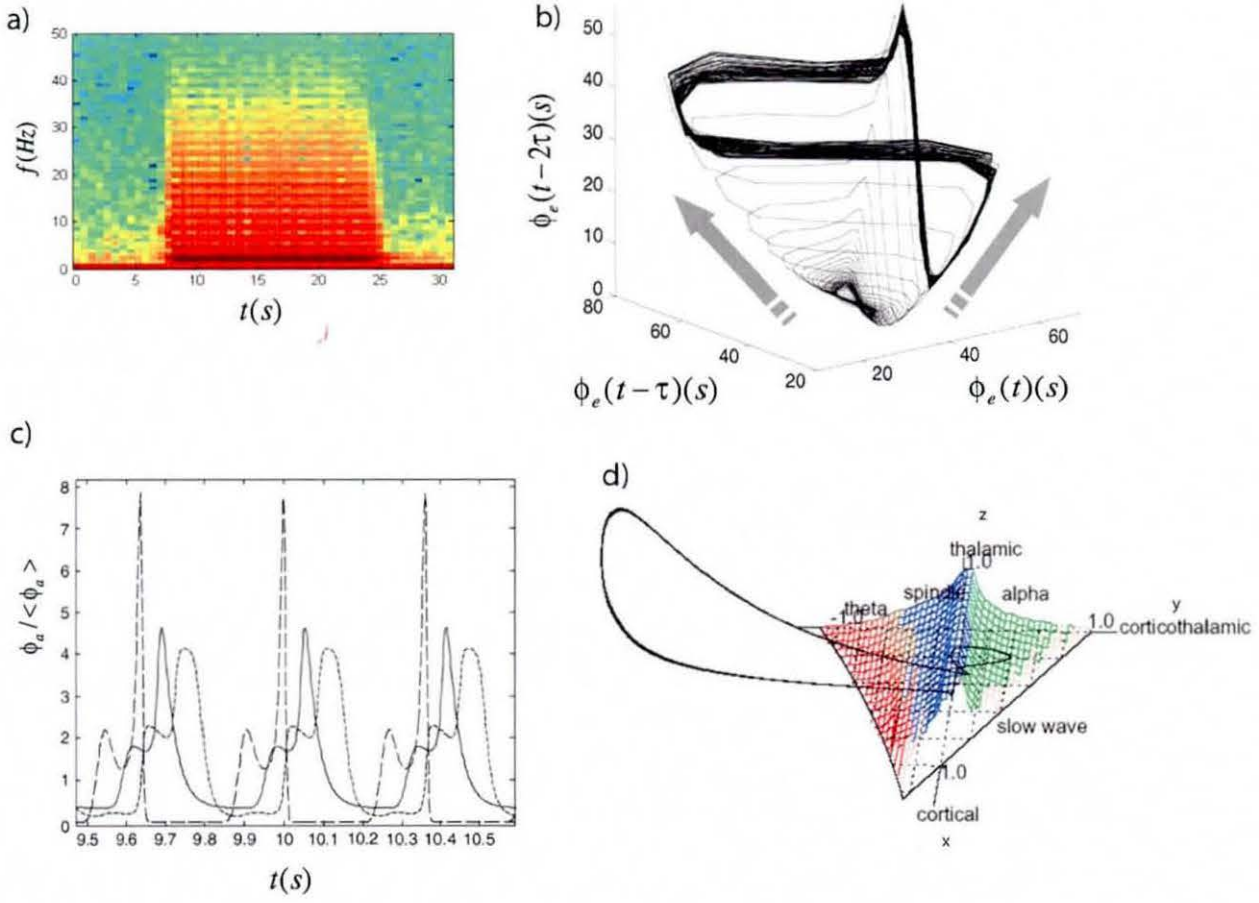


Figure 4.3: a) Contour representation of the dynamic spectrogram of ϕ_e . b) Time-delayed phase portrait of the seizure onset transient and seizure attractor. Arrows indicate the direction of the flow. c) Dynamics of the excitatory cortical ϕ_e (solid), specific thalamic ϕ_s (dotted), and reticular thalamic ϕ_r (dashed) activities rescaled against their mean values. c) Seizure plotted within the phase space spanned by the stability parameters x , y and z .

its negative feedback, inhibitory state ($t \sim 10.05s$). At time $t_0/2$ later, the peak in activity in the specific nuclei reaches the cortex and ϕ_e rises accordingly, with the peak slightly broadened by synaptic rise and decay time. Another $t_0/2s$ later, the spike activity in the cortex reaches the thalamus, exciting the reticular nucleus and hence further suppressing the specific nuclei ($t \sim 10.05s$). This represents negative corticothalamic feedback, and the response of ϕ_r results further broadening of the signal. With near-silence in the specific nuclei, the cortical neurons relax. At $t_0/2s$, there are no inputs to the reticular nucleus and hence it too relaxes, leading to a period of near-silence in all 3 fields ($t \sim 10.05s$). In the meantime, the specific nuclei have been receiving the external input stimulus ϕ_n , which is sufficient to cause the specific nuclei to reactivate once the reticular nucleus has been suppressed, and so ϕ_s rises. This

corresponds to the thalamus switching back to its positive feedback state. Immediately, ϕ_r responds slightly, enough to subdue the growth of ϕ_s but not before the increased activity is substantial enough to excite ϕ_e a time $t_0/2s$ later than the original intermediate value. Meanwhile, the specific nuclei have been receiving external stimuli continuously, and so while ϕ_r is still low, they are able to fire, completing a full cycle ($t \sim 10.05s$). The delicate balance of this process highlights the sensitivity of the shape of the waveform to changes in the various parameters. Indeed, a variety of spike and wave and polyspike morphologies are possible under modest changes in parameters. This may explain the varied morphologies observed in clinical absence seizure EEG recordings. It is also consistent with a previous study of absence seizures employing autoregressive nonlinear signal analysis methods, which showed that similar combinations of time-delayed nonlinear (quadratic) terms could explain a variety of spike-wave morphologies [141].

4.3.2 Results from the data

The first step of the experimental EEG data analysis was to test if seizures correspond to bifurcations from linearly stable to nonlinear oscillations. As discussed above, this is achieved by using a measure of nonlinear predictability and comparing EEG with phase-randomized surrogated data. An exemplar absence seizure (F_z electrode) is shown Fig. (4.4 a). In Fig. (4.4 c), the normalized nonlinear predictability index is given as the solid line. Plots obtained from occurrence of the seizure 19 surrogate sets are dashed lines. It can be seen that the occurrence of the seizure is coincident with a sudden and large increase in this index of nonlinear structure, consistent with the appearance of nonlinear oscillation. Also noteworthy is that the pre- and postictal EEG are associated with intermittent and weak nonlinearity, evident as an occasional increase in the nonlinear predictability of the real compared with surrogate data (arrows). This is consistent with noisy perturbations of a weakly damped nonlinear system. In other words, pre- and postictal states represent a system close to a bifurcation. Comparable results were observed for absence seizures studied. Fig. (4.4 b,d) illustrates an example of a numerically simulated absence seizure, integrated over a time frame comparable to the real seizure. Because the seizure was generated by pushing the system through a nonlinear ‘spike-bifurcation’, it is not surprising that a coincident increase in nonlinear structure is seen. Prior to and following the seizure, the system has been set just below the Hopf bifurcation (see

Fig. (4.2 a)). Hence, occasional slight increases in nonlinear structure in the model over the surrogate data time series (arrows) during these times are to be expected, when fluctuations toward the bifurcation occur.

The nature of the nonlinear oscillations in the absence seizure is studied in Fig. (4.5 a-f). Fig. (4.5 a) shows a complete seizure, revealing an approximately symmetrical appearance. The spectrum of this seizure (Fig. (4.5 c) is dominated by the 3Hz spike and wave morphology. Notably, the postictal spectrum returns rapidly to its relatively featureless preictal form. In diagrams Fig. (4.5 b) and Fig. (4.5 e), the onset and offset of simple periodic, then spike and wave oscillations are clearly visible. A time-delay-embedded reconstruction of this seizure is given in Fig. (4.5 e). The seizure onset ($t=3-5.8s$) is given in blue and the remainder of the seizure ($t=5.8-19.5s$) in black. This plot directly illustrates the outward periodic spiral (blue) of the system onto a large-amplitude oscillatory “attractor”, comparable with Fig. (4.3 b).

It finally remains to determine the nature of the oscillations during the clinical seizure. Calculating dynamic “invariants” such as Lyapunov exponents are avoided as these are notoriously unreliable in short, noisy time series data [40]. Rather, the Poincaré first-return map is used, which is an assumption-free method of visualizing the nature of oscillatory dynamics [164]. Briefly, level crossings of a dynamical variable are noted. Denoting the temporal period between successive crossings as T_n ; the graph of T_n against T_{n-1} gives a truncated representation of the full dynamics. A plot of the Poincaré first-return map is given in panel Fig. (4.5 f). For ease of interpretation, we plot $f_n = 1/T_n$ (the pointwise frequency of the system). The first feature to be noted is that the points fall close to the line $f_n = f_{n-1}$. That is, the system is nearly periodic (the level crossings was chosen below the spike so that in effect we produce a second-return plot (i.e. a true full period of the oscillation). As indicated, the frequency starts above 3Hz and quickly falls to approximately 2.6Hz. It then varies around 2.6Hz in a manner without any obvious geometrical structure, that is, not confined to any obvious low-dimensional invariant. We interpret this as noisy modulation of a fixed point (i.e a noisy limit cycle of the full dynamics). This is consistent with the findings of a purely empirical study using a different methodology [54].

In summary, the evolution of this seizure quantitatively matches that of the numerical seizure generated by the corticothalamic model in a number of crucial aspects, namely, the “spike

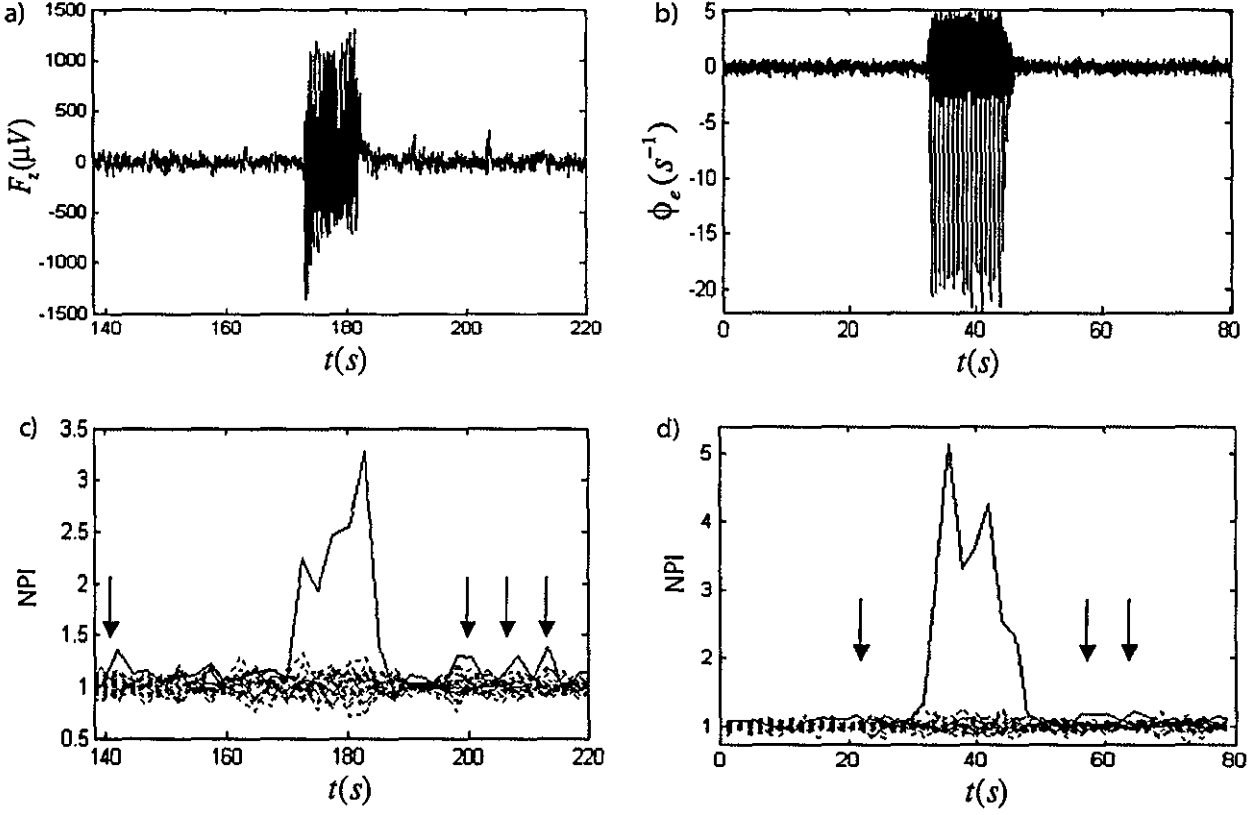


Figure 4.4: *Nonlinear time series analysis of the EEG absence seizure (left) and corticothalamic 3-Hz seizure (right). a) EEG seizure (F_z electrode) and b) evolution of the nonlinear predictability index (NPI). The solid line is the real data and dotted lines are derived from the 19 surrogate data sets. c) Excitatory cortical field ϕ_e and (d) corresponding NPI evolution of the corticothalamic model. Arrows show instances of weak nonlinear structure (slight increases in the real compared with the surrogate nonlinear indices) before and after the seizure.*

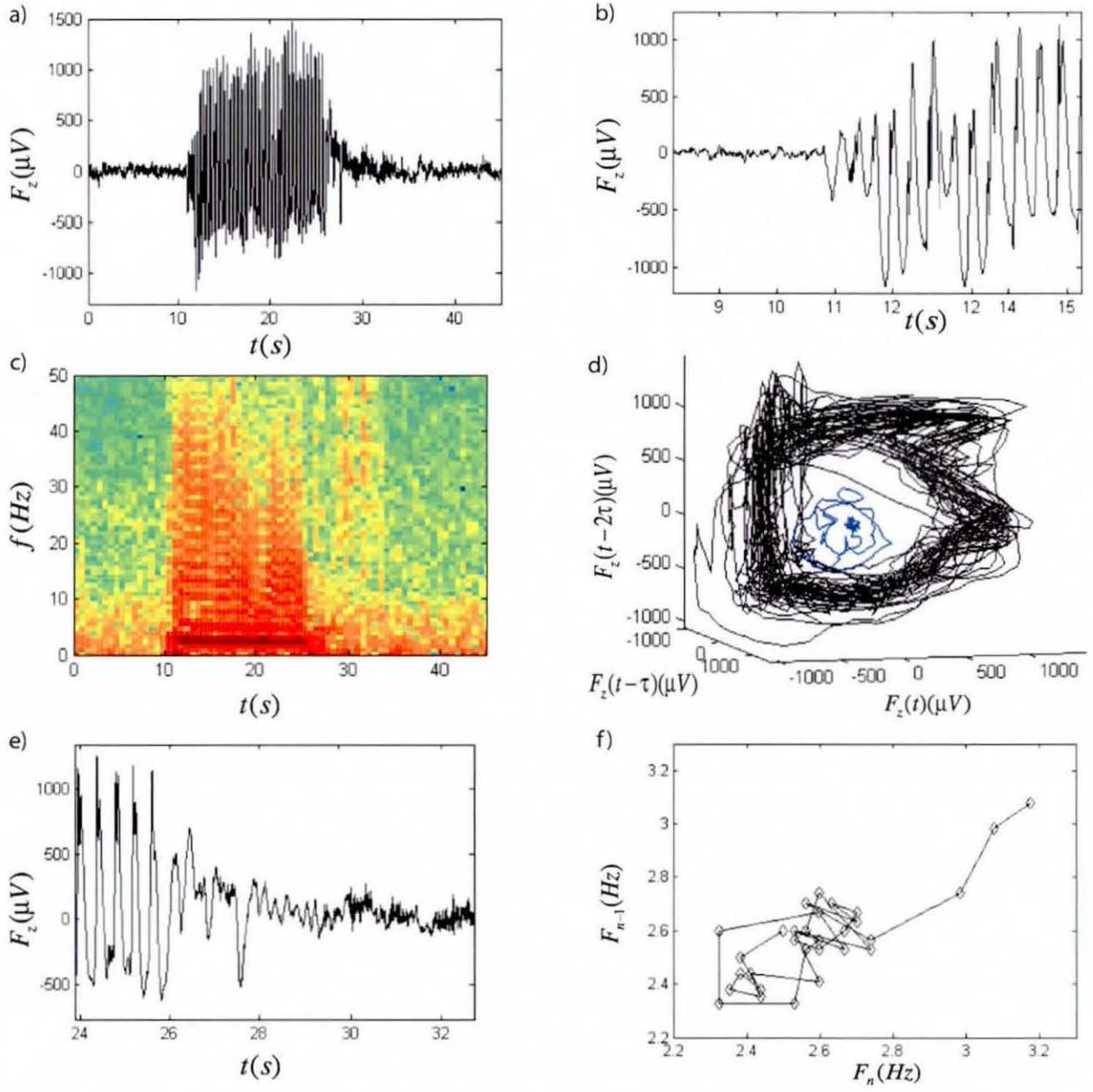


Figure 4.5: Analysis of scalp EEG data from channel F_z a) Entire seizure and b) The corresponding dynamic spectrogram showing a strong 3-Hz peak and multiple harmonics. Seizure onset c) and offset d). e) Time-delayed phase portrait. f) Peak-to-peak first-return map.

bifurcation" onset and offset, the similar pre and postictal spectra, and the periodic nature of the full seizure. The bifurcation plot of Fig. (4.2 a) explains these phenomena.

4.4 Two-bump solution in a piecewise linear reduction

The second stage of this study is to investigate the conditions for the appearance of 'spike-bifurcation' and provide some explanation of the genesis of spike wave activity. Motivated by key observations from the results presented in the first part of this chapter the model is reduced to a piecewise linear thalamic RKII set driven by an 'external signal'. This signal should be considered as an excitatory cortical drive. There are several motivating factors for this. Firstly, in clinical EEG recordings of the onset of absence seizures, the transition from pre-ictal to ictal dynamics is typically heralded by oscillatory behaviour, prior to spike-wave activity being observed, as illustrated in Fig. (4.6). Furthermore, in the absence of a cortical signal, the thalamic subsystem is quiescent and spike-wave activity (a periodic signal with an extra spike per period) was generated via periodic dynamics from the cortex fed into both specific relay nuclei and the reticular nuclei populations. Also motivating this reduction is that observations from the full model suggests that there is a phase shift in the dynamics of the *specific* neuronal populations when compared to both *cortical* and *reticular* populations, this is depicted in Fig. (4.3 c). This feature is supported by both *in-vivo* and *in-vitro* experiments [10, 41, 42, 43] that demonstrate spike-wave activity is first initiated in the specific relay nuclei, which then propagates to the cortex and is finally induced in the reticular nuclei.

Thus, as an approximation to the full model after the first nonlinear bifurcation has occurred, a driven thalamic circuitry is considered:

$$\begin{cases} \frac{1}{\alpha\beta} \left[\frac{d^2}{dt^2} V_r(t) + (\alpha + \beta) \frac{d}{dt} V_r(t) + \alpha\beta V_r(t) \right] = \nu_{rs} \varsigma[V_s(t)] + \nu_{re} \phi_{\text{cortical}}, \\ \frac{1}{\alpha\beta} \left[\frac{d^2}{dt^2} V_s(t) + (\alpha + \beta) \frac{d}{dt} V_s(t) + \alpha\beta V_s(t) \right] = \nu_{sr} \varsigma[V_r(t)] + \nu_{se} \phi_{\text{cortical}} + \nu_{sn} \phi_n. \end{cases} \quad (4.8)$$

where $\varsigma[V_r(t)]$ corresponds to the same equation (4.2) and all the parameters have the same interpretation as for the full model. This model is illustrated schematically in Fig. (4.7). A similar model for the study of olfaction has been considered in [170] where linear stability analysis was performed and stability curves in the parameters space were derived.

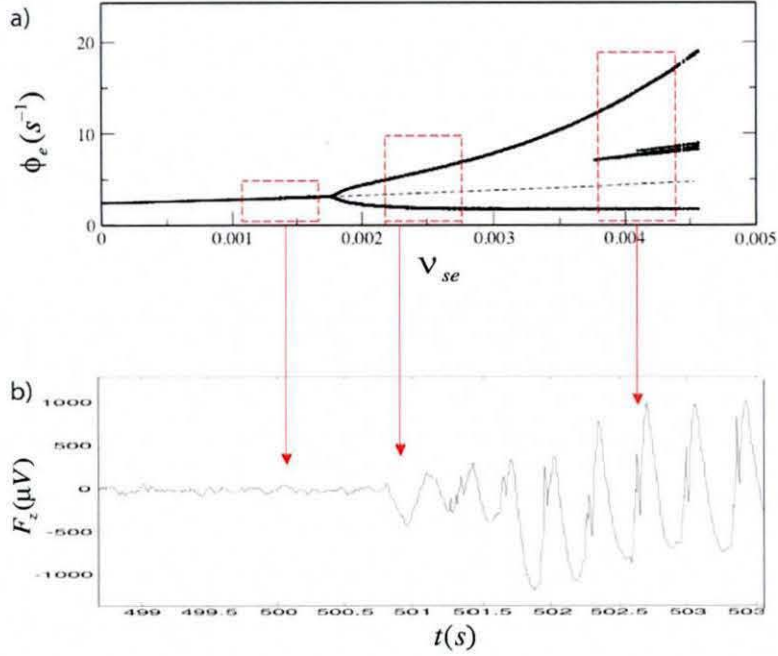


Figure 4.6: *Illustrating a comparison between the bifurcation diagram for the full model considered in the previous section (panel a)) and a clinical EEG recording during the onset of an absence seizure (panel b)). Upon varying the parameter ν_{se} there is a transition from steady-state to oscillatory dynamics, via a Hopf bifurcation, before a further transition gives rise to spike-wave like behaviour. This sequence of events replicates that observed in the clinical recording. The aim of the present section is to characterise the transition between stage 2 (oscillatory behaviour) and stage 3 (spike-wave). Consequently, we assume the cortex is generating a periodic oscillation and thus we drive the thalamic subsystem with a periodic signal of a type that is amenable to analysis.*

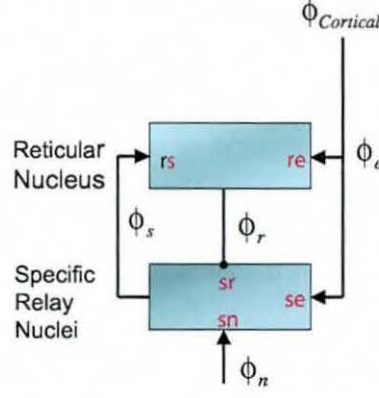


Figure 4.7: *Schematic of the RKII set with cortical drive. All interactions illustrated by arrows are assumed to be excitatory. The one between reticular and specific nuclei illustrated by a circle is inhibitory.*

4.5 Analysis of the periodically forced model

As mentioned previously, in-vivo and in-vitro experiments from animal models [43], as well as extensive numerical simulations of the full model suggests that the abnormal rhythms associated with absence seizures initially appear in the specific relay nuclei. Subsequently, if the excitation between specific to reticular, or specific to cortex, is strong enough then these abnormal rhythms may also be observed there. Simulations (Fig. 4.8) also indicate that the subthalamic input plays no part in the generation of abnormal rhythms. We further observe that the solutions to $V_r(t)$ are always periodic and that only the amplitude of these oscillations change when the parameters are varied.

Thus, for the purposes of understanding the genesis of abnormal activity in this reduced case, the following assumptions are made. First, assume that there are no interactions between the specific relay nuclei and the reticular nuclei populations, i.e. $\nu_{rs} = 0$. Second, assume that the subthalamic input is also zero, i.e. $\nu_{sn} = 0$.

Under these assumptions, the homogeneous solution V_a^h for the individual modules, $a = r, s$, is a combination of decaying exponentials. This can be seen by studying the roots of the characteristic polynomial derived from either of the differential operators in (4.8),

$$r^2 + (\alpha + \beta)r + \alpha\beta = 0,$$

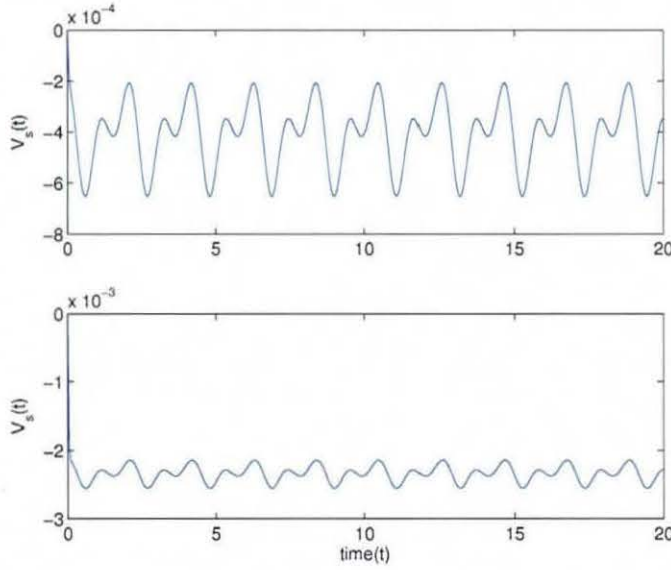


Figure 4.8: *In this plot, it is shown that the subthalamic interactions have no effect on the occurrence of spike-wave like activity. The two graphics are numerical simulations of system (4.8) using XPPAuto. The top graphic shows $V_s(t)$ with ν_{sr} non-zero. The bottom graphic shows the same system with $\nu_{sr} = 0$. In both cases the abnormal rhythm persists, with the subthalamic input acting effectively as an amplifier.*

the solution for which is given by

$$V_a^h(t) = Ae^{(-\alpha t)} + Be^{(-\beta t)}. \quad (4.9)$$

A further important point to note is that the dynamics of each individual system is overdamped; with the damping factor given by $\zeta = \frac{(\alpha+\beta)}{2\sqrt{(\alpha\beta)}} > 1$. This demonstrates that spike-wave activity can not occur due to any intrinsic dynamics within the individual thalamic modules.

4.5.1 Forcing function $\phi_{\text{cortical}} = \sin(\omega t)$

For the purposes of analysing the model, the following forcing function is employed, $\phi_{\text{cortical}} = \sin(\omega t)$. In the absence of the excitatory input from the specific relay nuclei, the solution for

the reticular nuclei can then be derived explicitly and is given by the particular solution:

$$V_r^p(t) = K \sin(\omega t + \delta), \quad (4.10)$$

where $K_a = \sqrt{(C_a^2 + D_a^2)}$ and $\delta_a = \arcsin(D_a/K_a)$ with

$$C_a = \frac{(\alpha\beta - \omega^2)\nu_{re}\alpha\beta}{((\alpha + \beta)^2\omega^2 + (\alpha\beta - \omega^2)^2)(\alpha\beta - \omega^2)}$$

and

$$D_a = -\frac{\omega\nu_{ae}\alpha\beta(\alpha + \beta)}{(\alpha + \beta)^2\omega^2 + (\alpha\beta - \omega^2)^2}$$

Note that this particular solution is also valid for the cortical forcing part of the specific module, i.e. $a = \{r, s\}$.

Consequently the long-time behaviour of the specific module, $V_s(t)$, is governed by the solution of the differential equation:

$$\frac{1}{\alpha\beta} \left[\frac{d^2}{dt^2} V_s(t) + (\alpha + \beta) \frac{d}{dt} V_s(t) + \alpha\beta V_s(t) \right] = \nu_{sr}\varsigma[V_r(t)] + \nu_{se}\phi_{\text{cortical}} \quad (4.11)$$

where $V_r(t)$ is given by the sum of equations (4.9) and (4.10).

Since $\varsigma(x)$ is a unipolar sigmoidal function, the resulting equation is transcendental and consequently an explicit solution to this equation is not possible. However, a result from [85] shows that it is possible to relate the stability of the full system to that of a related piecewise linearized system. Essentially, a piecewise linearization of the unforced system is performed and then the forcing term is reapplied in each case.

In order to do this, XPPAuto is used to determine the steady-states (V_r^* , V_s^*) of the system. Linearizing about these steady-states gives the following:

$$\frac{dx}{dt} = \mathbf{L}x + \mathbf{B}u, \quad (4.12)$$

where the vector \mathbf{B} comes from the cortical drive,

$$\mathbf{B} = \begin{pmatrix} 0 \\ \alpha\beta\nu_{se}\sin(\omega t) \\ 0 \\ \alpha\beta\nu_{re}\sin(\omega t) \end{pmatrix},$$

and \mathbf{L} is the piecewise linear vector field of the system,

$$\mathbf{L} = \begin{pmatrix} 0 & 1 & 0 & 0 \\ -\alpha\beta & -(\alpha + \beta) & \alpha\beta\nu_{sr}y_\sigma(V_r^*) & 0 \\ 0 & 0 & 0 & 1 \\ \alpha\beta\nu_{rs}y_\sigma(V_s^*) & 0 & -\alpha\beta & -(\alpha + \beta) \end{pmatrix}.$$

Essentially \mathbf{L} is the Jacobian matrix of the unforced system for each of the piecewise linear segments of the function $\varsigma(x)$. The first order Taylor approximation of this function at a point \mathbf{x}_0 , is given by

$$y(v)|_{x_0} = \frac{Q^{max}}{1 + e^{-\frac{\pi}{\sqrt{3}}(\frac{x_0 - \theta}{\sigma})}} + (v - x_0) \frac{\frac{Q^{max}\pi}{\sigma\sqrt{3}} e^{(-\frac{\pi}{\sqrt{3}}(\frac{x_0 - \theta}{\sigma}))}}{[1 + e^{(-\frac{\pi}{\sqrt{3}}(\frac{x_0 - \theta}{\sigma}))}]^2} + H.O.T. \quad (4.13)$$

Hence, the specific piecewise approximation we consider is

$$y_\sigma(v) = \begin{cases} y(v)|_{V_s^*} & -\infty \leq v < b, \\ y(v)|_{V_r^*} & b \leq v < \infty, \end{cases} \quad (4.14)$$

where $b > 0$ is the intersection point of the lines (at this point the derivative loses continuity). Note that we could have considered more line segments in the whole domain of the function $\varsigma(x)$. However, this would not change the conclusions, as the solution $V_r(t)$ is bounded and evolves around a steady state and consequently the solution for $V_s(t)$ will also be bounded. Considering more approximations will only smooth out the solutions obtained.

The composition of this piecewise linear approximation $y_\sigma(v)$ in (4.14) with the explicit solution for $V_r(t)$ given in (4.10) results in two regions of interest:

$$\text{Region}_I = \left\{ t \in \mathbb{R}, N \in \mathbb{Z} : \frac{\arcsin(\frac{b}{K}) - \delta + 2N\pi}{\omega} \leq t \leq \frac{\pi - \arcsin(\frac{b}{K}) - \delta + 2N\pi}{\omega} \right\} \quad (4.15)$$

$$\text{Region}_{II} = \left\{ t \in \mathbb{R}, N \in \mathbb{Z} : \frac{-\arcsin(\frac{b}{K}) - \pi - \delta + 2N\pi}{\omega} < t < \frac{\arcsin(\frac{b}{K}) - \delta + 2N\pi}{\omega} \right\} \quad (4.16)$$

It is now possible to explicitly solve this piecewise linear approximation to (4.11) using the method of variation of parameters, taking care to ensure that the boundary conditions for

each interval are satisfied (details of the calculation are shown in section B.4). The resulting asymptotic solution for $V_s(t)$ has the following form

$$V_s(t) = \begin{cases} K_s \sin(\omega t + \delta) + \mathcal{A}V_{s*}^m \sin(\omega t + \widehat{\delta}) + f(e^{-Kt}, c), & t \text{ in Region}_I, \\ K_s \sin(\omega t + \delta) + \mathcal{B}V_{r*}^m \sin(\omega t + \widehat{\delta}) + g(e^{-Kt}, c), & t \text{ in Region}_{II}, \end{cases} \quad (4.17)$$

where V_{r*}^m and V_{s*}^m are the amplitudes of the piecewise linear approximation to the steady state of V_r and V_s respectively. The parameters \mathcal{A} and \mathcal{B} incorporate the inhibitory effect of the reticular on the specific ν_{sr} , as well as α and β . There is also a different phase shift $\widehat{\delta}$ of the composite function compared to the cortical forcing. The functions f and g involve exponentially decaying and constant terms, which do not affect the asymptotic form of the solution.

4.5.2 Description of the spike-wave solution

The key aspects of the solution (4.17) are illustrated in Fig. (4.9). Essentially, the spike-wave oscillation arises as a result of the interaction of the sinusoid due to the excitatory cortical input and the opposite facing sinusoid-like function resulting from the composition of the piecewise linear approximation to ς with $V_r(t)$. This composite function has the same total period as the cortical signal, however, it consists of two sinusoids of different amplitudes and phases acting on each of the Regions I and II. The peaks of each bump in the combined solution correspond to the transition between regions. Noting that the area of Region_I is less than that of Region_{II}, this can be classed technically as a spike-wave oscillation, since the area of the spike part of the solution is less than that of the wave. A comparison between the explicit solution and that numerically generated for the same case using XPPAuto is given in Fig. (4.10). The fact that the solution of the two parts are opposite facing in each region is also crucial for the generation of the abnormal rhythm. Were both to point the same way, then only a one-bump solution would be observed. These opposite facing solutions are due to the inhibitory effect of the reticular nuclei on the specific relay nuclei and explains why no such solutions are ever observed in the reticular nuclei in the absence of activity in the specific relay, since the synaptic interactions between them are excitatory in nature. Finally, note that the gradient of the sigmoidal function ς varies dramatically between the two regions and it is this marked difference in gradient that leads to the different amplitudes on each Region,

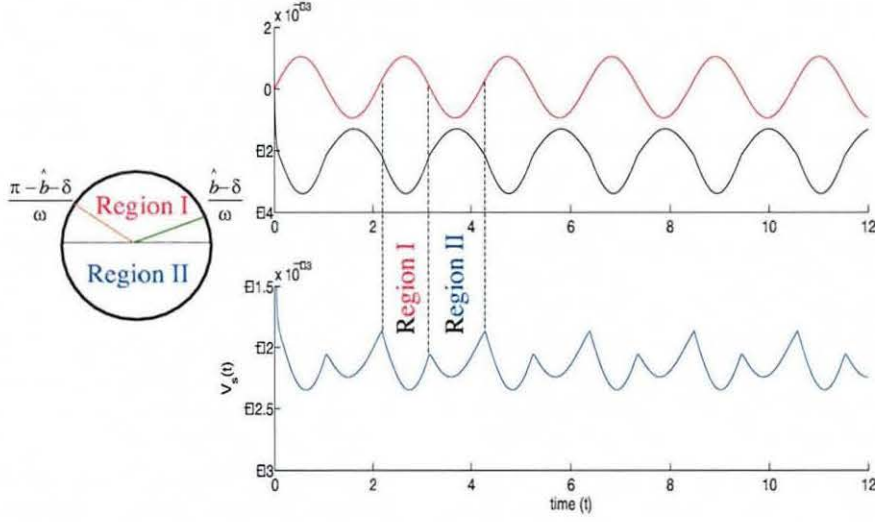


Figure 4.9: In the top graphic, the upper solution (in red) is the solution of the system when driven by the periodic forcing term $\nu_{se}\sin(\omega t)$ and the lower solution, is that of the system when driven by the composition of the piecewise linear approximation $y_\sigma(v)$, and $V_r(t)$. The difference in amplitudes of the second solution on each of the regions, combined with Region I being less than half the period gives rise to the spike-wave activity, illustrated in the lower graphic. The length of these regions can be adjusted by varying the parameters $\hat{b} = \arcsin\left(\frac{b}{K}\right)$ and δ as indicated on the circle.

which in turn gives the spike-wave solution. This illustrates the need for at least a piecewise linear approximation to ς and explains why previous attempts using linear stability analysis and Heaviside approximations to explain this phenomena were unsuccessful.

A final point concerns time-delays in the system. The mechanisms responsible for generation of the abnormal rhythms elucidated in this section do not require any time-delays, which is consistent with the work of [43]. However, the full model [130, 131, 132, 133], from which this reduced model was obtained, has delays between cortex and thalamus. Thus, it is imperative to determine the precise role that these time-delays play in the full system.

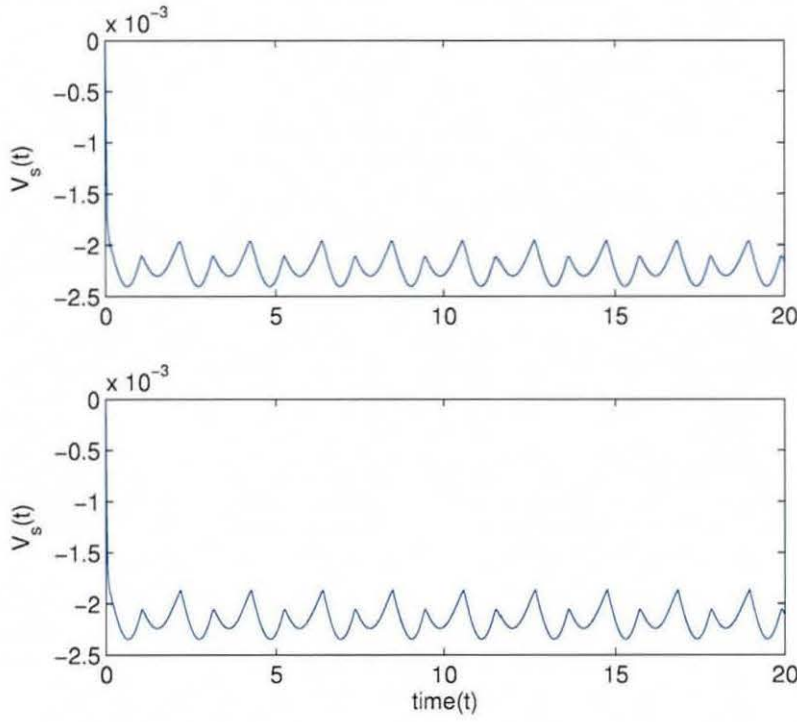


Figure 4.10: *The top graphic shows the solution of $V_s(t)$ from the numerical package XPPAuto for the piecewise linear system in the absence of ν_{sn} . The bottom graphic shows the explicit solution obtained, demonstrating precise agreement between the numerics and our analysis.*

4.6 Summary

In summary, the first part of this chapter performed a bifurcation analysis of a model of large-scale brain activity. A Hopf bifurcation to periodic dynamics with an initial (supercritical) instability commences the transition from healthy resting EEG to absence (3Hz) and beyond the (supercritical) Hopf an extra structure ('spike-wave') appears whose origin remains unresolved. This yielded a time series realisation with periodic spike and wave morphology that closely resemble scalp EEG data taken from an absence seizure data base. Moreover, the nature of the bifurcation set yields a symmetrical on-off character that is also observed in the EEG data. The results presented extend the predictions concerning the onset of epileptic activity [131] that seizure phenomena arises when corticothalamic dynamics lose linear stability in specific regions of parameter space. The model employed was initially proposed

to explain EEG temporal and spatial spectra in healthy resting and sleep states, when the activity is weakly damped and the nonlinearities can be neglected. However, surprisingly extending the analysis by studying nonlinear instabilities demonstrates that the model explains key features of absence seizures. Further results carried out in [21] also demonstrate that the model predicts tonic-clonic seizures showing that the model unifies in a unique framework the explanation of generalized seizures. The behaviour of the model's dynamical variables during nonlinear dynamics permits predictions to be made regarding real physiological processes. In this chapter, such prior predictions [131] were further elaborated and compared to physiological data. Finally a nonlinear prediction algorithm was employed in order to verify that the onset of generalized seizures corresponds to a bifurcation from damped to strongly nonlinear behaviour. The present study thus represents a predictive application of an existing model in a novel direction.

The second part of this chapter attempts to understand the nature of 'spike-wave' bifurcation to explain the genesis of these pathological oscillations. In this attempt, key observations of a time series resulting from thalamocortical model allows us to consider a reduced RKII set. In particular, by considering a piecewise linear approximation to the sigmoidal activation function we can write down a mathematical solution explaining the transition from oscillatory to spike-wave like dynamics, demonstrating that the phenomena is due to properties of the thalamic pathways, rather than intrinsic properties of the individual thalamic modules. These solution approximations are termed two-bump solutions which map to the spike and wave regions of the time series of the full system. The spike-wave activity arises first in the specific population as a combination of excitation from the cortical source and inhibition from the reticular nuclei. This finding demonstrates why spike-wave behaviour is not observed first in the cortex or reticular nuclei in this mean-field model, where only excitatory processes occur. Through feedback from the thalamus to the cortex (in the full system), such a two-bump solution would, given suitable conditions, be expected to iteratively reshape cortical output. In fact, this may explain why full spike-wave activity can only be maintained in the presence of cortical excitations [43]. Such a process of iterative reshaping would be expected to have a strong influence on the eventual spike-wave character of the observed Absence seizure waveform.

Chapter 5

Numerical continuation and Local stability of reduced model (RKII set)

The previous chapter demonstrates that the thalamocortical model exhibits limit cycles that emerge only if the connection strength from the cortex to the thalamus is “strong enough”. For this reason we focus only on the thalamic system and in particular understanding the oscillations arising in RKII sets. By first investigating a single RKII set and then extending the theoretical results to the dynamics of coupled RKII sets an understanding of the interactions of the thalamocortical loop will be provided. Interestingly, results for RKII networks with three hierarchical levels would offer insight in studies related to connections of three areas of the brain, for example interactions of cortical, thalamic and basal ganglia (striatum). This could shed light on understanding complex partial seizures [60]. Furthermore, extending these results to higher dimensional systems could provide a theoretical basis for exploring the genesis of other oscillatory patterns observed in EEG [57]. In this chapter we develop linear stability theory and contrast this with numerical continuation results obtained using XPPAuto.

5.1 Stability analysis

In this section an overview of results concerning linear stability analysis is provided, which we outline here for completeness. Bifurcation analysis of the model is performed, examining the

possible types of dynamics of the RKII set. Necessary conditions on the parameters of the model for stability of a limit cycle oscillation are shown.

Using the appropriate substitutions, system (4.8) (without cortical drive) is re-written as four coupled first order ODEs:

$$\begin{cases} \frac{d}{dt}V_s(t) = w(t), \\ \frac{d}{dt}w(t) = -\alpha\beta V_s(t) - (\alpha + \beta)w(t) + \alpha\beta(\nu_{sr}\varsigma[V_r(t)] + \nu_{sn}\phi_n) \\ \frac{d}{dt}V_r(t) = v(t), \\ \frac{d}{dt}v(t) = -\alpha\beta V_r(t) - (\alpha + \beta)v(t) + \alpha\beta\nu_{rs}\varsigma[V_s(t)]. \end{cases} \quad (5.1)$$

The stability of the equilibrium points of this first order system may be analysed by ensuring that the linearised version of (5.1) satisfies the Hartman-Großman theorem (Theorem 2.1.1). Thus, the Jacobian matrix of (5.1) is the following:

$$J = \begin{pmatrix} 0 & 1 & 0 & 0 \\ -\alpha\beta & -(\alpha + \beta) & \alpha\beta\nu_{sr}\varsigma'[V_r^*] & 0 \\ 0 & 0 & 0 & 1 \\ \alpha\beta\nu_{rs}\varsigma'[V_s^*] & 0 & -\alpha\beta & -(\alpha + \beta) \end{pmatrix}, \quad (5.2)$$

where V_s^* and V_r^* are the values of V_s and V_r at some equilibrium point and $\varsigma'[V_a] = \frac{d}{dV_a}\varsigma(V_a)$ (i.e. the derivative of $\varsigma(V_a)$ with respect to the transmembrane potential). The equilibrium state being determined by setting the RHS of system (5.1) equal to 0, thus giving:

$$\begin{cases} V_s = \nu_{sr}\varsigma[V_r] + \nu_{sn}\phi_n, \\ V_r = \nu_{rs}\varsigma[V_s]. \end{cases} \quad (5.3)$$

The eigenvalues of which are given by the roots of the characteristic equation (for completeness the derivations can be found in section §C.1) resulting in:

$$\lambda = \frac{-(\alpha + \beta) \pm \sqrt{(\alpha - \beta)^2 \pm 4i\alpha\beta\sqrt{|\nu_{sr}\nu_{rs}|\varsigma'[V_r^*]\varsigma'[V_s^*]}}}{2}. \quad (5.4)$$

Defining the square root of a complex number as

$$\sqrt{x + iy} = \frac{\sqrt{2}}{2} \left[\sqrt{\sqrt{x^2 + y^2} + x} + i \operatorname{sgn}(y) \sqrt{\sqrt{x^2 + y^2} - x} \right] \quad \text{where} \quad \operatorname{sgn}(y) = \begin{cases} 1 & y > 0 \\ 0 & y = 0 \\ -1 & y < 0. \end{cases}$$

Setting $x = (\alpha - \beta)^2$ and $y = 4\alpha\beta\sqrt{|\nu_{sr}\nu_{rs}|\zeta'[V_r^*]\zeta'[V_s^]}$ it is apparent that there exist two complex conjugate pairs of eigenvalues, with one pair trailing the other (by which it is meant the real part is smaller). Furthermore, the real parts of the eigenvalues are defined as

$$\text{Re}(\lambda) = \frac{1}{2} \left[-(\alpha + \beta) \pm \frac{\sqrt{2}}{2} \sqrt{\sqrt{(\alpha - \beta)^4 + (4\alpha\beta)^2 |\nu_{sr}\nu_{rs}|\zeta'[V_r^*]\zeta'[V_s^]} + (\alpha - \beta)^2} \right].$$

A Hopf bifurcation will occur when $\text{Re}(\lambda) = 0$. The form of this expression makes verification difficult and a more convenient treatment is to use the Lienard-Chipart criterion (derived from the more familiar Routh-Hurwitz Theorem) [59]. Using this criterion the same result obtained by Xu and Principe [170] is derived (refer to section §C.3.1), obtaining the following hyperbolic curve in the $|\nu_{sr}\nu_{rs}|$ parameter space:

$$|\nu_{sr}\nu_{rs}| > \frac{1}{\zeta'[V_r^*]\zeta'[V_s^]} \frac{(\alpha + \beta)^2}{\alpha\beta}. \quad (5.5)$$

A graphical representation of this is shown in Fig. 5.1(a). It is important to note that the right hand side of (5.5) is also a function of ν_{sr} and ν_{rs} , implying a nonlinear dependence on $|\nu_{sr}\nu_{rs}|$. If condition (5.5) is satisfied then the equilibrium has a transition from a stable to unstable equilibrium state, via a supercritical Hopf bifurcation. This may be proven analytically by considering the normal form of (5.1) which is developed in Chapter 6, or by evaluating the coefficients of curvature (refer to equation (2.13)).

In the following discussion, analysis of system (5.1) is carried out in the autonomous case and when driven by a time invariant signal. The latter case may be considered as a transformation of the coordinate system, describing the transition to instability in each scenario. The nullclines of the system may be calculated from (5.3) and an illustrative example is presented in Fig. 5.1(b). Observe that the system has a unique equilibrium state since $\zeta(V)$ is a monotone increasing function. Furthermore, the equilibrium state can be either in the first or the fourth quadrant of the state space (V_r, V_s) , depending on the strength of the external input ν_{sn} . A result of this is the following proposition:

Proposition 5.1.1 *Since $\nu_{rs} > 0$ and $\zeta(x) \geq 0, \forall x \in \mathbb{R}$, then $V_r^* \geq 0$. Further, since $\nu_{sr} < 0$, then if $\nu_{sn} = 0$ we have $V_s^* < 0$; else $V_s^* \geq 0$. Further, V_s^* will be in the first quadrant of the state space (V_r, V_s) if $\nu_{sn}\phi_n > \nu_{sr}\zeta(V_r^*)$.*

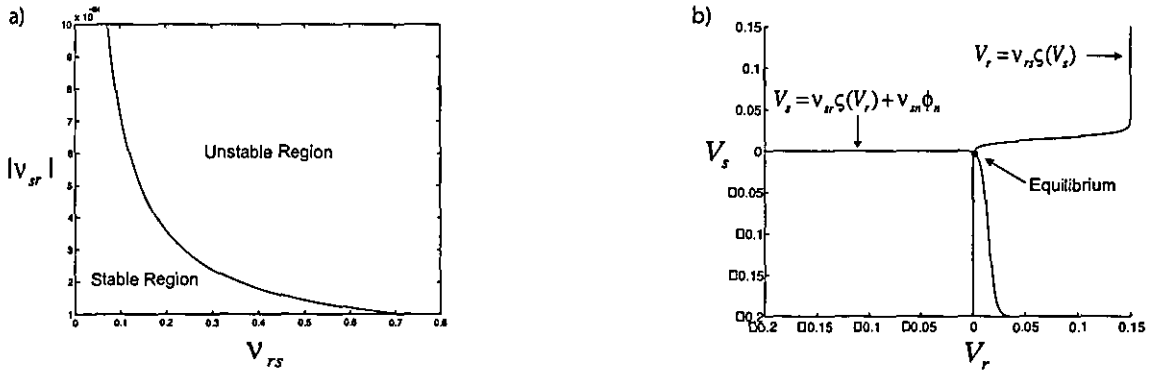


Figure 5.1: a) Illustrating the stability condition (5.5) in the parameter space $|\nu_{sr}\nu_{rs}|$. In this case, the values of the fixed point are given by $V_s^* = -0.01222$ and $V_r^* = 0.005962$. The curve is hyperbolic, giving a stable and an unstable region. This transition from stable to unstable defines the branch in parameter space where a supercritical Hopf bifurcation occurs. b) Illustrative example of the nullclines of system (5.1) in the state space (V_s, V_r) . Since the sigmoidal curve is monotonic, there exists a unique equilibrium point for a fixed set of parameters. The equilibrium can either be in the first or fourth quadrant of the state space (V_s, V_r) depending on the level of the strength of external input ν_{sn} .

5.1.1 Autonomous case

As previously discussed, in the autonomous case, the equilibrium is in the fourth quadrant of the state space (V_r, V_s) . Further, from Xu and Principe [170] the following properties of the equilibrium state are given:

- i) V_s^* is a decreasing function with respect to both u_{rs} and $|u_{sr}|$, that is, $\frac{dV_s^*}{du_{rs}} \leq 0$ and $\frac{dV_s^*}{d|u_{sr}|} \leq 0$
- ii) V_r^* is an increasing function with respect to u_{rs} but decreasing with respect to $|u_{sr}|$, i.e., $\frac{dV_r^*}{du_{rs}} \geq 0$ and $\frac{dV_r^*}{d|u_{sr}|} \leq 0$

A derivation of these properties is presented in the section-§C.2 for completeness.

From these properties, a local region is derived (since finding a global region is analytically intractable) for which the stability condition (5.5) is satisfied and hence gives rise to a transition between a stable equilibria and a stable limit cycle. For condition (5.5) to hold true

it is necessary that if $|\nu_{sr}\nu_{rs}|$ increases then $1/(\varsigma'[V_r^*]\varsigma'[V_s^*])$ should decrease to a minimum in order to satisfy the inequality. In other words, $\varsigma'[V_r^*]\varsigma'[V_s^*]$ should be maximized. Since $\varsigma'[V_r^*]$ is a Gaussian-like curve, depicted in Figs. (5.2:a) and (5.2:b), then the product of these two derivatives will also be Gaussian-like. Thus, the idea is then to maximize the area of the resulting function.

Ideally, one approach would be to apply the convolution operator to these two functions ($g(V) = \varsigma'[V_r^*] \otimes \varsigma'[V_s^*]$), and then search for a V such that $g(V) > \frac{1}{|\nu_{sr}\nu_{rs}|} \frac{(\alpha+\beta)^2}{\alpha\beta}$. Thus giving the resulting area of the Gaussian that is unstable. However the problem here is reobtaining the individual components V_s and V_r . Another way to define the region is by noticing that the equilibrium is in the fourth quadrant and by tuning the parameters ν_{rs} and ν_{sr} according to Properties (i) and (ii) (see Fig. 5.2). From this, we can find a lower and upper bound for V_s^* and V_r^* . Again, from Figs. (5.2:a) and (5.2:b), we have that if both $V_s < \theta$ and $V_r < \theta$ then the only form that maximises $\varsigma'[V_r^*]\varsigma'[V_s^*]$ is to first fix $\nu_{sr} = \nu_{sr}^*$ and then increase ν_{rs} until condition (5.5) is satisfied. Note that increasing ν_{rs} decreases V_s^* .

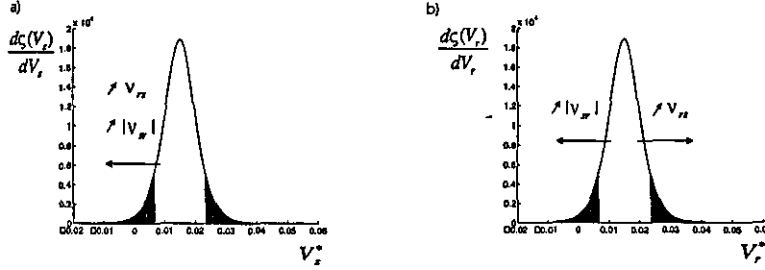


Figure 5.2: Both plots a) and b) represent the derivative of the sigmoidal $\varsigma(V_a)$ (with $a = \{r, s\}$), where the maximum is $\frac{Q^{max}\pi}{4\sigma\sqrt{3}}$ at $V_a = \theta$. The figures try to demonstrate how to use the control parameters ν_{rs} and $|\nu_{sr}|$ in order to satisfy condition (5.5). The right hand side of (5.5) depends on the product of the derivatives, i.e $\varsigma'(V_s^*)\varsigma'(V_r^*)$. To satisfy (5.5) the quantity $|\nu_{sr}\nu_{rs}|$ has to be increased whilst minimising $\frac{1}{\varsigma'(V_s^*)\varsigma'(V_r^*)}$, i.e maximising $\varsigma'(V_s^*)\varsigma'(V_r^*)$. Thus the shaded area “represents” the area where $\varsigma'(V_s^*)\varsigma'(V_r^*)$ is minimum and condition (5.5) is not satisfied. a) If $|\nu_{sr}|$ increases then the equilibrium V_s^* decreases, equally if ν_{rs} increases then V_s^* decreases. b) If $|\nu_{sr}|$ increases then the equilibrium V_r^* decreases, conversely if ν_{rs} increases then V_r^* increases. The change in parameters will allow the equilibrium to fall in or out of the stable region.

The following sections further investigate the behaviour of the RKII model numerically using the software package XPPAuto, both to examine the many interesting dynamical features of the model and also to verify the analytical findings. Consequently, the first investigation was to examine the (ν_{sr}, ν_{rs}) parameter space and compare these results with condition (5.5). Here, an unexpected result was that the stability curve in (ν_{sr}, ν_{rs}) parameter space was more far reaching than that expressed by condition (5.5). In addition to the hyperbolic curve described by condition (5.5), there was also a fold point on the same branch in parameter space. To obtain this branch numerically, first a Hopf bifurcation point was found and then two parameter continuation was carried out, depicted in Fig. 5.3.

The notation used is the same as the software package XPP to denote special points, i.e. *Supercritical Hopf* (HB), *Fold or Limit point* (LP) and *Branch point* (BP). Starting at any point on the (ν_{sr}, ν_{rs}) curve, for example HB1, and then by varying only ν_{rs} , it can be observed in the bifurcation diagram (V_a, ν_{rs}) that the system will have periodic orbits with increasing amplitude. This amplitude however decreases when the parameter ν_{rs} increases. An example of such a scenario is depicted in Fig. 5.4(a). Conversely, starting at HB1 and varying the parameter ν_{sr} by increasing it, an upper branch of the (ν_{rs}, ν_{sr}) curve is found which emanates from the fold LP1. Thus, the resulting diagram will have periodic orbits that have an increasing and subsequently decreasing amplitude until convergence at a second Hopf point. This latter idea is illustrated in Fig. 5.4(b).

The existence of a fold point in the (ν_{sr}, ν_{rs}) parameter space suggests that the parametric curve depicted in Fig. 5.3 is globally parabolic with the vertex given by the fold point (LP1) and locally hyperbolic as described by condition (5.5). The difference between these two curves (Fig. 5.1 and Fig. 5.3) is to plot condition (5.5) V_s^* and V_r^* must be fixed, so it is only a local representation. Another way of seeing this is by examining how Properties i) and ii) affect the stability condition (5.5). For convenience, we construct a table of all possible combinations of the direction of increase/decrease of the parameters ν_{sr} and ν_{rs} and observe how this changes the value of the equilibrium point (V_s^*, V_r^*) and consequently the change of condition (5.5). From Table (5.1) and following Fig. 5.3, notice that the first entry of the Table corresponds to the direction taken by the curve from LP1 to HB1, i.e. In the direction $LP1 \rightarrow HB1$ both parameters increase in size. For example, starting from LP1, an increase of $|\nu_{sr}|$ decreases

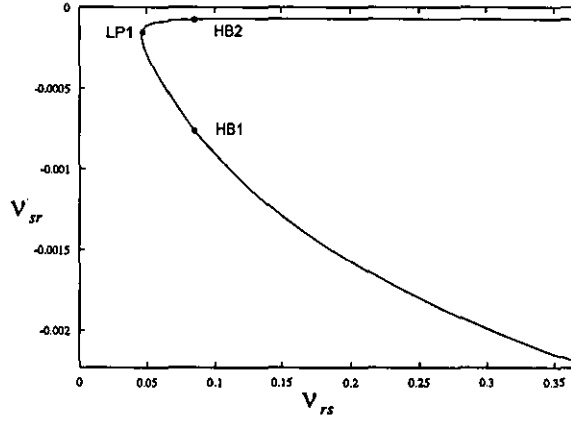


Figure 5.3: Illustrated is a two parameter branch of Hopf bifurcations in the (ν_{sr}, ν_{rs}) parameter space. A numerical continuation finds extra structure in this parameter space. The lower part of the curve confirms the hyperbolic nature of the (ν_{sr}, ν_{rs}) parameter space given by Eqn (5.5), however there is additionally a fold point (LP1). From this fold point, two Hopf bifurcations are born, both supercritical (HB1) and (HB2). All values of the special points depicted are given in Table (C.2) in section §C.4).

both V_s and V_r . The same direction implies increments on ν_{rs} and consequently causing a decrease in V_s . However V_r compensates by changing the growth direction and consequently the system would still be placed on Hopf point. The second entry corresponds to the opposite direction, HB1 to LP1. Equally, by applying the same arguments to the third and fourth entry it is verified that these relate to the upper branch of the (ν_{sr}, ν_{rs}) curve. Furthermore, taking the latter arguments and following the curve depicted in Fig. 5.1(a), a change in ν_{sr} will change the equilibrium locally as follows: $V_s^* \approx \nu_{sr} V_s$ and $V_r^* = \nu_{rs} \zeta(V_s^*)$, i.e. the equilibrium will mainly follow the $V_r = \nu_{rs} \zeta(V_s)$ equation. Conversely, a change in ν_{rs} will locally affect the equilibrium according to: $V_r^* \approx \nu_{rs} V_r$ and $V_s^* = \nu_{sr} \zeta(V_r^*)$.

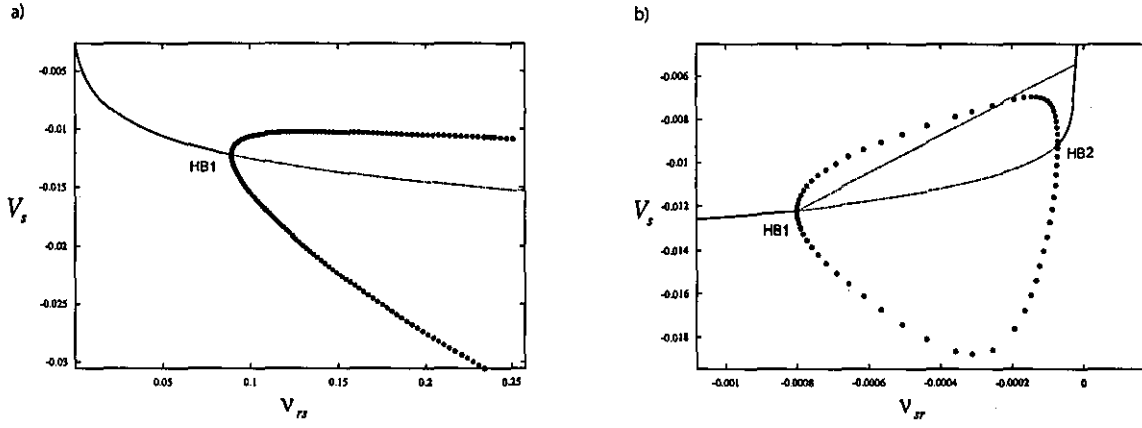


Figure 5.4: a) Plotted is a bifurcation diagram (V_s, ν_{rs}) for the autonomous case. Commencing from HB1 and varying ν_{rs} , the amplitude of the periodic orbits appearing from HB1 gradually augment to a maximum but never decays. This characteristic can be verified by examining the previous Fig. 5.3, since it is a parabolic curve. If the system starts from HB1 with ν_{sr} fixed and simultaneously varying ν_{rs} then the system never intersects a section of the (ν_{sr}, ν_{rs}) curve. The labelled points of interest have their actual values in Table (C.2) in section §C.4). b) Illustrating the bifurcation diagram (V_s, ν_{sr}) . Starting from HB1 and varying ν_{sr} the amplitude of the Hopf grows to a maximum and then decays until it finds HB2. Note the extra unstable fixed points starting from HB1 and moving up diagonally until it gains stability. The point where it gains stability is very close to the fold point LP2. This point was numerically unstable and XPP found it difficult to follow the Hopf bifurcation close to LP2. The special points marked in the figures have their corresponding values in Table (C.2) in section §C.4).

ν_{rs}	$ \nu_{sr} $	$V_s(\nu_{rs})$	$V_s(\nu_{sr})$	$V_r(\nu_{rs})$	$V_r(\nu_{sr})$
↑	↑	↓	↓	↑	↓
↓	↓	↑	↑	↓	↑
↑	↓	↓	↑	↑	↑
↓	↑	↑	↓	↓	↓

Table 5.1: Summarising how a change in parameters $|\nu_{sr}|$ and ν_{rs} affect the V_s and V_r . The arrows indicate respectively increase and decrease in value. For example the first entry indicates that if there is an increase (in modulus) in both of the parameters, then V_s will decrease, however V_r will vary respectively according to a specific parameter.

5.1.2 Analysis of RKII set driven by a constant signal

In the following sections a time invariant signal, $\phi_n = 1$ with $\nu_{sn} > 0$, applied to system (5.1) is considered and then a region of phase space where an instability occurs is determined. Since this driving force is constant, the resulting system is equivalent to the autonomous case with an applied coordinate transformation, thus the type of bifurcations that occur are essentially the same. However, the signal essentially adds extra dimensionality to the problem and consequently the manner in which the system is driven to instability may be different to the autonomous case. From [170] the following additional property is required:

- iii) The fixed points V_s^* and V_r^* are both monotonically increasing functions with respect to the strength of the external signal ν_{sn} , that is, $\frac{dV_s^*}{d\nu_{sn}} > 0$ and $\frac{dV_r^*}{d\nu_{sn}} > 0$.

Setting all parameters of the model to the physiologically realistic values shown in Table B.1 and only varying the amplitude of the external signal the bifurcation diagram in Fig. 5.5(a) is obtained. As the strength of the external signal is increased, a Hopf bifurcation occurs at the point HB3. Further increasing the strength of the external signal causes the amplitude of periodic oscillations arising subsequently to HB3 to increase for a time, but then subsequently a turning point occurs after which the amplitude of oscillations decreases until another supercritical Hopf bifurcation occurs at HB4 and the oscillatory behaviour ceases. The actual values for HB3 and HB4 are shown in Table C.2. The following proceeds in the same manner as per the autonomous case to investigate the (ν_{sr}, ν_{rs}) parameter space and see if there is any change in the structure of the curve in parameter space when the amplitude of the external signal ν_{sn} is increased. XPPAuto allows one to plot bifurcation diagrams of a system, whilst varying an additional parameter value on the same plot. We choose to use this facility for better comparison of the dynamics of the model during various regions, whilst varying the external forcing strength. Starting from HB3 (when $\nu_{sn} = 0.01707$) and numerically continuing this branch of Hopf bifurcations in (ν_{sr}, ν_{rs}) space a similar parabolic curve is obtained to that determined in the autonomous case with an additional fold point, LP2. However, if there is an increase in the amplitude of the external signal until $\nu_{sn} = 0.2073$, i.e. where the second Hopf, HB4 occurs, a widening of the parabolic curve is observed and this is geometrically very different to what would be expected from the study performed for the autonomous case. Both

of these curves are shown in Fig. 5.6. For the case where $\nu_{sn} = 0.2073$, the curve suggests that there were extra fold points in the (ν_{sr}, ν_{rs}) space, i.e. one very close to the point we denote HB6 and the other perhaps close to but lower than LP3. However, numerically XPPAuto did not identify these as being fold points and only the fold point LP3 was found, which is consistent with the autonomous case. The values for the special points HB3, HB4, LP2 and LP3 can be found in Table C.2 (in section §C.4). The precise nature of the points HB5 and HB6 will be elucidated later.

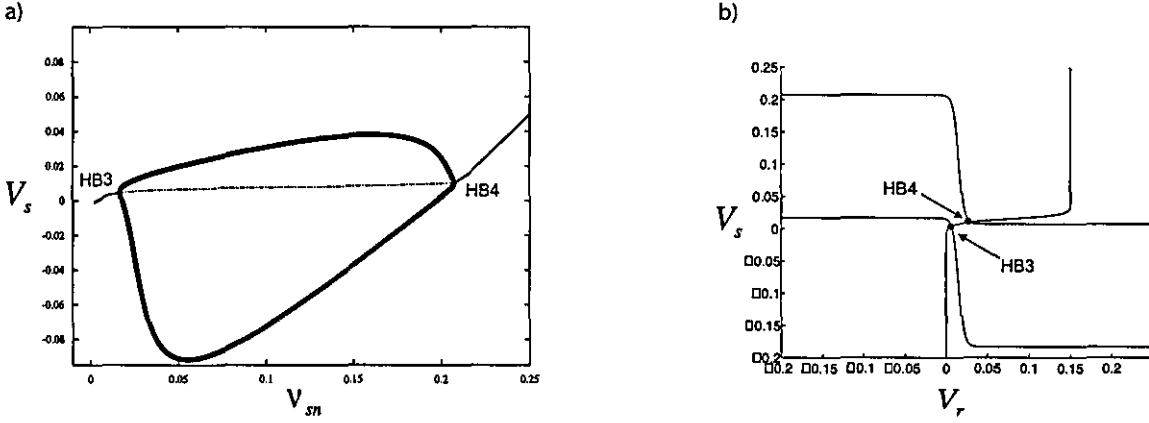


Figure 5.5: a) Bifurcation diagram in (V_s, ν_{sn}) space. An increase in the strength of the external signal will cause a Hopf Bifurcation HB3 and further increasing the strength will cause periodic oscillations to initially increase in amplitude before a decrease until another supercritical Hopf bifurcation, HB4, is found. The respective values for HB3 and HB4 can be found in Table C.2. Part b) complements part a), showing the configuration of the nullclines and the supercritical Hopf points HB3 and HB4 in the state space (V_r, V_s) for two different strengths of the external forcing. Note that the intersection points of the nullclines are both in the first quadrant. We further notice that the values assumed by V_s and V_r at the bifurcation points HB3 and HB4 are very close to the $\theta - \sigma$ and $\theta + \sigma$. The values for V_s and V_r can be verified in Table C.2.

Consider now the bifurcation diagrams generated for different amplitudes of the external forcing ν_{sn} . Note that although ν_{sn} increases the dimension of the parameter space by one, new forms of bifurcations are not observed. The following bifurcation diagrams only help to isolate the regions of the parameter space where a certain supercritical Hopf is generated or destroyed in the $(\nu_{rs}, \nu_{rs}, \nu_{sn})$ parameter space. Choosing initially the points HB3 and HB4, the parameters of interest ν_{sr} and ν_{rs} are then varied resulting in Figs. (5.7 - 5.11). From

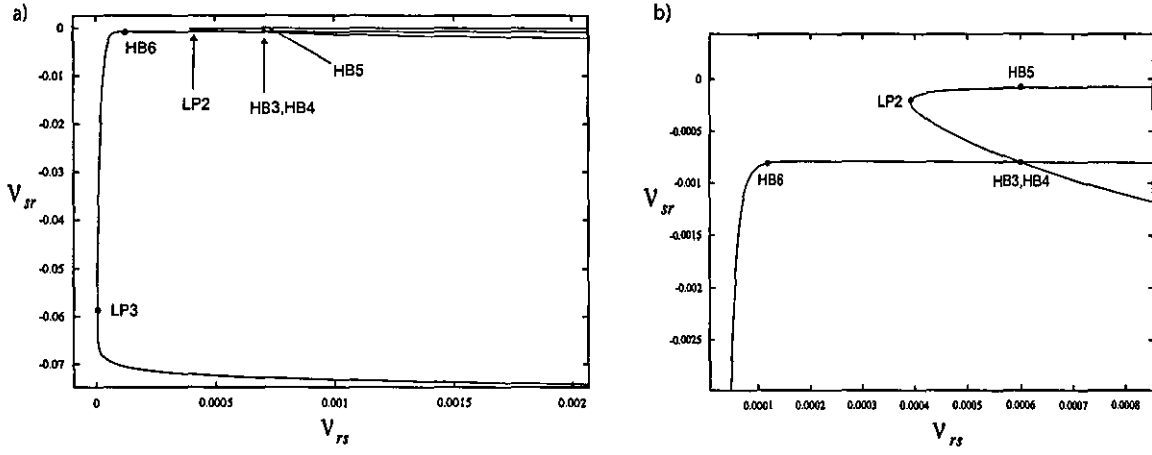


Figure 5.6: a) and b) represent the continuation of supercritical Hopf points in the (ν_{sr}, ν_{rs}) parameter space, where the diagram b) is a zoom in of a). Note, we use the numerical software package XPP feature to superimpose two continuation diagrams in the same plot, allowing a better comparison for different external strength case. Two cases are shown, for $\nu_{sn} = 0.01707$ we observe the curve consisting of points HB3, LP2 and HB5 and for the case $\nu_{sn} = 0.2073$ the curve is composed of points from HB4, HB6 to LP3. For the latter case, the curve (ν_{sr}, ν_{rs}) is much opened and geometrically very different to the former. This poses questions to whether extra fold points are born as the external strength ν_{sn} is increased. For the external inputs considered in this plot we observe fold points on both curves, thus, indicating that the curves are locally parabolic. The values of the special points in the Figures are given in Table C.2.

diagrams (5.7:a) and (5.7:b) observe that starting at HB3, where here $\nu_{sn} = 0.01707$, varying ν_{rs} results in oscillations of increasing amplitude as we move away from HB3. No fold occurs in this case, and further increasing ν_{rs} does not bring about a decrease in the amplitude of oscillations. However, upon increasing the amplitude of the external signal ($\nu_{sn} = 0.2073$), the structure changes dramatically. Here from the Hopf point at HB4, decreasing ν_{rs} , observe that the amplitude of oscillations increases initially as we move away from HB4, until what appears to be a fold occurs and the amplitude decreases, until we arrive at HB6 where oscillations cease. Considering the bifurcation curve in (ν_{rs}, ν_{sr}) parameter space (Fig. 5.6) does not result in a fold. This change is of particular interest, as it demonstrates that an external signal may be used to destroy oscillatory behaviour. If such oscillatory behaviour corresponded to seizure-like activity, the application of such external forcing would be highly significant. This change in amplitude from HB4 to HB6 can be explained by the Fold LP7 in the (ν_{rs}, ν_{sn}) parameter

space, see Fig. 5.8. Note also that in the same diagram, it is shown a second fold point exists, denoted LP6. The existence of LP6 justifies the alteration of the amplitude of the periodic orbits seen in Fig 5.5(a).

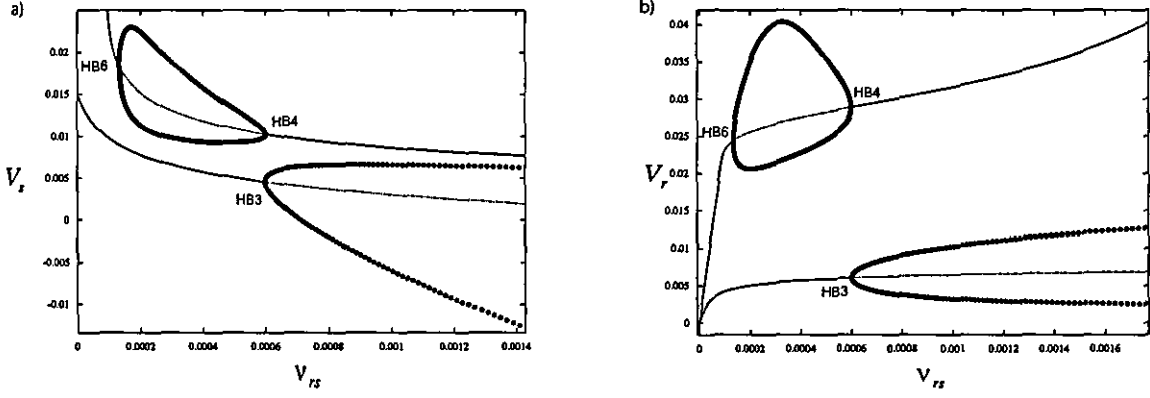


Figure 5.7: a) The plot shows the bifurcation diagram (V_s, ν_{rs}) at two different levels of the external signal strength, at $\nu_{sn} = 0.01707$ and $\nu_{sn} = 0.2073$. XPP allows one to automatically superimpose the two bifurcation allowing easy comparison. The supercritical Hopf HB3 corresponds to the lower level of external signal strength while HB4 and HB5 corresponds to a stronger input. The difference in external strength causes a change in the bifurcation diagram. The labeled points shown in the figures have their related values in Table C.2. b) The illustration shows the bifurcation diagram (V_r, ν_{rs}) at two different levels of the external signal strength, at $\nu_{sn} = 0.01707$ and $\nu_{sn} = 0.2073$ thus very similar to figure a) where here the objective is to observe the variable V_r and so only complements the previous plot. The turning point in the amplitudes of the periodic orbits emanating from either HB4 or HB6 is explained by the two parameter continuation diagram (5.8). The special marked points have their corresponding values laid up on Table C.2.

Conversely, in Fig. 5.9, a different scenario to the one just outlined is observed. Here both bifurcation diagrams, at different strengths of the external input, eventually have the same dynamical transitions. That is, an increase followed by a decrease in amplitude. This is because at each level of the external input there exists a fold living in (ν_{rs}, ν_{sr}) parameter space. This is illustrated in Fig. 5.6. Fig. 5.9 is slightly misleading for the case where $\nu_{sn} = 0.2073$ for the following reason: Commencing at HB3 where $\nu_{sn} = 0.01707$ and varying ν_{rs} increases the amplitude of the limit cycle oscillations, further increasing ν_{rs} , a fold point LP2 occurs in the (ν_{rs}, ν_{sr}) parameter space which causes a decrease in the amplitudes until HB5. Equally,

for the level of input $\nu_{sn} = 0.2073$ the scenario repeats, however crossing at the fold point LP3 depicted in Figure 5.6. It should be pointed out that the bifurcation diagram (V_a, ν_{sr}) for this level of external input is also misleading because for this input the effect of the turning point does not appear noticeable. This is because the scales of the two bifurcations are such that it would not be possible to represent both effectively on the scale of the fold point. Furthermore, examining closer the bifurcation diagram (V_s, ν_{sr}) with gradual transitions of the strength of external input reveals the existence of a limit point LP4 as shown in Fig. 5.10. From this diagram it is observed that as ν_{sn} is increased, the supercritical Hopf HB5 is shifted to the right and the parameter range of ν_{sr} , where the periodic orbits exists, increases. From the limit point LP4 a further increase of ν_{sn} will have the opposite effect of dragging the Hopf to the left, hence the previous Fig. 5.9. Additionally, the limit point marks the region where the second supercritical Hopf, for example HB7, ceases to exist in the (ν_{sr}, ν_{sn}) parameter space. This fact is also confirmed by the continuation of the two dimensional curve of supercritical Hopfs in the (ν_{sr}, ν_{sn}) parameter space illustrated in Fig. (5.8). Increasing ν_{sn} will only destroy the second Hopf in this parameter space, however it will persist in the projection onto (ν_{rs}, ν_{sr}) space, as may be seen in Fig. (5.6). Here, for example fixing all parameters and starting at some supercritical Hopf on the top branch of the two dimensional (ν_{rs}, ν_{sr}) curve and then smoothly decreasing ν_{sr} will only have the effect of meeting the bottom branch of the same curve. Furthermore, tracking the second Hopf through one parameter space and into the other, following ν_{sr} , for example, shows only an extension of the range of the parameter ν_{sr} , where the periodic orbits exist.

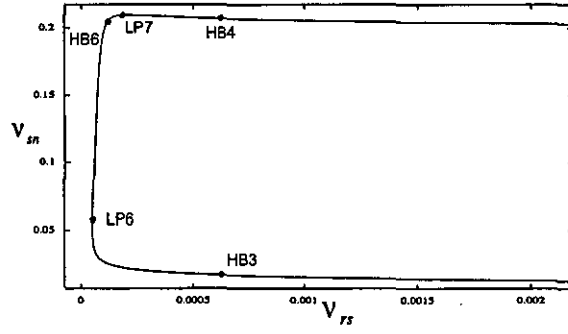


Figure 5.8: *Depicting a continuation of supercritical Hopf points in the (ν_{rs}, ν_{sn}) parameter space. The existence of two fold points (LP6 and LP7) indicate a change in the oscillations of the model when ν_{sn} or ν_{rs} is varied and the two dimensional curve is only locally parabolic near these two fold points.*

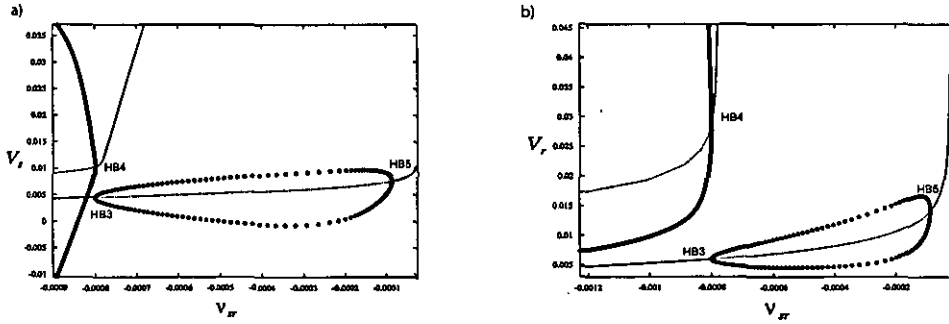


Figure 5.9: *a) Bifurcation diagram (V_s, ν_{sr}) at two different levels of the external signal strength, one at $\nu_{sn} = 0.01707$ and the other for $\nu_{sn} = 0.2073$. XPP allows one to automatically superimpose the two bifurcation allowing easy comparison. The bifurcation consisting of points HB3 and HB5 corresponds to the case when $\nu_{sn} = 0.01707$ and the other corresponding to the higher level of external input. An important point in this figure is to note that all oscillations emanating from HB4 will have an increase in amplitude but as ν_{sr} is further decreased the amplitudes will shrink to zero. For this point the reader is asked to refer to figure (5.6), showing the existence of the fold LP3. b) The illustration shows superimposed bifurcation diagrams (V_r, ν_{sr}) at two different levels of the external signal strength, at $\nu_{sn} = 0.01707$ and $\nu_{sn} = 0.2073$ thus very similar to figure a). Here the aim is to observe the variable V_r , which only complements the previous plot. The turning point in the amplitudes of the periodic orbits emanating from either HB3 or HB5 is explained by the existence of a fold point LP2 in the two parameter continuation diagram (5.6). The values corresponding to the labelled points is revealed in Table C.2).*

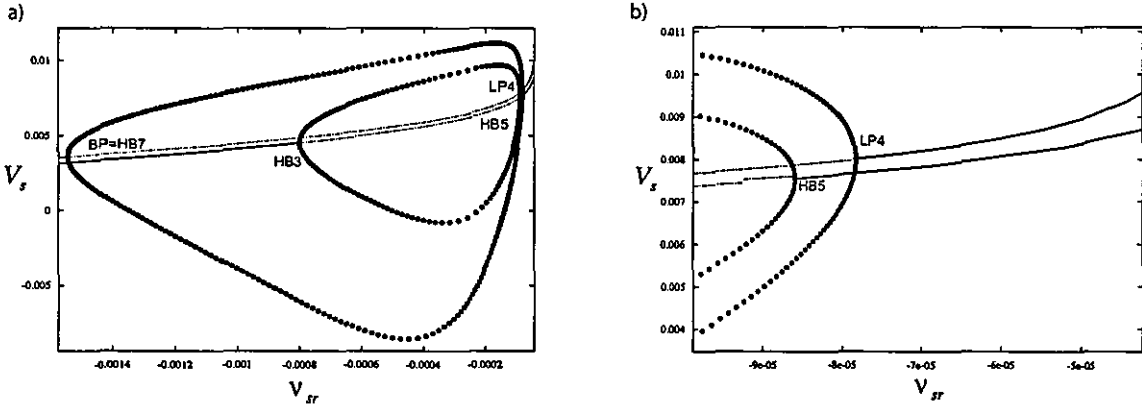


Figure 5.10: The plot shows the bifurcation diagram (V_s, ν_{sr}) at two different levels of the external signal strength, showing the gradual transition from $\nu_{sn} = 0.01707$ to a limit point $LP4$ (here $\nu_{sn} = 0.01955$). XPP allows one to automatically superimpose the two bifurcation allowing easy comparison. The figure on the right is a zoom in of the diagram on the left. As ν_{sn} increases there is a shift of the Hopf point $HB5$ to the right and a shift to the left of the Hopf point $HB3$, thus the domain of ν_{sr} where the periodic orbits exist augments. A further increase of ν_{sr} will destroy the $HB7$ (which is a branch point). A complement for the analysis of this figure is the next illustration (5.11). The actual values for the marked points can be obtained from table C.2.

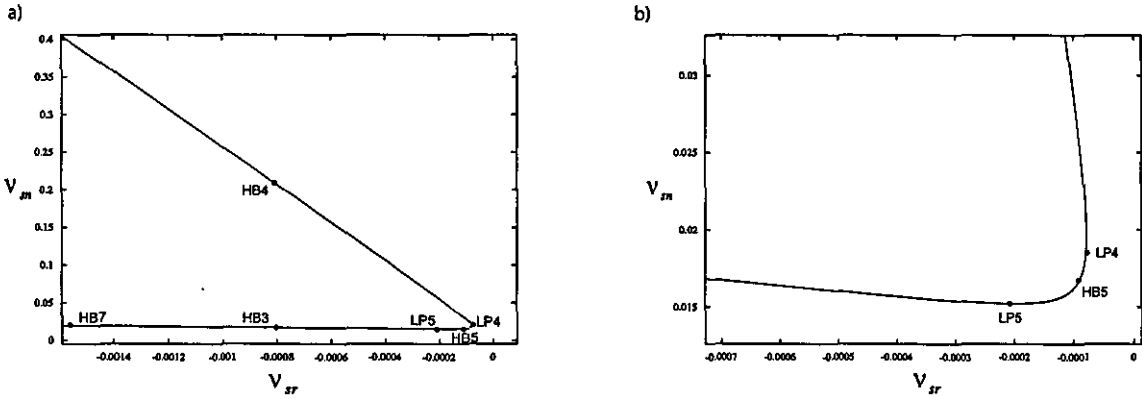


Figure 5.11: Both illustrations show a two parameter continuation of supercritical Hopf bifurcations in the (ν_{sr}, ν_{sn}) parameter space. The figure on the right is a zoom in of the diagram on the left. Surprisingly XPP detects at least two fold points in the (ν_{sr}, ν_{sn}) parameter space indicating that the curve is not parabolic, perhaps being only locally parabolic at the limit points $LP4$ and $LP5$. The concrete values for the indicated points can be obtained from Table C.2.

5.2 Summary

In this chapter, the dynamics of a RKII set are considered, with particular emphasis on the existence and local stability of limit cycle oscillations. Analytical stability conditions on the parameter space for the loss of stability of the RKII set is determined. Further, numerical analysis is carried out by employing the software package XPPAuto to numerically find the bifurcation set for both an autonomous and non-autonomous RKII set. The analysis performed in this chapter determined the appropriate parameter sets where the system is stable and where control of stimulus (in the non autonomous case) can be applied to control these oscillations. The results of this chapter are important in that it provides a foundation to understanding the coupled RKII set. A rigorous understanding of the dynamics and transitions is crucial to understanding patterns observed in RKII sets and coupled RKII models. The following chapter is a further step in this direction is taken by considering normal forms and using a recent formalism, *Global Analysis of Piecewise Linear Systems* [28].

Chapter 6

Normal forms and Global stability analysis of reduced model (RKII set)

The purpose of this chapter is to consider analytically the unfolding of bifurcations in a RKII set using normal forms to give sufficient conditions for the existence of limit cycles and to subsequently study global stability of these oscillations. To understand global properties of the limit cycles in a RKII set, a piece-wise linear reduction of the system is considered and global stability is proved for a restricted region of the parameter space. To achieve this a recent formalism termed, Global Analysis of Piecewise Linear Systems [28] is used. The formalism is applicable to piecewise linear systems (PLS) which are characterised by a finite set of linear dynamical models together with a set of rules determining switching between each model. The main idea consists of inferring global properties of a PLS solely by studying its behaviour at the switching surfaces which are determined by these rules. This is made possible by the study of impact maps, i.e. functions that map one switching surface to another. It is then possible to prove global stability by constructing quadratic Lyapunov functions on the switching surfaces. In general, impact maps are highly nonlinear, multi-valued, and discontinuous which makes it difficult to obtain analytical results. However, impact maps induced by Linear Time Invariant (LTI) systems between two switching surfaces can be represented as a linear transformation analytically parameterised by a scalar function of the present state. This representation permits the analysis of quadratic surface Lyapunov functions (SuLF) to be achieved by solving a set of Linear Matrix Inequalities (LMI) [122]. From this, global properties of the dynamical

system such as existence and stability of limit cycles can be inferred.

6.1 Normal form calculation for an RKII set

In Chapter 5, the linearised flow of the RKII model was investigated and necessary conditions for local stability were identified. In this situation varying the control parameters of the model will not change the structural stability of the system. However, from numerical simulations it is found that for some parameter regimes the RKII set produce limit cycles, i.e. a structural change in the flow. In this case the implicit function Theorem (2.1.4) shows that a solution cannot be continued smoothly because the Jacobian of the system becomes singular. In particular, according to the Hopf bifurcation Theorem (2.1.6) the instability emerges because two conjugate eigenvalues cross the imaginary axis which gives rise to dynamics in the centre space. To unfold the dynamics in the centre space the centre manifold Theorem (2.1.2) and the centre manifold reduction is used. The results of the previous chapter are extended by calculating the centre manifold of this system. Furthermore, through linear stability analysis only necessary conditions for the appearance of a supercritical Hopf bifurcation were made possible. However, according to the Hopf bifurcation Theorem (2.1.6), it is also necessary to demonstrate that the *curvature coefficient* is nonzero, which provides a sufficient condition for the Hopf bifurcation to occur. The sign of this coefficient determines the local stability and if positive (negative) indicates it is a supercritical (subcritical) bifurcation. In general, the expansion of the curvature coefficient becomes complicated for high dimensional systems. Alternatively, calculation of normal forms allows one to study the vector field locally in some neighbourhood. This is achieved through an iterative procedure, either simplifying or identifying the nonlinear terms from the Taylor approximation of the vector field that corresponds to the observed dynamics. From this method the minimal set of equations describing the flow is determined and indirectly provides the specific coefficients for the Hopf bifurcation. Once this set of equations has been determined then, for example, an option is to consider the coupling of the reduced nonlinear equations and look for dynamical features observed in the full system of coupled RKII sets (i.e. without normal forms). The calculations follow the methodology of Iooss and Adelemyer which is detailed in section (2.1.6).

6.1.1 Notation

The k^{th} order multivariate Taylor series expansion for $P \in C^k(\mathbb{R}^n \times \mathbb{R}^m; \mathbb{R}^n)$ may be represented concisely using the following formula:

$$P(z, \nu) = \sum_{\substack{\psi \in \Gamma^n \\ \chi \in \Lambda^m}} P_{|\psi|}^{|\chi|} [z^\psi, \nu^\chi] + \mathcal{O}(|z|^{|\psi|} + |\nu|^{|\chi|}), \quad (6.1)$$

where $z \in \mathbb{R}^n$, and $\nu \in \mathbb{R}^m$ is the set of parameters. The multi-index sets are defined by

$$\begin{aligned} \Gamma^n &= \{(\psi_1, \psi_2, \dots, \psi_n) | \psi_i \in \{0, 1, 2, \dots\}\}, \\ \Lambda^m &= \{(\chi_1, \chi_2, \dots, \chi_m) | \chi_i \in \{0, 1, 2, \dots\}\}, \end{aligned} \quad (6.2)$$

where the order of the polynomial is defined by the order of the multi-index $|\psi| = \psi_1 + \psi_2 + \dots + \psi_n$ and $|\chi| = \chi_1 + \chi_2 + \dots + \chi_m = k$. $P_{|\psi|}^{|\chi|} [z^\psi, \nu^\chi]$ is a $|\psi|$ -linear map on z and $|\chi|$ -linear map on the parameters, where $z^\psi = z_1^{\psi_1} \dots z_n^{\psi_n}$ and $\nu^\chi = \nu_1^{\chi_1} \dots \nu_m^{\chi_m}$. In coordinates, the i -th component is defined as follows

$$(P_{|\psi|}^{|\chi|} (z^\psi, \nu^\chi))_i = \sum_{|\psi|+|\chi|=k} (p_\psi^\chi z^\psi \nu^\chi)_i \quad (6.3)$$

where p_ψ^χ represents the polynomial coefficients expressed by

$$p_\psi^\chi = \frac{1}{(\psi_1! \dots \psi_n!)(\chi_1! \dots \chi_m!)} \left[\left(\frac{\partial}{\partial z_1} \right)^{\psi_1} \dots \left(\frac{\partial}{\partial z_n} \right)^{\psi_n} \left(\frac{\partial}{\partial \nu_1} \right)^{\chi_1} \dots \left(\frac{\partial}{\partial \nu_m} \right)^{\chi_m} \right]_{|(x,\nu)=(0,0)}$$

The above representations give a clearer illustration of the k -linear map property of the Taylor expansion, which provides a more abstract means for using the Taylor expansion to derive the normal forms.

6.1.2 Setup and Statement

Consider the RKII model (5.1) which has the following form:

$$\dot{x} = F(x, \nu) \quad x \in \mathbb{R}^4, \nu \in \mathbb{R}^2, \quad (6.4)$$

where $x = (V_s, w, V_r, v)$. $\nu = (\nu_{sr}, \nu_{rs})$ are the only parameters allowed to vary and the vector field $F \in C^k(\mathbb{R}^4, \mathbb{R}^2)$ for sufficiently large k . To simplify the complexity of the calculation,

we may rewrite system (5.1) by first considering a linear change of variables that shifts the Hopf bifurcation, say (x^*, ν^*) , to zero and then expand the vector field around $(\hat{x}, \hat{\nu}) = (0, 0)$. Setting the linear change of variables to $\hat{x} = x - x^*$ and $\hat{\nu} = \nu - \nu^*$ and substituting these appropriately into equations (5.1) we obtain the following:

$$\dot{\hat{x}} = F(\hat{x}, \hat{\nu}), \quad (6.5)$$

where $F(0, 0) = 0$. Further expanding the vector field with respect to \hat{x} gives:

$$\dot{\hat{x}} = J(\hat{x}) + N(\hat{x}), \quad N = \mathcal{O}(|\hat{x}|(\hat{x}, \hat{\nu})), \quad (6.6)$$

where J is the Jacobian (5.2) and N denotes the nonlinear terms. Specifically for a Hopf bifurcation the Taylor expansion should have terms that depend both linearly on the coordinates and also on the control parameters, resulting in the following:

$$N_1^{1,0}(\hat{x}) = \begin{pmatrix} 0 \\ \alpha\beta \frac{\partial \varsigma[V_r^*]}{\partial \hat{V}_r} \hat{\nu}_{sr} \hat{V}_r \\ 0 \\ 0 \end{pmatrix}, \quad N_1^{0,1}(\hat{x}) = \begin{pmatrix} 0 \\ 0 \\ 0 \\ \alpha\beta \frac{\partial \varsigma[V_s^*]}{\partial \hat{V}_s} \hat{V}_s \hat{\nu}_{rs} \end{pmatrix}.$$

The subscript (1) indicates derivative with respect to \hat{x} and the superscript (1,0) and (0,1) denotes derivative with respect to $\hat{\nu}_{sr}$ and $\hat{\nu}_{rs}$ respectively. Equally, the expansion of N should have terms that are cubic in the coordinate space, but independent of the parameters. Thus we have the subsequent expansions

$$N_2^0(\hat{x}_1, \hat{x}_2) = \frac{1}{2!} \begin{pmatrix} 0 \\ \alpha\beta \hat{\nu}_{sr}^* \frac{\partial^2 \varsigma[V_r^*]}{\partial \hat{V}_r^2} \widehat{V_{r,1} V_{r,2}} \\ 0 \\ \alpha\beta \hat{\nu}_{rs}^* \frac{\partial^2 \varsigma[V_s^*]}{\partial \hat{V}_s^2} \widehat{V_{s,1} V_{s,2}} \end{pmatrix}, \quad N_3^0(\hat{x}_1, \hat{x}_2, \hat{x}_3) = \frac{1}{3!} \begin{pmatrix} 0 \\ \alpha\beta \hat{\nu}_{sr}^* \frac{\partial^3 \varsigma[V_r^*]}{\partial \hat{V}_r^3} \widehat{V_{r,1} V_{r,2} V_{r,3}} \\ 0 \\ \alpha\beta \hat{\nu}_{rs}^* \frac{\partial^3 \varsigma[V_s^*]}{\partial \hat{V}_s^3} \widehat{V_{s,1} V_{s,2} V_{s,3}} \end{pmatrix},$$

where N_3^0 is the third order expansion with respect to \hat{x} and the superscript zero indicates no dependence on the parameters $\hat{\nu}$. The computation of the coefficients of the cubic terms N_0^3 depends indirectly on the quadratic coefficients N_0^2 shown above. The eigenvalues of J and the stability curves in the parameters space are as presented Chapter 5. At a Hopf bifurcation the stability curve given by equation (5.5) becomes an equality and substituting this into equation (5.4) we can determine the following four eigenvalues:

$$\begin{cases} \lambda_{1,2} = \pm i\sqrt{\alpha\beta} \\ \lambda_{3,4} = -(\alpha + \beta) \pm i\sqrt{\alpha\beta} \end{cases}, \quad (6.7)$$

and the associated eigenvectors can be evaluated for one of the conjugate pairs, giving:

$$E_{i\sqrt{\alpha\beta}} = \left\{ \begin{bmatrix} \frac{-\nu_{sr}^* \frac{\partial \varsigma[V_r^*]}{\partial V_r}}{(\alpha+\beta)} \hat{v} \\ \frac{-\nu_{sr}^* \frac{\partial \varsigma[V_r^*]}{\partial V_r} i\sqrt{\alpha\beta}}{(\alpha+\beta)} \hat{v} \\ \frac{-i\sqrt{\alpha\beta}}{\alpha\beta} \hat{v} \\ \hat{v} \end{bmatrix} : \hat{v} \in \mathbb{C} \right\} = \text{Span} \left\{ \begin{bmatrix} -\nu_{sr}^* \frac{\partial \varsigma[V_r^*]}{\partial V_r} \alpha\beta \\ -\nu_{sr}^* \frac{\partial \varsigma[V_r^*]}{\partial V_r} i\sqrt{\alpha\beta} \alpha\beta \\ -i\sqrt{\alpha\beta}(\alpha+\beta) \\ (\alpha+\beta)\alpha\beta \end{bmatrix} \right\} \quad (6.8)$$

$$E_{-(\alpha+\beta)+i\sqrt{\alpha\beta}} = \left\{ \begin{bmatrix} \frac{\nu_{sr}^* \frac{\partial \varsigma[V_r^*]}{\partial V_r} (1-i(\alpha+\beta)\sqrt{\alpha\beta})}{(\alpha+\beta)((\alpha+\beta)^2+\alpha\beta)} \hat{v} \\ \frac{i\sqrt{\alpha\beta}\nu_{sr}^* \frac{\partial \varsigma[V_r^*]}{\partial V_r}}{(\alpha+\beta)} \hat{v} \\ \frac{-(\alpha+\beta)-i\sqrt{\alpha\beta}}{(\alpha+\beta)^2+\alpha\beta} \hat{v} \\ \hat{v} \end{bmatrix} : \hat{v} \in \mathbb{C} \right\} = \text{Span} \left\{ \begin{bmatrix} \nu_{sr}^* \frac{\partial \varsigma[V_r^*]}{\partial V_r} (1-i(\alpha+\beta)\sqrt{\alpha\beta}) \\ i\sqrt{\alpha\beta}\nu_{sr}^* \frac{\partial \varsigma[V_r^*]}{\partial V_r} ((\alpha+\beta)^2+\alpha\beta) \\ -((\alpha+\beta)+i\sqrt{\alpha\beta})(\alpha+\beta) \\ (\alpha+\beta)((\alpha+\beta)^2+\alpha\beta) \end{bmatrix} \right\} \quad (6.9)$$

The linearly invariant centre space is spanned by $E_{i\sqrt{\alpha\beta}}$ and its corresponding conjugate eigenvector (i.e a two dimensional manifold), which is denoted by $E_0 = \text{span}\{e_0, \bar{e}_0\}$ and the linearly invariant hyperbolic space spanned by the remaining two eigenvectors, we denote by $E_h = \text{span}\{e_h, \bar{e}_h\}$. Note also that $\mathbb{R}^4 = E_h \oplus E_0$. According to the centre manifold and normal form arguments [78] (section (2.1.6)), there exists a neighbourhood $I \in \mathbb{R}^2$ around 0 and a neighbourhood $U \in \mathbb{R}^4$ around 0 and a smooth map $h \in C^k(E_0 \times \mathbb{R}^2; E_h)$ with the following properties:

1. $h(0,0) = 0$ and $D_z h(0,0) = 0$, for $z \in E_0$.
2. For $\hat{v} \in I$, the manifolds $M_0(\hat{v}) = \{(z, h(z, \hat{v})) | z \in E_0\}$ are locally invariant to system (6.5) and contain all solutions of the RKII set near to $\hat{x} = 0$, $\forall t \in \mathbb{R}$ and the map satisfies $D_z h(z, \hat{v}) \dot{z} = \dot{y}$, where $z \in E_0$ and $y \in E_h$.
3. According to the normal form theory [78](section (2.1.6)) it is possible to determine a polynomial $G \in C^k(E_0 \times \mathbb{R}^2; E_h)$, with $G(0,0) = 0$, $D_z G(0,0) = 0$ such that by a near identity coordinate transformation $\hat{x} = z + h(z, \hat{v})$, $z \in E_0$ the system (6.6) may be normalized to:

$$\dot{z} = Jz + G(z, \hat{v}), \quad G = \mathcal{O}(|z||(\hat{v})|). \quad (6.10)$$

In this particular instance, using the assumption that the flow on the centre manifold is locally periodic, the presence of the Hopf bifurcation implies that equation (6.10) has a known form. In particular the Jacobian of system (5.1) on the centre manifold has simple eigenvalues $\pm i\sqrt{\alpha\beta}$. Using complex notation the centre manifold can be expressed in the following way:

$$E_0 = \{z = Ze_0 + \bar{Z}\bar{e}_0 \mid Z \in \mathbb{C}\}. \quad (6.11)$$

Here Z and \bar{Z} are the coordinates on the manifold and it follows that the normalized flow is given by:

$$\begin{cases} \dot{Z} = i\sqrt{\alpha\beta}Z + ZQ(|Z|^2, \hat{\nu}_{sr}, \hat{\nu}_{rs}) + \mathcal{O}(|Z|^{2k+3}) \\ \dot{\bar{Z}} = -i\sqrt{\alpha\beta}\bar{Z} + \bar{Z}\bar{Q}(|Z|^2, \hat{\nu}_{sr}, \hat{\nu}_{rs}) + \mathcal{O}(|Z|^{2k+3}) \end{cases}, \quad (6.12)$$

where $Q(|Z|^2, \hat{\nu}_{sr}, \hat{\nu}_{rs})$ is a complex polynomial of degree k in $|Z|^2$ with $Q(0, 0) = 0$ that depends smoothly on the control parameters $(\hat{\nu}_{sr}, \hat{\nu}_{rs})$. In particular, expanding $ZQ(|Z|^2, \hat{\nu}_{sr}, \hat{\nu}_{rs})$ using (6.1) gives:

$$ZQ(|Z|^2, \hat{\nu}_{sr}, \hat{\nu}_{rs}) = g_{1,0}^{1,0}\hat{\nu}_{sr}Z + g_{1,0}^{0,1}\hat{\nu}_{rs}Z + \dots + g_{2,1}^0Z^2\bar{Z} + \dots + g_{2,1}^{1,0}\hat{\nu}_{sr}Z^2\bar{Z} + \dots, \quad (6.13)$$

where the coefficients $g_{1,0}^{1,0} \neq 0$, $g_{1,0}^{0,1} \neq 0$ and $g_{2,1}^0 \neq 0$ are to be determined. Polar coordinates are used to simplify the equations:

$$Z = re^{i\phi}, \quad r \in \mathbb{R}^+, \quad \phi \in \mathbb{R}/2\pi\mathbb{Z}.$$

Substitution into equation (6.12) results in the following

$$\begin{cases} e^{i\phi}\frac{dr}{dt} + ire^{i\phi}\frac{d\phi}{dt} = i\sqrt{\alpha\beta}re^{i\phi} + g_{1,0}^{1,0}\hat{\nu}_{sr}re^{i\phi} + g_{1,0}^{0,1}\hat{\nu}_{rs}re^{i\phi} + g_{2,1}^0r^3e^{i\phi} + h.o.t., \\ e^{i\phi}\frac{dr}{dt} - ire^{i\phi}\frac{d\phi}{dt} = i\sqrt{\alpha\beta}re^{i\phi} + g_{0,1}^{1,0}\hat{\nu}_{sr}re^{i\phi} + g_{0,1}^{0,1}\hat{\nu}_{rs}re^{i\phi} + g_{1,2}^0r^3e^{i\phi} + h.o.t. \end{cases} \quad (6.14)$$

Proving persistence of periodic solutions is beyond the scope of this work and hence higher order terms are ignored. Solving the above equations (6.14) with respect for $\frac{dr}{dt}$ and $\frac{d\phi}{dt}$ we get:

$$\begin{cases} \frac{dr}{dt} = \frac{g_{1,0}^{1,0} + g_{0,1}^{1,0}}{2}\hat{\nu}_{sr}r + \frac{g_{1,0}^{0,1} + g_{0,1}^{0,1}}{2}\hat{\nu}_{rs}r + \frac{g_{2,1}^0 + g_{1,2}^0}{2}r^3 \\ \frac{d\phi}{dt} = \sqrt{\alpha\beta} + \frac{g_{1,0}^{1,0} - g_{0,1}^{1,0}}{2i}\hat{\nu}_{sr}r + \frac{g_{1,0}^{0,1} - g_{0,1}^{0,1}}{2i}\hat{\nu}_{rs}r + \frac{g_{2,1}^0 - g_{1,2}^0}{2i}r^2 \end{cases} \quad (6.15)$$

Introduce the following constants $c_{10}^r = \frac{g_{1,0}^{1,0} + g_{0,1}^{1,0}}{2} \Leftrightarrow \text{Re}(g_{1,0}^{0,1})$, $c_{10}^i = \frac{g_{1,0}^{0,1} - g_{0,1}^{0,1}}{2i} \Leftrightarrow \text{Im}(g_{1,0}^{0,1})$, $c_{01}^r = \text{Re}(g_{1,0}^{0,1})$, $c_{01}^i = \text{Im}(g_{1,0}^{0,1})$, $c_{12}^r = \text{Re}(g_{1,2}^0)$ and $c_{12}^i = \text{Im}(g_{1,2}^0)$. Since the above equations (6.15) are now decoupled we can first solve for r and by quadrature solve for ϕ . Furthermore, in equation (6.15), $\frac{dr}{dt}$ defines the normal form for either the supercritical (subcritical) pitchfork

bifurcation dependent on whether the sign of c_{12}^r is positive (negative) respectively and the equilibrium points are given by:

$$r^* = \pm \sqrt{\frac{\hat{\nu}_{sr}c_{10}^r + \hat{\nu}_{rs}c_{01}^r}{c_{12}^r}}, \quad r^* = 0 \quad (6.16)$$

Of particular interest are the non-trivial, stable states. These are satisfied for small $(\hat{\nu}_{sr}, \hat{\nu}_{rs})$ parameters, provided $\frac{\hat{\nu}_{sr}c_{10}^r + \hat{\nu}_{rs}c_{01}^r}{c_{12}^r} > 0$ which implies that the vector field admits in a small neighbourhood about $0 \in \mathbb{R}^2$ a unique periodic orbit with radius r^* . Substituting r^* into $\frac{d\phi}{dt}$ a stable solution ϕ^* is obtained which describes the phase of the orbit and consequently the solution is locally a periodic limit cycle defined by $Z = r^*e^{i\phi^*t}$ with period $T = \frac{2\pi}{\sqrt{\alpha\beta}}$.

The next section provides the computation of the normal forms obtained by applying the methodology of Iooss and Adelmeyer [78](section (2.1.6)). The main idea of the method is the so called the homological equation which incorporates the nonlinear term $N(\hat{x}, \hat{\nu})$ of equation (6.6) and assumes that the higher order terms $G(z, \hat{\nu})$ of (6.10) and the centre manifold reduction function $h(z, \hat{\nu})$ have a known structure. These assumptions reduce the number of steps to compute the normal form coefficients.

6.1.3 Computation of the normal form

The derivation of the homological equation is given in section (D.1). From the operator, we can determine the coefficients of the Taylor expansion of the reduction function $h \in C^k(E_0 \times \mathbb{R}^2; E_h)$ and the coefficients of the polynomial $G \in C^k(E_0 \times \mathbb{R}^2; E_h)$ can be determined. Define the operator as follows:

$$Jh(z, \hat{\nu}) - D_z[h(z, \hat{\nu})](Jz) = G(z, \hat{\nu}) - N(z + h(z, \hat{\nu}), \hat{\nu}) + D_z[h(z, \hat{\nu})](G(z, \hat{\nu})), \quad (6.17)$$

where the Ansatz is given by

$$\begin{cases} h(z, \hat{\nu}) = \sum_{\substack{\psi \in \Gamma^n \\ |\psi| > 2 \\ \chi \in \Lambda^m}} h_{\psi}^{\chi}[z^{\psi}, \hat{\nu}^{\chi}] = h_{|\psi|=2}^{\chi} z^{\psi} \hat{\nu}^{\chi} + h_{|\psi|=3}^{\chi} z^{\psi} \hat{\nu}^{\chi} + \dots, \text{ with } h = \mathcal{O}(|z|(|z, \hat{\nu}|)), \\ G(z, \hat{\nu}) = \sum_{\substack{\psi \in \Gamma^n \\ |\psi|=2n+1 \\ n \in \mathbb{N} \\ \chi \in \Lambda^m \\ (|\psi|, |\chi|) \neq (1, 0)}} G_{\psi}^{\chi}[z^{\psi}, \hat{\nu}^{\chi}] = g_{|\psi|=1}^{\chi} z^{\psi} \hat{\nu}^{\chi} + g_{|\psi|=3}^{\chi} z^{\psi} \hat{\nu}^{\chi} + \dots, \text{ with } G = \mathcal{O}(|z|(|z|^2, \hat{\nu}|)), \\ N(\hat{x}, \hat{\nu}) = \sum_{\substack{\psi \in \Gamma^n \\ |\psi| > 2 \\ \chi \in \Lambda^m}} N_{\psi}^{\chi}[\hat{x}^{\psi}, \hat{\nu}^{\chi}] = N_{|\psi|=2}^{\chi} \hat{x}^{\psi} \hat{\nu}^{\chi} + N_{|\psi|=3}^{\chi} \hat{x}^{\psi} \hat{\nu}^{\chi} + \dots, \text{ with } N = \mathcal{O}(|\hat{x}|(|\hat{x}, \hat{\nu}|)). \end{cases} \quad (6.18)$$

First identifying terms in equation (6.18) of the same order in both coordinates and control parameters are identified, i.e. $(\hat{z}, \hat{\nu})$, and replaced in the homological equation (6.17). For terms that are linear in z and linear in the control parameters, that is, $\mathcal{O}(z\hat{\nu})$ the following first order homological operator is obtained:

$$Jh_1^1(z, \hat{\nu}) - D_z[h_1^1(z, \hat{\nu})](Jz) = G_1^1(z, \hat{\nu}) - N_1^1(z\hat{\nu}). \quad (6.19)$$

Expanding and evaluating the individual terms in equation (6.19) and then grouping those of the same order (details in section D.2) gives rise to the following four equations:

$$\begin{cases} (J - i\sqrt{\alpha\beta}I)h_{1,0}^{1,0} = g_{1,0}^{1,0}e_0 - N_1^{1,0}(e_0), \\ (J - i\sqrt{\alpha\beta}I)h_{1,0}^{0,1} = g_{1,0}^{0,1}e_0 - N_1^{0,1}(e_0), \\ g_{0,1}^{1,0} = \overline{g_{1,0}^{1,0}}, \\ g_{1,0}^{0,1} = \overline{g_{0,1}^{0,1}}. \end{cases} \quad (6.20)$$

In equation (6.20) the constants $g_{1,0}^{1,0}$ and $g_{1,0}^{0,1}$ must be obtained. These are the first order coefficients of the normal form. However, the operator $(J - i\sqrt{\alpha\beta}I)$ is not invertible. Hence, for a solution $h_{1,0}^{1,0}$ or $h_{1,0}^{0,1}$ to exist, the right-hand side must belong to $\text{Range}(J - i\sqrt{\alpha\beta}I)$. However, $\text{Range}(J - i\sqrt{\alpha\beta}I) = \text{Ker}(J^* + i\sqrt{\alpha\beta}I)^\perp$, where J^* is the adjoint operator of J . Hence, equation (6.20) has a solution if the inner product of the right hand side with $\overline{f_0}$ is zero, where $\overline{f_0}$ is the adjoint dual base of e_0 and with the following form

$$\overline{f_0} = \begin{pmatrix} \frac{-\alpha\beta\nu_{rs}^* \frac{\partial \zeta[V_s^*]}{\partial V_s} ((\alpha+\beta)^2 + \alpha\beta)}{-\alpha\beta(\alpha+\beta) + i\sqrt{\alpha\beta}(\alpha+\beta)^2} \\ \frac{\nu_{rs}^* \frac{\partial \zeta[V_s^*]}{\partial V_s} (\alpha\beta - i\sqrt{\alpha\beta}(\alpha+\beta))}{-((\alpha+\beta)^2 + i\sqrt{\alpha\beta}(\alpha+\beta))} \\ -i\sqrt{\alpha\beta} \\ 1 \end{pmatrix}. \quad (6.21)$$

Thus to obtain the coefficients $g_{1,0}^{1,0}$ and $g_{1,0}^{0,1}$ project every term of equation (6.20) onto the space $\text{Ker}(J^* + i\sqrt{\alpha\beta}I)^\perp$, which corresponds to applying the following procedure:

$$\begin{cases} \langle (J - i\sqrt{\alpha\beta}I)h_{1,0}^{1,0}, \overline{f_0} \rangle = g_{1,0}^{1,0} \langle e_0, \overline{f_0} \rangle - \langle N_1^{1,0}(e_0), \overline{f_0} \rangle \\ \langle (J - i\sqrt{\alpha\beta}I)h_{1,0}^{0,1}, \overline{f_0} \rangle = g_{1,0}^{0,1} \langle e_0, \overline{f_0} \rangle - \langle N_1^{0,1}(e_0), \overline{f_0} \rangle \end{cases} \quad (6.22)$$

where $\langle \cdot, \cdot \rangle$ denotes the inner product of two vectors. Given that for any any vectors $a, b \in \mathbb{C}$ then $\langle Ja, b \rangle = \langle a, J^*b \rangle$ and $\langle \lambda a, b \rangle = \langle a, \bar{\lambda}b \rangle$ (where J is the linear operator, J^* the adjoint operator and λ an eigenvalue), then the left hand side of equation (6.22) equates

to $\langle h_{1,0}^{1,0}, (J^* + i\sqrt{\alpha\beta}I)\bar{f}_0 \rangle = 0$ and $\langle h_{1,0}^{0,1}, (J^* + i\sqrt{\alpha\beta}I)\bar{f}_0 \rangle = 0$. Hence:

$$\begin{aligned} g_{1,0}^{1,0} &= \frac{\langle N_1^{1,0}(e_0), \bar{f}_0 \rangle}{\langle e_0, \bar{f}_0 \rangle} \\ &\Leftrightarrow -\frac{(\alpha\beta)^2 \nu_{rs}^* \frac{\partial \varsigma[V_s^*]}{\partial \bar{V}_s} \frac{\partial \varsigma[V_r^*]}{\partial \bar{V}_r}}{4\alpha\beta(\alpha + \beta) + i\sqrt{\alpha\beta}(\alpha + \beta)^2} \hat{\nu}_{sr}, \end{aligned} \quad (6.23)$$

and for the other coefficient:

$$\begin{aligned} g_{1,0}^{0,1} &= \frac{\langle N_1^{0,1}(e_0), \bar{f}_0 \rangle}{\langle e_0, \bar{f}_0 \rangle} \\ &\Leftrightarrow -\frac{(\alpha\beta)^2 \nu_{sr}^* \frac{\partial \varsigma[V_s^*]}{\partial \bar{V}_s} \frac{\partial \varsigma[V_r^*]}{\partial \bar{V}_r}}{4\alpha\beta(\alpha + \beta) + i\sqrt{\alpha\beta}(\alpha + \beta)^2} \hat{\nu}_{rs}. \end{aligned} \quad (6.24)$$

Only the real parts need to be considered, which corresponds to a negative value in both cases. To evaluate higher order terms of the normal form, in this case the cubic terms, first it is necessary to resolve terms that are quadratic in the coordinates of the centre space and that have no dependence on the parameters ν , (i.e. $\mathcal{O}(Z^2)$). The reasoning becomes clearer as the calculations progress.

By reducing the homological operator to quadratic terms the following is obtained:

$$Jh_2^0(z) - D_z[h_2^0(z)](Jz) = -N_2^0(z, z). \quad (6.25)$$

From equation (6.25) the following coefficients are determined (for details of this calculation refer to section (D.3)):

$$\begin{cases} h_{2,0}^0 = -(J - 2i\sqrt{\alpha\beta})^{-1} N_2(e_0, e_0), \\ h_{1,1}^0 = -J^{-1} N_2(e_0, \bar{e}_0), \\ h_{0,2}^0 = \overline{h_{2,0}^0}, \end{cases} \quad (6.26)$$

thus,

$$h_{2,0}^0 = \frac{-(\alpha\beta)^2 \nu_{sr}}{2! \det(J - 2i\sqrt{\alpha\beta})} H, \quad (6.27)$$

where

$$H = \begin{pmatrix} (-3\alpha\beta + 2i\sqrt{\alpha\beta}(\alpha + \beta))[-(\alpha + \beta)^2 \frac{\partial^2 \varsigma[V_r^*]}{\partial \bar{V}_r^2}] + (\alpha\beta)^2 (\nu_{sr}^*)^2 \nu_{rs}^* \frac{\partial^2 \varsigma[V_s^*]}{\partial \bar{V}_s^2} \left(\frac{\partial \varsigma[V_r^*]}{\partial \bar{V}_r} \right)^3 \\ (\alpha\beta)(\alpha + \beta)^2 \frac{\partial^2 \varsigma[V_r^*]}{\partial \bar{V}_r^2} [4(\alpha + \beta) + 6i\sqrt{\alpha\beta}] + 2i\sqrt{\alpha\beta}(\alpha\beta)^2 (\nu_{sr}^*)^2 \nu_{rs}^* \frac{\partial^2 \varsigma[V_s^*]}{\partial \bar{V}_s^2} \left(\frac{\partial \varsigma[V_r^*]}{\partial \bar{V}_r} \right)^3 \\ -\alpha\beta(\alpha + \beta)^2 \nu_{rs}^* \frac{\partial \varsigma[V_s^*]}{\partial \bar{V}_s} \frac{\partial^2 \varsigma[V_r^*]}{\partial \bar{V}_r^2} + \alpha\beta \nu_{rs}^* \nu_{sr}^* \frac{\partial^2 \varsigma[V_s^*]}{\partial \bar{V}_s^2} \left(\frac{\partial \varsigma[V_r^*]}{\partial \bar{V}_r} \right)^2 [-3\alpha\beta + 2i\sqrt{\alpha\beta}(\alpha + \beta)] \\ -2i\sqrt{\alpha\beta}(\alpha\beta)(\alpha + \beta)^2 \nu_{rs}^* \frac{\partial \varsigma[V_s^*]}{\partial \bar{V}_s} \frac{\partial^2 \varsigma[V_r^*]}{\partial \bar{V}_r^2} - 2(\alpha\beta)^2 \nu_{rs}^* \nu_{sr}^* \frac{\partial^2 \varsigma[V_s^*]}{\partial \bar{V}_s^2} \left(\frac{\partial \varsigma[V_r^*]}{\partial \bar{V}_r} \right)^2 [2(\alpha + \beta) + 3i\sqrt{\alpha\beta}] \end{pmatrix},$$

and $\det(J - 2i\sqrt{\alpha\beta}) = 3\alpha\beta((\alpha^2 + \beta^2) + \alpha\beta) + 4i\sqrt{\alpha\beta}(\alpha + \beta)$. For the other coefficient:

$$h_{1,1}^0 = \frac{(\alpha\beta)^2 \nu_{sr}^*}{2![(\alpha + \beta)^2 + \alpha\beta]} \begin{pmatrix} (\alpha + \beta)^2 \frac{\partial^2 \varsigma[V_r^*]}{\partial \bar{V}_r^2} + (\alpha\beta) \frac{\partial^2 \varsigma[V_r^*]}{\partial \bar{V}_s^2} \left(\frac{\partial \varsigma[V_r^*]}{\partial \bar{V}_r} \right)^3 \nu_{rs}^* (\nu_{sr}^*)^2 & 0 \\ \nu_{rs}^* [(\alpha + \beta)^2 \frac{\partial \varsigma[V_s^*]}{\partial \bar{V}_s} \frac{\partial^2 \varsigma[V_r^*]}{\partial \bar{V}_r^2} + (\alpha\beta) \nu_{sr}^* \frac{\partial^2 \varsigma[V_s^*]}{\partial \bar{V}_s^2} \left(\frac{\partial \varsigma[V_r^*]}{\partial \bar{V}_r} \right)^2] & 0 \end{pmatrix}. \quad (6.28)$$

Having evaluated the quadratic coefficients, terms that are cubic in the coordinates of the centre space and that have no dependence on the control parameters are now determined. These are precisely the coefficients for the unfolding of a Hopf bifurcation. Reducing the homological operator to cubic terms gives the following:

$$Jh_3^0(z) - D_z[h_3^0(z)](Jz) = G_3^0 - 2N_2^0(z, h_2^0(z)) - N_3(z, z, z). \quad (6.29)$$

Expanding the individual terms in the homological operator and grouping terms of the following orders $Z^2\bar{Z}$, $Z\bar{Z}^2, Z^3$ and \bar{Z}^3 four equations are obtained (details of the calculations can be found in Section D.3.1). However, for the Hopf bifurcation only those equations that depend on $Z\bar{Z}^2$, $Z^2\bar{Z}$ need to be considered:

$$\begin{cases} (L - i\sqrt{\alpha\beta}I)h_{2,1}^0 = g_{2,1}^{0,0}e_0 - 2N_2^0(\bar{e}_0, h_{2,0}^{0,0}) - 2N_2^0(e_0, h_{1,1}^{0,0}) - 3N_3^0(e_0, e_0, \bar{e}_0) \\ g_{1,2}^{0,0} = \bar{g}_{2,1}^{0,0}. \end{cases} \quad (6.30)$$

From equation (6.30) $g_{1,2}^{0,0}$ and $g_{2,1}^{0,0}$ must be evaluated. Similarly to before, the operator $(J - i\sqrt{\alpha\beta}I)$ is not invertible and the same procedure as performed for the first order terms is used, that is, to apply the inner product to all the terms of equation (6.30) with the adjoint dual base of e_0 , denoted then by \bar{f}_0 . This gives:

$$\begin{aligned} \langle (L - i\sqrt{\alpha\beta}I)h_{2,1}^0, \bar{f}_0 \rangle &= g_{2,1}^{0,0} \langle e_0, \bar{f}_0 \rangle - 2 \langle N_2^0(\bar{e}_0, h_{2,0}^{0,0}), \bar{f}_0 \rangle - 2 \langle N_2^0(e_0, h_{1,1}^{0,0}), \bar{f}_0 \rangle \\ &- 3 \langle N_3^0(e_0, e_0, \bar{e}_0), \bar{f}_0 \rangle. \end{aligned} \quad (6.31)$$

The left hand side of equation (6.31) equates to $\langle (L - i\sqrt{\alpha\beta}I)h_{2,1}^0, \bar{f}_0 \rangle \Leftrightarrow \langle h_{2,1}^0, (J^* + i\sqrt{\alpha\beta}I)\bar{f}_0 \rangle = 0$, thus resulting in the following cubic coefficient for the Hopf bifurcation

$$g_{1,2}^{0,0} = \frac{2 \langle N_2^0(\bar{e}_0, h_{2,0}^{0,0}), \bar{f}_0 \rangle + 2 \langle N_2^0(e_0, h_{1,1}^{0,0}), \bar{f}_0 \rangle + 3 \langle N_3^0(e_0, e_0, \bar{e}_0), \bar{f}_0 \rangle}{\langle e_0, \bar{f}_0 \rangle} \quad (6.32)$$

Once again, only consider the real parts, giving:

$$c_{12}^r = \text{Re}(g_{1,2}^{0,0}) = -\frac{(\alpha\beta)^3 \nu_{sr}^* \nu_{rs}^* (c1 + c2 + c3)}{2!3[(\alpha^2 + \alpha\beta + \beta^2)^2 + 16\alpha\beta(\alpha + \beta)^2][(\alpha + \beta)^2 + \alpha\beta][(\alpha + \beta)^2 + \alpha\beta](\alpha + \beta)},$$

where $c1$ corresponds to

$$\begin{aligned}
c1 = & 2((\alpha + \beta)^2 + \alpha\beta) \left(2(\alpha\beta)^2(\alpha + \beta)^3 \nu_{rs}^* \nu_{sr}^* \left(\frac{\partial^2 \varsigma[V_r^*]}{\partial \widehat{V}_r^2} \right)^2 \left(\frac{\partial \varsigma[V_s^*]}{\partial \widehat{V}_s} \right)^2 \right. \\
& + 6(\nu_{sr}^* - 1)(\alpha\beta)^2(\alpha + \beta)^2 \frac{\partial \varsigma[V_r^*]}{\partial \widehat{V}_r} \frac{\partial^2 \varsigma[V_r^*]}{\partial \widehat{V}_r^2} \frac{\partial^2 \varsigma[V_s^*]}{\partial \widehat{V}_s^2} \\
& + (\alpha\beta)^2(\nu_{sr}^*)^3 \nu_{rs}^* (-6(\alpha\beta)^2 + (\alpha + \beta)^2) \left(\frac{\partial^2 \varsigma[V_s^*]}{\partial \widehat{V}_s^2} \right)^2 \left(\frac{\partial \varsigma[V_r^*]}{\partial \widehat{V}_r} \right)^4 \\
& \left. + \nu_{sr}^* (\alpha + \beta)^4 ((\alpha + \beta)^2 + 15\alpha\beta) \left[\frac{\partial \varsigma[V_r^*]}{\partial \widehat{V}_r} - \frac{\partial \varsigma[V_s^*]}{\partial \widehat{V}_s} \right] \right),
\end{aligned}$$

and the constant $c2$ is given by:

$$\begin{aligned}
c2 = & 12\alpha\beta\nu_{sr}^* [(\alpha^2 + \alpha\beta + \beta^2)^2 + 16\alpha\beta(\alpha + \beta)^2] \left(\nu_{rs}^* \frac{\partial^2 \varsigma[V_r^*]}{\partial \widehat{V}_r^2} \frac{\partial \varsigma[V_s^*]}{\partial \widehat{V}_s} \left[(\alpha + \beta)^2 \frac{\partial \varsigma[V_s^*]}{\partial \widehat{V}_s} \frac{\partial^2 \varsigma[V_r^*]}{\partial \widehat{V}_r^2} \right. \right. \\
& + \alpha\beta\nu_{sr}^* \frac{\partial^2 \varsigma[V_s^*]}{\partial \widehat{V}_s^2} \left(\frac{\partial \varsigma[V_r^*]}{\partial \widehat{V}_r} \right)^2 \left. \right] + \frac{\partial^2 \varsigma[V_s^*]}{\partial \widehat{V}_s^2} \frac{\partial \varsigma[V_r^*]}{\partial \widehat{V}_r} \left[(\alpha + \beta)^2 \frac{\partial^2 \varsigma[V_r^*]}{\partial \widehat{V}_r^2} \right. \\
& \left. \left. + \alpha\beta(\nu_{sr}^*)^2 \nu_{rs}^* \frac{\partial^2 \varsigma[V_s^*]}{\partial \widehat{V}_s^2} \left(\frac{\partial \varsigma[V_r^*]}{\partial \widehat{V}_r} \right)^3 \right] \right).
\end{aligned}$$

Finally the constant $c3$ has the following form:

$$\begin{aligned}
c3 = & 12[(\alpha^2 + \alpha\beta + \beta^2)^2 + 16\alpha\beta(\alpha + \beta)^2]((\alpha + \beta)^2 + \alpha\beta) \left((\alpha + \beta)^2 \frac{\partial^3 \varsigma[V_r^*]}{\partial \widehat{V}_r^3} \frac{\partial \varsigma[V_s^*]}{\partial \widehat{V}_s} \right. \\
& \left. + \alpha\beta(\nu_{sr}^*)^2 \frac{\partial^3 \varsigma[V_s^*]}{\partial \widehat{V}_s^3} \left(\frac{\partial \varsigma[V_r^*]}{\partial \widehat{V}_r} \right)^3 \right).
\end{aligned}$$

Numerically c_{12}^r is observed to be a negative coefficient, however some analytical considerations can be made to determine that this is indeed the case, by first noticing that all parameters are positive except ν_{sr}^* and then comparing term by term. This implies that the system exhibits a supercritical Hopf bifurcation, confirming the numerical results of Chapter 5 Furthermore, the reduction function $h(z)$ is composed of the quadratic coefficients $h_{2,0}^0$, $h_{1,1}^0$ and $h_{0,2}^0$.

6.2 Global analysis of limit cycles in the piecewise linear model

Having used the normal forms to determine analytically local stability results, global stability of limit cycles is now considered. The approach chosen to study global properties of the limit

cycle is developed from *Constructive Global Analysis of Hybrid Systems* [28] (section (2.2)). This theory allows the construction of a piecewise linear approximation of a system and to study analytically both the local and global properties of the dynamics. In particular global stability analysis of limit cycles of PLS can be proven using quadratic stability of Poincaré maps. The procedure consists of first finding suitable switching surfaces and to then express Poincaré maps induced by an LTI (Linear time invariant) flow between two switching surfaces as linear transformations analytically parameterised by a scalar function of the state. The central idea here is to compute quadratic Lyapunov functions for the Poincaré maps where these functions are obtained by solving a set of LMI (linear matrix inequalities). In the following sections results are presented for the model (5.1) under consideration. The model can be reformulated in the form of a LTI system where it is essentially separated into linear and nonlinear terms and re-written in the following form:

$$\begin{cases} \dot{x} = Ax + Bu, \\ y = Cx + Du, \end{cases}$$

where $x = (V_s, w, V_r, v)$. The matrix A contains only linear terms, while B contains the coefficients of the nonlinear and the forcing terms, in the case of model (5.1), u corresponds to the sigmoidal functions. $y = Cx + Du$ denotes the output equation where for this case $D = 0$ (the feed matrix). The matrix A is defined as follows:

$$A = \begin{pmatrix} \tilde{A} & 0 \\ 0 & \tilde{A} \end{pmatrix}, \quad \tilde{A} = \begin{pmatrix} 0 & 1 \\ -\alpha\beta & -(\alpha + \beta) \end{pmatrix}$$

Note that A is invertible and all the eigenvalues lie in the left half plane. The definition of the matrix B and the vector u , and consequently the switching surfaces will depend on the specific form of the piecewise approximation of the nonlinear functions. The first approximation of the saturating function $\varsigma[V_a(t)]$ considered is a Heaviside function. The original saturating function is unipolar (i.e. it assumes only positive values), but for the purpose of this discussion and generality we will neglect this limitation and will assume that it may also attain negative values:

$$u = \Theta(y - \theta) = \begin{cases} a & y \leq \theta, \\ b & \text{otherwise} \end{cases}$$

where we assume that $(a, b, \theta) \in \mathbb{R}$. Since the saturating functions are dependent on the dynamic variables V_s and V_r an approximation for each function is defined independently,

allowing for more general results. Further, two switching surfaces are obtained (one for each function), by allowing the LTI flow from the lower asymptote (a) to the upper asymptote (b) of the Heaviside function. Hence, the complete formulation is as follows:

$$\begin{cases} \dot{x} = Ax + \tilde{B}_0\tilde{u}_0 + \tilde{B}_1\tilde{u}_1 + \tilde{B}_2\tilde{u}_2 \Leftrightarrow Ax + Bu, \\ y = C_0x, \\ y = C_1x, \end{cases}$$

where $C_0 = [0, 0, 1, 0]^T$, $C_1 = [1, 0, 0, 0]^T$ and

$$\tilde{u}_i = \Theta_i(y - \theta_i) = \begin{cases} a_i & y \leq \theta_i, \\ b_i & \text{otherwise} \end{cases}$$

with $i = \{0, 1\}$ and the vector $u = [\tilde{u}_0, \tilde{u}_1, \tilde{u}_2]^T$. Note \tilde{u}_2 is due to the ϕ_n term in system (5.1) and here it assumes the form, $\phi_n = 1$. The matrix B is then defined as:

$$B = \begin{pmatrix} 0 & 0 & 0 \\ \alpha\beta\nu_{sr} & 0 & \alpha\beta\nu_{sn} \\ 0 & 0 & 0 \\ 0 & \alpha\beta\nu_{rs} & 0 \end{pmatrix}.$$

Since A is invertible, the equilibrium of $\dot{x} = Ax + Bu$ can be readily evaluated as $x^* = -A^{-1}Bu$ and has the following form:

$$x^* = \begin{pmatrix} \nu_{sr}\tilde{u}_0 + \nu_{sn}\tilde{u}_2 \\ 0 \\ \nu_{rs}\tilde{u}_1 \\ 0 \end{pmatrix},$$

where

$$A^{-1} = \begin{pmatrix} \hat{A} & 0 \\ 0 & \hat{A} \end{pmatrix}, \quad \hat{A} = \begin{pmatrix} \frac{-(\alpha+\beta)}{\alpha\beta} & \frac{-1}{\alpha\beta} \\ 1 & 0 \end{pmatrix}.$$

A schematic of the reformulated model is depicted in Fig. 6.1.

Furthermore the two switching surfaces (hyperplanes in \mathbb{R}^3) are defined as follows:

$$S_0 = \{x \in \mathbb{R}^4 : C_0x = \theta_0\} \quad \text{and} \quad S_1 = \{x \in \mathbb{R}^4 : C_1x = \theta_1\}.$$

Since there exists two switching surfaces it means that the projection onto the (V_s, V_r) state space is divided into four regions, where the dynamics of each region is governed by a separate

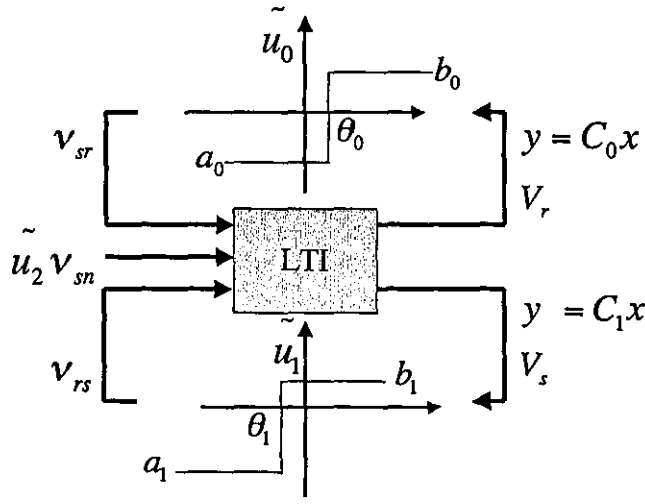


Figure 6.1: The diagram shows the piecewise approximations applied to the original model. The nonlinear terms are approximated and are seen as driving terms to the LTI system and since the system also includes a time invariant signal thus three vectors representing inputs to the system are defined ($\tilde{u}_0, \tilde{u}_1, \tilde{u}_2$). The two most relevant hyper-planes are defined as C_0x and C_1x for which the systems solutions intersect.

system of the form $\dot{x}_i = Ax + Bu_i$ with $i \in \{1, 2, 3, 4\}$. Denote each of these by System_i . Fig. (6.2) schematically depicts this, from which the conditions for the existence of a globally stable limit cycle are derived.

The existence of a limit cycle depends on several different factors, for example whether or not the matrix A for each system is stable, and in which region the equilibrium of each system lies. Depending on the location of the equilibrium points, the model may give rise to rich and complicated dynamics and even chaotic behavior. Finally the initial conditions also play an important role. If the matrix A of each system is stable then a limit cycle can occur if each system has an equilibrium point in a different region. That is, for example, System_1 (in the third quadrant) must not have its equilibrium in the third quadrant. If System_1 contains its equilibrium elsewhere (except region 3), then the LTI flow will intersect a hyperplane S_0 or S_1 at some finite time moment t^* when the governing equations of some other system will take over (in this case either system 2 or 4) and the same scenario could repeat until a closed trajectory is formed. However, it is important to note that this scenario does not guarantee

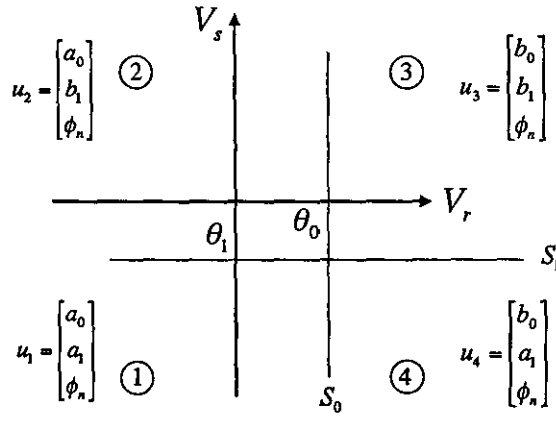


Figure 6.2: The figure shows the state space (V_s, V_r) and how the hyperplanes situate in this projection space. The hyperplanes are defined as C_0x and C_1x which are orthogonal to one another and which are denoted as the switching surfaces S_0 and S_1 respectively. Each subspace is defined by an independent LTI flow of the form $\dot{x} = Ax + Bu$, where all the four systems differ in how the vector u is defined. The vectors are defined as $u_i = [\tilde{u}_0, \tilde{u}_1, \tilde{u}_2]^T$, with $i \in \{1, 2, 3, 4\}$. The values assumed by \tilde{u}_0 and \tilde{u}_1 are related to where System $_i$ situates with respect to the Heaviside function thresholds θ_0 and θ_1 respectively and here $\tilde{u}_2 = \phi_n = 1$.

a limit cycle since the system can be chaotic. On the other hand, if matrix A was unstable it could be that all systems have equilibrium points in their own region, however the overall model possesses a limit cycle, since the equilibrium would be unstable and so depend on the initial conditions.

In general, solving the existence conditions for limit cycles is non-trivial (as it involves exponential matrices), however using results given in ([28], pp. 43-46) allows one for example, to simulate the system and obtain switching times and intersection points when the trajectory traverses a switching surface. This information then permits verification of the stability of a limit cycle. For system (5.1) the matrix A is stable (having all its eigenvalues on the left half plane), and so four systems are stable. However, the equilibrium state of each system lies in a different region, due to the different vectors u_i , with $i \in \{1, 2, 3, 4\}$.

For ease of derivation of the limit cycle conditions, denote Bu_i as simply B_i , then the following are necessary conditions for the appearance of limit cycles:

Proposition 6.2.1 *The switching surfaces S_0 and S_1 (governed respectively by the equations of the hyperplanes C_0x and C_1x) divide the state space (V_s, V_r) into four regions, each of which has an independent LTI flow $\dot{x}_i = Ax + B_i$ with $i \in \{1, 2, 3, 4\}$. Since A is a stable matrix, then the existence of a globally stable limit cycle is only true if the following necessary conditions are satisfied:*

1. System 1: $-C_0A^{-1}B_1 > \theta_0$ or $-C_1A^{-1}B_1 > \theta_1 = \{ \nu_{rs}a_1 > \theta_0 \text{ or } \nu_{sr}a_0 + \phi_n\nu_{sn} > \theta_1 \}$.
2. System 2: $-C_0A^{-1}B_2 > \theta_0$ or $-C_1A^{-1}B_2 < \theta_1 = \{ \nu_{rs}b_1 > \theta_0 \text{ or } \nu_{sr}a_0 + \phi_n\nu_{sn} < \theta_1 \}$.
3. System 3: $-C_0A^{-1}B_3 < \theta_0$ or $-C_1A^{-1}B_3 < \theta_1 = \{ \nu_{rs}b_1 < \theta_0 \text{ or } \nu_{sr}b_0 + \phi_n\nu_{sn} < \theta_1 \}$.
4. System 4: $-C_0A^{-1}B_4 < \theta_0$ or $-C_1A^{-1}B_4 > \theta_1 = \{ \nu_{rs}a_1 < \theta_0 \text{ or } \nu_{sr}b_0 + \phi_n\nu_{sn} > \theta_1 \}$.

To study the local and global stability of a limit cycle, a region of interest in parameter space is selected from the numerical results of Chapter 5. Without loss of generality, a band is chosen centred around HB1 (refer to Table C.2) with small variations in the parameter ν_{sr} and the parameter ν_{rs} is allowed to vary freely. In this parameter window it is verified that the dynamic variable V_r is always positive and gradually goes from sub-threshold to supra-threshold as ν_{rs} is increased (where the threshold in the nonlinear function is θ). There are numerous ways for determining a reasonable approximation to the nonlinear function. For example, one easy way is to generate the time series of the dynamic variables and use these as an input to the nonlinear functions. This method allows investigation of the region of nonlinear function space being visited. The approximation chosen for V_r in this parameter regime is a Heaviside function with parameters $(a_0, b_0, \theta_0) = (0, 250, 0.015)$. In this case θ_0 coincides with the threshold of the sigmoidal function. Conversely V_s has only sub-threshold dynamics occupying mostly the lower asymptote of the nonlinear function. The sigmoidal function considered is very steep indeed and a small variation in the input has dramatic changes in the output, so the approximation must be chosen carefully. Since V_s lies mostly on the lower asymptote, a function of the form $u(t) = \max\{0, Cx + \theta_1\}$, where C is some vector could be used. However, for the purpose of demonstrating global stability a simpler function will suffice. In this case, a reasonable choice is a Heaviside function with the parameters $(a_1, b_1, \theta_1) = (0, 250, -0.015)$. As an example, we present a simulation using a MATLAB code we developed using the *symbolic math toolbox* (see Fig 6.3).

The code uses the ideas discussed where a limit cycle is generated and the switching times and the Poincaré surface coordinates are determined. Here the code is run with the initial conditions $x_0^* = [0, 0, 0, 0]^T$ and with the control parameters fixed to $(\nu_{sr}, \nu_{rs}, \nu_{sn}) = (-0.008, 0.006, 0)$. We observe a limit cycle in the clockwise direction where we can easily interpret the results using the derived conditions from Proposition 1. In this simulation System₂ in the second quadrant, starts running and its trajectory tends towards its equilibrium point which lies in the first quadrant. As it evolves, a switch occurs at S_0 where then System₁ takes over and the same scenario for the other systems repeats as the limit cycle develops. The code is run long enough until the switching times reaches a tolerance ($|t_i^* - t| < TOL$, where TOL is some time parameter). The switching times and Poincaré surface coordinates are stored in Table D.1.

6.2.1 Limit Cycle γ with period t^*

Here use is made of the proof of existence of limit cycles given in ([28] pp. 43-46) which provides an algorithm to derive the analytical solution of the trajectory of a limit cycle. From the numerical simulation it is observed that the trajectory $\phi(t)$ of the limit cycle γ traverses each switching surface S_k with $k \in \{0, 1\}$ twice, in a sequential manner. Denote S_k^i as the subsection of a switching surface S_k where the trajectory first intersects it and t_i^* as the time moment of the intersection, where $i = j(\text{mod} 4)$, with $j \in \mathbb{N}_0^+$. For example, S_0^0 is the subsection of the switching surface S_0 where the trajectory traverses it at time instant t_0^* (since it is a limit cycle we consider $t_0^* = t_4^*$ since $t_i^* = t_{j \text{ mod } 4}^*$). Hence the limit cycle γ starting at the some initial condition $x_i^* \in S_k^i$ has period $t^* = t_1^* + t_2^* + t_3^* + t_4^*$ and satisfies:

1. $\phi(t_1^*) = x_1^* \in S_1^1$
2. $\phi(t_1^* + t_2^*) = x_2^* \in S_0^2$
3. $\phi(t_1^* + t_2^* + t_3^*) = x_3^* \in S_1^3$
4. $\phi(t_1^* + t_2^* + t_3^* + t_4^*) = x_4^* \in S_0^0$

Each System _{i} has a solution of the following form

$$x(t)_i = e^{At}(x_0 + A^{-1}B_i) - A^{-1}B_i.$$

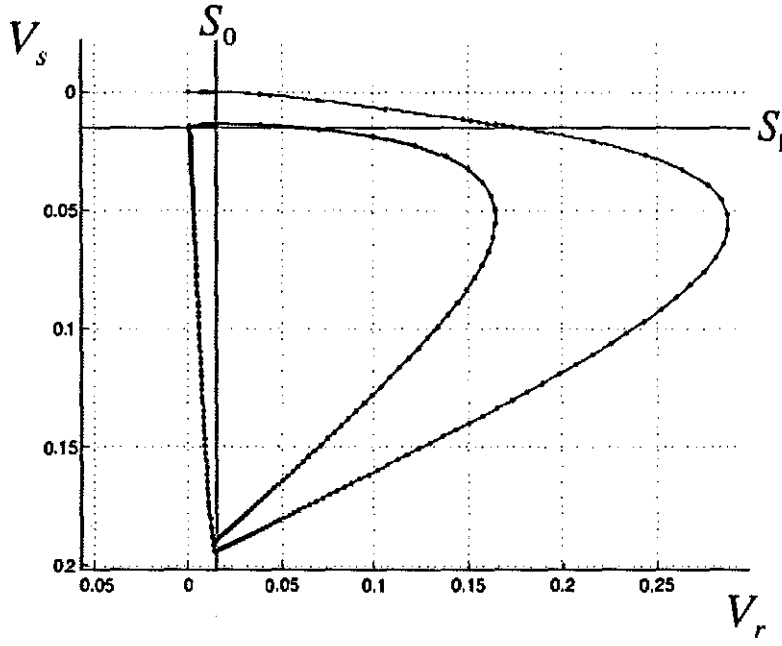


Figure 6.3: Simulation of the four systems of each partition of the state space and with the initial condition $x_0^* = [0, 0, 0, 0]^T$. The control parameters are set to $\nu_{sr} = -0.008$, $\nu_{rs} = 0.006$ and $\nu_{sn} = 0$ which corresponds to the Hopf bifurcation point HB1 (Table C.2). System₂ starts running and its trajectory is towards its equilibrium point which lies in the first quadrant and a switch occurs at S_0 . In the first quadrant System₃ takes over and moves towards its own equilibrium on the fourth quadrant and a second switch occurs at S_1 . For the other two final systems (4 and 1) identical scenarios occur, where System₁ has its equilibrium on the second quadrant and System₄ on the third quadrant. Note that if S_1 was shifted slightly upwards then the limit cycle condition would no longer be satisfied and the limit cycle would vanish. Thus this also explains the generation of the Hopf bifurcation HB1.

From Proposition (2.2.1) the piecewise trajectory $\phi(t)$ is governed by the following switching conditions

$$\begin{cases} g_0(t_1^*, t_2^*, t_3^*, t_4^*) = C_0 x_0^* - \theta_0 = 0 \\ g_1(t_1^*, t_2^*, t_3^*, t_4^*) = C_1 x_1^* - \theta_1 = 0 \\ g_2(t_1^*, t_2^*, t_3^*, t_4^*) = C_0 x_2^* - \theta_0 = 0 \\ g_3(t_1^*, t_2^*, t_3^*, t_4^*) = C_1 x_3^* - \theta_1 = 0 \end{cases}$$

where C_0 and C_1 are the output matrices (describing the hyperplanes) defined in the previous section and the periodic solution of the piecewise linear approximation is obtained with any

of the initial conditions:

$$\begin{aligned}
x_0^* &= (I - e^{A(t_4^*+t_3^*+t_2^*+t_1^*)})^{-1} \left[e^{A(t_4^*+t_3^*+t_2^*)} (e^{At_1^*} - I) A^{-1} B_1 + e^{A(t_4^*+t_3^*)} (e^{At_2^*} - I) A^{-1} B_2 \right. \\
&\quad \left. e^{At_4^*} (e^{At_3^*} - I) A^{-1} B_3 + (e^{At_4^*} - I) A^{-1} B_4 \right], \\
x_1^* &= (I - e^{A(t_1^*+t_4^*+t_3^*+t_2^*)})^{-1} \left[e^{A(t_1^*+t_4^*+t_3^*)} (e^{At_2^*} - I) A^{-1} B_2 + e^{A(t_1^*+t_4^*)} (e^{At_3^*} - I) A^{-1} B_3 \right. \\
&\quad \left. e^{At_1^*} (e^{At_4^*} - I) A^{-1} B_4 + (e^{At_1^*} - I) A^{-1} B_1 \right], \\
x_2^* &= (I - e^{A(t_2^*+t_1^*+t_4^*+t_3^*)})^{-1} \left[e^{A(t_2^*+t_1^*+t_4^*)} (e^{At_3^*} - I) A^{-1} B_3 + e^{A(t_2^*+t_1^*)} (e^{At_4^*} - I) A^{-1} B_4 \right. \\
&\quad \left. e^{At_2^*} (e^{At_1^*} - I) A^{-1} B_1 + (e^{At_2^*} - I) A^{-1} B_2 \right], \\
x_3^* &= (I - e^{A(t_3^*+t_2^*+t_1^*+t_4^*)})^{-1} \left[e^{A(t_3^*+t_2^*+t_1^*)} (e^{At_4^*} - I) A^{-1} B_4 + e^{A(t_3^*+t_2^*)} (e^{At_1^*} - I) A^{-1} B_1 \right. \\
&\quad \left. e^{At_3^*} (e^{At_2^*} - I) A^{-1} B_2 + (e^{At_3^*} - I) A^{-1} B_3 \right].
\end{aligned}$$

6.2.2 Local stability of Limit cycle γ

The local stability of the limit cycle can be verified by considering a Poincaré map, P , from some point $x_i^* \in S_k^i$, to the point when the trajectory returns to S_k^i . i.e $P : S_k^i \rightarrow S_k^i$ and then verifying that the Jacobian of the map has all its eigenvalues inside the unit disc. The Jacobian defined in Proposition (2.19) is derived by considering small perturbations in time and space in each intermediate switching surface and then neglecting higher order terms. The Jacobian, W , of a piecewise linear system is then determined as being the composition of all the intermediate perturbations and defined as $W = W_3 W_2 W_1 W_0$ where,

$$W_i = \left(I - \frac{v_i C_k}{C_k v_i} \right) e^{At_i^*},$$

and $v_i = Ax_i^* + B_i$ and $k = i(\text{mod}2)$. Substituting the values from Table D.1 gives

$$W = \begin{pmatrix} 5.47\text{e-}4 & 2.71\text{e-}6 & 9.58\text{e-}03 & 4.79\text{e-}5 \\ -2.73\text{e-}2 & -1.36\text{e-}4 & -4.79\text{e-}1 & -2.39\text{e-}3 \\ 0 & 0 & 0 & 0 \\ 2.64\text{e-}05 & 1.31\text{e-}7 & 4.62\text{e-}4 & 2.31\text{e-}06 \end{pmatrix}.$$

W does have all its eigenvalues inside a unit disc, therefore the limit cycle is locally stable.

6.2.3 Global stability of limit cycle γ

The fundamentally new concept introduced in *Constructive Global Analysis of Hybrid Systems* [28] is to infer global dynamical properties of a system through finding quadratic Lyapunov functions on the switching surface. Earlier studies [122, 69] had proposed continuity of the Lyapunov functions along the switching surfaces and this result lead to the idea that the intersection of two Lyapunov functions at a switching surfaces (one from each side) defined a unique quadratic Lyapunov function on the switching surface. It is then demonstrated in [28] that a quadratic Lyapunov function on the switching surface in a PLS denoted *Quadratic Surface Lyapunov Function* (SuLF) exists and that SuLF (as opposed to searching for Lyapunov functions in the state space) is sufficient to efficiently analyse global stability of limit cycles. This follows since a PLS behaves linearly inside a region (partitioned state space). In order to analyse the PLS using SuLF it is first necessary to define *impact maps* from one switching surface to the next and by combining all the impact maps associated with the PLS it is possible to infer global stability. An *impact map* associated to the LTI flow in each of the four regions is defined following Theorem (2.2.1):

$$H_i(t) = e^{At} + (x_i^*(t) - x_{i+1}^*)w_i(t)$$

and for each region i the following

$$\begin{aligned} w_0(t) &= \frac{C_1 e^{At}}{\theta_1 - C_1 x_0^*(t)} \quad , \quad w_1(t) = \frac{C_0 e^{At}}{\theta_0 - C_0 x_1^*(t)} \quad , \\ w_2(t) &= \frac{C_1 e^{At}}{\theta_1 - C_1 x_2^*(t)} \quad , \quad w_3(t) = \frac{C_0 e^{At}}{\theta_0 - C_0 x_3^*(t)} \quad , \end{aligned}$$

Since an impact map is nonlinear, multi-valued and discontinuous then for every impact map i define for a given initial condition in S_k^i a set of all expected switching times $t_i \in \mathcal{T}_i$. This allows each impact to be represented as a linear transformation analytically parameterised by the switching time. Then for any $\Delta_i \in S_k^i - x_i^*$ there exists a set of expected switching times $t_i \in \mathcal{T}_i$ such that the impact maps are given by

$$\Delta_{i+1} = H_i(t_{i+1})\Delta_i$$

where each t_i is the switching time associated to each perturbation Δ_i . Furthermore, parameterising the impact map with t_i defines the set of initial conditions $S_{t_i}^k \in S_k^i$ in a given switching surface that have the same switching time. This set of initial conditions $S_{t_i}^k$ is found in [28] to be a convex subset of a linear manifold of dimension $n - 2$ (in this case an \mathbb{R}^2 surface). To show that these four impact maps are contracting in some sense, define a SuLF on each S_k^i given by

$$V_i(x) = x^T P_i x - 2x^T g_i + \alpha_i.$$

Global asymptotically stability of the limit cycle follows if there exists $P_i > 0$ (positive definite), g_i , α_i , such that

$$V_{i+1}(\Delta_{i+1}) < V_i(\Delta_i) \Leftrightarrow V_i(\Delta_i) + V_{i+1}(H_i(t_{i+1})\Delta_i) > 0 \quad \forall \Delta_i \in S_k^i - x_i^*$$

The above inequality is computationally hard, however using the fact that maps from one switching surface to the next are linear in $S_{t_i}^k$ and that as t_i ranges over \mathcal{T}_i , $S_{t_i}^k$ covers every point in S_k^i , it is possible to define approximations with a set of LMI. Conservative conditions given by Theorem 4.1 and Corollary 4.2 (refer to [28] pp. 62) are used, which is computationally very efficient. Equivalently, the limit cycle is globally asymptotically stable if there exist $P_i > 0$ and g_i , $\beta_i = \alpha_i - \alpha_{i+1}$ such that

$$\begin{cases} R_i(t_{i+1}) = P_i - H_i^T(t_{i+1})P_{i+1}H_i(t_{i+1}) - 2(g_i - H_i^T(t_{i+1})g_{i+1})w_i(t_{i+1}) + w_i^T(t_{i+1})\beta_i w_i(t_{i+1}) \\ R_i(t_{i+1}) > 0 \quad \text{on} \quad S_{t_i}^k - x_i^* \quad \text{for all expected switching times} \quad t_i \in \mathcal{T}_i. \end{cases}$$

Furthermore, parameterising the impact map by a switching time corresponds to defining a linear operator $H : \mathbb{R}^{n-1} \rightarrow \mathbb{R}^{n-1}$. In view of this, while Δ_i are vectors in \mathbb{R}^n , the impact maps have solutions restricted to hyperplanes in \mathbb{R}^{n-1} . Consequently, this allows the definition a *basis* for the switching surfaces where each vector $\Delta_i \in S_k^i$ can be expressed as linear combination of the *basis* $\Delta_i = \Pi_i \delta_i$ (with Π_i being the *basis* and $\delta_i \in \mathbb{R}^{n-1}$). An easy choice for the *basis* is the *orthogonal complements* to C_i , i.e $\Pi_i \in C_i^\perp$. It then follows that the last LMI condition can be rewritten as

$$\begin{cases} R_i(t_{i+1}) = Q_i - F_i^T(t_{i+1})Q_{i+1}F_i(t_{i+1}) - 2(\rho_i - F_i^T(t_{i+1})\rho_{i+1})\omega_i(t_{i+1}) + \omega_i^T(t_{i+1})\psi_i\omega_i(t_{i+1}) \\ R_i(t_{i+1}) > 0 \quad \text{on} \quad S_{t_i}^k - x_i^* \quad \text{for all expected switching times} \quad t_i \in \mathcal{T}_i, \end{cases} \quad (6.33)$$

where $Q_i = \Pi_{i+1}^T P_i \Pi_i$, $F_i(t) = \Pi_{i+1}^T H_i(t) \Pi_i$, $\rho_i = \Pi_{i+1}^T g_i \Pi_i$, $\psi_i = \Pi_{i+1}^T \beta_i \Pi_i$ and $\omega_i(t) = \Pi_{i+1}^T w_i(t) \Pi_i$. Since the systems within a single region are linear, then simple candidates for

the quadratic surface coefficients are $\rho_i = 0$ and $\psi_i = 0$. The final aspect to note about condition (6.33) is that it defines an infinite set of LMI for all $t_i \in \mathcal{T}_i$. Computationally, to overcome this difficulty it is necessary to grid this set in order to obtain a finite subset of expected switching times $t_i^- = t_i^0 < t_i^1 < \dots < t_i^j = t_i^+$, for some $j \in \mathbb{N}$. To compute the above conditions a set of MATLAB routines using the *IQC β toolbox* was developed [82]. The objective being to find $Q_i > 0$ and to confirm that (6.33) is satisfied for all switching times $[t_i^-, t_i^+]$ by plotting the minimum eigenvalue of (6.33) on $[t_i^-, t_i^+]$, and thus showing that this is indeed positive definite. The largest switching time sets for which (6.33) are satisfied were $\mathcal{T}_1=[5.71\text{e-}2, 7\text{e-}2]$, $\mathcal{T}_2=[1\text{e-}2, 2.5\text{e-}2]$, $\mathcal{T}_3=[2.2\text{e-}3, 8.85\text{e-}3]$ and $\mathcal{T}_4=[1.5\text{e-}2, 6.4\text{e-}2]$ which can be confirmed in Fig. 6.4. In particular, for the switching times presented in Table C.2 the following positive definite matrices exist:

$$\begin{aligned} Q_1 &= \begin{pmatrix} 3.63 & 1.38\text{e-}2 & 0 \\ 1.38\text{-}2 & 8.97\text{e-}1 & 0 \\ 0 & 0 & 2.39\text{e-}1 \end{pmatrix}, \quad Q_2 = \begin{pmatrix} 2.33\text{e-}01 & 0 & 0 \\ 0 & 4.88 & -2\text{e-}01 \\ 0 & -2\text{e-}01 & 9.17\text{e-}01 \end{pmatrix} \\ Q_3 &= \begin{pmatrix} 1.61 & -1.61\text{e-}02 & 0 \\ -1.61\text{e-}02 & 3.16\text{e-}01 & 0 \\ 0 & 0 & 2.54\text{e-}02 \end{pmatrix}, \quad Q_4 = \begin{pmatrix} 2.37\text{e-}03 & 0 & 0 \\ 0 & 2.49 & 4.22\text{e-}03 \\ 0 & 4.22\text{e-}03 & 7.75\text{e-}02 \end{pmatrix}. \end{aligned}$$

Thus satisfying Theorem (2.2.1) the proof that the piecewise linear approximation is globally asymptotically stable is complete. Other piecewise approximations could have been used but the approximation considered is sufficient to prove global stability. Note that global stability can equally be proven for this PLS system with time invariant inputs by applying the same procedure. For this case in particular, a more straightforward approach could be used by first applying a coordinate transformation. Having proven global stability of the limit cycle for a subset of the control parameters, it leaves the question of how to obtain a suitable approximation for the nonlinear functions that permits analysis of the system for the complete parameter range. Clearly, consideration of higher order piecewise approximations will increase the accuracy of the system, whilst also increasing the computational complexity of the LMIs, which seems to be unnecessary. Naturally an interesting extension of this work would be to determine the simplest partition of the state space (V_s, V_r) that permits the global analysis of the limit cycle for the whole parameter domain.

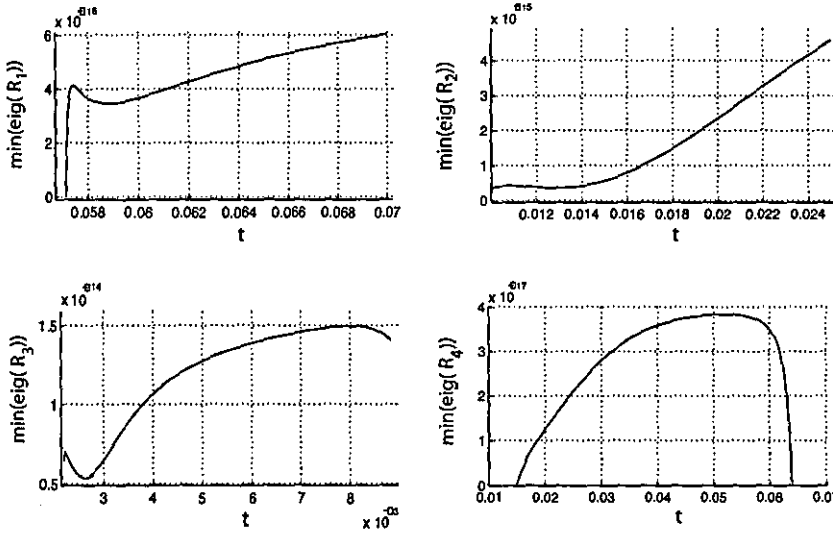


Figure 6.4: *SuLF* for all the four impact maps are stable. Each plot shows the minimum eigenvalue of (6.33) on the respective sets of switching times T_i for each impact map. The eigenvalues of (6.33) are always positive for T_i (feasible) meaning that a positive definite matrix always exists and thus a *SuLF* for each impact map exists and is stable. In this way it is shown that the limit cycle is globally asymptotically stable.

6.3 Summary

This chapter provided theoretical and computational insights into the dynamics of an RKII set. Using normal forms and the theory of centre manifolds the coefficients of the Hopf bifurcations of the RKII set were determined. The coefficients confirmed the supercritical nature of these bifurcations as observed numerically in Chapter 5. The second part of this chapter then considered a piecewise linear reduction of the RKII set and global stability the of limit cycle arising in this approximation is shown for a narrow region in parameter space. This was achieved by employing a *Constructive Global Analysis of Hybrid Systems* [28]. The strength of this methodology suggests the potential for understanding coupled RKII sets and possibly the Ki set hierarchy.

Chapter 7

General discussion and conclusions

7.1 Discussion

The main purpose of this thesis was to investigate the mechanisms underlying the development of abnormal oscillations in a neural mass model and to provide insight into spike-wave oscillations arising from thalamocortical circuits. The model incorporates key anatomical structures and physiological features, however it assumes that some level of understanding of a neuronal system is possible without consideration of all the detailed features of the underlying thalamocortical components. Thus, the model groups neuronal structures governed by plausible physiological dynamics and indirectly combines some of the important system variables into parameters where then different system solutions are identified by varying the relevant parameters. These neural mass model cannot be proven to be sound or correct, however to increase confidence in a model, model predictions should be confirmed experimentally. Indeed, previous analysis of the model have demonstrated its descriptive validity in a wide range of healthy states and yielded specific predictions with regards to seizure activity [131] (Fig. B.1 of section (B.2) illustrates the main EEG oscillations predicted by the model within a restricted parameter space). This work further extends these results by specifically looking into absence seizures and encouragingly, further analysis reveals that the model also accounts for tonic-clonic seizures [21]. In particular, by performing bifurcation analysis of the full corticothalamic model a supercritical Hopf bifurcation is found commencing the transition

from healthy resting EEG to periodic pathological oscillations and discover a further ‘spike-bifurcation’ which initiates (3Hz) absence seizures. This yielded time series realizations with periodic spike and wave morphology that closely resembled scalp EEG data taken from an absence seizure data-base. Furthermore, the nature of the bifurcation set yields a symmetrical on-off character that is also found in the EEG data and the power spectrum of pre- and postictal EEG is comparable to the data. Interestingly, although there are some differences in comparison to the Destexhe and Sejnowski model [43], both models emphasize increased excitatory loops between the cortex and the specific and reticular nuclei, of the thalamus underlying the generalized seizures. Furthermore, the onset of seizures is demarcated in Destexhe and Sejnowski model [43] by a phase shift of the voltage trace of the TC neurons when compared to the oscillations of the RE neurons and the cortical neurons which suggests that spike activity is initiated in the specific neurons. Similarly, the phenomena is also observed in field activity of the full corticothalamic model. Destexhe and Sejnowski treated axonal propagation times as negligible, and hence, there was no time delay. However, the activation of seizures is mediated by $GABA_B$ receptors between the reticular and the specific nuclei which is a slow or delayed process that is activated once the corticothalamic feedback is strong enough. In contrast, the presence of time-delay in the corticothalamic model is a crucial parameter in the generation of absence seizures waveform. In fact, qualitatively similar spike-wave oscillations can be generated by our model with a variety of time-delayed feedback loops that differ in some detail from those presented in this thesis. This is interesting because it is known experimentally that absence seizures can arise as a result of changes in a number of different neuronal pathways. However, the present model incorporates the important components of the corticothalamic system together with time delays that, due to finite axonal conduction speeds. Finally, the corticothalamic model employed here does not explicitly include ionic currents such as I_T and I_H or receptors such as $GABA_B$ within the thalamus. Although the present model is not inconsistent with such channels, future research would benefit by considering mappings of the full corticothalamic model to more detailed physiological approaches which then would bridge the gap in our understanding. In fact, one challenging objective of neural mass models is to identify relevant parameters of the observed activity and then try to decompose the parameters into the state variables or parameters of the real physical system [77]. Specifically for the delay incorporated in the corticothalamic model, future studies would benefit by numerically continuing the bifurcations arising due to the delay as these may

be global bifurcations.

The second part of this thesis addresses oscillations arising from the thalamic system, as motivated by a number of key observations. Firstly, in clinical recordings of the onset of absence seizures, the transition from pre-ictal to ictal dynamics is typically heralded by oscillatory behaviour, prior to spike-wave activity being observed. Furthermore, in the absence of a cortical signal, the thalamic system is quiescent and spike-wave activity generated via periodic dynamics from the cortex fed both into both the specific and reticular nuclei populations. Also motivating this reduction is a phase shift of oscillations arising in the specific nuclei when compared both with the cortex and reticular populations, which suggests that absence seizures originate in the thalamus. Thus, the cortex was decoupled from the thalamus and this gives rise to a reduced system of equations that Freeman termed RKII sets. An unexpected finding was to observe through simulations that an RKII set driven by sinusoidal signals generated ‘two-bump’ solutions resembling spike-wave morphology. Moreover, through simulations it was observed that varying the coupling strength between the specific and reticular neurons does not influence the wave form of the oscillations, only the amplitudes of the signals arising in the reticular neurons varies. Thus, a functional composition of the incoming signal from the cortex with the sigmoidal activation functions of the reticular neurons can be considered as an appropriate approximation of the wave form. Consequently as a first approach to understand these solutions, a reduction of the RKII set with a piecewise linear saturation function was considered which determined two regions of interest for the solution. The two regions were then compared with the spike-wave activity, where one region is associated with ‘spike’ and the second region with the ‘wave’ explaining the two-bump solutions observed in RKII set and potentially offering insights to spike-wave oscillations. However, these solutions should be regarded as approximations and as such future studies would benefit by further investigation.

To further understand RKII sets, existence and local stability of limit cycles by developing linear stability theory and contrasting with numerical continuations results obtained using XPPAuto was considered. Stability curves in parameter space were found explaining the transitions to limit cycle oscillations in the thalamic system. A further contribution of this thesis was to calculate normal forms to determine the unfolding coefficients of the Hopf bifurcations arising in the thalamic system thus determining sufficient conditions for the observed limit cycles. An interesting option of study would be to consider the coupling of the unfolded

equations and investigate local behaviour of these oscillations, in particular the normal form equations driven by sinusoidal inputs. However, the motivation here was to first understand the global properties of oscillations arising in RKII set as these properties could lead to interesting theoretical results which would benefit the understanding of the activity arising from coupled RKII sets. To achieve this a new methodology termed constructive global analysis of hybrid systems [28] which allows one to consider piecewise linear approximations of a system and to study both the local and global flows of the non-smooth vector field. In particular global stability is proven for the RKII set within a subset of the parameter space and for a particular piecewise approximation. However, several interesting questions remain to be answered in all the above research avenues followed in this thesis. Therefore, the discussion is concluded with possible future continuation of the present study.

7.2 Future directions

7.2.1 Mapping between Neural mass and conductance models

An interesting future study is to consider the mapping between different scales of neuronal activity. As mentioned above, one aim of neural mass models is to decompose a set of parameters into a set of meaningful variables and parameters of the real underlying system. This mapping could for instance be applied between the corticothalamic model considered in this thesis and the Destexhe and Sejnowski models [43]. This would enable consideration of ionic currents and synaptic receptors believed to be significant in the genesis of absence seizures. In particular, mapping between the Freeman Neural Mass model and conductance based models is proposed and conditions are given for the mathematical mapping to hold true. However, this is only one possible mapping and other strategies should be also considered.

Assume a population of inhibitory and excitatory neurons where these could either be cortical or thalamic neurons. Furthermore, these neurons can either be treated as a pointwise system or a system in a homogenous 2-D medium. Considering the activity at a microscale the post

synaptic potential (PSP) $V(t, \hat{r})$ is calculated using a conductance based model:

$$\begin{aligned} C \frac{dV}{dt} &= -g_L(V - V_L) + I_s \\ I_s &= -g_E(V - V_E) - g_I(V - V_I) + I^{ext}, \end{aligned} \quad (7.1)$$

where V_L is the neurons voltage steady state, g_L is the specific neurone membrane conductance, C is the specific membrane capacity (the membrane time constant $\tau_m = \frac{C}{g_L}$) and I_s is the sum of inhibitory synaptic currents mediated by GABA receptors, here denoted with the subscript I, excitatory synaptic currents mediated by AMPA, NMDA receptors, denoted E and by some external current I^{ext} . The synaptic conductances depend on incoming spike pulse frequency ϕ_j (with $j=\{I, E\}$) from pre-synaptic cells and obey a second order differential equation which describes the response to these impulses.

$$\tau_j^r \tau_j^d \frac{d^2 g_j(t)}{dt^2} + (\tau_j^r + \tau_j^d) \frac{dg_j(t)}{dt} + g_j(t) = \bar{g}_j \hat{\tau} \phi_j(t), \quad (7.2)$$

where τ_j^r and τ_j^d ($j=\{I, E\}$) are the rise and decay times respectively of the response, \bar{g}_j is the maximal conductance and $\hat{\tau}$ is only a scale parameter. For a mapping between the Freeman model (which is second order in voltage) and a conductance model to hold true a reduction of equation (7.2) is necessary. A possible simplification is assuming the rise time of the response τ_j^r is zero and the decay time is finite, that is, the rise is infinitely rapid response and only a decay is observed. Dropping this parameter can be justified for small times scales and intense inputs to a neuron, giving rise to a first order response of the conductances in the following way:

$$\tau_j^d \frac{dg_j(t)}{dt} + g_j(t) = \bar{g}_j \hat{\tau} \phi_j(t). \quad (7.3)$$

A simplification of the synaptic currents I_s in the conductance model (7.2) should also be considered. Here it is assumed that the $V - V_E$ and $V - V_I$ terms are constants which is a strong assumption, but nevertheless necessary for the derivations to be possible and thus $I_s = -g_E(V - V_E) - g_I(V - V_I) + I^{ext} \approx c_E g_E + c_I g_I + I^{ext}$, where c_E and c_I are constants. However, it is worth bearing in mind that the current amplitudes $g_E(V - V_E)$ and $g_I(V - V_I)$ are approximately of the same order, but $V_I \ll V_E$ and $g_I \gg g_E$ where g_I generally has large fluctuations. Multiplying both sides of equation (7.3) with the constant c_E and another instance by c_I gives two equations with the following form:

$$[\tau_j^d \frac{d}{dt} + 1] c_j g_j(t) = c_j \bar{g}_j \hat{\tau} \phi_j(t). \quad (7.4)$$

summing the two instances of equation (7.4) and some external current I^{ext} gives

$$\begin{aligned} [\tau_E \frac{d}{dt} + 1] c_E g_E(t) + [\tau_I \frac{d}{dt} + 1] c_E g_I(t) + [\tau_{ext} \frac{d}{dt} + 1] I^{ext} = \\ \hat{\tau} (c_E \bar{g}_E \phi_E(t) + c_I \bar{g}_I \phi_I(t) + c_{ext} \bar{g}_{ext} \phi_{ext}(t)). \end{aligned} \quad (7.5)$$

A further assumption is setting $\tau_I^d = \tau_E^d = \tau_{ext}^d = \tau_S$ to obtain

$$\begin{aligned} [\tau_S \frac{d}{dt} + 1] (c_E g_E(t) + c_E g_I(t) + I^{ext}) = \hat{\tau} (c_E \bar{g}_E \phi_E(t) + c_I \bar{g}_I \phi_I(t) + c_{ext} \bar{g}_{ext} \phi_{ext}(t)) \\ \Leftrightarrow [\tau_S \frac{d}{dt} + 1] I_s = \hat{\tau} (c_E \bar{g}_E \phi_E(t) + c_I \bar{g}_I \phi_I(t) + c_{ext} \bar{g}_{ext} \phi_{ext}(t)). \end{aligned} \quad (7.6)$$

Using equation (7.2) to obtain I_s and substituting in the above equation (7.6) results in a formulation which is second order in voltage:

$$\begin{aligned} [\tau_S \frac{d}{dt} + 1] [C \frac{dV}{dt} + g_L(V - V_L)] = \hat{\tau} (c_E \bar{g}_E \phi_E(t) + c_I \bar{g}_I \phi_I(t) + c_{ext} \bar{g}_{ext} \phi_{ext}(t)) \\ \Leftrightarrow [\tau_S \frac{d}{dt} + 1] [\tau_m \frac{d}{dt} + 1] V = \frac{\hat{\tau} (c_E \bar{g}_E \phi_E(t) + c_I \bar{g}_I \phi_I(t) + c_{ext} \bar{g}_{ext} \phi_{ext}(t))}{g_L} - V_L \end{aligned} \quad (7.7)$$

On the other hand, for the macroscopic dynamics consider the following thalamic Freeman model, with two neuronal populations (inhibitory population - Reticular nucleus denoted by r and excitatory neurons - Specific nucleus denoted by s).

$$\begin{cases} [\frac{1}{\alpha} \frac{d}{dt} + 1] [\frac{1}{\beta} \frac{d}{dt} + 1] V_s(r, t) = \alpha \beta (\nu_{sr} \phi_r(r, t) + \nu_{se} \phi_{ext}(t)), \\ [\frac{1}{\alpha} \frac{d}{dt} + 1] [\frac{1}{\beta} \frac{d}{dt} + 1] V_s(r, t) = \alpha \beta \nu_{rs} \phi_s(r, t) + \nu_{re} \phi_{ext}(t), \end{cases} \quad (7.8)$$

where the variables V_a ($a = \{r, s\}$) generally represent averaged post-synaptic dendritic potentials evaluated by extracellular measurements of EEGs. Each thalamic submodule (specific and reticular neuron) is governed by a second order ordinary differential equation which captures a population's characteristic responses when stimulated with incoming dendritic pulses ϕ_a . The parameters α and β are constants representing the inverse rise and decay times parameterising the dendritic response to these impulses. The conversion from pulse density ϕ_a to wave amplitude is implicit in the synaptic weights $\nu_{sr} \in \mathbb{R}^-$ and $\nu_{rs} \in \mathbb{R}^+$. $\nu_{se} \phi_{ext}(t)$ and $\nu_{re} \phi_{ext}(t)$ represents external inputs to the thalamic specific and reticular neurons respectively. Note that synaptic weights are not directly measured experimentally and can only be inferred through modelling, i.e. an indirect measure of the synaptic transmission. In other words these synaptic weights may be thought of as of the form $\nu_{ab} = N_{ij} S_j$, representing the coupling strength between neuronal populations i and j . N_{ij} is anatomical or structural in character representing the mean number of connections from neurons of type j on a neuron of type

i. The term S_j is physiological or functional in nature representing the size of the impulse response associated with synapses of type j .

For the mapping between the microscopic and macroscopic level to be possible it is necessary further to assume that the intracellular activity is in some sense proportional to the extracellular activity (in this case EEG). Finally, comparing the left hand side of equations (7.7) and (7.8) we obtain a possible interpretation for the macroscopic parameters written as $\frac{1}{\alpha} = \tau_s$ representing the synaptic time constant and $\frac{1}{\beta} = \tau_m$ corresponding to the membrane time constant.

The advantage of coupled systems consisting of equation (7.7) is that $GABA_B$ receptors, I_T and I_H ionic currents which are believed to play an important role in absence seizures can be directly incorporated. Also a direct comparison between the neural mass corticothalamic model and Destexhe and Sejnowski model [43] can be achieved to investigate the nature and importance of delays in abnormal oscillations. Thus the proposed method will be considered in the near future to further improve understanding, in particular of the thalamic system underlying the epileptogenesis of absence seizures.

7.2.2 Bifurcation and synchronization of piecewise RKII sets

RKII sets appear to be the important functional unit of neural mass models and their interpretation is crucial if progress is to be made towards understanding EEG in the framework proposed by Freeman. Global stability for a particular case of a piecewise linear RKII system and for a narrow region in the parameter space has been shown. Extensions of these results are possible by defining finer piecewise linear approximations, thus ‘smoothing’ the nonsmooth RKII system to enable the study of a wider region of parameter space. However, it is important to note that a direct comparison between a piecewise linear approximation and a smooth dynamical system is not trivial and perhaps in some cases not possible. For the case of RKII models and in general neuroscience this question is very important indeed. It is believed in general that these approximations and in particular for firing rate functions are justified. Recall that the firing rate is not necessarily a smooth function. In particular, for the microscale models such as Hodgkin and Huxley type models [73], these will typically

have a non-smooth firing rate. Only by considering a population of neurons with dispersion of voltages are these functions smoothed out, for example by, a Gaussian. Thus, approximations to the “true” firing rate function (which is generally not accessible) are implicitly determined at what ever scale and detail a neuronal system is modelled. Hence, from this perspective approximations seem plausible. Moreover, an emerging theory called “regularization” (the name has not yet been formalized) has as its objective to understand and compare the dynamical behaviour between a smooth dynamical system and a nonsmooth version of the same system. However, this theory has only just begun to take shape and will take some time before any concrete answers to this question can be given. Other research avenues is to develop techniques for studying coupled RKII sets and synchronization between them as well determining the bifurcation sets for the nonsmooth RKII systems. Again these questions are very complex as the theories for non smooth systems are again only emerging and fundamental results do not exist. The main reason for this is that mathematical perturbation tools were designed for smooth dynamical systems and are theories for local analysis. For example the Taylor series expansion considers local derivatives however, it assumes continuum systems in a local neighbourhood where then analysis, such as bifurcations is possible. In contrast, it is not possible to consider a local neighbourhood in a nonsmooth dynamical system and by this argument piecewise linear systems are therefore global problems. Global theories, such as global bifurcations and global analysis are in general non trivial problems.

7.2.3 Seizure prediction

An interesting question, which can be addressed, is whether the identification of mechanisms in a model that explains the transition to seizure, can contribute to improvement of epilepsy treatment in clinical practice. For example, to simulate complex pharmacological effects, seizure suppression or even predict seizures. The answer to this question is a crucial one as it is the ultimate predictability test for a model. The corticothalamic model employed in this thesis shows that particular changes in a single parameter, governing the rate of synaptic interactions between cortex and specific relay nuclei (ν_{se}), provides an explanation of the transitions to absence seizures, as well as demonstrating a good agreement to clinical data. Consequently, an interesting step forward with the corticothalamic model would be to test the predictability of the model by implementing a seizure prediction method based on parameter

fitting of the model parameters from clinical data. This could be achieved by the development of a parameter-fitting code which tracks changes in parameters of interest in the model when fitted to different segments (epochs) of EEG. Most of the parameters would be constrained to a close interval of the initial inter-ictal state and the parameter(s) of interest fitted using subsequent epochs of data. Therefore a potentially useful algorithm would be to issue a warning if parameters came within some distance ϵ of determined bifurcation points δ . The precise value of ϵ would need to be statistically determined so as to maximise the anticipation rate, and minimise the false positive detection rate. This would need to be determined on a subject-to-subject basis. δ will also be determined on a subject-to-subject basis, as numerics have illustrated that changes in the other parameters of the model result in slightly different values of the bifurcation point. The parameter fitting algorithm will also have to ensure the underestimation of the parameter by taking into account system noise, measurement errors as well as the nonlinear nature of the clinical data. If this methodology proves to be successful then it could also be extended to other forms of seizure, for instance complex partial seizures. However, this extension is not trivial as this depends on the type of the bifurcation associated with the transition from normal to pathological state. The difficulty, lies in the fact that the nature of bifurcation associated with a particular transition is hardly accessible from signals generated by a system. This work is our current focus and is funded by the EPSRC.

Appendix A

This appendix provides some very basic terminology used to describe neuronal activity. For a more detailed review on the biophysics of neuronal activity the reader is asked to refer to [143].

A.1 Elements of a neuronal system

This section provides very basic terminology used to describe neuron activity. For a more detailed review on the biophysics of neuronal activity the reader is asked to refer to [143]. The elementary processing unit in the brain are neurons which are connected to each other forming very complex networks. A schematic illustrating the relevant concepts are shown in Fig. (A.1). In real brains, neurons and their connections are packed into a dense network with more than 10^4 somas and several kilometers of axons per cubic millimeter. In all areas of the brain there exists different neurons of different sizes and shapes.

A typical neuron can be divided into three functional parts: 1) *dendrites*; 2) *soma*; 3) *axon*. The dendrites play a role of input devices that collects signals from other neurons and transmits them to the soma. The soma is the central processing unit that activates nonlinearly if the total input exceeds a certain threshold, then an output signal is (action potential or spike) is generated. The output signal is propagated along the axon which delivers signal to other neurons. The junction between two neurons is called *synapse*. The sending neuron is commonly referred as the *presynaptic* neuron and to the receiving as the *postsynaptic* neuron.

Generally the axon of a presynaptic neuron makes contact with either a soma or a synapse of

a postsynaptic cell. The most common type of synapse is a chemical synapse. At a chemical synapse, the axon terminal comes very close to the postsynaptic neuron, leaving only a tiny gap between pre- and postsynaptic cell membranes, called the synaptic cleft. When an action potential arrives at a synapse, it triggers a complex chain of biochemical processing steps that lead to the release of neurotransmitter from the presynaptic terminal into the synaptic cleft. As soon as the transmitter molecules have reached the synaptic side, they will be detected by specialized receptors in the postsynaptic cell membrane and open (either directly or via a biochemical signaling chain) specific channels so that ions from the extracellular fluid flow into the cell. Examples of receptors mentioned in this thesis are excitatory receptors: AMPA and NMDA and inhibitory receptors: $GABA_A$ and $GABA_B$. The ion flux, in turn, leads to a change of the membrane potential at the postsynaptic site so that, in the end, the chemical signal is translated into an electrical response. The voltage response of the postsynaptic neuron to a presynaptic action potential is called the postsynaptic potential.

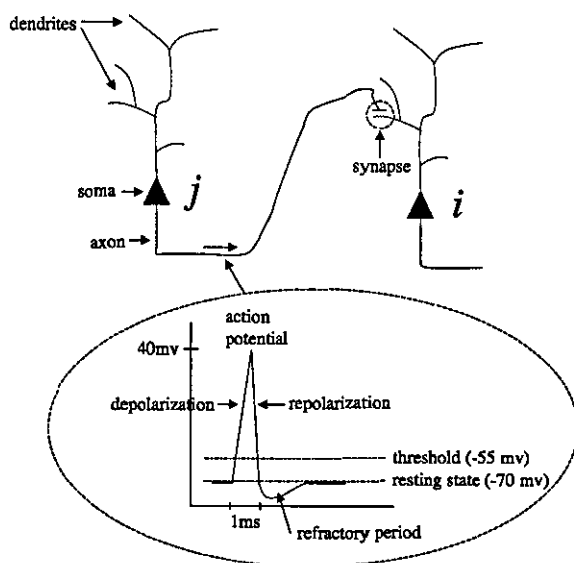


Figure A.1: Figure showing the relevant components in neuronal systems: Dendrite, soma and axon. The inset shows an example of a neuronal action potential (schematic). The action potential is a short voltage pulse of 1-2ms duration and an amplitude of about 100mv. This signal is transmitted from a presynaptic neuron *j* to a postsynaptic neuron *i*. The synapse is marked as a small dashed circle.

A.2 EEG frequency bands

The most common EEG frequencies are shown in Fig. (A.2) and are described as follows:

1. Delta (δ) activity (0.5-4Hz) is not normally recorded in the awake adult but it is a prominent feature of sleep and becomes increasingly dominant during the progress from stage 2 to stage 4 sleep. Delta waves have the largest amplitudes, normally between 20-200 μ V.
2. Theta (θ) patterns (4-7Hz) are seen in normal drowsiness and sleep, and during wakefulness in young children. Theta is also present in normal waking adults. It is generally noted that lower theta is associated with drowsiness and higher theta activity with cognitive effort.
3. Alpha (α) rhythms tend to be the most dominant brain oscillations in the human EEG. However it does tend to increase in amplitude during rest and relaxation (e.g. awake and eyes closed) and desynchronizes or becomes suppressed during intellectual functioning. Alpha rhythms often have a mean frequency centering around 10Hz with the maximum voltage over the parietal and occipital lobes, where amplitudes vary in the range 15 to 50 μ V. Evidence provided by Klimesch [92] indicates that within 8-13Hz alpha range, different frequency bands should be differentiated. These studies were able to show that desynchronization in the range of about 6-10Hz (lower alpha) reflects attentional processes whereas upper alpha desynchronization (in the range of about 10-12Hz) is selectively associated with processing of sensory-semantic information. The α -rhythm is thought to be generated in *thalamocortical feedback loops*.
4. Beta (β) waves (> 14 Hz) occur in all individuals, are usually of low amplitude and are normally distributed maximally over the frontal and central regions. Generally speaking beta rhythms signal an activated cortex.
5. Gamma (30-80 Hz) and Ripples (100-600Hz) these fast and ultra fast activities frequently coexist and may be present at various states of vigilance. Spontaneous brain rhythms during different states of vigilance may lead to increased responsiveness and plastic changes in the strength of connections among neurons, thus affecting information flow in the thalamocortical system.

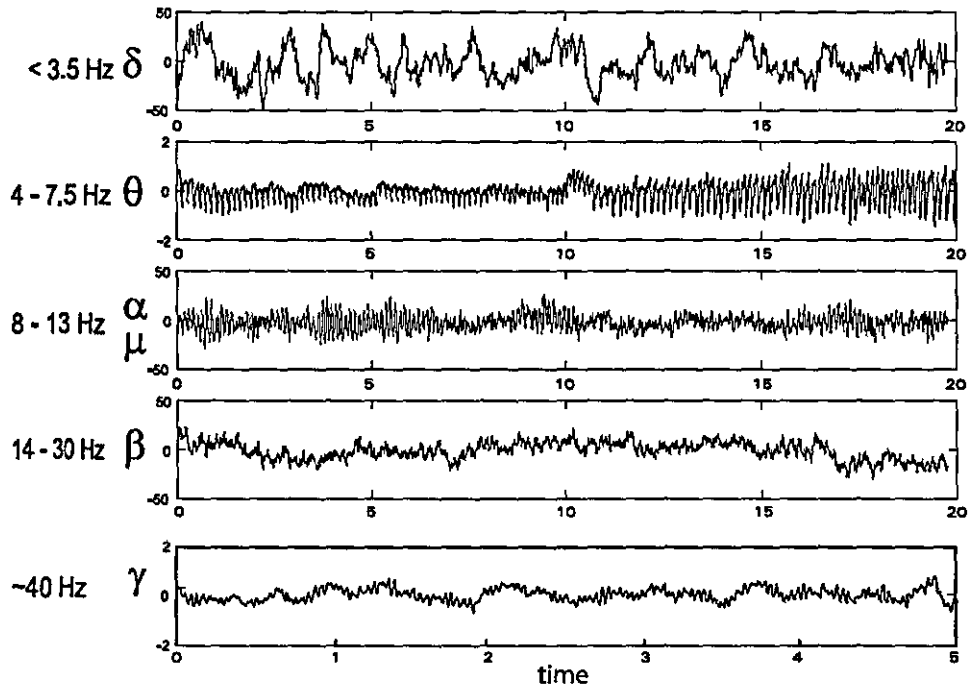


Figure A.2: *Example of various EEG rhythms. The delta, alpha and beta are Scalp EEG electrodes. The theta and gamma oscillations are depth electrodes. The X axis is seconds, Y axis: μV (δ , α and β), mV (θ and γ). Figure adapted from [157].*

A.3 EEG electrode placement

According to the international 10-20 system 20 electrodes are placed on the scalp for recording EEG. In this system each electrode is placed in terms of its proximity to particular brain regions - Frontal, Central, Temporal, Parietal and Occipital (in general the interelectrode distance is 60mm). Sites are given an odd number when on the left side of the head and an even number on the right, and midline electrodes are labeled 'z'. A schematic of the system is illustrated in Fig.(A.3).

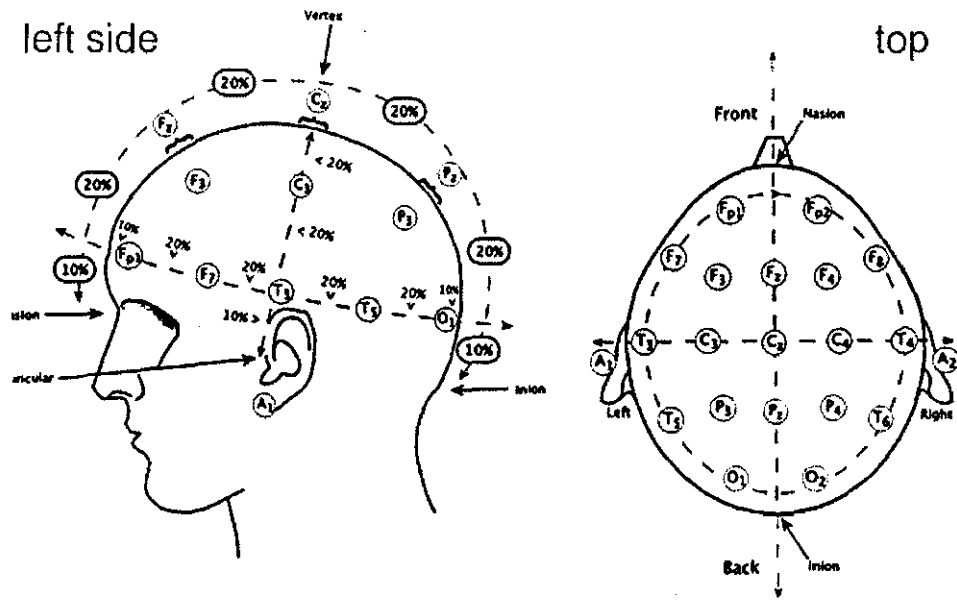


Figure A.3: F-Frontal lobe, T-Temporal lobe, C-Central lobe, P-Parietal lobe and O-Occipital lobe. "Z" refers to an electrode placed on the mid-line. (Figure obtained from the internet: <http://www.dcc.uchile.cl/~peortega/abi>)

Appendix B

This appendix provides the derivation of the continuum mean field model describing the temporal dynamics of a corticothalamic network and the parameter values used to simulate absence seizures activity. A brief description of the linear stability variables x , y and z for low frequencies is presented and results of the nonlinear analysis performed by software packages XPPAuto and DDE-Biftool is presented. The final section derives an analytical solution for two-bump wave form to provide an approximation of spike-wave oscillations.

B.1 First order delay differential equations for the global invariant model

Starting with the propagation of fields in the cortex and only considering spatial invariant solutions allows one to drop the Laplacian term, $\nu_a^2 \nabla^2$ in equation 4.3, which results in the following:

$$\frac{1}{\gamma_e^2} \frac{d^2}{dt^2} \phi_e(t) + \frac{2}{\gamma_e} \frac{d}{dt} \phi_e(t) + \phi_e(t) = Q_e(t). \quad (\text{B.1})$$

Equation (B.1) is equivalent to the following first order system:

$$\begin{cases} \frac{d}{dt} \phi_e(t) = y(t), \\ \frac{d}{dt} y(t) = \gamma_e^2 (-\phi_e(t) + \varsigma[V_e(t)]) - 2\gamma_e y(t), \end{cases}$$

by the following transformation:

$$\begin{cases} \frac{d}{dt} \phi_e(t) = y(t), \\ \frac{d}{dt} y(t) = \frac{d^2}{dt^2} \phi_e(t), \end{cases}$$

where the equality $Q_e = \varsigma[V_e(t)]$ has been applied. The same transformations are also applied for the synaptic coupling between the different brain regions. Consider first the cortical synaptic activity:

$$\left[\frac{1}{\alpha\beta} \frac{\partial^2}{\partial t^2} + \left(\frac{1}{\alpha} + \frac{1}{\beta} \right) \frac{\partial}{\partial t} + 1 \right] V_e(r, t) = \nu_{ee}\phi_e(r, t) + \nu_{ei}\phi_i(r, t) + \nu_{es}\phi_s(r, t - \tau).$$

Applying the following transformation:

$$\begin{cases} \frac{d}{dt} V_e(t) = z(t), \\ \frac{d}{dt} z(t) = \frac{d^2}{dt^2} V_e(t), \end{cases}$$

and further using the model assumptions from Chapter 4, the following equalities are employed: spatial symmetry considered in [131] between pyramidal cells and interneurons allows the following $-\nu_{ei}\phi_i(t) \simeq \nu_{ee}\phi_e(t)$. Furthermore, considering local approximations, $\nu_{ei}\phi_e(t) \simeq \nu_{ei}\varsigma[V_e(t)]$, and $\nu_{es}\phi_s(t - \tau) \simeq \nu_{es}\varsigma[V_s(t - \tau)]$, allows us to derive the following:

$$\begin{cases} \frac{d}{dt} V_e(t) = z(t), \\ \frac{d}{dt} z(t) = \alpha\beta (-V_e(t) + \nu_{ei}\phi_e(t) + \nu_{ee}\varsigma[V_e(t)] + \nu_{es}\varsigma[V_s(t - \tau)]) - (\alpha + \beta)z(t). \end{cases}$$

The same procedure is applied for the following couplings:

$$\begin{aligned} \left[\frac{1}{\alpha\beta} \frac{\partial^2}{\partial t^2} + \left(\frac{1}{\alpha} + \frac{1}{\beta} \right) \frac{\partial}{\partial t} + 1 \right] V_r(r, t) &= \nu_{re}\phi_e(r, t - \tau) + \nu_{rs}\phi_s(r, t), \\ \left[\frac{1}{\alpha\beta} \frac{\partial^2}{\partial t^2} + \left(\frac{1}{\alpha} + \frac{1}{\beta} \right) \frac{\partial}{\partial t} + 1 \right] V_s(r, t) &= \nu_{se}\phi_e(r, t - \tau) + \nu_{sr}\phi_r(r, t) + \nu_{sn}\phi_n(r, t), \end{aligned}$$

with the following transformations respectively:

$$\begin{cases} \frac{d}{dt} v_r(t) = v(t), \\ \frac{d}{dt} v(t) = \frac{d^2}{dt^2} V_r(t), \end{cases} \quad \text{and} \quad \begin{cases} \frac{d}{dt} V_s(t) = w(t), \\ \frac{d}{dt} w(t) = \frac{d^2}{dt^2} V_s(t), \end{cases}$$

which finally results in the global invariant averaged brain-corticothalamic field model

$$\begin{cases} \frac{d}{dt} \phi_e(t) = y(t), \\ \frac{d}{dt} y(t) = \gamma_e^2 [-\phi_e(t) + \varsigma(V_e(t))] - 2\gamma_e y(t), \\ \frac{d}{dt} V_e(t) = z(t), \\ \frac{d}{dt} z(t) = \alpha\beta [-V_e(t) + \nu_{ee}\phi_e(t) + \nu_{ei}\varsigma(V_e(t)) + \nu_{es}\varsigma(V_s(t - \tau))] - (\alpha + \beta)z(t), \\ \frac{d}{dt} V_s(t) = w(t), \\ \frac{d}{dt} w(t) = \alpha\beta [-V_s(t) + \nu_{sn}\phi_n + \nu_{se}\phi_e(t - \tau) + \nu_{sr}\varsigma(V_r(t))] - (\alpha + \beta)w(t), \\ \frac{d}{dt} V_r(t) = v(t), \\ \frac{d}{dt} v(t) = \alpha\beta [-V_r(t) + \nu_{re}\phi_e(t - \tau) + \nu_{rs}\varsigma(V_s(t))] - (\alpha + \beta)v(t). \end{cases} \quad (\text{B.2})$$

B.1.1 Parameters values employed in the model

The parameters values used to simulate absence seizures are given in the following table:

Quantity	Description	<i>Petit Mal</i>
γ_e	Average ratio between pulse velocity and axon range.	100 s^{-1}
θ	Threshold of membrane potential before a cell fires.	0.015 V
σ	Standard deviation (versus voltage) of an ensembles firing rate.	0.006 V
Q^{max}	Average maximum firing rate of a cell.	250 s^{-1}
α	Receptor inverse of decay time of potential produced at synapse.	50 s^{-1}
β	Receptor inverse rise time of potential produced at synapse.	200 s^{-1}
t_0	Corticothalamic return time (complete return loop).	$80ms$
ν_{ei}	Inhibitory corticocortical coupling strength.	$-18e-4 \text{ Vs}$
ν_{ee}	Excitatory corticocortical coupling strength.	$10e-4 \text{ Vs}$
ν_{es}	Specific thalamic nuclei to cortical coupling.	$32e-4 \text{ Vs}$
ν_{se}	Cortical to specific thalamic nuclei connection strength.	0.0044 Vs
ν_{sr}	Thalamic reticular to specific thalamic nucleus coupling strength.	$-8e-4 \text{ Vs}$
ν_{sn}	Nonspecific subthalamic input strength into specific neurons.	$20e-4 \text{ Vs}$
ν_{re}	Excitatory cortical to thalamic reticular nucleus parameter.	$16e-4 \text{ Vs}$
ν_{rs}	Specific to reticular thalamic nuclei coupling strength.	$6e-4 \text{ Vs}$

Table B.1: Parameter values for absence seizures (*Petit mal* or spike-wave activity).

B.2 Frequency domain linear stability analysis and reduced parameter space

Studying the linear stability criteria for the above system (B.2) permits mapping of the boundary that marks the transition between steady-state behaviour and nonlinear oscillations. Previous studies of the model for realistic parameter ranges revealed a small number of key instabilities that constrain the way nonlinear oscillations may arise [131]. In these earlier studies, the model reveals the following instabilities: 3-Hz (which is further analysed in this

thesis), alpha, slow-wave ($< 1\text{Hz}$) and spindle (approximately 12 Hz). The occurrence of only a small number of instabilities suggests that it may also be possible to study the dynamics and stability of the brain in a phase space of low dimensionality. Indeed formal analysis of low-frequency instabilities suggest that 3 variables x , y and z (parameterising corticocortical, corticothalamic, and intrathalamic instability) capture the parameter combinations at which the brain model loses instability. Figure B.1 illustrates the boundaries and the variables are defined as follows

$$\begin{cases} x = \frac{G_{ee}}{1-G_{ei}}, \\ y = \frac{G_{ese}+G_{esre}}{(1-G_{srs})(1-G_{ei})}, \\ z = -\frac{G_{srs}\alpha\beta}{(\alpha+\beta)^2} \end{cases} \quad (\text{B.3})$$

where the gain $G_{ab} = \rho_a \nu_{ab}$ is the response in neurons a to unit input from neurons b , sigmoid slope $\rho_a = d\zeta(V_a)/dV_a$, with $G_{ese} = G_{es}G_{se}$, $G_{esre} = G_{es}G_{sr}G_{re}$ and $G_{srs} = G_{sr}G_{rs}$. In [131], these parameters have only been used in the steady state where they were derived. In this thesis these are redefined to define a coordinate transformation of the dynamical variables $V_a(t)$. The parameters x, y and z give a measure of the level of activity in the brain structures comprising the model. Specifically x describes purely cortical activity, y describes activity in the 2 corticothalamic loops (i.e between the reticular and specific nuclei). Thus, x, y and z relate to cortical, corticothalamic, and intrathalamic stabilities respectively.

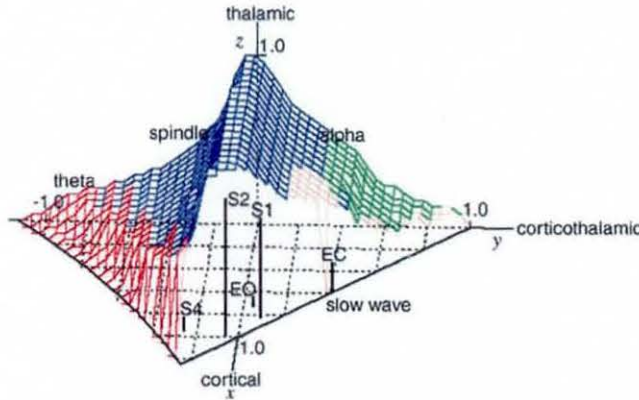


Figure B.1: The linear stability zone for the corticothalamic model within the truncated space spanned by the 3 stability variables x , y and z . The shaded surface represents the values at which the system loses stability at theta (red), spindle (blue), and alpha (green) frequencies. Within the tent are shown representative values for eyes closed, eyes open, and sleep stages 1, 2 and 4. The present study concerns the onset of nonlinear oscillations as the system passes outside of the stability zone. Figure from [131].

B.3 DDE-Biftool results for corticothalamic model

This section provides complementary results obtained by DDE-Biftool and XPP auto. In DDE-Biftool, solution branches are computed and stability analysis are performed in each branch point. To numerically follow solutions branches, initial data (preferably stable) obtained from simulations have to be entered into the software package. Thus, a natural starting point for the continuation process is by entering stable fixed points data obtained from numerical simulations of the delay equations (B.2). Focusing on the cortical field (ϕ_e) and the parameter of interest ν_{se} allows one to follow the stable branch solution shown in Fig. (B.2 a). Note that DDE-Biftool does not distinguish graphically between unstable and stable points. Instead it is necessary to iterate along a solution branch and determine for each branch point the corresponding eigenvalues. At $\nu_{se} \approx 1.8 \times 10^{-3}Vs$ a supercritical Hopf bifurcation is found and this highlighted by the first dashed box in Fig. (B.2). The corresponding eigenvalues are plotted in Fig. (B.2 c) which shows two conjugate pairs (in red stars) crossing the imaginary axis. Note on the left hand side of the complex plane an infinite number of eigenvalues, this is due the characteristic quasi polynomial obtained from the delay equation (see section 2.4.6). Continuing varying ν_{se} the stable fixed point becomes unstable (however this is not graphically differentiated by DDE-Biftool) and further along the branch a saddle node bifurcation are found at $\nu_{se} \approx 1.5 \times 10^{-2}Vs$ (shown in the following red dashed box). The eigenvalues corresponding to the saddle node bifurcation is shown in Fig. (B.2 d) which illustrates a single eigenvalue crossing the imaginary axis. Coexistence of stable and unstable solutions lie in the region $1.8 \times 10^{-3}Vs \leq \nu_{se} \leq 1.5 \times 10^{-2}Vs$, where the stable steady state corresponds to $\phi_e = Q^{max}$ (maximum firing rate of a neuronal population). Subsequently, following the Hopf solution branch shown in Fig. (B.2 b) illustrate the amplitude of the limit cycles gradually increasing. Towards the end of the continuation branch of the periodic solutions, a curve (ϕ_e, ν_{se}) folds back towards itself is found. Its precise nature and stability is yet to be determined. A close up of this curve is illustrated in Fig. (B.3). Further analysis of this solution path was not possible as DDE-Biftool becomes rather unstable. However, interesting future work would be to determine precisely the behaviour of the solution path by determining the Floquet-multipliers to verify if these are in fact unstable solutions.

Recall from section 4.3.1 that the ‘spike-bifurcation’ related to the spike-wave form of absence

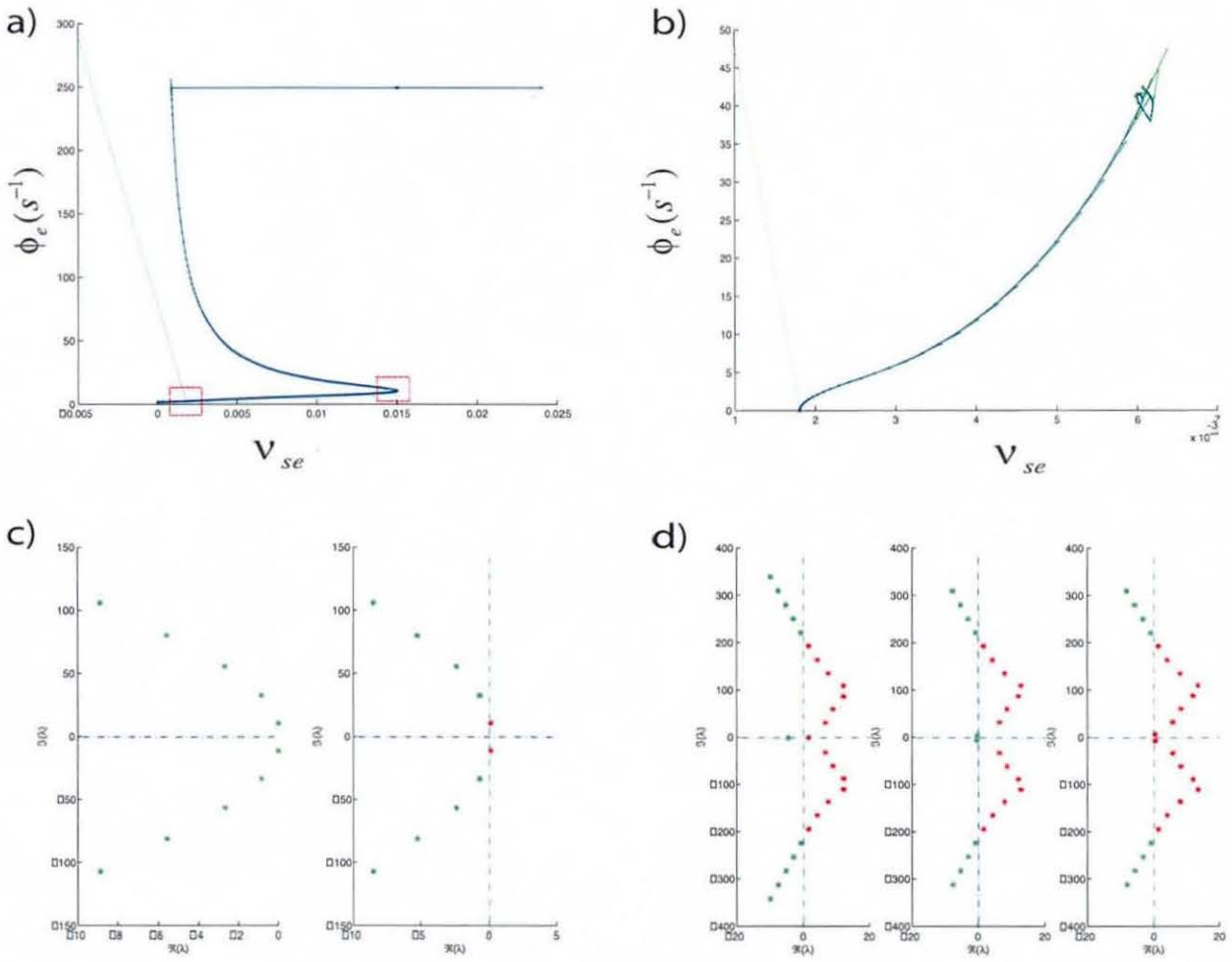


Figure B.2: a) Continuation of steady state solutions. The first red dashed box indicates a Hopf bifurcation at $\nu_{se} \approx 1.8 \times 10^{-3}$ Vs. Subsequently varying the parameter results in a saddle node bifurcation which is highlighted by the second red dashed box at $\nu_{se} \approx 1.5 \times 10^{-2}$ Vs. Coexistence of stable and unstable solutions lie in the region 1.8×10^{-3} Vs $\leq \nu_{se} \leq 1.5 \times 10^{-2}$ Vs, where the stable steady state corresponds to $\phi_e = Q^{max}$ (maximum firing rate of a neuronal population). b) Continuation of periodic solutions (Hopf branch). At $\nu_{se} > 6 \times 10^{-3}$ Vs, the branch turns back on itself and its precise nature and stability is yet to be found. Future work will further investigate this solution path by determining the Floquet-multipliers. c) A plot of the eigenvalues (for $\nu_{se} \approx 1.8 \times 10^{-3}$ Vs) demonstrating a conjugate pair crossing the imaginary axis (red stars) Hopf bifurcation. d) A plot of the eigenvalues corresponding to the saddle node bifurcation at ($\nu_{se} \approx 1.5 \times 10^{-2}$ Vs). The saddle occurs when a zero eigenvalue crosses the imaginary axis as the parameter ν_{se} varies through the following values: $\nu_{se} = 1.499 \times 10^{-2}$, $\nu_{se} = 1.497 \times 10^{-2}$, $\nu_{se} = 1.492 \times 10^{-2}$.

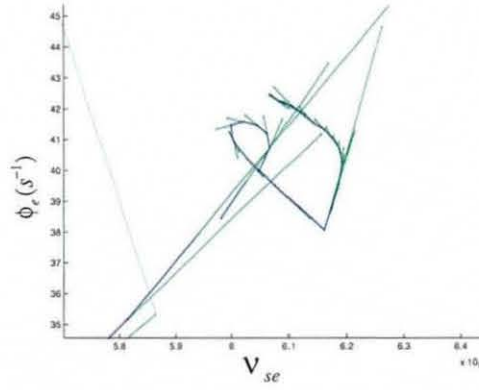


Figure B.3: A close up of Fig. (B.2) highlighting that via numerical continuation the branch of periodic solutions folds back on itself at $\nu_{se} > 6 \times 10^{-3}$ Vs. The precise nature of the solution path will be investigated by determining the Floquet-multipliers.

seizures remained unresolved. This difficulty was because DDE-Biftool was unable to flag the conditions for this bifurcation as these could correspond to global bifurcations. However, a time series realization of the ‘spike-bifurcation’ shows an extra period per oscillation. This almost seems like a period-doubling, however the bifurcation branch takes the same minimum as the previous period oscillation but a different maxima when compared to the first period oscillation. Furthermore, numerically varying the delay parameter τ the “spike-bifurcation” initiates at different parameter sets of ν_{se} , where an increase in τ give rise to “spike-bifurcation” appearing in the solution branch of previous Hopf solutions. That is, the periodic solutions seem to bifurcate in a similar way as it would occur in a period doubling. This is illustrated in Fig. (B.4 a). Further, by removing the delay term in the corticothalamic model it is verified that the “spike-bifurcation” disappears and this is shown in Fig. (B.4 b). Unfortunately running DDE-Biftool with the ‘period-doubling’ point obtained from numerical simulation results in a non-convergence of the solution branch, therefore the software package fails to follow it. Future work remains to determine the nature of these solutions which could be important to reveal the genesis of absence seizure observed at macroscopic levels.

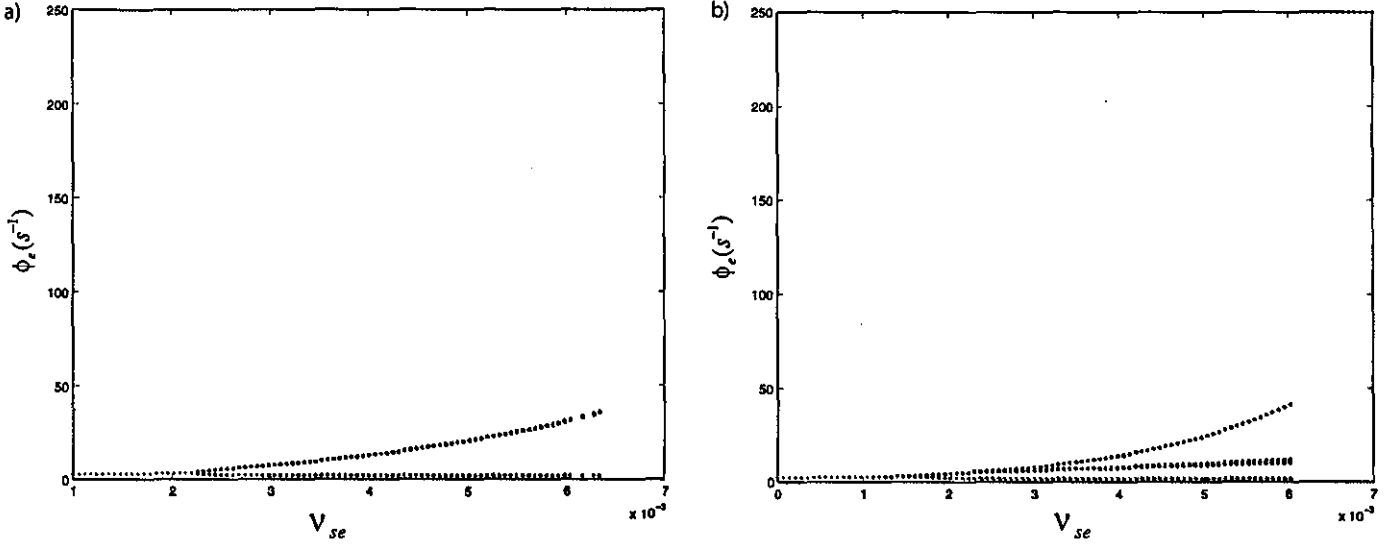


Figure B.4: A comparison of the bifurcations to determine the nature of 'spike bifurcation'. An increase in the parameter τ has the effect of increasing the parameter range window of ν_{se} where the 'spike-bifurcation' is observed. A further increase seem to give rise to a bifurcation similar to a period-doubling. Here the 'period-doubling' results in a periodic solution with the same minima of the previous period solutions but with a different maxima. However, the origin of this bifurcation remains unresolved. a) System with increased delay $\tau = 0.2$. b) System without delay.

B.3.1 XPPAuto results for corticothalamic model without delay

Results from DDE-Biftool are here complemented with those obtained by XPPAuto. The corticothalamic model is reduced by removing the time delays and a complete bifurcation is carried out. The removal of delays is justified when trying to find steady solutions of the corticothalamic delayed model. The precise formalization of the steady state of a delay equation is given in section (2.4.6) by equation (2.32). Carrying out the continuation of the solution branch (ϕ_e, ν_{se}) the steady state solutions of the delay equations are observed and these results can be compared to those obtained by DDE-biftool. Starting from a branch of fixed point solutions and varying ν_{se} a Hopf bifurcation is born at $\nu_{se} = 0.0022$ Vs. Further varying ν_{se} , the branch of steady solutions becomes unstable and subsequently the unstable fixed point bifurcates to an unstable saddle node bifurcation appearing at $u_{se} = 0.0149$. The unstable saddle node then leads to a stable branch giving rise to multi-stability. Coexistence of stable and unstable solutions lie in the region $0.0022 \text{ Vs} \leq u_{se} \leq 0.0149 \text{ Vs}$, where the stable steady state corresponds to $\phi_e = Q^{max}$ (maximum firing rate of a neuronal population).

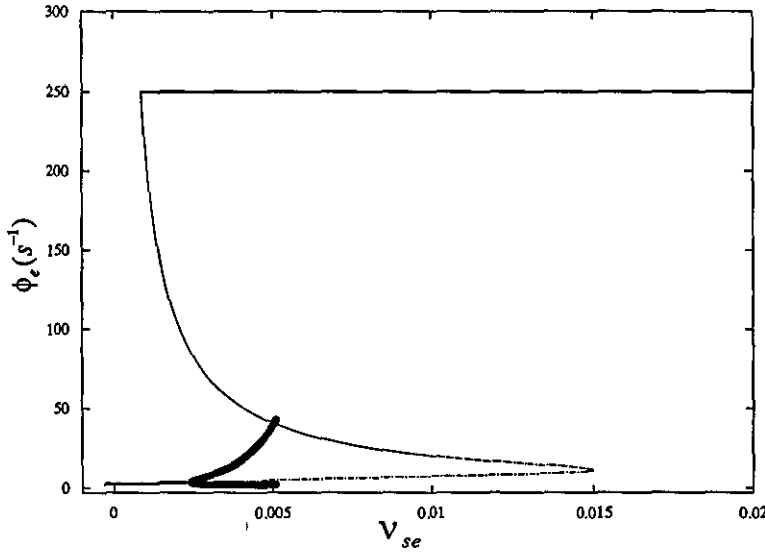


Figure B.5: *XPPAuto solution branch continuation for the corticothalamic model without delay for the absence seizure case. A Hopf bifurcation is born at $u_{se} = 0.0022$ and an unstable saddle node bifurcation appears at $u_{se} = 0.0149$ Vs. Multistability exists for parameter regimes $0.0022 \text{ Vs} \leq u_{se} \leq 0.0149 \text{ Vs}$.*

B.4 Two-bump solution of a reduced piecewise linear RKII set

This section presents the calculation of the piecewise approximation equations for a ‘two-bump’ wave form arising in specific relay nuclei. This equation of motion for the specific relay nuclei is given as follows:

$$\ddot{V}_s + (\alpha + \beta)\dot{V}_s + \alpha\beta V_s = \nu_{sr}\alpha\beta\varsigma[V_r(t)] + \nu_{se}\phi_{\text{external}}. \quad (\text{B.4})$$

As indicated in section 4.5, the homogeneous solution for the specific neurons are identical to that for the reticular neurons hence,

$$V_s^H(t) = Ae^{(-\alpha t)} + Be^{(-\beta t)}.$$

Equation (B.4) can be solved for each part of the RHS separately, thus the solution for the external forcing is equivalent to that in system (4.10) (section 4.5), replacing the parameter ν_{re} by ν_{se} in the appropriate coefficients. For the remaining part, the aim is to find a solution of equation (B.4) using the method of variation of parameters. Specifically, we seek to find functions $c_1(t)$ and $c_2(t)$ satisfying,

$$F(t) = V_s^P(t) = c_1(t)e^{-\alpha t} + c_2(t)e^{-\beta t}, \quad (\text{B.5})$$

such that,

$$\dot{c}_1(t)e^{(-\alpha t)} + \dot{c}_2(t)e^{(-\beta t)} = 0, \quad (\text{B.6})$$

$$-\alpha\dot{c}_1(t)e^{(-\alpha t)} - \beta\dot{c}_2(t)e^{(-\beta t)} = F(t), \quad (\text{B.7})$$

where

$$F(t) = \alpha\beta\nu_{sr}\varsigma[V_r(t)].$$

Finding an analytical solution in the present form is not possible due to the sigmoidal nature of the function $\varsigma(x)$. In order to obtain a closed form solution an approximation solution to ς must be taken. From numerical simulations of the system, it was observed that the solution of $V_s(t)$ was bounded in a region determined by oscillations about steady-state solutions for $V_r(t)$ and $V_s(t)$. Interestingly, for all parameter regimes considered, these steady-states occupied the lower part of the sigmoidal curve where the transition from a shallow to a steep gradient

occurred. This nonlinear phenomena could not be captured either by linearizing about one of these steady-states nor by taking a Heaviside approximation, hence a piecewise linear approximation was chosen for ς . This was chosen by linearizing about each of the steady-state solutions for $V_r(t)$ and $V_s(t)$ (which was determined by XPPAuto) and the linearised equations is given in section 4.5 equation (4.14).

This resulted in the following form:

$$\tilde{\varsigma}[V_r(t)] = \begin{cases} V_{s*}^m \sin(\omega t + \delta) + V_{s*}^b, & \frac{2N\pi}{\omega} < t \leq \frac{2N\pi + \hat{b} - \delta}{\omega}, \\ V_{r*}^m \sin(\omega t + \delta) + V_{r*}^b, & \frac{2N\pi + \hat{b} - \delta}{\omega} < t \leq \frac{(2N+1)\pi - (\hat{b} + \delta)}{\omega}, \\ V_{s*}^m \sin(\omega t + \delta) + V_{s*}^b, & \frac{(2N+1)\pi - (\hat{b} + \delta)}{\omega} < t \leq \frac{(2N+1)\pi}{\omega}, \end{cases} \quad (\text{B.8})$$

where V_{a*}^m and V_{a*}^b are the gradient and intercept respectively of the linearization for the steady-state solution of $V_a(t)$ and $\hat{b} = \arcsin\left(\frac{b}{K}\right)$ is the intersection point of the two linearizations (i.e. the point at which the derivative loses continuity). Rearranging (B.6) and (B.7) results in

$$(\beta - \alpha) e^{-\alpha t} \dot{c}_1(t) = \tilde{F}(t), \quad (\text{B.9})$$

$$(\alpha - \beta) e^{-\beta t} \dot{c}_2(t) = \tilde{F}(t), \quad (\text{B.10})$$

where

$$\tilde{F}(t) = \alpha\beta\nu_{sr}\tilde{\varsigma}[V_r(t)].$$

The aim is now to solve (B.9) and (B.10) for each of the intervals for t in (B.8). Without loss of generality, solutions for the first period only are presented, assuming the initial conditions to be zero. Thus, solutions of $c_1(t)$ and $c_2(t)$ are given by

$$c_1(t) = \frac{1}{(\beta - \alpha)} \left(\int_0^t \frac{\tilde{F}(\tau)}{e^{-\alpha\tau}} d\tau \right), \quad (\text{B.11})$$

$$c_2(t) = \frac{1}{(\alpha - \beta)} \left(\int_0^t \frac{\tilde{F}(\tau)}{e^{-\beta\tau}} d\tau \right), \quad (\text{B.12})$$

on each of the appropriate intervals.

B.4.1 Interval I: $0 \leq t \leq \frac{\hat{b}-\delta}{\omega}$

From equation (B.11) we obtain

$$\begin{aligned}
 c_1(t) &= \frac{V_{s*}^m}{(\beta - \alpha)} \int_0^t e^{\alpha\tau} \sin(\omega\tau + \delta) d\tau + \frac{V_{s*}^b}{(\beta - \alpha)} \int_0^t e^{\alpha\tau} d\tau, \\
 &= \frac{\alpha V_{s*}^m}{(\alpha^2 + \omega^2)(\beta - \alpha)} \left(e^{\alpha t} \left(\sin(\omega t + \delta) - \frac{\omega}{\alpha} \cos(\omega t + \delta) \right) - \sin \delta + \frac{\omega}{\alpha} \cos \delta \right) \\
 &\quad + \frac{V_{s*}^b}{\alpha(\beta - \alpha)} (e^{\alpha t} - 1), \\
 &= \frac{\alpha V_{s*}^m}{(\alpha^2 + \omega^2)(\beta - \alpha)} \left(e^{\alpha t} \left(\mathcal{A}_\alpha \sin(\omega t + \widehat{\delta}_\alpha^-) \right) - \mathcal{A}_\alpha \sin \widehat{\delta}_\alpha^- \right) \\
 &\quad + \frac{V_{s*}^b}{\alpha(\beta - \alpha)} (e^{\alpha t} - 1), \tag{B.13}
 \end{aligned}$$

where

$$\mathcal{A}_r = \sqrt{1 + \frac{\omega^2}{r^2}}$$

and

$$\widehat{\delta}_r^\pm = \delta + \arcsin\left(\frac{\pm\omega}{r\mathcal{A}_r}\right).$$

Note from comparison of (B.11) and (B.12) that solutions for $c_2(t)$ are similar to those for $c_1(t)$, the coefficients α and β being transposed in (B.13) resulting in the following form for $c_2(t)$:

$$\begin{aligned}
 c_2(t) &= \frac{\beta V_{s*}^m}{(\beta^2 + \omega^2)(\alpha - \beta)} \left(e^{\beta t} \left(\mathcal{A}_\beta \sin(\omega t + \widehat{\delta}_\beta^-) \right) - \mathcal{A}_\beta \sin \widehat{\delta}_\beta^- \right) \\
 &\quad + \frac{V_{s*}^b}{\beta(\alpha - \beta)} (e^{\beta t} - 1). \tag{B.14}
 \end{aligned}$$

Substituting (B.13) and (B.14) into (B.5) the solution to the particular function $F(t)$ on the first interval is obtained:

$$\begin{aligned}
 V_s^P(t) &= \frac{\alpha V_{s*}^m \mathcal{A}_\alpha}{(\alpha^2 + \omega^2)(\beta - \alpha)} \left(\sin(\omega t + \widehat{\delta}_\alpha^-) - e^{-\alpha t} \sin \widehat{\delta}_\alpha^- \right) + \frac{V_{s*}^b}{\alpha(\beta - \alpha)} (1 - e^{-\alpha t}) \\
 &\quad + \frac{\beta V_{s*}^m \mathcal{A}_\beta}{(\beta^2 + \omega^2)(\alpha - \beta)} \left(\sin(\omega t + \widehat{\delta}_\beta^-) - e^{-\beta t} \sin \widehat{\delta}_\beta^- \right) \\
 &\quad + \frac{V_{s*}^b}{\beta(\alpha - \beta)} (1 - e^{-\beta t}). \tag{B.15}
 \end{aligned}$$

It is important to note that this solution consists of decaying terms and a periodic term, with phase shift $\widehat{\delta}$, which is different to that for the external forcing, which has phase shift δ .

B.4.2 Interval II: $\frac{\hat{b}-\delta}{\omega} < t \leq \frac{\pi-\hat{b}-\delta}{\omega}$

To solve for $c_1(t)$ and $c_2(t)$ on this second region, note that the solutions will be dependent on the behaviour of the functions on the previous interval. Denoting $f_\rho(t) = V_{\rho*}^m \sin(\omega t + \delta) + V_{\rho*}^b$, the solution to $c_1(t)$ will behave as

$$\begin{aligned} c_1(t) &= \frac{1}{(\beta - \alpha)} \left(\int_0^t \frac{\tilde{F}(\tau)}{e^{-\alpha\tau}} d\tau \right), \\ &= \frac{1}{(\beta - \alpha)} \left(\int_0^{\frac{\hat{b}-\delta}{\omega}} e^{\alpha\tau} f_s(\tau) d\tau + \int_{\frac{\hat{b}-\delta}{\omega}}^t e^{\alpha\tau} f_r(\tau) d\tau \right). \end{aligned} \quad (\text{B.16})$$

Calculating the integrals in (B.16) results in

$$\begin{aligned} c_1(t) &= \frac{\alpha \mathcal{A}_\alpha}{(\beta - \alpha)(\alpha^2 + \omega^2)} \left(V_{r*}^m e^{\alpha t} \sin(\omega t + \widehat{\delta}_\alpha^-) \right. \\ &\quad + (V_{s*}^m - V_{r*}^m) e^{\frac{\alpha(\hat{b}-\delta)}{\omega}} \sin(\hat{b} + \widehat{\delta}_\alpha^- - \delta) - V_{s*}^m \sin \widehat{\delta}_\alpha^- \Big) \\ &\quad + \frac{1}{\alpha(\beta - \alpha)} \left(V_{r*}^b e^{\alpha t} + (V_{s*}^b - V_{r*}^b) e^{\frac{\alpha(\hat{b}-\delta)}{\omega}} - V_{s*}^b \right). \end{aligned} \quad (\text{B.17})$$

In a similar fashion to the previous subsection, the solution for $c_2(t)$ is found by transposing the coefficients α and β in (B.17) to give

$$\begin{aligned} c_2(t) &= \frac{\beta \mathcal{A}_\beta}{(\alpha - \beta)(\beta^2 + \omega^2)} \left(V_{r*}^m e^{\beta t} \sin(\omega t + \widehat{\delta}_\beta^-) \right. \\ &\quad + (V_{s*}^m - V_{r*}^m) e^{\frac{\beta(\hat{b}-\delta)}{\omega}} \sin(\hat{b} + \widehat{\delta}_\beta^- - \delta) - V_{s*}^m \sin \widehat{\delta}_\beta^- \Big) \\ &\quad + \frac{1}{\beta(\alpha - \beta)} \left(V_{r*}^b e^{\beta t} + (V_{s*}^b - V_{r*}^b) e^{\frac{\beta(\hat{b}-\delta)}{\omega}} - V_{s*}^b \right). \end{aligned} \quad (\text{B.18})$$

Finally substituting (B.17) and (B.18) into (B.5) the solution to the particular function $F(t)$ on the second interval is determined:

$$\begin{aligned} V_s^P(t) &= \frac{\alpha \mathcal{A}_\alpha}{(\beta - \alpha)(\alpha^2 + \omega^2)} \left(V_{r*}^m \sin(\omega t + \widehat{\delta}_\alpha^-) + (V_{s*}^m - V_{r*}^m) e^{\frac{\alpha(\hat{b}-\delta-\omega t)}{\omega}} \sin(\hat{b} + \widehat{\delta}_\alpha^- - \delta) \right. \\ &\quad - V_{s*}^m e^{-\alpha t} \sin \widehat{\delta}_\alpha^- \Big) + \frac{1}{\alpha(\beta - \alpha)} \left(V_{r*}^b + (V_{s*}^b - V_{r*}^b) e^{\frac{\alpha(\hat{b}-\delta-\omega t)}{\omega}} - V_{s*}^b e^{-\alpha t} \right) \\ &\quad + \frac{\beta \mathcal{A}_\beta}{(\alpha - \beta)(\beta^2 + \omega^2)} \left(V_{r*}^m \sin(\omega t + \widehat{\delta}_\beta^-) + (V_{s*}^m - V_{r*}^m) e^{\frac{\beta(\hat{b}-\delta-\omega t)}{\omega}} \sin(\hat{b} + \widehat{\delta}_\beta^- - \delta) \right. \\ &\quad - V_{s*}^m e^{-\beta t} \sin \widehat{\delta}_\beta^- \Big) + \frac{1}{\beta(\alpha - \beta)} \left(V_{r*}^b + (V_{s*}^b - V_{r*}^b) e^{\frac{\beta(\hat{b}-\delta-\omega t)}{\omega}} - V_{s*}^b e^{-\beta t} \right). \end{aligned} \quad (\text{B.19})$$

For this period of time, the periodic component has the same phase shift, $\widehat{\delta}_r^-$, but a different amplitude, V_{r*}^m .

B.4.3 Interval III: $\frac{\pi-\hat{b}-\delta}{\omega} < t \leq \frac{2\pi}{\omega}$

Once again the solutions for $c_1(t)$ and $c_2(t)$ on this final region, will be dependent on their behaviour in both of the previous regions. Proceeding in a similar manner to subsection B.4.2, the solution for $c_1(t)$ will be given by:

$$\begin{aligned} c_1(t) &= \frac{1}{(\beta - \alpha)} \left(\int_0^t \frac{\tilde{F}(\tau)}{e^{-\alpha\tau}} d\tau \right), \\ &= \frac{1}{(\beta - \alpha)} \left(\int_0^{\frac{\hat{b}-\delta}{\omega}} e^{\alpha\tau} f_s(\tau) d\tau + \int_{\frac{\hat{b}-\delta}{\omega}}^{\frac{\pi-\hat{b}-\delta}{\omega}} e^{\alpha\tau} f_r(\tau) d\tau + \int_{\frac{\pi-\hat{b}-\delta}{\omega}}^t e^{\alpha\tau} f_s(\tau) d\tau \right). \end{aligned} \quad (\text{B.20})$$

The solution of (B.20) is given by

$$\begin{aligned} c_1(t) &= \frac{\alpha \mathcal{A}_\alpha}{(\beta - \alpha)(\alpha^2 + \omega^2)} \left(V_{s*}^m e^{\alpha t} \sin(\omega t + \widehat{\delta}_\alpha^-) + (V_{r*}^m - V_{s*}^m) e^{\frac{\alpha(\pi-\hat{b}-\delta)}{\omega}} \sin(\hat{b} + \widehat{\delta}_\alpha^+ - \delta) \right) \\ &+ (V_{s*}^m - V_{r*}^m) e^{\frac{\alpha(\hat{b}-\delta)}{\omega}} \sin(\hat{b} + \widehat{\delta}_\alpha^- - \delta) - V_{s*}^m \sin \widehat{\delta}_\alpha^- \\ &+ \frac{1}{\alpha(\beta - \alpha)} \left(V_{s*}^b e^{\alpha t} + (V_{r*}^b - V_{s*}^b) e^{\frac{\alpha(\pi-\hat{b}-\delta)}{\omega}} + (V_{s*}^b - V_{r*}^b) e^{\frac{\alpha(\hat{b}-\delta)}{\omega}} - V_{s*}^b \right) \end{aligned} \quad (\text{B.21})$$

From (B.21) the solution for $c_2(t)$ is obtained by transposing α 's and β 's to give

$$\begin{aligned} c_2(t) &= \frac{\beta \mathcal{A}_\beta}{(\alpha - \beta)(\beta^2 + \omega^2)} \left(V_{s*}^m e^{\beta t} \sin(\omega t + \widehat{\delta}_\beta^-) + (V_{r*}^m - V_{s*}^m) e^{\frac{\beta(\pi-\hat{b}-\delta)}{\omega}} \sin(\hat{b} + \widehat{\delta}_\beta^+ - \delta) \right) \\ &+ (V_{s*}^m - V_{r*}^m) e^{\frac{\beta(\hat{b}-\delta)}{\omega}} \sin(\hat{b} + \widehat{\delta}_\beta^- - \delta) - V_{s*}^m \sin \widehat{\delta}_\beta^- \\ &+ \frac{1}{\beta(\alpha - \beta)} \left(V_{s*}^b e^{\beta t} + (V_{r*}^b - V_{s*}^b) e^{\frac{\beta(\pi-\hat{b}-\delta)}{\omega}} + (V_{s*}^b - V_{r*}^b) e^{\frac{\beta(\hat{b}-\delta)}{\omega}} - V_{s*}^b \right) \end{aligned} \quad (\text{B.22})$$

Finally substituting (B.21) and (B.22) into (B.5) the solution to the particular function $F(t)$ on this third region is found:

$$\begin{aligned} V_s^P(t) &= \frac{\alpha \mathcal{A}_\alpha}{(\beta - \alpha)(\alpha^2 + \omega^2)} \left(V_{s*}^m \sin(\omega t + \widehat{\delta}_\alpha^-) + (V_{r*}^m - V_{s*}^m) e^{\frac{\alpha(\pi-\hat{b}-\delta-\omega t)}{\omega}} \sin(\hat{b} + \widehat{\delta}_\alpha^+ - \delta) \right) \\ &+ (V_{s*}^m - V_{r*}^m) e^{\frac{\alpha(\hat{b}-\delta-\omega t)}{\omega}} \sin(\hat{b} + \widehat{\delta}_\alpha^- - \delta) - V_{s*}^m e^{-\alpha t} \sin \widehat{\delta}_\alpha^- \\ &+ \frac{1}{\alpha(\beta - \alpha)} \left(V_{s*}^b + (V_{r*}^b - V_{s*}^b) e^{\frac{\alpha(\pi-\hat{b}-\delta-\omega t)}{\omega}} + (V_{s*}^b - V_{r*}^b) e^{\frac{\alpha(\hat{b}-\delta-\omega t)}{\omega}} - V_{s*}^b e^{-\alpha t} \right) \\ &+ \frac{\beta \mathcal{A}_\beta}{(\alpha - \beta)(\beta^2 + \omega^2)} \left(V_{s*}^m \sin(\omega t + \widehat{\delta}_\beta^-) + (V_{r*}^m - V_{s*}^m) e^{\frac{\beta(\pi-\hat{b}-\delta-\omega t)}{\omega}} \sin(\hat{b} + \widehat{\delta}_\beta^+ - \delta) \right) \\ &+ (V_{s*}^m - V_{r*}^m) e^{\frac{\beta(\hat{b}-\delta-\omega t)}{\omega}} \sin(\hat{b} + \widehat{\delta}_\beta^- - \delta) - V_{s*}^m e^{-\beta t} \sin \widehat{\delta}_\beta^- \\ &+ \frac{1}{\beta(\alpha - \beta)} \left(V_{s*}^b + (V_{r*}^b - V_{s*}^b) e^{\frac{\beta(\pi-\hat{b}-\delta-\omega t)}{\omega}} + (V_{s*}^b - V_{r*}^b) e^{\frac{\beta(\hat{b}-\delta-\omega t)}{\omega}} - V_{s*}^b e^{-\beta t} \right) \end{aligned} \quad (\text{B.23})$$

These solutions may then be continued for all time intervals of (B.8) by matching boundary conditions for each interval. For reasons of conciseness these are not presented, as to understand the origin of the 'two-bump' solution a single period is sufficient. Observe that the three regions highlighted in (B.8) may be reduced to only two which is finally given by equations (4.15) and (4.16) (see section 4.5).

Appendix C

This appendix provides all the necessary calculations made for the RKII set. The first section presents the computation of the eigenvalues of RKII model, the following section evaluates in a small neighbourhood of parameter space how the equilibriums of RKII change. Subsequent sections then evaluate through the Lienard-Chipart criterion the region in parameter space where the RKII set loses stability. The Lienard-Chipart theorem is provided on the next subsection. Finally, all the critical points evaluated by XPPAuto (see 2.4.1)) are shown in Table C.2. For notation, here the apostrophe is used denote the derivative. For example $f'(x)$ is the derivative of f .

C.1 Eigenvalues of the RKII model

Applying the determinant rule to the jacobian (5.2) gives:

$$|\lambda \mathbf{I} - \mathbf{J}| = \begin{vmatrix} \lambda & -1 & 0 & 0 \\ \alpha\beta & \lambda + (\alpha + \beta) & -\alpha\beta u_{sr}\zeta'[V_r^*] & 0 \\ 0 & 0 & \lambda & -1 \\ -\alpha\beta u_{rs}\zeta'[V_s^*] & 0 & \alpha\beta & \lambda + (\alpha + \beta) \end{vmatrix}$$

Since $\det(\lambda \mathbf{I} - \mathbf{A}) = \sum_{i=1}^k a_{ij} C_{ij}$, where C_{ij} is the cofactor of a_{ij} defined by $C_{ij} = (-1)^{i+j} M_{ij}$ and M_{ij} is the minor of entry a_{ij} . This operation results in

$$\lambda(\lambda(\lambda + (\alpha + \beta))^2 + \alpha\beta(\lambda + (\alpha + \beta))) + \alpha\beta(\lambda(\lambda + (\alpha + \beta)) + \alpha\beta) - (\alpha\beta)^2 u_{sr} u_{rs} \zeta'[V_r^*] \zeta'[V_s^*] = 0$$

Simplifying the above equation (C.1) results in the following:

$$\begin{aligned}
& [\lambda(\lambda + (\alpha + \beta)) + \alpha\beta]^2 - (\alpha\beta)^2 u_{sr} u_{rs} \varsigma' [V_r^*] \varsigma' [V_s^*] = 0 \Leftrightarrow \\
& \lambda(\lambda + (\alpha + \beta)) + \alpha\beta = \pm (\alpha\beta) \sqrt{u_{sr} u_{rs} \varsigma' [V_r^*] \varsigma' [V_s^*]} \Leftrightarrow \\
& \lambda^2 + \lambda(\alpha + \beta) = -\alpha\beta \pm (\alpha\beta) \sqrt{u_{sr} u_{rs} \varsigma' [V_r^*] \varsigma' [V_s^*]} \Leftrightarrow \\
& 4\lambda^2 + 4\lambda(\alpha + \beta) = -4\alpha\beta \pm 4(\alpha\beta) \sqrt{u_{sr} u_{rs} \varsigma' [V_r^*] \varsigma' [V_s^*]} \Leftrightarrow \\
& 4\lambda^2 + 4\lambda(\alpha + \beta) + (\alpha + \beta)^2 - (\alpha + \beta)^2 = -4\alpha\beta \pm 4(\alpha\beta) \sqrt{u_{sr} u_{rs} \varsigma' [V_r^*] \varsigma' [V_s^*]} \Leftrightarrow \\
& (2\lambda + (\alpha + \beta))^2 = (\alpha + \beta)^2 - 4\alpha\beta \pm 4(\alpha\beta) \sqrt{u_{sr} u_{rs} \varsigma' [V_r^*] \varsigma' [V_s^*]} \Leftrightarrow \\
& \lambda = \frac{-(\alpha + \beta) \pm \sqrt{(\alpha - \beta)^2 \pm 4(\alpha\beta) \sqrt{u_{sr} u_{rs} \varsigma' [V_r^*] \varsigma' [V_s^*]}}}{2}
\end{aligned}$$

Since u_{sr} is negative the following implicit formula can be equated:

$$\lambda = \frac{-(\alpha + \beta) \pm \sqrt{(\alpha - \beta)^2 \pm i4(\alpha\beta) \sqrt{|u_{sr} u_{rs}| \varsigma' [V_r^*] \varsigma' [V_s^*]}}}{2}$$

C.2 Rate of change of Equilibria with respect to parameters

This section provides only the derivation of the derivative of V_s^* with respect to the control parameter ν_{rs} . The derivations for $\frac{dV_s^*}{d\nu_{sr}}$, $\frac{dV_s^*}{d\nu_{sn}}$, $\frac{dV_r^*}{d\nu_{sr}}$, $\frac{dV_r^*}{d\nu_{rs}}$ and $\frac{dV_r^*}{d\nu_{sn}}$ follow the same steps as the one here demonstrated.

From the nullclines equations (5.3) the following holds:

$$V_s^* = \nu_{sr} \varsigma [V_r^*] + \nu_{sn} \phi_n \quad (C.1)$$

Applying the derivative with respect to ν_{rs} equates to:

$$\begin{aligned}
\frac{dV_s^*}{d\nu_{rs}} &= \frac{d(\nu_{sr} \varsigma [V_r^*]) + \nu_{sn} \phi_n}{d\nu_{rs}} \\
&=_{f(g(x))=g(x)'} \frac{\nu_{sr} \varsigma' [V_r^*] \frac{dV_r^*}{d\nu_{rs}}}{d\nu_{rs}} \\
&=_{use \text{ eq (5.3)}} \frac{\nu_{sr} \varsigma' [V_r^*] \frac{d(\nu_{rs} \varsigma [V_s^*])}{d\nu_{rs}}}{d\nu_{rs}} \\
&=_{(f(x)g(x))'=f(x)'+g(x)'} \nu_{sr} \varsigma' [V_r^*] \left(\varsigma [V_s^*] \frac{d\nu_{rs}}{d\nu_{rs}} + \nu_{rs} \varsigma' [V_s^*] \frac{dV_s^*}{d\nu_{rs}} \right) \quad (C.2)
\end{aligned}$$

From the above equation (C.2) results in the following:

$$\begin{aligned}
\frac{dV_s^*}{d\nu_{rs}} - \nu_{sr}\zeta'[V_r^*]\nu_{rs}\zeta'[V_s^*]\frac{dV_s^*}{d\nu_{rs}} &= \nu_{sr}\zeta'[V_r^*]\zeta[V_s^*] \Leftrightarrow \\
\frac{dV_s^*}{d\nu_{rs}} \left(1 - \nu_{sr}\nu_{rs}\zeta'[V_s^*]\zeta'[V_r^*]\right) &= \nu_{sr}\zeta'[V_r^*]\zeta[V_s^*] \Leftrightarrow \\
\frac{dV_s^*}{d\nu_{rs}} &= \frac{\nu_{sr}\zeta'[V_r^*]\zeta[V_s^*]}{1 - \nu_{sr}\nu_{rs}\zeta'[V_s^*]\zeta'[V_r^*]} \Leftrightarrow \\
\frac{dV_s^*}{d\nu_{rs}} &= \frac{-|\nu_{sr}\zeta'[V_r^*]\zeta[V_s^*]|}{1 + |\nu_{sr}\nu_{rs}\zeta'[V_s^*]\zeta'[V_r^*]|} \quad (C.3)
\end{aligned}$$

Since all terms of the right hand side of equation (C.3) are ≥ 0 it can be concluded that $\frac{dV_s^*}{d\nu_{rs}} \leq 0$.

C.3 Calculation of the stability curve

C.3.1 Stability curve in parameter space

Applying the Lienard-Chipart criterion (given in the next section C.3.2 for completeness) enables one to calculate the stability region of the system, based on the coefficients of the characteristic polynomial, which it is here denoted by the vector $\underline{a} = (a_0, a_1, \dots, a_n)$. This criterion requires that any one of four equivalent conditions be satisfied in order for the roots of the characteristic polynomial to lie in the left half-plane and hence the system be stable. These conditions involve the n^{th} element and in addition all of the odd or all of the even elements of the vector \underline{a} , denoted $\text{Coef}_a^{\text{odd}}$ and $\text{Coef}_a^{\text{even}}$, and the determinants of specific matrices defined in terms of the elements of the vector \underline{a} :

$$\Delta_i = \begin{vmatrix} a_1 & a_3 & a_5 & \cdots & a_{2i-1} \\ a_0 & a_2 & a_4 & \cdots & a_{2i-2} \\ 0 & a_1 & a_3 & \cdots & a_{2i-3} \\ \vdots & \vdots & \vdots & \ddots & \vdots \\ 0 & 0 & 0 & \cdots & a_i \end{vmatrix}$$

Again, we are concerned with either all of the odd determinants, \det_a^{odd} or all of the even ones,

\det_a^{even} . In particular, we the following condition $\{\text{Coef}_a^{\text{odd}} \wedge \det_a^{\text{odd}} > 0\}$ for stability is used.

The characteristic polynomial of system (5.1) gives

$$\underline{a} = (1, 2(\alpha + \beta), (\alpha + \beta)^2 + 2\alpha\beta, 2\alpha\beta(\alpha + \beta), (\alpha\beta)^2(1 - \nu_{sr}\nu_{rs}\zeta'[V_r^*]\zeta'[V_s^*])).$$

Hence, the following is obtained:

$$\begin{aligned} \text{Coef}_a^{\text{odd}} &= (a_4 > 0) \wedge (a_3 > 0) \wedge (a_1 > 0) \\ \det_a^{\text{odd}} &= (\Delta_1 > 0) \wedge (\Delta_3 > 0) \\ &\Leftrightarrow a_1 > 0 \wedge \begin{vmatrix} a_1 & a_3 & 0 \\ a_0 & a_2 & a_4 \\ 0 & a_1 & a_3 \end{vmatrix} > 0 \\ &\Leftrightarrow 2(\alpha + \beta) > 0 \wedge a_1 a_2 a_3 - a_1^2 a_4 - a_0 a_3^2 > 0 \end{aligned}$$

Knowing that $\nu_{sr} < 0$, then the last condition can be rewritten as the following implicit expression:

$$\det_a^{\text{odd}} = 2(\alpha + \beta) > 0 \wedge |\nu_{sr}\nu_{rs}| > \frac{1}{\zeta'[V_r^*]\zeta'[V_s^*]} \frac{(\alpha + \beta)^2}{\alpha\beta}$$

This defines a stability curve in $|\nu_{sr}\nu_{rs}|$ parameter space.

C.3.2 The Lienard-Chipart stability criterion

The Lienard-Chipart criteria is a set of conditions on the coefficients of a polynomial that is both necessary and sufficient for the roots of the polynomial to belong to the complex open left-half plane $\mathbb{C}_- = \{r \in \mathbb{C}; \text{Re}(r) < 0\}$ where r are the roots of a polynomial of degree n with real coefficients.

$$P(r) = \sum_{j=0}^n a_{n-j} r^j \tag{C.4}$$

The Lienard-Chipart is simpler than the Routh-Hurwitz criterion [59] in that involves odd or even coefficients of the polynomial and Hurwitz determinants defined by the logical statements:

$$\begin{aligned}
Coe f_a^{odd} &= a_n > 0 \wedge a_{n-1} > 0 \wedge a_{n-3} > 0 \wedge \dots \wedge a_1 > 0, \\
Coe f_a^{even} &= a_n > 0 \wedge a_{n-2} > 0 \wedge a_{n-4} > 0 \wedge \dots \wedge a_1 > 0, \\
Det^{odd} &= \Delta_1 > 0 \wedge \Delta_3 > 0 \dots, \\
Det^{even} &= \Delta_2 > 0 \wedge \Delta_4 > 0 \dots
\end{aligned}$$

Where

$$\Delta_i = \begin{vmatrix} a_1 & a_3 & a_5 & \dots & a_{2i-1} \\ a_0 & a_2 & a_4 & \dots & a_{2i-2} \\ 0 & a_1 & a_3 & \dots & a_{2i-3} \\ 0 & a_0 & a_2 & \dots & a_{2i-4} \\ \cdot & \cdot & \cdot & \dots & \cdot \\ \cdot & \cdot & \cdot & \dots & a_i \end{vmatrix}$$

The indices in each row increases by two, whereas the indices in each column decrease by one. The term a_i is set to zero if $i < 0$ or $i > n$.

Theorem (Lienard-Chipart Criterion): The Polynomial C.4 with a_0 is Hurwitz stable if and only if any one of the four conditions

$$\{Coe f_a^{odd} \wedge Det^{odd}\}, \{Coe f_a^{odd} \wedge Det^{even}\}, \{Coe f_a^{even} \wedge Det^{odd}\}, \{Coe f_a^{even} \wedge Det^{even}\}$$

is true. This means that the simplest of the four formulas is sufficient to imply the polynomial is Hurwitz, and the polynomial being Hurwitz implies all four conditions are true.

Polynomial Property	Definition
Huwirtz Stable	$\forall r \in \mathbb{C} \{P(r) = 0 \Rightarrow \text{Re}(r) < 0\}$
Unstable	$\exists r \in \mathbb{C} \{P(r) = 0 \Rightarrow \text{Re}(r) > 0\}$
Neutrally Stable	$\forall r \in \mathbb{C} \{P(r) = 0 \Rightarrow \text{Re}(r) \leq 0\}$
Skew	$\forall r \in \mathbb{C} \{P(r) = 0 \Rightarrow \text{Re}(r) = 0\}$

Table C.1: Left-plane stability properties of polynomial P(r).

C.4 Numerical Bifurcations in RKII set

The following table contains the relevant bifurcation points found by numerically continuing the solution paths in the RKII model using the numerical package XPPAuto.

Label	Type	V_s	V_r	ν_{sn}	ν_{sr}	ν_{rs}
LP1	Fold point from which two Hopf are born.	-0.008262	0.01026	0	-0.0001714	0.04654
HB1	Supercritical Hopf.	-0.01222	0.005962	0	-0.0008	0.0894
HB2	Supercritical Hopf.	-0.009158	0.01504	0	-7.28e-5	0.0894
HB3	Supercritical Hopf.	0.00452	0.006057	0.01707	-0.0008	0.0006
HB4	Supercritical Hopf.	0.01026	0.02887	0.2073	-0.0008	0.0006
LP2	Fold point from which two Hopf are born.	0.007693	0.009741	0.01707	-0.0002215	0.0003938
LP3	Fold point from which two Hopf are born.	0.01488	0.0007072	0.2073	-0.05868	5.765e-6
LP4	Fold point from which two Hopf are born.	0.008016	0.0162	0.01955	-7.824e-5	0.0006
LP5	Fold point from which two Hopf are born.	0.006247	0.009935	0.1521	-0.0002017	0.0006
LP6	Fold point from which two Hopf are born.	0.01858	0.009692	0.05205	-0.0008	5.191e-5
LP7	Fold point from which two Hopf are born.	0.01522	0.02685	0.2098	-0.0008	0.0002079
HB5	Supercritical Hopf.	0.00752	0.01425	0.01707	-8.595e-5	0.0006
HB6	Supercritical Hopf.	0.01831	0.0244	0.2073	-0.0008	0.0001335
HB7	Supercritical Hopf.	0.003583	0000	0.01955	-0.001541	0.0006

Table C.2: The relevant critical points for the numerical unfolding of the RKII model.

Appendix D

For completeness this section provides additional material relating to the calculation of the normal forms for the RKII model.

D.1 Derivation of the Homological Equation

The normal form and centre manifold methodology introduced by Iooss and Adelmeyer (see section 2.1.6) is based on the homological operator. The theory states that the transformation of some vector field to a normal form is possible by the following near identity coordinate transformation $\hat{x} = z + h(z, \hat{\nu})$, where $\hat{x} = (z, y) \in \mathbb{R}^n$ with z a vector on the centre manifold (i.e. from equation (6.11) $z = Ze_0 + \overline{Z}\overline{e_0}$), y a vector on the hyperbolic space and $\hat{\nu} \in \mathbb{R}^n$ the control parameters. To illustrate this, consider the following vector field

$$\dot{\hat{x}} = J\hat{x} + N(x, \hat{\nu}), \quad (\text{D.1})$$

where J is the linear operator (note that Iooss and Adelmeyer consider the Jacobian) and $N \in C^k(\mathbb{R}^n \times \mathbb{R}^m; \mathbb{R}^n)$ contain the nonlinear terms. The objective is to transform (D.1) to a normal form on the centre space having the following structure:

$$\dot{z} = Jz + G(z, \hat{\nu}), \quad (\text{D.2})$$

where $G \in C^k(\mathbb{R}^n \times \mathbb{R}^m; \mathbb{R}^n)$. First, apply the derivative operator to the near identity transformation which gives rise to:

$$\dot{\hat{x}} = \dot{z} + D_z[h(z, \hat{\nu})](\dot{z}). \quad (\text{D.3})$$

Applying (D.1) to the above equation (D.3) results in

$$\dot{z} + D_1[h(z, \hat{\nu})](\dot{z}) = J\hat{x} + N(\hat{x}, \hat{\nu}). \quad (\text{D.4})$$

Again, introducing the identity transformation into the above equation (D.3) generates

$$\dot{z} + D_1[h(z, \hat{\nu})](\dot{z}) = Jz + Jh(z, \hat{\nu}) + N(z + h(z, \hat{\nu}), \hat{\nu}). \quad (\text{D.5})$$

Finally applying (D.2) to the previous derivation (D.5) and rearranging terms results in the homological operator:

$$Jh(z, \hat{\nu}) - D_z[h(z, \hat{\nu})](Jz) = G(z, \hat{\nu}) - N(z + h(z, \hat{\nu}), \hat{\nu}) + D_z[h(z, \hat{\nu})](G(z, \hat{\nu})).$$

D.2 Derivation of the $\mathcal{O}(1)$ normal form coefficients

The terms that depend linearly on the parameters and coordinates give rise to a homological operator with the following form:

$$Jh_1^1(z, \hat{\nu}) - D_z[h_1^1(z, \hat{\nu})](Jz) = G_1^1(z, \hat{\nu}) - N_1^1(z\hat{\nu}).$$

Since $z = Ze_0 + \bar{Z}\bar{e}_0$ and control parameters are $\hat{\nu} = (\hat{\nu}_{sr}, \hat{\nu}_{rs})$ then the expansion for h_1^1 have the following form:

$$h_1^1 = h_{1,0}^{1,0}\nu_{sr}Ze_0 + h_{1,0}^{0,1}\nu_{rs}Ze_0 + h_{0,1}^{1,0}\nu_{sr}\bar{Z}\bar{e}_0 + h_{0,1}^{0,1}\nu_{rs}\bar{Z}\bar{e}_0. \quad (\text{D.6})$$

Applying the linear operator J to the above equation (D.6) results in

$$Jh_1^1 = Jh_{1,0}^{1,0}\hat{\nu}_{sr}Ze_0 + Jh_{1,0}^{0,1}\hat{\nu}_{rs}Ze_0 + Jh_{0,1}^{1,0}\hat{\nu}_{sr}\bar{Z}\bar{e}_0 + Jh_{0,1}^{0,1}\hat{\nu}_{rs}\bar{Z}\bar{e}_0. \quad (\text{D.7})$$

Also apply the multivariate derivative operator D_z to equation (D.6) to obtain

$$\begin{cases} D_z[h_1^0(z, \hat{\nu})] = h_{1,0}^{1,0}\hat{\nu}_{sr}e_0 + h_{1,0}^{0,1}\hat{\nu}_{rs}e_0 \\ D_{\bar{Z}}[h_1^0(z, \hat{\nu})] = h_{0,1}^{1,0}\hat{\nu}_{sr}\bar{e}_0 + h_{0,1}^{0,1}\hat{\nu}_{rs}\bar{e}_0 \end{cases}. \quad (\text{D.8})$$

The term Jz in the homological equation equates to:

$$\begin{aligned} Jz &= J(Ze_0 + \bar{Z}\bar{e}_0) \\ &\Leftrightarrow ZJ(e_0) + \bar{Z}J(\bar{e}_0) \\ &\Leftrightarrow i\sqrt{\alpha\beta}Ze_0 - i\sqrt{\alpha\beta}\bar{Z}\bar{e}_0. \end{aligned} \quad (\text{D.9})$$

The expansion of the polynomial G_1^1 has the following form:

$$G_1^1 = g_{1,0}^{1,0} \hat{\nu}_{sr} Z e_0 + g_{1,0}^{0,1} \hat{\nu}_{rs} Z e_0 + g_{0,1}^{1,0} \hat{\nu}_{sr} \overline{Z} \overline{e_0} + g_{0,1}^{0,1} \hat{\nu}_{rs} \overline{Z} \overline{e_0} \quad (D.10)$$

and the nonlinear term N_1^1 is the following

$$N_1^1 = \hat{\nu}_{sr} Z N_1^{0,1}(e_0) + \hat{\nu}_{rs} N_1^{0,1} \overline{Z}(\overline{e_0}). \quad (D.11)$$

Finally substituting equations (D.7),(D.8),(D.9),(D.10) and (D.11) into the homological operator and then equating terms of the same order gives rise to the following four equations:

$$\begin{cases} (J - i\sqrt{\alpha\beta}I)h_{1,0}^{1,0} = g_{1,0}^{1,0}e_0 - N_1^{1,0}(e_0), \\ (J - i\sqrt{\alpha\beta}I)h_{1,0}^{0,1} = g_{1,0}^{0,1}e_0 - N_1^{0,1}(e_0), \\ g_{0,1}^{1,0} = \overline{g_{1,0}^{1,0}}, \\ g_{1,0}^{0,1} = \overline{g_{0,1}^{0,1}}. \end{cases} \quad (D.12)$$

Only the following terms are considered $g_{1,0}^{1,0}$ and $g_{0,1}^{0,1}$. To evaluate these coefficients the inner product with the adjoint dual basis of e_0 and here we denote it as $\overline{f_0}$ must be applied to all terms of the first two equations of (D.12). This results in the following:

$$\begin{cases} g_{1,0}^{1,0} \langle e_0, \overline{f_0} \rangle = \langle N_1^{1,0}(e_0), \overline{f_0} \rangle, \\ g_{1,0}^{0,1} \langle e_0, \overline{f_0} \rangle = \langle N_1^{0,1}(e_0), \overline{f_0} \rangle, \end{cases} \quad (D.13)$$

where the operator $\langle \cdot, \cdot \rangle$ denotes the inner product of two vectors and $\langle a, b \rangle = a^*b$. $a, b \in \mathbb{C}$ and a^* is the complex conjugate transpose of vector a and $\overline{f_0}$ is given by equation (6.21) (refer back to chapter 6), thus:

$$\langle e_0, \overline{f_0} \rangle = \alpha\beta[2(\alpha + \beta) - (\alpha\beta)] + i(\alpha + \beta)[\sqrt{\alpha\beta}(\alpha + \beta) + \alpha\beta] \quad (D.14)$$

and

$$N_1^{1,0}(e_0) = \begin{pmatrix} 0 \\ -\alpha\beta \frac{\partial \varsigma[V_r^*]}{\partial V_r} i\sqrt{\alpha\beta}(\alpha + \beta) \hat{\nu}_{sr} \\ 0 \\ 0 \end{pmatrix}, \quad N_1^{0,1}(e_0) = \begin{pmatrix} 0 \\ 0 \\ 0 \\ -(\alpha\beta)^2 \nu_{sr}^* \frac{\partial \varsigma[V_s^*]}{\partial V_s} \frac{\partial \varsigma[V_r^*]}{\partial V_r} \hat{\nu}_{rs} \end{pmatrix}$$

D.3 Derivation of the $\mathcal{O}(2)$ normal form coefficients

From the order 2 homological equation the coefficients h_0^2 can be determined. The equation is written in following form:

$$Jh_2^0(z) - D_z[h_2^0(z)](Jz) = -N_2^0(z, z)$$

Using the same steps as applied to the order one coefficients and by first performing the Taylor expansion for $h(z)$ of order 2 in z and no dependence on parameters results in

$$h_2^0 = h_{2,0}^0 Z^2 + h_{1,1}^0 Z \bar{Z} + h_{0,1}^0 \bar{Z}^2. \quad (\text{D.15})$$

Applying the linear operator J to equation (D.15) gives

$$Jh_2^0 = Jh_{2,0}^0 Z^2 + Jh_{1,1}^0 Z \bar{Z} + Jh_{0,1}^0 \bar{Z}^2. \quad (\text{D.16})$$

Applying the multivariate derivative operator D_z to equation (D.15) results in

$$\begin{cases} D_z[h_2^0(z)] = 2h_{2,0}^0 Z + h_{1,1}^0 \bar{Z} \\ D_{\bar{z}}[h_2^0(z)] = h_{1,1}^0 Z + 2h_{0,2}^0 \bar{Z} \end{cases}. \quad (\text{D.17})$$

Since $Jz = [i\sqrt{\alpha\beta}Z, -i\sqrt{\alpha\beta}\bar{Z}]^T$ and then by combining with (D.17) results in the following:

$$D_z[h_2^0(z)](Jz) = 2h_{2,0}^0 i\sqrt{\alpha\beta}Z^2 - 2h_{0,2}^0 i\sqrt{\alpha\beta}\bar{Z}^2. \quad (\text{D.18})$$

For the nonlinear term N_2^0 , we use the bilinear property of the Taylor expansion for second order terms, which then N_2^0 equates to:

$$N_2^0(z, z) = N_2^0(Ze_0 + \bar{Z}\bar{e}_0, Ze_0 + \bar{Z}\bar{e}_0) \Leftrightarrow Z^2 N(e_0, e_0) + 2Z\bar{Z} N(e_0, \bar{e}_0) + \bar{Z}^2 N(\bar{e}_0, \bar{e}_0). \quad (\text{D.19})$$

Substituting (D.9), (D.15), (D.18) and (D.19) back into the homological equation and grouping terms of the same order gives:

$$\begin{cases} (J - 2i\sqrt{\alpha\beta}I)h_{2,0}^0 = -N_2(e_0, e_0) \\ Jh_{1,1}^0 = -N_2(e_0, \bar{e}_0) \\ (J + 2i\sqrt{\alpha\beta}I)\bar{h}_{2,0}^0 = -N_2(\bar{e}_0, e_0) \end{cases}. \quad (\text{D.20})$$

Note that the eigenvalues of J include $\pm i\sqrt{\alpha\beta}$, so the operator $(J - \eta I)$ is invertible for $\eta \neq \pm i\sqrt{\alpha\beta}$, thus allowing to determine the coefficients $h_{2,0}^0, \bar{h}_{2,0}^0$ and $h_{1,1}^0$. Where the inverse of the linear operator J at the bifurcation point is given by

$$J^{-1} = \begin{pmatrix} -\frac{\alpha+\beta}{((\alpha+\beta)^2+\alpha\beta)} & -\frac{1}{((\alpha+\beta)^2+\alpha\beta)} & -\frac{\nu_{sr}(\alpha+\beta)\frac{\partial \zeta[V_r^*]}{\partial V_r}}{((\alpha+\beta)^2+\alpha\beta)} & -\frac{\nu_{sr}\frac{\partial \zeta[V_r^*]}{\partial V_r}}{((\alpha+\beta)^2+\alpha\beta)} \\ 1 & 0 & 0 & 0 \\ -\frac{\nu_{rs}(\alpha+\beta)\frac{\partial \zeta[V_s^*]}{\partial V_s}}{((\alpha+\beta)^2+\alpha\beta)} & -\frac{\nu_{rs}\frac{\partial \zeta[V_s^*]}{\partial V_s}}{((\alpha+\beta)^2+\alpha\beta)} & -\frac{\alpha+\beta}{((\alpha+\beta)^2+\alpha\beta)} & -\frac{1}{((\alpha+\beta)^2+\alpha\beta)} \\ 0 & 0 & 1 & 0 \end{pmatrix}, \quad (\text{D.21})$$

and also at the Hopf bifurcation point the following holds true:

$$(J - 2i\sqrt{\alpha\beta})_{\text{Column 1}}^{-1} = \frac{1}{\det(J - 2i\sqrt{\alpha\beta})} \begin{pmatrix} -7\alpha\beta(\alpha + \beta) + 2i\sqrt{\alpha\beta}((\alpha + \beta)^2 - 3\alpha\beta) \\ \alpha\beta(-2i\sqrt{\alpha\beta}(\alpha + \beta) - (\alpha + \beta)^2 + 3\alpha\beta) \\ \alpha\beta\nu_{rs}\frac{\partial\varsigma[V_r^*]}{\partial V_s}(\alpha + \beta + 2i\sqrt{\alpha\beta}) \\ \alpha\beta\nu_{rs}\frac{\partial\varsigma[V_s^*]}{\partial V_s}(-4\alpha\beta + 2i\sqrt{\alpha\beta}(\alpha + \beta)) \end{pmatrix} \quad (\text{D.22})$$

$$(J - 2i\sqrt{\alpha\beta})_{\text{Column 2}}^{-1} = \frac{1}{\det(J - 2i\sqrt{\alpha\beta})} \begin{pmatrix} -3\alpha\beta + 2i\sqrt{\alpha\beta}(\alpha + \beta) \\ -\alpha\beta(4(\alpha + \beta) + 6i\sqrt{\alpha\beta}) \\ \alpha\beta\nu_{rs}\frac{\partial\varsigma[V_s^*]}{\partial V_s} \\ 2i\sqrt{\alpha\beta}\nu_{rs}\frac{\partial\varsigma[V_s^*]}{\partial V_s} \end{pmatrix}, \quad (\text{D.23})$$

$$(J - 2i\sqrt{\alpha\beta})_{\text{Column 3}}^{-1} = \frac{1}{\det(J - 2i\sqrt{\alpha\beta})} \begin{pmatrix} \alpha\beta\nu_{sr}\frac{\partial\varsigma[V_r^*]}{\partial V_r}(\alpha + \beta + 2i\sqrt{\alpha\beta}) \\ \alpha\beta\nu_{sr}\frac{\partial\varsigma[V_r^*]}{\partial V_r}(-4\alpha\beta + 2i\sqrt{\alpha\beta}(\alpha + \beta)) \\ -7\alpha\beta(\alpha + \beta) + 2i\sqrt{\alpha\beta}((\alpha^2 + \beta^2) - \alpha\beta) \\ \alpha\beta(3\alpha\beta - (\alpha + \beta)^2 - 2i\sqrt{\alpha\beta}(\alpha + \beta)) \end{pmatrix} \quad (\text{D.24})$$

$$(J - 2i\sqrt{\alpha\beta})_{\text{Column 4}}^{-1} = \frac{1}{\det(J - 2i\sqrt{\alpha\beta})} \begin{pmatrix} \alpha\beta\nu_{sr}\frac{\partial\varsigma[V_r^*]}{\partial V_r} \\ \alpha\beta\nu_{sr}\frac{\partial\varsigma[V_r^*]}{\partial V_r}2i\sqrt{\alpha\beta} \\ -3\alpha\beta + 2i\sqrt{\alpha\beta}(\alpha + \beta) \\ -2\alpha\beta(2(\alpha + \beta) + 3i\sqrt{\alpha\beta}) \end{pmatrix}, \quad (\text{D.25})$$

where $\det(J - 2i\sqrt{\alpha\beta}) = 3\alpha\beta(((\alpha^2 + \beta^2) + \alpha\beta) + 4i\sqrt{\alpha\beta}(\alpha + \beta))$.

Furthermore, the bilinear terms have the following form:

$$N_2^0(e_0, e_0) = \frac{1}{2!} \begin{pmatrix} 0 \\ -(\alpha\beta)^2(\alpha + \beta)\nu_{sr}^*\frac{\partial^2\varsigma[V_r^*]}{\partial V_r^2} \\ 0 \\ (\alpha\beta)^3\nu_{rs}^*(\nu_{sr}^*)^2\frac{\partial^2\varsigma[V_s^*]}{\partial V_s^2}\left(\frac{\partial\varsigma[V_r^*]}{\partial V_r}\right)^2 \end{pmatrix}, \quad (\text{D.26})$$

$$N_2^0(e_0, \bar{e}_0) = \frac{1}{2!} \begin{pmatrix} 0 \\ (\alpha\beta)^2(\alpha + \beta)^2\nu_{sr}^*\frac{\partial^2\varsigma[V_r^*]}{\partial V_r^2} \\ 0 \\ (\alpha\beta)^3\nu_{rs}^*(\nu_{sr}^*)^2\frac{\partial^2\varsigma[V_s^*]}{\partial V_s^2}\left(\frac{\partial\varsigma[V_r^*]}{\partial V_r}\right)^2 \end{pmatrix}, \quad (\text{D.27})$$

D.3.1 Derivation of the $\mathcal{O}(3)$ normal form coefficients

From the order 3 homological equation, it is possible to extract the coefficients that are cubic in the coordinates of the centre space and independent of the control parameters, that is, $Z\mathcal{O}(|Z|^2)$. The operator takes the following form:

$$Jh_3^0(z) - D_z[h_3^0(z)](Jz) = G_3^0 - 2N_2^0(z, h_2^0(z)) - N_3(z, z, z). \quad (\text{D.28})$$

The third order Taylor expansion of $h(z)$ gives the following:

$$h_3^0 = h_{3,0}^0 Z^3 + h_{2,1}^0 Z^2 \bar{Z} + h_{1,2}^0 Z \bar{Z}^2 + h_{0,3}^0 \bar{Z}^3. \quad (\text{D.29})$$

In same way as for order one and two coefficients, the linear operator J to equation (D.29) is applied. Also, applying the differential operator D_z to (D.29) gives:

$$\begin{cases} D_z[h_3^0(z)] = 3h_{3,0}^0 Z^2 + 2h_{2,1}^0 Z \bar{Z} + h_{1,2}^0 \bar{Z}^2 \\ D_{\bar{z}}[h_3^0(z)] = h_{2,1}^0 Z^2 + 2h_{1,2}^0 Z \bar{Z} + 3h_{0,3}^0 \bar{Z}^2 \end{cases} \quad (\text{D.30})$$

Then by combining (D.30) and (D.9) this gives rise to:

$$D_z[h_3^0(z)](Jz) = i\sqrt{\alpha\beta}(3h_{3,0}^0 Z^3 + h_{2,1}^0 Z^2 \bar{Z} - h_{1,2}^0 Z \bar{Z}^2 - 3h_{0,3}^0 \bar{Z}^3). \quad (\text{D.31})$$

In this case the nonlinear term N_2^0 and its derivation is as follows:

$$\begin{aligned} N_2^0(z, h_2^0(z)) &= N_2^0(Ze_0 + \bar{Z}\bar{e}_0, h_{2,0}^0 Z^2 + h_{1,1}^0 Z \bar{Z} + h_{0,2}^0 \bar{Z}^2) \\ &\Leftrightarrow N_2^0(e_0, h_{2,0}^0) Z^3 + N_2^0(e_0, h_{1,1}^0) Z^2 \bar{Z} + N_2^0(e_0, h_{0,2}^0) Z \bar{Z}^2 \\ &\quad + N_2^0(\bar{e}_0, h_{2,0}^0) \bar{Z} Z^2 + N_2^0(\bar{e}_0, h_{1,1}^0) \bar{Z} \bar{Z}^2 + N_2^0(\bar{e}_0, h_{0,2}^0) \bar{Z}^3. \end{aligned} \quad (\text{D.32})$$

Equally for the third order of the same nonlinearity results in:

$$\begin{aligned} N_3^0(z, z, z) &= N_3^0(e_0, e_0, e_0) Z^3 + 3N_3^0(e_0, e_0, \bar{e}_0) Z^2 \bar{Z} \\ &\quad + 3N_3^0(e_0, \bar{e}_0, \bar{e}_0) Z \bar{Z}^2 + N_3^0(\bar{e}_0, \bar{e}_0, \bar{e}_0) \bar{Z}^3. \end{aligned} \quad (\text{D.33})$$

The expansion for the cubic terms of the normal form G has the following structure:

$$G_3^0 = g_{2,1}^{0,0} |Z|^2 e_0 + g_{1,2}^{0,0} \bar{Z} |Z|^2 \bar{e}_0 \quad (\text{D.34})$$

$$\Leftrightarrow g_{2,1}^{0,0} Z^2 \bar{Z} e_0 + g_{1,2}^{0,0} Z \bar{Z}^2 \bar{e}_0. \quad (\text{D.35})$$

Substituting (D.9), (D.29), (D.31), (D.32), (D.33) and (D.35) back into the homological equation of order 3 and grouping terms of the same order results in:

$$\begin{cases} (L - i3\sqrt{\alpha\beta}I)h_{3,0}^0 = -2N_2^0(e_0, h_{2,0}^0) - N_3^0(e_0, e_0, e_0), \\ (L + i3\sqrt{\alpha\beta}I)h_{0,3}^0 = -2N_2^0(\bar{e}_0, h_{0,2}^0) - N_3^0(\bar{e}_0, \bar{e}_0, \bar{e}_0), \\ (L - i\sqrt{\alpha\beta}I)h_{2,1}^{0,0} = g_{2,1}^{0,0}e_0 - 2N_2^0(\bar{e}_0, h_{2,0}^{0,0}) - 2N_2^0(e_0, h_{1,1}^{0,0}) - 3N_3^0(e_0, e_0, \bar{e}_0), \\ (L + i\sqrt{\alpha\beta}I)h_{1,2}^0 = g_{1,2}^{0,0}\bar{e}_0 - 2N_2^0(e_0, h_{0,2}^{0,0}) - 2N_2^0(\bar{e}_0, h_{1,1}^{0,0}) - 3N_3^0(e_0, \bar{e}_0, \bar{e}_0). \end{cases} \quad (D.36)$$

Here, only the following coefficients are evaluated $g_{1,2}^{0,0}$ and $g_{2,1}^{0,0}$. To solve them apply to the last two equations of (D.36) the inner product with the adjoint dual basis of e_0 which we denote as \bar{f}_0 , which gives:

$$\begin{cases} g_{2,1}^{0,0} \langle e_0, \bar{f}_0 \rangle = 2 \langle N_2^0(\bar{e}_0, h_{2,0}^{0,0}), \bar{f}_0 \rangle + 2 \langle N_2^0(e_0, h_{1,1}^{0,0}), \bar{f}_0 \rangle + 3 \langle N_3^0(e_0, e_0, \bar{e}_0), \bar{f}_0 \rangle \\ g_{1,2}^{0,0} = \bar{g}_{2,1}^{0,0} \end{cases} \quad (D.37)$$

where $\langle e_0, \bar{f}_0 \rangle$ is given by equation (D.14) in section §D.2, and

$$N_2^0(e_0, h_{1,1}^0) = \frac{-(\alpha\beta)^3(\nu_{sr}^*)^2\nu_{rs}^*}{4[(\alpha + \beta)^2 + \alpha\beta]} N_{11} \quad (D.38)$$

$$N_{11} = \begin{pmatrix} 0 \\ i\sqrt{\alpha\beta}(\alpha + \beta) \frac{\partial^2 \varsigma[V_r^*]}{\partial \widehat{V}_r^2} [(\alpha + \beta)^2 \frac{\partial \varsigma[V_s^*]}{\partial \widehat{V}_s} \frac{\partial^2 \varsigma[V_r^*]}{\partial \widehat{V}_r^2} + \alpha\beta\nu_{sr}^* \frac{\partial^2 \varsigma[V_s^*]}{\partial \widehat{V}_s} (\frac{\partial \varsigma[V_r^*]}{\partial \widehat{V}_r})^2] \\ 0 \\ \alpha\beta \frac{\partial^2 \varsigma[V_s^*]}{\partial \widehat{V}_s^2} \frac{\partial \varsigma[V_r^*]}{\partial \widehat{V}_r} [(\alpha + \beta)^2 \frac{\partial^2 \varsigma[V_r^*]}{\partial \widehat{V}_r^2} + \alpha\beta\nu_{rs}^*(\nu_{sr}^*)^2 \frac{\partial^2 \varsigma[V_s^*]}{\partial \widehat{V}_s^2} (\frac{\partial \varsigma[V_r^*]}{\partial \widehat{V}_r})^3] \end{pmatrix}.$$

Furthermore,

$$\begin{aligned} \langle N_2^0(e_0, h_{1,1}^0), \bar{f}_0 \rangle &= \frac{-(\alpha\beta)^2(\nu_{sr}^*)^2\nu_{rs}^*}{4[(\alpha + \beta)^2 + \alpha\beta]} \left(\nu_{rs}^* \frac{\partial \varsigma[V_s^*]}{\partial \widehat{V}_s} \frac{\partial^2 \varsigma[V_r^*]}{\partial \widehat{V}_r^2} \left[(\alpha + \beta)^2 \frac{\partial \varsigma[V_s^*]}{\partial \widehat{V}_s} \frac{\partial^2 \varsigma[V_r^*]}{\partial \widehat{V}_r^2} \right. \right. \\ &+ \left. \left. (\alpha\beta)\nu_{sr}^* \frac{\partial^2 \varsigma[V_s^*]}{\partial \widehat{V}_s^2} (\frac{\partial \varsigma[V_r^*]}{\partial \widehat{V}_r})^2 \right] + \frac{\partial^2 \varsigma[V_s^*]}{\partial \widehat{V}_s^2} \frac{\partial \varsigma[V_r^*]}{\partial \widehat{V}_r} \left[(\alpha + \beta)^2 \frac{\partial^2 \varsigma[V_r^*]}{\partial \widehat{V}_r^2} \right. \right. \\ &+ \left. \left. (\alpha\beta)\nu_{rs}(\nu_{sr})^2 \frac{\partial^2 \varsigma[V_s^*]}{\partial \widehat{V}_s^2} (\frac{\partial \varsigma[V_r^*]}{\partial \widehat{V}_r})^3 \right] \right). \end{aligned} \quad (D.39)$$

The next term equates to the following:

$$N_2^0(\bar{e}_0, h_{2,0}^0) = -\frac{(\alpha\beta)^4(\nu_{sr}^*)^2\nu_{rs}^*}{4\det(J - 2i\sqrt{\alpha\beta})} M_{20}, \quad (D.40)$$

where M_{20} is the subsequent matrix

$$M_{20} = \begin{pmatrix} 0 & i\sqrt{\alpha\beta}(\alpha + \beta) \frac{\partial^2 \zeta[V_r^*]}{\partial \widehat{V}_r^2} [-(\alpha + \beta)^2 \frac{\partial \zeta[V_s^*]}{\partial \widehat{V}_s} \frac{\partial^2 \zeta[V_r^*]}{\partial \widehat{V}_r^2} + \nu_{sr}^* \frac{\partial^2 \zeta[V_s^*]}{\partial \widehat{V}_s^2} (\frac{\partial \zeta[V_r^*]}{\partial \widehat{V}_r})^2] (-3\alpha\beta + 2i\sqrt{\alpha\beta}(\alpha + \beta))] \\ 0 & -\frac{\partial^2 \zeta[V_s^*]}{\partial \widehat{V}_s^2} \frac{\partial \zeta[V_r^*]}{\partial \widehat{V}_r} (-3\alpha\beta + 2i\sqrt{\alpha\beta}(\alpha + \beta)) [-(\alpha + \beta)^2 \frac{\partial^2 \zeta[V_r^*]}{\partial \widehat{V}_r^2} + (\alpha\beta)^2 (\nu_{sr}^*)^2 \nu_{rs}^* \frac{\partial^2 \zeta[V_s^*]}{\partial \widehat{V}_s^2} (\frac{\partial \zeta[V_r^*]}{\partial \widehat{V}_r})^3] \end{pmatrix}$$

which then applying the inner product with \bar{f}_0 results in

$$\begin{aligned} \langle N_2^0(\bar{e}_0, h_{2,0}^0), \bar{f}_0 \rangle &= -\frac{(\alpha\beta)^4 (\nu_{sr}^*)^2 \nu_{rs}^*}{4 \det(J - 2i\sqrt{\alpha\beta})} \left(-(\alpha\beta) \nu_{rs}^* \frac{\partial^2 \zeta[V_r^*]}{\partial \widehat{V}_r^2} \frac{\partial \zeta[V_s^*]}{\partial \widehat{V}_s} \left[(\alpha + \beta)^2 \frac{\partial^2 \zeta[V_r^*]}{\partial \widehat{V}_r^2} \frac{\partial \zeta[V_s^*]}{\partial \widehat{V}_s} \right. \right. \\ &+ \left. \left. \nu_{sr} \frac{\partial^2 \zeta[V_s^*]}{\partial \widehat{V}_s^2} (\frac{\partial \zeta[V_r^*]}{\partial \widehat{V}_r})^2 [3\alpha\beta + 2i\sqrt{\alpha\beta}(\alpha + \beta)] \right] \right. \\ &+ \left. \frac{\partial^2 \zeta[V_s^*]}{\partial \widehat{V}_s^2} \frac{\partial \zeta[V_r^*]}{\partial \widehat{V}_r} (3\alpha\beta + 2i\sqrt{\alpha\beta}(\alpha + \beta)) \left[-(\alpha + \beta)^2 \frac{\partial^2 \zeta[V_r^*]}{\partial \widehat{V}_r^2} \right. \right. \\ &+ \left. \left. (\alpha\beta)^2 (\nu_{sr}^*)^2 \nu_{rs}^* \frac{\partial^2 \zeta[V_s^*]}{\partial \widehat{V}_s^2} (\frac{\partial \zeta[V_r^*]}{\partial \widehat{V}_r})^3 \right] \right). \end{aligned} \quad (D.41)$$

The third order nonlinearities are given by the following:

$$N_3^0(e_0, e_0, \bar{e}_0) = -\frac{1}{3!} \begin{pmatrix} 0 & i\sqrt{\alpha\beta}(\alpha\beta)^2(\alpha + \beta)^3 \nu_{sr}^* \frac{\partial^3 \zeta[V_r^*]}{\partial \widehat{V}_r^3} \\ 0 & (\alpha\beta)^4 (\nu_{sr}^*)^3 \nu_{rs}^* \frac{\partial^3 \zeta[V_s^*]}{\partial \widehat{V}_s^3} (\frac{\partial \zeta[V_r^*]}{\partial \widehat{V}_r})^3 \end{pmatrix}$$

and

$$\begin{aligned} \langle N_3^0(e_0, e_0, \bar{e}_0), \bar{f}_0 \rangle &= -\frac{(\alpha\beta)^3 \nu_{sr}^* \nu_{rs}}{3!} \left((\alpha + \beta)^2 \frac{\partial \zeta[V_s^*]}{\partial \widehat{V}_s} \frac{\partial^3 \zeta[V_r^*]}{\partial \widehat{V}_r^3} \right. \\ &+ \left. (\nu_{sr})^2 (\alpha\beta) \frac{\partial^3 \zeta[V_s^*]}{\partial \widehat{V}_s^3} (\frac{\partial \zeta[V_r^*]}{\partial \widehat{V}_r})^3 \right) \end{aligned}$$

D.4 Poincaré surface coordinates of the piecewise linear RKII set

The following table contains the Poincaré surface of coordinates determined for the piecewise linear RKII set. Each entry corresponds to the coordinates and the switching times for the hyperplanes S_1^1 , S_0^2 , S_1^3 and S_0^0 (refer to chapter 6 for discussion).

Switching times	Poincaré surface coordinates
$t_1^* = 5.8\text{e-}02$	$x_1^* = [-1.48\text{e-}02, 7.41\text{e-}01, 8.39\text{e-}04, -4.19\text{e-}02]^T$
$t_2^* = 1.6\text{e-}02$	$x_2^* = [-1.38\text{e-}02, 6.88\text{e-}01, 1.57\text{e-}02, 1.87\text{e+}01]^T$
$t_3^* = 3.0\text{e-}03$	$x_3^* = [-1.58\text{e-}02, -2.5\text{e+}00, 7.01\text{e-}02, 3.42\text{e+}01]^T$
$t_4^* = 6.3\text{e-}02$	$x_4^* = [-1.90\text{e-}01, -5.15\text{e-}01, 1.45\text{e-}02, -7.25\text{e-}01]^T$

Table D.1: Switching times and coordinates intersecting the hyperplanes: S_1^1 , S_0^2 , S_1^3 and S_0^0 .

Bibliography

- [1] M. Abeles. *Local cortical circuits: an electrophysiological study*. Springer, Berlin Heidelberg New York, 1982.
- [2] M. Abramowitz and A. S. Irene. *Handbook of Mathematical Functions with formulas, graphs, and mathematical tables*. Dover Publications, INC., New York, 1972.
- [3] E. Adrian. The impulses produced by sensory nerve endings: Part 2. the response of a single end organ. *Journal of Physiology*, 61:151–71, 1926.
- [4] S. Amari. Dynamics of pattern formation in lateral-inhibition type neural fields. *Biol. Ceybern*, 27:77–87, 1977.
- [5] R. G. Andrezejak, K. Laehnertz, F. Mormann, C. Rieke, P. David, and C. E. Elger. Indications of nonlinear deterministic and finite-dimensional structure in time series of brain electrical activity: dependence on recording region and brain state. *Physical Review E*, 64(061907), 2001.
- [6] J. F. Annegers. *The epidemiology of epilepsy*. Wyllie E., 2001.
- [7] J. F. Annegers. *The treatment of epilepsy: Principles and practice*. Philadelphia, Lippincott Williams and Wilkins, 3 edition edition, 2001.
- [8] H. Arndt. Numerical solution of retarded initial value problems: Local and global error and stepsize control. *Numerical Mathematics*, 43:343–360, 1989.
- [9] G. Avazani, M. Curtis, S. Franceschetti, G. Sancini, and R. Spreafico. Cortical versus thalamic mechanisms underlying spike and wave discharges in gaers. *Epilepsy Res.*, 26:37–44, 1996.

- [10] G. Avazani, M. de Curtis, F. Panzica, and R. Spreafico. Intrinsic properties of nucleus reticularis thalami neurons of the rat studied in vitro. *Physical Review E*, 416:111–12, 1989.
- [11] G. Avazani, M. Vergnes, R. Spreafico, and C. Marescaux. Calcium-independent regulation of genetically determined spike and waves by reticular nucleus of rats. *Epilepsia*, 34:1–7, 1993.
- [12] C. T. H. Baker, C. A. H. Paul, and D. R. Willie. A bibliography on the numerical solution of delay differential equations. Technical Report 269, University of Manchester, 1995.
- [13] T. Bal, M. Von Krosigk, and D. A. McCormick. Role of the ferret perigeniculate nucleus in the generation of synchronized oscillations in vitro. *J. Physiol*, 483:665–85, 1995.
- [14] T. Bal and D. A. McCormick. Mechanisms of oscillatory activity in guinea-pig nucleus reticularis thalami in vitro, a mammalian pacemaker. *Journal of Physiology*, 468:669–91, 1993.
- [15] T. Bal and D. A. McCormick. What stops synchronized thalamocortical oscillations? *Neuron*, 17:297–308, 1996.
- [16] E. Behrens, J. Schramm, J. Zentner, and R. König. Surgical and neurological complications in a series of 708 epilepsy surgery procedures. *Neurosurgery*, 41(1)(1-9), 1997.
- [17] M. J. Berry, D. K. Warland, and M. Meister. The structure and precision of retinal spike trains. *Proc. Natl. Acad. Sci. USA*, 94(10):5411–5416, 1997.
- [18] A. Borst and F. E. Theunissen. Information theory and neural coding. *Nat. Neurosci.*, 2(11):947–957, 1999.
- [19] V. Braitenberg and A. Schüz. *Anatomy of the cortex: statistics and geometry*. Springer-Verlag, New York, 1991.
- [20] F. Brauer and J. A. Nohel. *The qualitative theory of ordinary differential equations*. W. A. Benjamin, Inc., 1969.

- [21] M. Breakspear, J. A. Roberts, J. R. Terry, S. Rodrigues, N. Mahant, and P. A. Robinson. A unifying explanation of primary generalized seizures through nonlinear brain modeling and bifurcation analysis. *Cerebral Cortex*, 16:1296–1313, 2006.
- [22] M. Breakspear and J. R. Terry. Topographic organization of nonlinear interdependence in multichannel human EEG. *NeuroImage*, 16:822–835, 2001.
- [23] M. Breakspear and J. R. Terry. Nonlinear interdependence in neural systems: Motivation, theory and relevance. *International J. Neuroscience*, 112:1263–1284, 2002.
- [24] P. Broca and C. E. Brown-Sequard. Propriété et fonctions de la moelle épinière: Rapport quelques experiences de M. Borwn-sequard. *Sequard. Lu a la Société de biologies le 21 juillet (Bonaventure et Ducsois)*, 1:2001, 1855.
- [25] D. Buck, G. A. Baker, and A. Jacoby. Patients experiences of injury as a result of epilepsy. *Epilepsia*, 38:439–444, 1997.
- [26] T. Holmes Bullock. Grades in neural complexity: How large is span? *Integ. and Comp. Biol.*, 42:757–761, 2002.
- [27] G. Buzsaki, R. G. Bickford, G. Ponomareff, L. J. Thal, R. Mandel, and F. H. Gage. Nucleus basalis and thalamic control of neocortical activity in the freely moving rat. *J. Neurosci.*, 8:4007–26, 1988.
- [28] Jorge Manuel Mendes Silva Gonçalves. *Constructive Global Analysis of Hybrid Systems*. PhD thesis, Massachusetts Institute of Technology, Dept. Of Electrical Engineering and Computer, 2000.
- [29] M. Casdagli. Nonlinear prediction of chaotic time series. *Physica D*, 35:335–357, 1989.
- [30] H. Chang and W. J. Freeman. Parameter optimization in models of the olfactory neural system. *Neural Networks*, 9(1):1–14, 1996.
- [31] A. V. Chizhov. The model of neuron populations as a unit of a large-scale network. *Neurocomput. Design Appl.*, 2-3(60-68), 2004.
- [32] A. V. Chizhov, L. J. Graham, and A. A. Turbin. Simulation of neural population dynamics with a refractory density approach and a conductance-based threshold neuron model. *Neurocomputing*, 70:252–262, 2006.

- [33] P. S. Churchland and T. J. Sejnowski. Prospective of cognitive neuroscience. *Science*, 247:741–745, 1988.
- [34] O. C. Cockerell, A. L. Johnson, J. W. Sander, Y. M. Hart, D. M. Goodridge, and S. D. Shorvon. Mortality from epilepsy: results from a prospective population-based study. *Lancet*, 344:918–921, 1994.
- [35] B. W. Connors and Y. Amitai. *Generation of epileptiform discharges by local circuits in neocortex: Epilepsy: Models, Mechanisms and Concepts*. Cambridge University Press, 1993.
- [36] A. D. Contreras. *Oscillatory properties of cortical and thalamic neurons and the generation of synchronized rhythmicity in the corticothalamic network*. PhD thesis, Laval University, Quebec, Canada, 1996.
- [37] S. Coombes and M.R. Owen. Evans functions for integral neural field equations with heaviside firing rate function. *SIAM Journal on Applied Dynamical Systems*, 34:574–600, 2004.
- [38] O. Creutzfeld and J. Houchin. *Neuronal basis of EEG-waves in: Handbook of Electroencephalography and Clinical Neurophysiology*, volume 2. Elsevier Amsterdam, 1974.
- [39] V. Crunelli and N. Leresche. Childhood absence epilepsy: genes, channels, neurons and networks. *Nat. Rev. Neurosci.*, 3:371–382, 2002.
- [40] M. Damming and F. Mitschke. Estimation of lyapunov exponents from time series: the stochastic case. *Physica Letters A*, 178:385–394, 1993.
- [41] A. Destexhe, A. D. Contreras, and T. J. Sejnowski. A model for 8-10hz spindling in interconnected thalamic relay and reticularis neurons. *Biophysics Journal*, 65(2474-8), 1993.
- [42] A. Destexhe, D. Contreras, and M. Steriade. Mecahanisms underlying the synchronizing action of corticothalamic feedback through inhibition of thalamic relay cells. *J. Neurophysiol.*, 79:999–1016, 1998.
- [43] A. Destexhe and T. J. Sejnowski. *Thalamocortical Assemblies. How ion channels, single neurons and large-scale networks organize sleep oscillations*. Oxford University Press, 2001.

- [44] E. J. Doedel. AUTO, a program for the automatic bifurcation analysis of autonomous systems. *Congr. Numer.*, 30:265–384, 1981.
- [45] E. J. Doedel. Numerical analysis of bifurcation problems. Technical report, Hamburg-Hamburg Summer Schools, 1999.
- [46] E. J. Doedel, A. R. Champneys, T. F. Fairgrieve, Y. A. Kuznetsov, B. Sandstede, and X. J. Wang. AUTO97: Continuation and bifurcation software for ordinary differential equations (with homcont). Technical report, Computer Science, Concordia University, Montreal, Canada, 1997.
- [47] J. Eggert and J. L. van Hemmen. Modeling neuronal assemblies: Theory and implementation. *Neural Computation*, 13:1923–1974, 2001.
- [48] M. Elhilali, J. B. Fritz, D. J. Klein, J. Z. Simon, and S. A. Shamma. Dynamics of precise spike timing in primary auditory cortex. *J. Neurosci.*, 24(5):1159–1172, 2004.
- [49] C. Elphick, E. Tirapegui, M. E. Brachet, P. Couillet, and G. Iooss. A simple global characterization for normal forms of singular vector fields. *Physica D*, 29:95–127, 1987.
- [50] L. E. El'sgol'ts and S. B. Norkin. *Introduction to the Theory of Differential Equations with Deviating Arguments*. Academics Press, New York, 1971.
- [51] K. Engelborghs, T. Luzyanina, and G. Samaey. DDE-BIFTOOL v.200 user manual: A Matlab package for bifurcation analysis of delay differential equations. Technical report tw-330, Department of Computer Science, K. U. Leuven, Leuven, Belgium, 2001.
- [52] B. Ermentrout. *Simulating, Analyzing, and Animating Dynamical Systems, A Guide to XPPAUT for Researchers and Students*. University of Pittsburgh, Siam, 2002.
- [53] R. H. Mattson et. al. Comparison of carbamazepine, phenobarbital, phenytoin and primidone in partial and secondarily generalized tonic-clonic seizures. *N. Engl. J. Med*, 313:145–151, 1985.
- [54] M. Feucht, U. Moller, H. Witte, K. Schmidt, M. Arnold, F. Benninger, K. Steinberger, and M. H. Friedrich. Nonlinear dynamics of 3hz spike-and-wave discharges recorded during typical absence seizures in children. *Cerebral Cortex*, 8:524–533, 1998.

- [55] A. Filippov. *Differential equations with discontinuous right-hand sides*. Kluwer Academic Publishers, Dordrecht, 1988.
- [56] J. A. Fodor and Z. Pylyshyn. Connectionism and cognitive architecture: a critical analysis. *Cognition*, 28:3–71, 1988.
- [57] W. J. Freeman. *Mass Action In The Nervous System. Examination of the Neurophysiological Basis of Adaptive Behavior through the EEG*. Academic Press New York San Francisco London, 1975.
- [58] Y. Futatsugi and J. J. Riviello Jr. Mechanisms of generalized absence epilepsy. *Brain Dev*, 20:795–9, 1998.
- [59] F. R. Gantmacher. *Application Of The Theory Of Matrices*. Interscience Pub. New York, 1959.
- [60] W. R. Garnett. *Epilepsy in Pharmacotherapy: A Pathophysiologic Approach*, volume 3rd edition. Appleton and Lange, Stamford CT, 1997.
- [61] T. V. Gelder. The dynamical hypothesis in cognitive science. *Behavioral and Brain Sciences*, 21:615–665, 1988.
- [62] W. Gerstner and W. M. Kistler. *Spiking Neuron Models: single neurons, populations, plasticity*. Cambridge university Press, 2002.
- [63] J. Guckenheimer and P. Holmes. *Nonlinear Oscillations, Dynamical Systems and Bifurcation of Vector Fields*, volume 41 of *Applied Mathematical Science*. Springer, New York, 1983.
- [64] P. Gloor, M. Avoli, and G. Kostopoulos. *Thalamocortical relationships in generalized epilepsy with bilaterally synchronous spike-and-wave discharge*. In *Generalized Epilepsy, Neurobiological Approaches*. Boston: Birkhauser, 1990.
- [65] P. Gloor and R. G. Fariello. Generalized epilepsy: some of its cellular mechanisms differ from those of focal epilepsy. *Trends in Neuroscience*, 11:63–68, 1988.
- [66] M. Golubitsky, I. Stewart, and D. G. Schaeffer. *Singularities and groups in bifurcation theory*, volume I. Applied Mathematical Sciences, Springer Verlag, 1985.

- [67] L. M. Harrison, O. David, and K. J. Friston. Stochastic models of neuronal dynamics. *Phil. Trans. R. Soc. B*, 360(1457):1075–1091, 2005.
- [68] D. Harter and R. Kozma. Chaotic neurodynamics for autonomous agents. *IEEE Transactions on Neural Networks*, 16(3):565–579, 2005.
- [69] A. Hassibi and S. Boyd. Quadratic stabilization and control of piecewise-linear systems. *American Control Conference*, 6:3659–3664, 1998.
- [70] M. S. Hämmäläinen, R. Hari, R. J. Knuutila, and O. V. Lounasmaa. Magnetoencephalography — theory, instrumentation, and applications to noninvasive studies of the working human brain. *Rev. Mod. Phys.*, 65:413–497, 1993.
- [71] J. Heller, J. A. Hertz, T. W. Kjaer, and B. J. Richmond. Information flow and temporal coding in primate pattern vision. *J. Comput. Neurosci.*, 2(3):175–193, 1995.
- [72] I. A. Hiskens and M. A. Pai. Trajectory sensitivity analysis of hybrid systems. *IEEE Trans. on Circuits and Systems I*, 47(2):204–220, 2000.
- [73] A. L. Hodgkin and A. F. Huxley. A quantitative description of membrane current and its application to conduction and excitation in nerve. *Journal of Physiology*, 117:500–44, 1952.
- [74] E. Hopf. Bifurcations of a periodic solution from a stationary solution of a system of differential equations. *Berichten der Mathematische Physikalische Klassen der Sachsischen Acad. Wissenschaften, Leipzig*, XCIV:3–22, 1942.
- [75] D. A. Hosford, S. Clark, Z. Cao, W. A. Wilson Jr, and F. H Lin et al. The role of $GABA_B$ receptor activation in absence seizures of lethargic (ih/ih) mice. *Science*, 257:398–401, 1992.
- [76] J. I. Hubbard, R. Llinas, and D. M. J. Quastel. *Electrophysiological analysis of synaptic transmission*. London: Edward Arnold, 1969.
- [77] L. Ingber. Statistical mechanics of neocortical interactions: A scaling paradigm applied to electroencephalography. *Physical Review A*, 44(6):4017–4060, 1991.
- [78] G. Iooss and M. Adelmeyer. *Topics in Bifurcation Theory and Applications, advanced series in nonlinear dynamics*, volume 3. World Scientific, Singapore, 1992.

- [79] H. Jahnsen and R. R. Llinás. Electrophysiological properties of guinea-pig thalamic neurons: An invitro study. *Journal of Physiology*, 349:205–26, 1984.
- [80] H. Jahnsen and R. R. Llinás. Ionic basis for the electroresponsiveness and oscillatory properties of guinea-pig thalamic neurons in vitro. *Journal of Physiology*, 349:227–47, 1984.
- [81] H. H. Jasper and J. Droogleever-Fortuyn. Experimental studies on the functional anatomy of petit mal epilepsy. *Assoc Res Nerv Ment Dis*, 26:272–98, 1947.
- [82] U. Jönsson, C. Kao, A. Megretski, and A. Rantzer. *A Guide to IQC β : A Matlab toolbox for Robust Stability and Performance Analysis*.
- [83] V. K. Jirsa. Connectivity and dynamics of neural information processing. *Neuroinformatics*, 2(1-22), 2004.
- [84] V. K. Jirsa and H. Haken. Field theory of electromagnetic brain activity. *Phys. Rev. Lett*, 77:960, 1996.
- [85] D. W. Jordan and P. Smith. *Nonlinear Ordinary Differential Equations*. Oxford University Press, 1999.
- [86] E. R. Kandel. *Principles of Neuroscience*. Amsterdam: Elsevier Science publication, 1991.
- [87] J. Keener and J. Sneyd. *Interdisciplinary applied mathematics, mathematical biology, mathematical physiology*, volume 8. Springer-Verlag, New York, 1998.
- [88] P. Kellaway. Sleep and epilepsy. *Epilepsia*, 26(S):15–30, 1985.
- [89] H. B. Keller. *Numerical solution of bifurcation and nonlinear eigenvalue problems in Applications of Bifurcation theory*. Academic Press, New York, 1977.
- [90] A. V Kim and V. G. Pimenov. Numerical methods for time-delay systems on the basis of i-smooth analysis. *Computational Mathematics*, 1:193–196, 1997.
- [91] U. Kim, M. V. Sanchez-Vives, and D. A. McCormick. Functional dynamics of GABAergic inhibition in the thalamus. *Science*, 278:130–34, 1997.

- [92] W. Klimesch, M. Doppelmayr, D. Rohm, D. Pollhuber, and W. Stadler. Simultaneous desynchronization and synchronization of different alpha responses in the human electroencephalograph: A neglected paradox? *Neurosci. Lett.*, 1:97–100, 2000.
- [93] G. K. Kostopoulos. Involvement of thalamocortical system in epileptic loss of consciousness. *Epilepsia*, 42:13–9, 2001.
- [94] R. Kozma and W. J. Freeman. Chaotic resonance - methods and applications for robust classification of noisy and variable patterns. *International Journal Bifurcation and Chaos*, 11(6):2307–2322, 2001.
- [95] M. Von Krosigk, T. Bal, and D. A. McCormick. Cellular mechanisms of a synchronized oscillation in the thalamus. *Science*, 261:361–4, 1993.
- [96] M. Kubicek and M. Marek. *Computational Methods in Bifurcation Theory and Dissipative Structures*. Springer-Verlag, 1983.
- [97] Y. Kuznetsov, L. Kuznetsov, and J. Marsde. *Elements of Applied Bifurcation theory*. Springer-Verlag, New York, 1998.
- [98] W. F. Langford. Periodic and steady state interactions lead to tori. *SIAM J. Appl. Math.*, 37:22–48, 1979.
- [99] M. S. Lewicki. A review of methods of spike sorting with wavelets and superparamagnetic clustering. *Comput. Neural Sys.*, 9(R):53–78, 1998.
- [100] Z. Liu, M. Vergnes, A. Depaulis, and C. Marescaux. Involvement of intrathalamic $GABA_B$ neurotransmission in the control of absence seizures in the rat. *Neuroscience*, 48:87–93, 1992.
- [101] T. Lu and X. Wang. Information content of auditory cortical responses to time-varying acoustic stimuli. *J. Neurophysiol.*, 91(1):301–313, 2004.
- [102] H. J. Luhmann, T. Mittmann, G. van Luijtelaar, and U. Heinemann. Impairment of intracortical GABAergic inhibition in a rat model of absence epilepsy. *Epilepsy Res.*, 22:43–51, 1995.
- [103] Z. F. Mainen and T. J. Sejnowski. Reliability of spike timing in neocortical neurons. *Science*, 14(11):2531–2560, 2002.

- [104] S. Makeig. Mining event-related brain dynamics. *Trends in Cognitive Science*, 8:204–210, 2004.
- [105] E. M. Marcus and C. W. Watson. Bilateral synchronous spike wave electrographic patterns in the cat. *Arch Neurol*, 14:601–10, 1966.
- [106] R.M. M. Mattheij and J. Molenaar. *Ordinary Differential Equations in Theory and Practice*. John Wiley and Sons - New york, 1996.
- [107] D. A. McCormick. Neurotransmitter actions in the thalamus and cerebral cortex and their role in neuromodulation of thalamocortical activity. *prog. Neurobiol.*, 39:337–88, 1992.
- [108] D. A. McCormick and H. C Pape. Properties of a hyperpolarization-activated cation current and its role in rhythmic oscillations in thalamic relay neurons. *J. Physiol*, 431:291–318, 1990.
- [109] A. I. Mees. *Dynamics of feedback systems*. Wiley-Interscience, 1981.
- [110] A.I. Mees and L. O. Chua. The Hopf bifurcation theorem and its applications to non-linear oscillations in circuits and systems. *IEEE Trans. on Circuits and Systems*, CAS-26(3):235–254, 1979.
- [111] M. R. Mehta, A. K. Lee, and M. A. Wilson. Role of experience and oscillations in transforming a rate code into a temporal code. *Nature*, 417(6890):741–746, 2002.
- [112] V. B. Mountcastle. An organization principle of cerebral function: The unit module and distributed system. In F. O. Schmit and F. G. Worden, editors, *In The Neuroscience Fourth Study Program*. MIT, Cambridge, MA, 1979.
- [113] P. L. Nunez. *Electric Fields of the Brain*. Oxford University Press, 1981.
- [114] P. L. Nunez. *Neocortical Dynamics and Human EEG Rhythms*. Oxford University Press, 1995.
- [115] J. G. Ojemann. Managing epilepsy III: Surgery for intractable epilepsy. *Nepal Journal of Neuroscience*, 1:92–97, 2004.

- [116] A. Omurtag, B. W. Knight, and L. Sirovich. On the simulation of large populations of neurons. *Journal of computational neuroscience*, 8:51–63, 2000.
- [117] Commission on Classification and Terminology of the International League Against Epilepsy. Proposal for revised classification of epilepsies and epileptic syndromes. *Epilepsia*, 30:389–99, 1989.
- [118] W. W. Orrison, J. D. Lewine, J. A. Sanders, and M. F. Harthshorne. *Functional brain imaging*. Mosby Ed., St. louis, 1995.
- [119] T. S. Parker and L.O. Chua. *Practical Numerical Algorithms for Chaotic Systems*. Springer-Verlag, New York, NY, 1989.
- [120] C. A. H. Paul. Developing a delay differential equation solver. *Applied Numerical Mathematics*, 9:403–414, 1992.
- [121] C. A. H. Paul. The treatement of derivative discontinuities in differential equations. Technical Report Report 337, University of Manchester, Dep. of Mathematics, 1999.
- [122] S. Pettersson and B. Lennartson. An LMI approach for stability analysis of nonlinear systems. In Department of Control Engineering, editor, *Conf. ID 596*. Proc. of the 4th European Control Conference, Brussels, Belgium, 1997.
- [123] D. Pinault, N. Leresche, S. Charpier, J. M. Deniau, C. Marescaux, M. Vergnes, and V. Crunelli. Intracellular recordings in thalamic neurones during spontaneous spike spike and wave discharges in rats with absence epilepsy. *Physiol*, 509:449–456, 1998.
- [124] D. J. Pinto, J. C. Brumberg, D. J. Simons, and G. B. Ermentrout. A quantitative population model of whisker barrels: re-examining the wilson-cowan equations. *J. Comput. Neurosci.*, 3:247–264, 1996.
- [125] R. J. Porter. The absence epilepsies. *Epilepsia*, 34:S42–48, 1993.
- [126] W. H. Press, B. P. Flannery, S. A. Teukolsky S. A., and W. T. Vetterling. *Numerical Recipes in C*. Cambridge university Press, 2 edition edition, 1992.
- [127] D. Prichard and J. Threiler. Generating surrogate data for time series with several simultaneously measured variables. *Phys. Rev. Lett*, 73:951–954, 1994.

- [128] J. Principe, V. Tavares, J. Harris, and W. Freeman. Design and implementation of a biologically realistic olfactory cortex in analog VLSI. *Proc. IEEE*, 89(7):569–571, 2001.
- [129] W. Rall and G. M. Shepherd. Theoretical reconstruction of field potentials and dendro-dendritic synaptic interactions in olfactory bulb. *J. Neurophysiol.*, 31:884–915, 1968.
- [130] P. A. Robinson, C. J. Rennie C, and J. J. Wright. Propagation and stability of waves of electrical activity in the cerebral cortex. *Physical Review E*, 56:826, 1997.
- [131] P. A. Robinson, C. J. Rennie, and D. L. Rowe. Dynamics of large-scale brain activity in normal arousal states and epileptic seizures. *Physical Review E*, 65(041924), 2002.
- [132] P. A. Robinson, C. J. Rennie, D. L. Rowe, and S. C. O Connor. Estimation of multiscale neurophysiologic parameters by electroencephalographic means. *Human Brain Mapping*, 23:53–72, 2004.
- [133] P. A. Robinson, C. J. Rennie, J. J. Wright, H. Bahramali, E. Gordon, and D. L. Rowe. Prediction of electroencephalographic spectra from neurophysiology. *Physical Review E*, 63(021903), 2001.
- [134] S. Rodrigues, J. Gonçalves, and J. R. Terry. Limit cycle oscillations in a macroscopic neuronal population model. II. normal forms and global stability. Submitted to *Physica D*, August 2006.
- [135] S. Rodrigues and J. R. Terry. Limit cycle oscillations in a macroscopic neuronal population model. I. existence and local stability. Submitted to *Physica D*, August 2006.
- [136] S. Rodrigues, J. R. Terry, and M. Breakspear. On the genesis of spike-wave activity in a mean-field model of human thalamic and cortico-thalamic dynamics. *Physics Letters A*, 355:352–357, 2005.
- [137] P. E. Roland. *Brain Activation*. New York: John Wiley and Sons, 1993.
- [138] D. L. Rowe, P. A. Robinson, and C. J. Rennie. Estimation of neurophysiologic parameters from the waking using a biophysical model of brain dynamics. *Journal of Theoretical Biology*, 231:413–433, 2004.
- [139] M. V. Sanchez-Vives, T. Bal, and D. A. McCormick. Inhibitory interactions between perigeniculate gabaergic neurons. *J. Neurosci.*, 17:8894–908, 1997.

- [140] S. C. Schachter. Epilepsy. *Neurol clin*, 19:57–78, 2001.
- [141] N. D. Schiff, J. D. Victor, A. Canel, and D. R. Labar. Characteristic nonlinearities of the 3/s ictal electroencephalogram identified by nonlinear autoregressive analysis. *Biol. Ceybern*, 72:519–526, 1995.
- [142] R. Seydel. *From Equilibrium to Chaos. Pratical Bifurcation and Stability Analysis*, volume second edition. Springer-Verlag, New York, 1984.
- [143] G. M. Shepherd. *Neurobiology*. Oxford University Press, New York, 1994.
- [144] L. Silva. *Electroencephalography: Basic Principles, Clinical Applications, and Related Fields.*, volume 4th edition. Williams and Wilkins, Baltimore, 1999.
- [145] O. C. Snead. Basic mechanisms of generalized absence seizures. *Ann Neurol*, 37:147–57, 1995.
- [146] V. S. Sohal, M. M. Huntsman, and J. R. Huguenard. Reciprocal inhibitory connections regulate the spatiotemporal properties of intrathalamic oscillations. *J. Neurosci.*, 20:1735–45, 2000.
- [147] D. C. Somers, S. B. Nelson, and M. Sur. An emergent model of orientation selectivity in cat visual cortex simple cells. *J. Neurosci.*, 15:5448–5465, 1995.
- [148] C. J. Stam and W. Pritchard. Dynamics underlying rhythmic and non-rhythmic variants of abnormal, waking delta activity. *Int. J. Psychophysiol*, 34:5–20, 1997.
- [149] A. Stepanyants and D. B. Chklovskii. Neurogeometry and potential synaptic connectivity. *Trends in Neuroscience*, 28(7):387–394, 2005.
- [150] M. Steriade. Interneuronal epileptic discharges related to spike-and-wave cortical seizures in behaving monkeys. *Electroencephal. Clin. Neurophysiol.*, 37:247–63, 1974.
- [151] M. Steriade. *Neuronal substrates of sleep and epilepsy*. Cambridge University Press, 2003.
- [152] M. Steriade, F. Amzica, D. Neckelmann, and I. Timofeev. Spike-wave complexes and fast components of cortically generated seizures. ii. extra- and intracellular patterns. *J. Neurophysiol.*, 80:1456–79, 1998.

- [153] M. Steriade and R. W. McCarley and. *Brainstem Control of Wakefulness and Sleep*. Plenum Press, New York, 1990.
- [154] M. Steriade and D. Contreras. Spike-wave complexes and fast components of cortically generated seizures. I. role of neocortex and thalamus. *J. Neurophysiol.*, 80:1439–55, 1998.
- [155] M. Steriade, D. Contreras, and F. Amzica. Synchronised sleep oscillations and their paroxysmal developments. *Trends in Neuroscience*, 17:113–22, 1994.
- [156] M. Steriade, M. Deschenes, L. Domich, and C. Mulle. Abolition of spindle oscillation in thalamic neurons disconnected from nucleus reticularis thalami. *Journal of Neurophysiology*, 54:1473–97, 1985.
- [157] P. Suffczynski. *Neural dynamics underlying brain thalamic oscillations investigated with computational models*. PhD thesis, Institute of experimental physics, department of physics, Warsaw University, 2000.
- [158] J. Szentagothai. The neuron network of the cerebral cortex: a functional interpretation. *Proc. R. Soc. Lond*, 201:219–248, 1978.
- [159] C. P. Taylor and F. E. Dudek. Synchronous neural aftercharges in rat hippocampal slices without active chemical synapses. *Science*, 218:810–812, 1982.
- [160] C. P. Taylor and F. E. Dudek. Excitation of hippocampal pyramidal cells by an electrical field effect. *J. Neurophysiol.*, 52:126–142, 1984.
- [161] J. R. Terry and M. Breakspear. An improved algorithm for the detection of dynamical interdependence in bivariate time series. *Biological Cybernetics*, 88:129–136, 2003.
- [162] J. Threiler, S. Eubank, A. Longtin, B. Galdrikian, and J. Farmer. Testing for nonlinearity: the method of surrogate data. *Physica D*, 58:77–94, 1992.
- [163] D. Ulrich and J. R. Huguenard. $GABA_B$ receptor-mediated responses in GABAergic projection neurones of rat nucleus reticularis thalami in vitro. *J. Physiol*, 493:845–54, 1996.

- [164] J. L Perez Valezquez, M. A. Cortez, O. Carter Snead III, and R. Wennberg. Dynamical regimes underlying epileptiform events: role of instabilities and bifurcations in brain activity. *Physica D*, 186:205–220, 2003.
- [165] J. D. Victor. How the brain uses time to represent and process visual information. *Brain Res.*, 886(1-2):33–46, 2000.
- [166] M. Wehr and G. Laurent. Odour encoding by temporal sequences of firing in oscillating neural assemblies. *Nature*, 384(6605):162–166, 1996.
- [167] D. Williams. A study of thalamic and cortical rhythms in petit mal. *Brain*, 76:50–69, 1953.
- [168] H. R. Wilson and J. D. Cowan. Excitatory and inhibitory interactions in localized populations of model neurons. *Biophysical Journal*, 12:1–24, 1972.
- [169] H. R. Wilson and J. D. Cowan. A mathematical theory of the functional dynamics of cortical and thalamic nervous tissue. *Kybernetik*, 13:55–80, 1973.
- [170] D. Xu and J. C Principe. Dynamical analysis of neural oscillators in an olfactory cortex model. *IEEE Transactions on Neural Networks*, 15(5):1053–1062, 2004.

